

# **Halogen Bonding in Supramolecular Liquid Crystals and its Application in Photonic Sensing**

## **DISSERTATION**

Zur Erlangung des akademischen Grades eines  
Doktor der Naturwissenschaften  
– Dr. rer. nat. –

vorgelegt von

**Matthias Spengler**  
geboren in Gladbeck

Fakultät für Chemie  
Universität Duisburg-Essen

# DuEPublico

Duisburg-Essen Publications online

UNIVERSITÄT  
DUISBURG  
ESSEN

*Offen im Denken*

ub | universitäts  
bibliothek

Diese Dissertation wird via DuEPublico, dem Dokumenten- und Publikationsserver der Universität Duisburg-Essen, zur Verfügung gestellt und liegt auch als Print-Version vor.

**DOI:** 10.17185/duepublico/74157

**URN:** urn:nbn:de:hbz:465-20220302-083559-0

Alle Rechte vorbehalten.





---

The results presented in this thesis were prepared in collaboration with the Faculty of Chemistry of the University of Duisburg-Essen, Germany, under supervision of Jun. Prof. Dr. Michael Giese in the time from November 2016 to December 2020.

First Reviewer: Jun. Prof. Dr. Michael Giese

Second Reviewer: Prof. Dr. Gebhard Haberhauer

Date of oral examination: 08.03.2021

---



---

## Some parts of this thesis have already been published or presented:

Saccone, M.; Spengler, M.; Pfletscher, M.; Kuntze, K.; Virkki, M.; Wölper, C.; Gehrke, R.; Jansen, G.; Metrangolo, P.; Priimagi, A.; Giese, M., 'Photo-Responsive Halogen-Bonded Liquid Crystals: The Role of Aromatic Fluorine Substitution', *Chemistry of Materials* **2019**, 31 (2), 462–470.

Giese, M.; Spengler, M., 'Cellulose Nanocrystals in Nanoarchitectonics – Towards Photonic Functional Materials', *Molecular Systems Design & Engineering* **2019**, 4 (1), 29–48.

Spengler, M.; Dong, R. Y.; Michal, C. A.; Hamad, W. Y.; MacLachlan, M. J.; Giese, M., 'Hydrogen-Bonded Liquid Crystals in Confined Spaces – Toward Photonic Hybrid Materials', *Advanced Functional Materials* **2018**, 28 (26).

Quintieri, G.; Saccone, M.; Spengler, M.; Giese, M.; Gröschel, A. H., 'Supramolecular Modification of ABC Triblock Terpolymers in Confinement Assembly', *Nanomaterials* **2018**, 8 (12).

Dong, R. Y.; Michal, C. A.; Saccone, M.; Spengler, M.; Wölper, C.; Giese, M., 'On the blue phase structure of hydrogen-bonded liquid crystals via  $^{19}\text{F}$  NMR', *Chemical Physics Letters* **2018**, 710, 39–44.

Spengler, M.; Dong, R. Y.; Michal, C. A.; Pfletscher, M.; Giese, M., 'Fluorination of Supramolecular Liquid Crystals – Tuning Tool and Analytical Probe', *Journal of Materials Chemistry C* **2017**, 5 (9), 235–2239.

### Poster Presentations

- 06/2019 International Symposium on Macrocyclic and Supramolecular Chemistry 2019 (ISMSC), Lecce, Italy.
- 03/2019 German Liquid Crystal Conference 2019, Paderborn.
- 11/2019 CENIDE Annual Meeting 2019, Duisburg.
- 11/2018 CENIDE Annual Meeting 2018, Essen.
- 11/2017 CENIDE Annual Meeting 2017, Duisburg.
- 04/2017 MAINZ Masterclass on 'Supramolecular Functional Materials'.
- 04/2017 2<sup>nd</sup> German-British Liquid Crystal Conference, Würzburg.
- 04/2017 JCF Spring Symposium 2017, Johannes-Gutenberg-Universität Mainz.
- 02/2017 SupraChem, RWTH Aachen.

### Oral Presentations

- 01/2019 New Year's Colloquium, Universität Duisburg-Essen.
- 02/2018 CENIDE Conference 2018, Bergisch-Gladbach.
- 11/2017 CENIDE Annual Meeting, Duisburg.
- 03/2017 JCF Spring Symposium, Johannes-Gutenberg-Universität Mainz.

### Bachelor Theses

- 08/2017 Rudolph, K., „Nichtklassische Wasserstoffbrückenbindungen in supramolekularen Flüssigkristallen“
  - 08/2018 Ernst, S. „Induktion von Chiralität in supramolekularen Flüssigkristallen über Halogenbindungen“
-



---

*Für meine Familie*

---



---

## Table of Contents

---

<b>Abbreviations</b>	<b>XIII</b>
<b>1. Introduction</b>	<b>1</b>
1.1 Supramolecular Chemistry	1
1.2 The Halogen Bond	1
1.2.1 $\sigma$ -Hole Theory	2
1.2.2 Directionality	3
1.2.3 Tunability	4
1.2.4 Hydrophobicity	7
1.3 Liquid Crystals	7
1.3.1 Classification of Liquid Crystals	7
1.3.2 Chirality in Liquid Crystals	10
1.3.3 Supramolecular Liquid Crystals	14
<b>2. Idea and Concept</b>	<b>19</b>
<b>3. Results and Discussion</b>	<b>21</b>
3.1 Fluorination of Halogen-Bonded Liquid Crystals	21
3.1.1 Synthesis of XB-Donor and Acceptor Molecules	22
3.1.2 Formation of Supramolecular Assemblies	23
3.1.3 Mesomorphic Behavior	31
3.1.4 Photo-Physical Properties	37
3.1.5 Conclusion	44
3.2 Induction of Chirality using Halogen-Bonded Assemblies	46
3.2.1 Halogen-Bonded Chiral Liquid Crystals	47
3.2.2 Mesomorphic Behavior of Chiral Assemblies	48
3.2.3 Induction of Chirality in Pristine Materials	53
3.2.4 Induction of Chirality in 5CB	55
3.2.5 Conclusions	59
3.3 Chirality Transfer for Sensing Applications	61
3.3.1 Synthesis of the Chiral Dopants	64
3.3.2 Determination of HTP Values	68
3.3.3 Manipulation of the Photonic Properties	70
3.3.4 Gas sensing	74
3.3.5 Conclusions	82
3.4 Halogen Bonding for Sensing Applications	84

---

3.4.1	Synthesis of Halogen Bond Acceptor Dopants <b>L4</b> and <b>L4Cu</b>	85
3.4.2	HTP and Structural Color	86
3.4.3	Conclusions	92
<b>4.</b>	<b>Summary and Outlook</b>	<b>93</b>
<b>5.</b>	<b>Zusammenfassung und Ausblick</b>	<b>97</b>
<b>6.</b>	<b>Experimental Section</b>	<b>103</b>
6.1	Materials and Methods	103
6.2	Analytical Methods	104
6.3	Synthetic Procedures and Analytical Data	109
6.3.1	Synthesis of Amine Precursor <b>23</b>	109
6.3.2	Synthesis of XB-Donator and XB-Acceptor Precursors	111
6.3.3	Synthesis of XB-Donator and XB-Acceptor Molecules	117
6.3.4	Formation of Halogen-Bonded Complexes	135
6.3.5	Synthesis of Chiral Dopants for Sensing Applications	143
6.3.6	Synthesis of BINIM Dopants <b>L1</b> – <b>L4</b>	150
6.3.7	Synthesis of BINIM Copper Complexes <b>L1Cu</b> – <b>L4Cu</b>	153
6.3.8	Synthesis of 4-Octyloxy-2,3,5,6-tetrafluoroiodophenol ( <b>IC8</b> )	155
6.3.9	Formation of XB-bonded BINIM complexes	156
<b>7.</b>	<b>Appendix</b>	<b>159</b>
7.1	Supplementary Information to Chapter 3.1.2	159
7.2	Supplementary Information to Chapter 3.1.3	162
7.3	Supplementary Information to Chapter 3.1.4	167
7.4	Supplementary Information to Chapter 3.2.2	169
7.5	Supplementary Information to Chapter 3.2.3	175
7.6	Supplementary Information to Chapter 3.3	176
7.1	Supplementary Information to Chapter 3.4	178
<b>8.</b>	<b>Literature</b>	<b>181</b>
<b>9.</b>	<b>Acknowledgements</b>	<b>189</b>
<b>10.</b>	<b>Curriculum Vitea</b>	<b>191</b>

---

---

**Abbreviations**


---

°C	degree Celsius	H <sub>2</sub> S	hydrogen sulfide
$\lambda$	wavelength	HB	hydrogen-bond
$\mu$	micro	HR-MS	high resolution mass spectrometry
2D	two-dimensional	HTP	helical twisting power
ACN	acetonitrile	Hz	hertz
BINAM	binaphthyldiamine	I	iodine
BINIM	binaphthyldiimine	<i>I</i>	isotropic
Br	bromine	L	liter
C	carbon	LC	liquid crystal
CB	cyanobiphenyl	LCD	liquid crystal display
CD	circular dichroism	LR-MS	low resolution mass spectrometry
CDCl <sub>3</sub>	deuterated chloroform	M	mega
CHCl <sub>3</sub>	chloroform	m	meter
Cl	chlorine	M	molar
CO	carbon monoxide	MeOH	methanol
CO <sub>2</sub>	carbon dioxide	mg	milligram
CPL	circularly polarized light	min	minute(s)
<i>Cr</i>	crystal	mp	melting point
Cy	cyclohexane	MS	mass spectrometry
d	days	<i>n</i>	reflection order
DCM	dichloromethane	$\vec{n}$	molecular director
DEE	diethyl ether	<i>n</i> <sub>avg</sub>	average refractive index
DI	deionized	<i>N</i>	nematic
DMF	<i>N,N</i> -dimethyl-formamide	<i>N</i> *	chiral nematic
DMSO	<i>N,N</i> -dimethyl-sulfoxide	NBS	<i>N</i> -bromosuccinimide
DSC	differential scanning calorimetry	<i>N</i> <sub>col</sub>	columnar nematic
EA	ethyl acetate	<i>N</i> <sub>D</sub>	discotic nematic
eq.	equivalent	neg.	negative
ESP	electrostatic surface potential	<i>n</i> -hex	<i>n</i> -hexane
<i>et al.</i>	and others	nm	nanometer
EtOH	ethanol	NMR	nuclear magnetic resonance
F	flourine	NO	nitric oxide
g	gram	NO <sub>2</sub>	nitrogen dioxide
h	hour(s)	O	oxygen
H	hydrogen	<i>P</i>	helical pitch

---

POM	polarized optical microscopy
pos.	positive
ppm	parts per million
PVA	polyvinylalcohol
PVP	polyvinylpyrrolidone
r.t.	room temperature
s	second(s)
sat.	saturated
SAXS	small angle x-ray scattering
<i>sCr</i>	soft crystal
<i>Sm</i>	smectic
<i>Sm*</i>	chiral smectic
SMLC	supramolecular liquid crystal
TADDOL	$\alpha,\alpha,\alpha',\alpha'$ -Tetraaryl-1,3-dioxolan-4,5-dimethanol
$T_C$	clearing point temperature
TFA	trifluoro acetic acid
<i>TGB</i>	twist grain boundary
TLC	thin layer chromatography
vs.	versus
WAXS	wide angle x-ray scattering
XB	halogen bond

---

---

## 1. Introduction

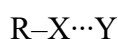
---

### 1.1 Supramolecular Chemistry

Once described by *Jean-Marie Lehn* as “*chemistry beyond the molecule*”, supramolecular chemistry has become one of the most interdisciplinary fields of experimental chemistry.<sup>[1]</sup> It exceeds the consideration of single molecules and instead focuses on the chemistry of non-covalent interactions, self-assembly, and self-organization. The investigation of these processes has led to a completely new field of research and has expanded the scientific scope of functional materials toward “smart materials” with an enormous diversity of tailor-made properties. The understanding of the underlying principles of the self-assembly of small molecules to complex nanostructures such as host-guest complexes<sup>[2-4]</sup>, supramolecular polymers<sup>[5-6]</sup>, or liquid crystals<sup>[7-9]</sup> has had a significant impact on the development of research in this field over the past decades. Processes, where smaller molecules self-organize to superstructures of higher order by ionic, van-der-Waals, or  $\pi$ - $\pi$  interactions, or the formation of hydrogen-bonds, have always been part of biological systems like the self-organization of amphiphilic lipids to cell membranes<sup>[10]</sup>, or the condensation of DNA<sup>[11]</sup> to a densely packed macromolecule. The remarkable advantage of non-covalently bound moieties over classic covalently bound molecules is their flexibility and, depending on the binding motif, switchability of their state of aggregation by external stimuli like changes of the pH value<sup>[12-13]</sup> or UV-irradiation.<sup>[14]</sup> Owing to the reversibility of the aggregation process, single molecules can leave the network and reintegrate into the assembly enabling molecular self-healing as response to macroscopic damages to the material.<sup>[15-18]</sup> The systematic understanding of the underlying structure-property relationships enables the design of materials with tailor-made properties which can be manipulated by the intrinsic molecular information.<sup>[19-20]</sup>

### 1.2 The Halogen Bond

One of the many supramolecular binding motifs is the halogen bond (XB). Although first reported in 1814 already, XBs have only drawn considerable attention of researchers in supramolecular chemistry within the past two decades.<sup>[21]</sup> As alternative for hydrogen bonds (HBs) or as extension of the variety of non-covalent interactions in supramolecular aggregates, it was defined as attractive interaction with high directionality between an electron poor halogen atom (X) and an electron rich XB-acceptor.<sup>[22]</sup> Typically, the halogen bond is described as



with the three dots representing the bond between the electrophilic XB-donator R–X and the electron donating XB-acceptor Y. In this case, Y can be any Lewis base, heteroatom with a lone pair of electrons, or aromatic  $\pi$ -system. In special cases, Y can also be another halogen atom (R–X $\cdots$ X–R). Numerous researchers have since discovered the potential of halogen bonds in different fields of supramolecular chemistry such as crystal engineering<sup>[23-25]</sup>, polymer chemistry<sup>[26-28]</sup> or liquid crystal (LC) design.<sup>[29-34]</sup>

### 1.2.1 $\sigma$ -Hole Theory

In many ways, the halogen bond stands out from other non-covalent interactions due to its advanced and exceptional properties like directionality, tunability and hydrophobicity.<sup>[35]</sup> All these characteristics are the results of the unique electrostatic properties of halogen atoms. In this respect, the electrostatic surface potential (ESP) plays a major role in the description of the halogen bond. The ESP is a property of a system which, for a free halogen atom in its ground state (neutral), is considered as a positive potential equally distributed around the atom.<sup>[36]</sup> This is, since the contribution of the positively charged nucleus outweighs the effects of the dispersed electrons. Whenever one such atom is covalently bound to another atom, its ESP gets anisotropically distributed.<sup>[37]</sup>

For halogen atoms (Figure 1.1), the change of the ESP results in a region of negative ESP in a ring around the plane of the  $\sigma$ -bond (blue) and a positive potential in elongation of the covalent bond (red). This positively polarized area is called the  $\sigma$ -hole which can attractively interact with nucleophilic electron donor sites.<sup>[38-39]</sup>

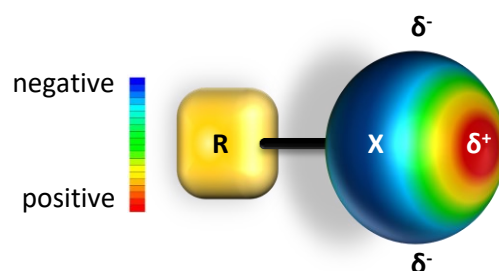


Figure 1.1: Schematic illustration of the  $\sigma$ -hole on a halogen atom (X) which is covalently bound to a residue (R), showing the positive (red), neutral (green), and negative polarization (blue).

Although, early studies already suggested that the halogen bond is a matter of the interaction of electron deficient areas on the halogen atom with electron rich nucleophiles, it was not before *Politzer* and coworkers who first established the term  $\sigma$ -hole.<sup>[40-41]</sup> By calculating the

electrostatic surface potential  $V(r)$  for different  $\text{CF}_3\text{-X}$  ( $\text{X} = \text{F}, \text{Cl}, \text{Br}, \text{I}$ ) derivatives (Figure 1.2), they gave a rational explanation for the ability of halogen atoms to attractively interact with both other halogen atoms and electron donating nucleophiles. Due to the shift of the electron density from the elongated bond axis of the halogen atom to the region perpendicular to the bond axis, the geometry of the halogen atom is changed from formerly spherical to oblate. This process is also known as “polar-flattening” and has been described for several different elements.<sup>[42]</sup> Therefore it is commonly recognized that the electrophilic behavior of a halogen atom can be explained by the presence of a  $\sigma$ -hole, whereas size and magnitude determine the directionality and strength of the halogen bond.

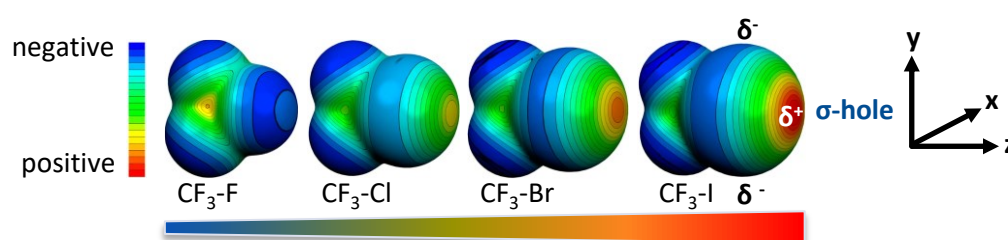


Figure 1.2: Polarization of the XB-donating halogen atom in  $\text{CF}_3\text{-X}$  molecules ( $\text{X} = \text{F}, \text{Cl}, \text{Br}, \text{I}$ ). Adapted with permission from Springer Nature.<sup>[40]</sup> Copyright (2007) Springer Nature.

*Poltzer et al.* explained the nature of the  $\sigma$ -hole with a model of an asymmetric electron configuration of a chlorine atom. While the five remaining valence electrons are usually distributed to equal parts (5/3) onto the three p-orbitals ( $p_x, p_y, p_z$ ), the model assumes that the electrons are distributed in the configuration  $s^2p_x^2p_y^2p_z^1$  with the half-filled  $p_z$ -orbital being directly involved in the covalent bond to the adjacent atom. As a result of this electron distribution, the ESP appears positive in  $-z$  and  $+z$  direction and negative in a belt around the atom in directions  $-x$  and  $+x$  and  $-y$  and  $+y$ , respectively.  $\sigma$ -Hole bonding is known and has been observed for many covalently bound elements of groups V (Pnictogens)<sup>[43-44]</sup>, VI (Chalcogens)<sup>[45-46]</sup>, and VII (Halogens).

### 1.2.2 Directionality

As a result of the anisotropic electron density distribution and the formation of the positively polarized  $\sigma$ -hole, the XB features an especially high directionality which exceeds HBs or ionic interactions.<sup>[32]</sup> When it comes to halogen-halogen interactions ( $\text{R-X}\cdots\text{X-R}$ ), the two halogen atoms involved can preferentially orient according to two different geometries of their  $\text{R-X}\cdots\text{X}$  angles ( $\theta_n$ ). These were classified by *Desiraju* and *Parthasarathy* as Type I

( $\theta_1 = \theta_2$ ) and Type II ( $\theta_1 \approx 90^\circ$ ,  $\theta_2 = 180^\circ$ ) interactions (Figure 1.3A).<sup>[47]</sup> Type I interactions are found for all halogens and are generally the result of close packing where the neutral regions of the involved halogen atoms face each other in order to reduce electrostatic repulsion. Type II interactions, however, are the consequence of attractive forces between the electrophilic (positive) region of one halogen atom with the nucleophilic (negative) region on the other. This kind of interaction results in an orthogonal arrangement of the molecules. According to the definition of the halogen bond (see Section 1.2), only Type II interactions can thus be considered as actual halogen bonds.<sup>[22, 48]</sup> The strong amphoteric character of the polarized halogen atom enables the interaction with both electrophiles and nucleophiles which results in distinct geometries of the XB (Figure 1.3B).

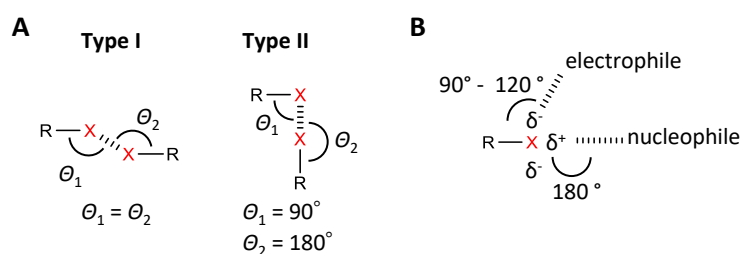


Figure 1.3: Type I and Type II halogen-halogen interactions (A). Interaction of a halogen atom with a nucleophile and electrophile (B).

Upon interaction with an electrophile, the resulting angle of the XB relative to the covalent bond of the halogen atom is between  $90^\circ$  and  $120^\circ$ . On the other hand, the approach of a nucleophilic XB-acceptor occurs preferentially in plane with the covalent bond in an angle close to  $180^\circ$ . This high directionality makes it possible to reliably predict the geometric orientation of the halogen-bonded aggregate making XBs especially attractive for supramolecular chemists and crystal engineers. The most commonly used XB acceptors in supramolecular chemistry are nucleophilic heteroatoms such as nitrogen, oxygen, sulfur, phosphorus, or heteroaromatic derivatives like pyridines or pyrazines. Whereas assemblies with pyridines tend to form linear aggregates with  $C-N\cdots X$  angles of about  $180^\circ$ <sup>[27, 49]</sup>, carbonyl<sup>[50-51]</sup>, sulfonyl<sup>[52]</sup>, and phosphoryl<sup>[53]</sup> groups can act as mono- and bidentate binding sites that predominantly form tetrahedral aggregates along their donating n-pair axes.

### 1.2.3 Tunability

As shown by *Politzer* and coworkers, the XB strength strongly depends on the size and magnitude of the  $\sigma$ -hole which increases with increasing electron withdrawing capability of the

covalently bound atom or group. It also follows the increasing polarizability (*i.e.* decrease of electronegativity) of the halogen atom in the order  $\text{Cl} < \text{Br} < \text{I}$ . Generally seen, the strength of the XB can be influenced by any structural change to the covalently bound residue that alters the ability of the group to withdraw electron density from the halogen atom. In 2005 for instance, *Zuo et al.* investigated the effects of hybridization of the carbon atom bound to the halogen atom on the XB strength and found a decrease of the binding strength with increasing hybridization from  $\text{sp} > \text{sp}^2 > \text{sp}^3$ .<sup>[54]</sup>

Another well-established approach often used to change the electron withdrawing capability of the residue, is the hydrogen substitution with fluorine atoms or other strongly electron withdrawing groups like cyano or nitro groups. In 2000, *Walsh et al.* found a decrease of the  $\text{N}\cdots\text{I}$  contact distances in single crystals of bipyridines with diiodo- (3.032 Å) and per-fluorodiiodobenzenes (2.851 Å). In 2009, *Präsang et al.* extended these findings by systematically studying the evolution of the  $\text{N}\cdots\text{I}$  distances in cocrystals of 4-(*N,N*-dimethylamino)pyridine (DMAP) and a series of fluorinated iodofluorobenzenes (Figure 1.4A). They could show that the XB strength not only correlates with the number of substituted fluorine atoms attached to the aromatic ring but also that it depends on the fluorination pattern itself due to intermolecular short contacts of fluorine substituents with adjacent aromatic rings.<sup>[55]</sup>

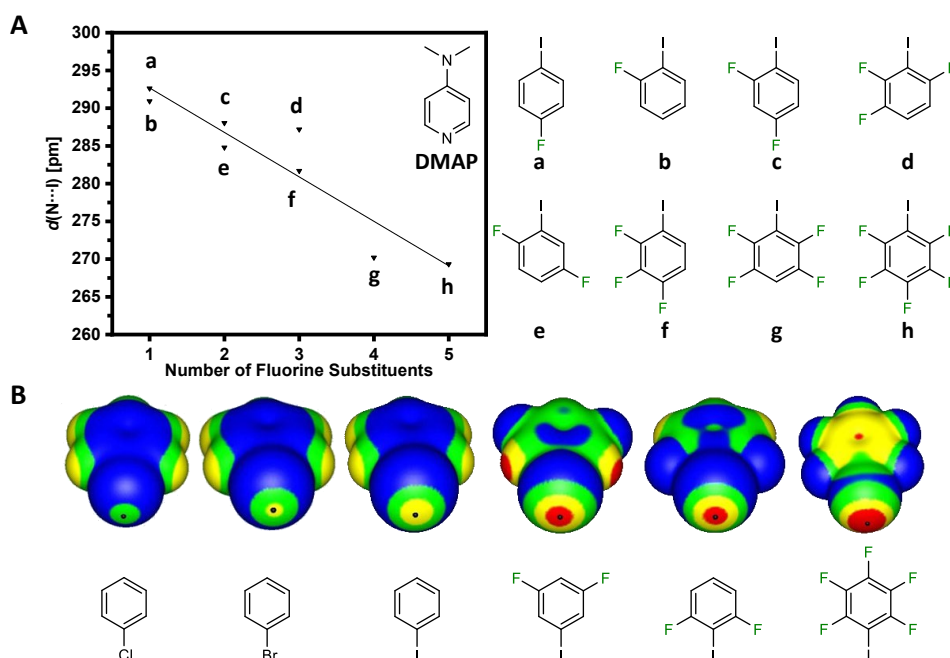


Figure 1.4: Evolution of the  $\text{N}\cdots\text{I}$  contact distances as a function of the number of fluorine substituents and fluorination pattern in  $\text{DMAP}\cdots\text{I}-\text{R}$  assemblies (A). Calculated polarization of the  $\sigma$ -hole as a function of the donating XB-atom and the fluorination degree. Color range (kcal/mol): red, greater than 20; yellow, between 20 and 10; green, between 10 and 0; blue negative. *Adapted with permission from Springer Nature.*<sup>[56]</sup> Copyright (2011) Springer Nature.

These findings were supported by computational studies of *Riley et al.* who investigated the evolution of the dimension and magnitude of the  $\sigma$ -hole as a function of the XB-donating atom and fluorination degree (Figure 1.4B).<sup>[56]</sup> The calculated ESP maxima ( $V_{s,max}$ ) for the different halo- and fluorohalobenzenes revealed a remarkable increase of the positive polarization from chlorine through bromine to iodine. They also explained the shorter  $X\cdots O$  contacts of *ortho*-difluorinated derivatives to acetone, despite having a lower  $V_{s,max}$  than the *meta*-derivatives, with additional intermolecular interactions of the fluorine atoms with the  $CH_3$  group of the acetone molecule.

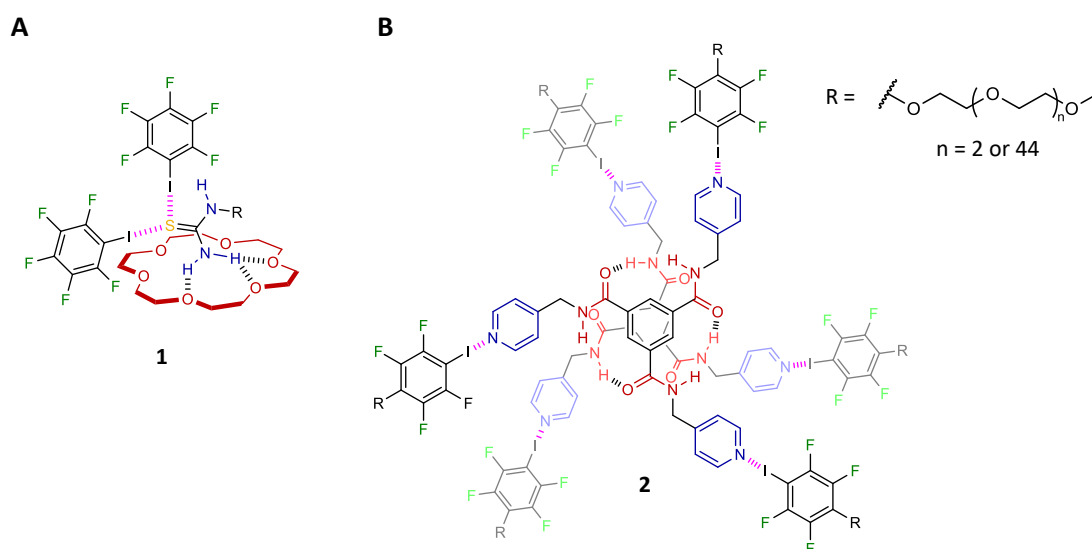


Figure 1.5: Orthogonal halogen and hydrogen bonding. Supramolecular assembly **1** of a crown ether, thiourea, and a halogen bond donor (A). Molecular structure of helical supramolecular polymer **2** using halogen bonding for hydrophobic shielding.

The selective and independent manipulation of the XB strength allows for a widespread application in supramolecular systems. Especially in combination with hydrogen bonding as orthogonal binding motif, the halogen bond has attracted much attention. In 2016, *Rissanen* and coworkers established an approach for the formation of ternary cocrystals (**1**) of crown ethers, thiourea and perfluorohalocarbons by orthogonal hydrogen and halogen bonding (Figure 1.5A).<sup>[57]</sup> Just recently, *Jamadar* and *Das* reported on supramolecular pH-switchable polymer **2** constructed of orthogonally bound hydrogen and halogen bond building blocks which was only successfully achieved due to the hydrophobic shielding of the halogen bond (Figure 1.5B).<sup>[58]</sup>

### 1.2.4 Hydrophobicity

Hydrophobicity is a well-known phenomenon when halogen atoms are considered. Because the interaction energies and geometries of halogen bonds are almost unaffected by polar solvents like water, they are often considered as a hydrophobic counterpart to the hydrophilic hydrogen bond. Especially halogen-bonded assemblies can increase the hydrophobicity of a given system. This enables ion transport across cell membranes<sup>[59-61]</sup>, improvement of peptide binding<sup>[62]</sup>, or shielding of hydrophilic regions of a given molecular assembly in polar solvents which prevents the supramolecular aggregate from dismantling (see also Figure 1.5B).<sup>[58, 61]</sup>

## 1.3 Liquid Crystals

Since their discovery in the late 19<sup>th</sup> century, liquid crystals, or mesogens (from greek ‘μέσος (*mésos*)’ for ‘*in between*’ and the suffix ‘-γενής (*-genēs*)’ for ‘*producer of something*’), have gained more and more attention throughout the last decades. Often described as the fourth state of matter, or the state in-between, they combine the high molecular order of crystalline materials with the different dynamic properties of liquids such as fluidity or switchability.<sup>[63-66]</sup> The molecular units are sufficiently disordered to provide a certain degree of softness or flow properties but yet retain a high enough degree of short and long range order which depend on the type of liquid crystal phase (Figure 1.6). Due to their unique properties, these materials have created a broad field of interdisciplinary research and proved to have great application potential in many technical and biological fields, like temperature<sup>[67-69]</sup> and pressure sensors<sup>[70-71]</sup>, liquid crystal displays (LCDs)<sup>[72-74]</sup>, or drug<sup>[75-77]</sup> and gene<sup>[78-79]</sup> delivery systems.

### 1.3.1 Classification of Liquid Crystals

Liquid crystals can be categorized based on their molecular shape or their surrounding physical conditions necessary for the exhibition of LC properties. The most common structural shapes of LC molecules are calamitic (rod-like), discotic (disk-like) and bent-shaped (bent-core) which usually consist of a rigid core (*e.g.* aromatic system, cyclohexyl groups) and a flexible side chain (*e.g.* alkyl, fluoroalkyl) (Figure 1.6A).<sup>[80]</sup>

Based on the surrounding physical environment, LCs can be further classified into thermotropic or lyotropic LCs. The former exhibit their mesomorphic behavior depending on the surrounding temperature upon solvent free heating and/or cooling of a sample to or from the

isotropic melt (Figure 1.6B). On the other hand, besides the temperature, the mesomorphic properties of lyotropic mesogens (*e.g.* lipids) predominantly rely on the molar concentration of the liquid crystalline unit in a solvent, or the pH value and ionic strength of the solution (Figure 1.6C). With increasing surfactant concentration, the amphiphilic molecules form spherical aggregates (*e.g.* micelles or vesicles), tubes, or lamellar structures which induce anisotropy inside the solution.<sup>[81]</sup> The nature of this anisotropy is a crucial characteristic to differentiate the several mesophases and is determined by the intrinsic molecular information. However, due to the relevance for this work, only thermotropic liquid crystalline phases will be described in more detail.

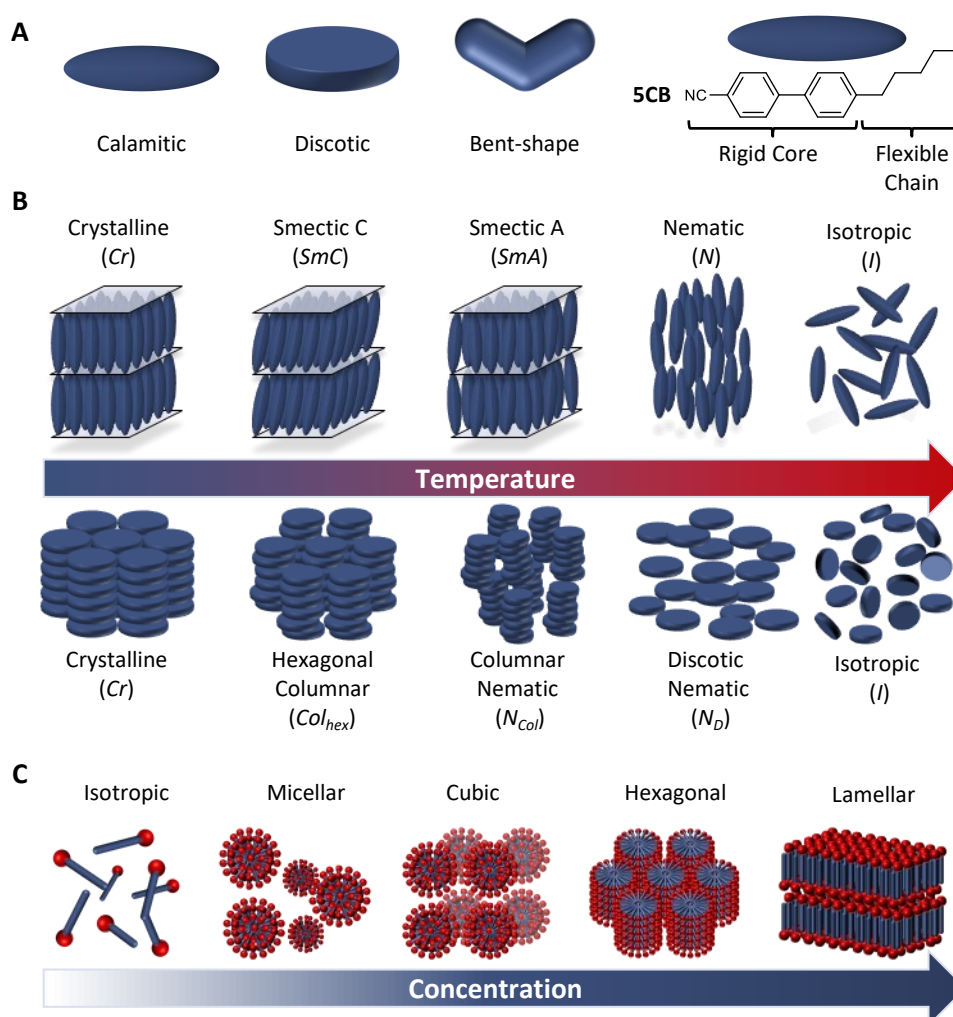


Figure 1.6: Classification of liquid crystals based on their molecular shape (A) and their behavior into thermotropic (B) and lyotropic LCs (C).

The simplest and least ordered thermotropic LC phase is the nematic phase. This phase is preferentially formed by calamitic (*N*) or discotic mesogens (*N<sub>D</sub>*, *N<sub>col</sub>*) which tend to minimize the excluded volume between the molecules leading to long range orientational order

along one director  $\vec{n}$ .<sup>[63, 82]</sup> Combination of sufficiently long rigid and flexible segments in a rod-like molecule can increase the positional long-range order which supports nano-segregation of the rigid and flexible segments and the formation of layered smectic phases (*Sm*). These can be further classified according to the order inside the smectic layers. In the *SmA* phase the molecules have no particular order and preferentially orient along the director  $\vec{n}$  perpendicular to the layer lattices. In the *SmC* phase the order degree is further increased and the mesogenic units tend to orient in a uniformly tilted direction in a specific angle. Depending on the increasing orientational and positional order within the distinct layers, the smectic phase can be also classified as *SmB*, *SmE*, *SmF*, etc.<sup>[63, 83]</sup>

The mesomorphic behavior of thermotropic liquid crystals is not limited to the exhibition of one mesophase but may arise in a sequence of several different phases (polymorphism) upon cooling (monotropic) or heating and cooling of a sample (enantiotropic). The phase transition temperatures are usually given as T in degree Celsius ( $^{\circ}\text{C}$ ) with an index indicating the respective phases (e.g.  $T_{N-I}$  for a transition from the nematic to the isotropic phase). The complete transition sequence of a samples is listed in alternating order of phase symbol and upper temperature limit upon heating from left to right starting with the crystalline state (*Cr*) and ending with the isotropic state (*I*). Monotropic phases appear in parentheses, e.g.  $Cr_1 45 Cr_2 57 (SmA 65) N 88 I$ , designating a compound with a crystal to crystal transition at 45  $^{\circ}\text{C}$ , a monotropic *SmA* phase, and a nematic isotropic transition at 88  $^{\circ}\text{C}$  (clearing point,  $T_C$ ). For monotropic LC phases, the upper transition temperatures are determined on reheating from the formed LC phase upon cooling, giving the true thermodynamic transition temperature.<sup>[29]</sup>

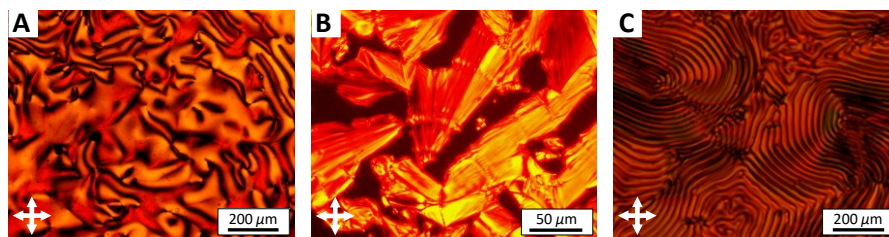


Figure 1.7: Representative POM images showing the characteristic *Schlieren* texture of a nematic phase (A), the focal conic fan texture of a smectic A phase (B) and the fingerprint texture of a chiral nematic phase (C).

A versatile technique to characterize liquid crystal phases and to determine the phase transitions and mesophase ranges, is temperature variable polarized optical microscopy (POM). Due to the distinct molecular order and viscous properties each LC phase exhibits characteristic birefringent textures under crossed polarizers.<sup>[84]</sup> These textures allow a first assignment

of the type of mesophase. Figure 1.7 displays representative POM images under crossed polarizers at different magnifications which show the characteristic *Schlieren* texture of a nematic phase (A), focal conic fan texture of a smectic A phase (B), and fingerprint texture of a chiral nematic phase (C).

### 1.3.2 Chirality in Liquid Crystals

Chirality in liquid crystalline systems is usually observed when molecules with intrinsic chiral information (*e.g.* chiral center, chiral axis, asymmetric substitution) are present.<sup>[85-86]</sup> In some cases, chirality can also be observed for achiral liquid crystals due to spontaneous symmetry breaking or organization in highly ordered tilted mesophases.<sup>[87]</sup> The most common chiral mesophases are the chiral nematic or cholesteric ( $N^*$ ) and chiral smectic phase ( $Sm^*$ ). In addition to their usual long range positional and orientational order, the  $N^*$  and  $Sm^*$  phases form helical superstructures. In case of a nematic LC (Figure 1.8A) where the molecules are oriented along the director  $\vec{n}$ , each nematic layer is slightly tilted to one another in a sense that the director  $\vec{n}$  changes direction perpendicular to the molecular axis in a helical fashion.

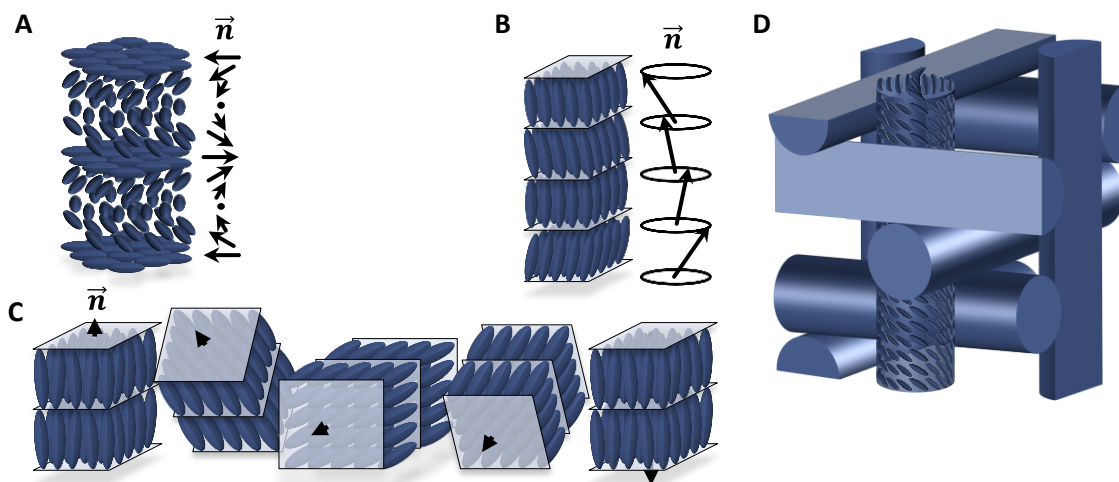


Figure 1.8: Schematic illustration of the molecular order in a chiral nematic phase (A), a chiral smectic C\* phase (B), a twist grain boundary A\* phase (C), and a blue phase I (D).

In the chiral smectic C\* ( $SmC^*$ , Figure 1.8B) phase, the director of the tilted molecules gradually rotates with each proceeding layer. Another chiral mesophase which is considered as a substructure of the  $SmA^*$  phase, is the twist grain boundary A\* ( $TGBA^*$ ) phase. This phase is usually observed at phase transitions of strongly chiral systems from the isotropic melt or

the  $N^*$  phase to the layered smectic state. When the helical structure of the  $N^*$  phase collapses to form the layered  $SmA^*$  structure, two competing effects arise. On the one hand the molecules are required to align in a helical macrostructure, but on the other hand also strive to form the energetically favored layered smectic state. Since a coexistence of these two states without the formation of defects is not possible, a quasi-helical alignment is formed where small blocks of molecules with a local smectic orientation are twisted with respect to each other along their interfaces (grain boundaries) (Figure 1.8C).<sup>[86, 88]</sup> Another group of chiral mesophases which have attracted significant attention for the design of high performance LCDs in the past decade, are blue phases (BP).<sup>[89-92]</sup> Strongly related to the  $N^*$  phase with highly complex three-dimensional cubic double twisted superstructures, these LC phases pose extraordinary optical properties (Figure 1.8D).<sup>[93]</sup>

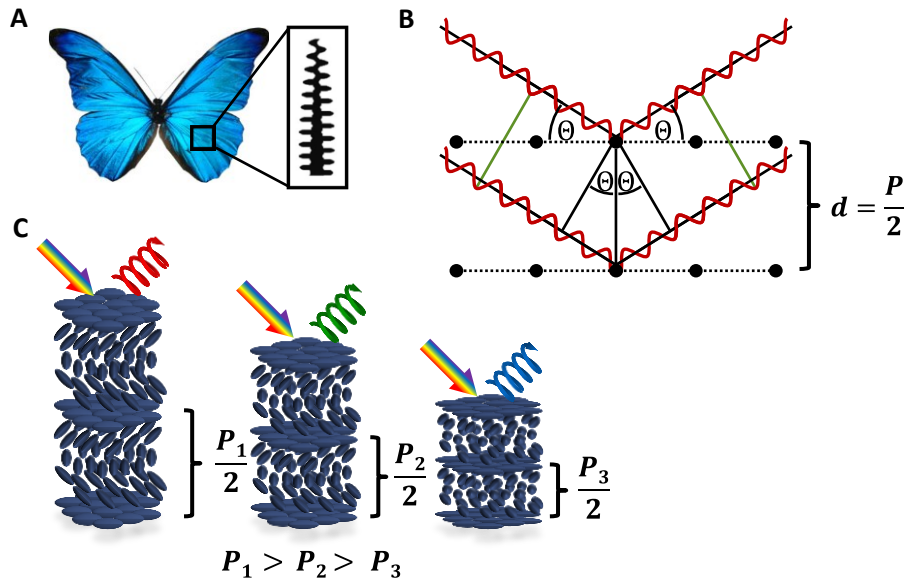


Figure 1.9: Image of the blue structural color of *Morpho* butterfly wings caused by the nanoscopic lattice structure on the surface of the wings (A). Reprinted with permission from Springer Nature.<sup>[94]</sup> Copyright (2013) Springer Nature. Principles of the selective reflection of light on a multivalent diffraction surface (B) and reflection of circularly polarized light using chiral nematic liquid crystals with different pitch lengths (C).

The repeating periodicity of the helical superstructure (*i.e.* photonic structure) leads to a selective reflection of light according to Bragg's Law:<sup>[95]</sup>

$$n\lambda = 2d \cdot \sin \theta. \quad (1)$$

This phenomenon has been used by nature ever since to produce a colorful diversity of materials and biological species without the energy consuming production of colored pigments (Figure 1.9A).<sup>[94, 96]</sup> According to Equation (2), the wavelength of the reflected light is equivalent to the length of the helical pitch  $P$ , which corresponds to a full  $360^\circ$  rotation of the

molecular director  $\vec{n}$ , the average refractive index of the material ( $n_{Avg}$ ), and the angle of incidence ( $\theta$ ) of the incident light beam (Figure 1.9B):

$$\lambda_{max} = n_{Avg} \cdot P \cdot \sin \theta. \quad (2)$$

Therefore, a change of the helical pitch of the chiral nematic phase with a pitch in the range of the wavelength of visible light, leads to a direct change of the wavelength of the reflected light (Figure 1.9C).

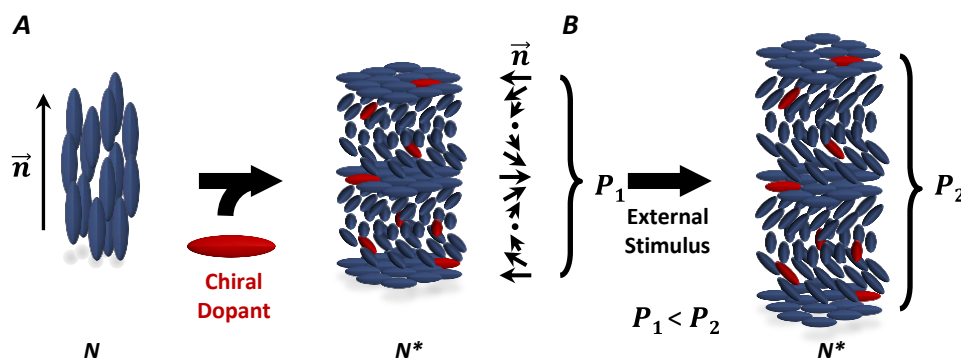
A versatile method to induce chirality in a liquid crystalline system is the use of small amounts of a chiral additive *i.e.* a dopant molecule which comprises chirality in its molecular structure. This approach allows to alter existing LC properties or to even induce the exhibition of completely new meso- or macroscopic characteristics (*e.g.* structural color).<sup>[97-99]</sup> The addition of a chiral dopant (guest) to a nematic LC host leads to the formation of an  $N^*$  phase as the host molecules reorient according to the intrinsic chiral information of the additive (Scheme 1.1A).<sup>[97]</sup>

The efficiency of the chiral transfer of a dopant is rationalized by the molar helical twisting power ( $\beta_M$ ) and is defined as

$$\beta_M = \frac{1}{P \cdot ee \cdot \omega} \quad (3)$$

where  $P$  represents the helical pitch,  $ee$  describes the enantiomeric excess of the chiral dopant, and  $\omega$  represents the molar fraction of the dopant.<sup>[100-102]</sup> The value and sign of the helical twisting power (HTP) are inherent for each individual chiral compound and strongly depend on the used host and the temperature. They not only define the handedness of the helical arrangement (positive = right handed (P) and negative = left handed (M)), but also indicate the amount of additive which is needed to induce an  $N^*$  phase with a distinct helical pitch.<sup>[103]</sup> The nature of the formed cholesteric LC is given by the individual structural properties of the chiral additive.<sup>[97]</sup> This allows to directly manipulate the structural color of a liquid crystalline sample by addition of distinct amounts of chiral dopant or manipulation of the helical twisting power due to an external stimulus which makes this principle suitable for photonic sensing applications (see also Scheme 1.1B and Figure 1.9C).

---



Scheme 1.1: Principle of chiral transfer: Addition of a chiral dopant to a nematic LC host induces a reorganization of the host molecules according to the inherent chirality of the dopant into a helical alignment of a chiral nematic liquid crystal. Changing the HTP of a dopant due to an external stimulus leads to a change of the helical pitch.

The simplest approach to design a chiral dopant is to functionalize a chiral molecule with a mesogenic unit to enhance its solubility in the LC host. For example, the functionalization of *R*-octan-2-ol (**3**) with a mesogenic unit resembling *p*-methoxybenzylidene-*p*-butylaniline (MBBA) increases its HTP from  $0.8 \mu\text{m}^{-1}$  to  $19.4 \mu\text{m}^{-1}$  for chiral dopant **4** (Figure 1.10).<sup>[104]</sup> Higher HTPs can be achieved by using binaphthyl derivatives (*e.g.* dopants **5**, **6**, and **7**).<sup>[103]</sup> These are especially suitable for the chiral induction in LC host systems due to their intrinsically locked chirality along their chiral C–C axis. In this case, the HTP is directly dependent on the dihedral angle between the two naphthalene planes which can be easily altered by straining the molecule.<sup>[105]</sup> Binaphthyl derivatives can be easily functionalized in different positions and pose high structural similarity with biphenyl based LC hosts like 5CB (4-cyano-4'-pentylbiphenyl) or E7 (binaphthyl-based LC mixture, composition see Chapter 3.3). This allows for the selective manipulation of the HTP value of the chiral dopants.<sup>[103, 106]</sup>

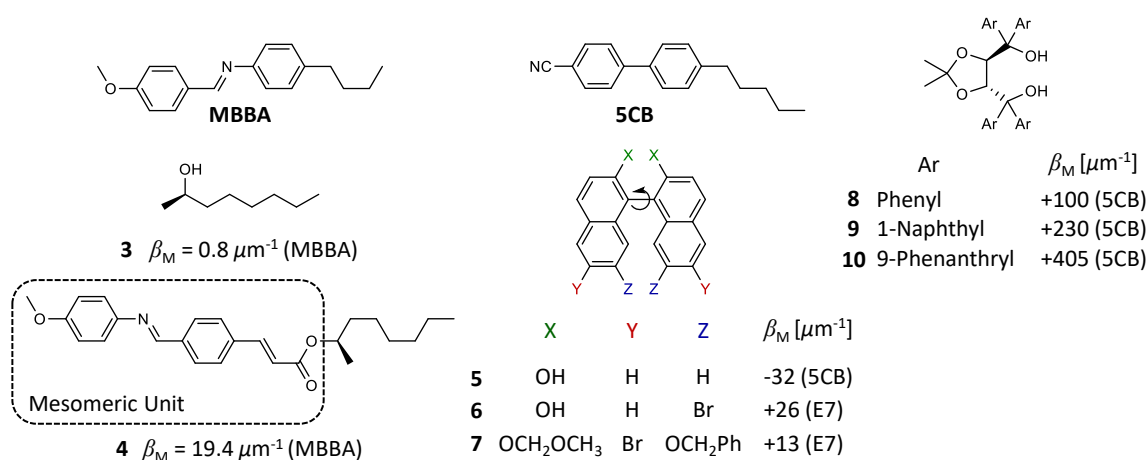


Figure 1.10: Dopants and their HTPs for the chiral induction in different LC hosts.

Another class of chiral dopants which exhibit extraordinarily high HTP values due to their intrinsic chirality are 1,3-dioxolan-based  $\alpha,\alpha,\alpha',\alpha'$ -tetraaryl-1,3-dioxolane-4,5-dimethanol (TADDOL) derivatives. Originally synthesized as chiral auxiliaries, *Kuball et al.* found HTP values of up to  $405 \mu\text{m}^{-1}$  in 5CB for TADDOLS **8**, **9**, and **10**.<sup>[107]</sup> Such high HTP values enable the induction of structural color in an LC host with only very small amounts of dopant of a few mol%.

### 1.3.3 Supramolecular Liquid Crystals

Most commercially available LCs are covalently bound molecules or mixtures of different molecules with LC properties which allows the simple manipulation of the LC properties. However, over the past decades, supramolecular liquid crystals (SMLCs) have drawn significant attention and have been studied by numerous groups all over the world. Since *Kato, Frechét* and *Lehn*<sup>[108-109]</sup> first used supramolecular complementary hydrogen bonding to manipulate the properties of liquid crystalline polymer **11** (Figure 1.11), this approach has become a well-recognized tool for the design of SMLC materials.<sup>[110]</sup> Incorporation of specifically designed non-covalent complementary binding motifs into monomeric units (*e.g.* hydrogen bonds, ionic interactions or halogen bonds) results in a great variety of new effects like increase or decrease of the mesophase stability, transition temperatures, or changes of mesophase morphology.<sup>[8, 111-112]</sup> Using non-covalent interactions can even lead to the induction of liquid crystallinity from non-mesogenic starting materials.<sup>[9, 113-114]</sup> With their enhanced properties the resulting materials can be used in catalysis<sup>[115]</sup>, sensors<sup>[116]</sup>, or in biomedical applications<sup>[5]</sup> as well as base of liquid crystalline composites like gels<sup>[117]</sup>, or fibers<sup>[118]</sup>.

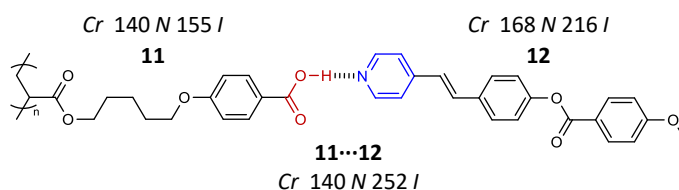


Figure 1.11: Manipulation of the LC properties of liquid crystalline polymer **11** by supramolecular binding of pyridine-based LC **12**.

One of the biggest advantages of SMLCs over their covalent analogues is their improved flexibility. Employing complementary supramolecular binding motifs allows for comprehensive structure-property relationship studies by simple combination of a library of donor

and acceptor molecules. The derived design principles enable the development of LC materials with tailor-made properties in terms of mesophase stability, morphology or stimuli-responsive behavior.<sup>[29]</sup> Recent investigations employed these approaches to delve into the understanding of the underlying complex interplay of inter- and intramolecular interactions and investigated the impact of specific structural changes of the molecular moieties on the macroscopic liquid crystalline properties. Within the scope of relevance for this work, this chapter focuses on the recent advances in the field of hydrogen- and halogen-bonded thermotropic SMLCs.

While early examples of SMLCs commonly employed benzoic acid and pyridine derivatives to form mono- or dihydrogen-bonded linear aggregates<sup>[108-109, 119-121]</sup>, more recent approaches went over to more complex systems and employed supramolecular tectons with more than one binding site. *Suárez et al.* used trimeric 4,5-dialkyloxyphthalhydrazide **13** to form columnar phases by self-assembly upon heating to the isotropic melt (Figure 1.12).<sup>[7]</sup>

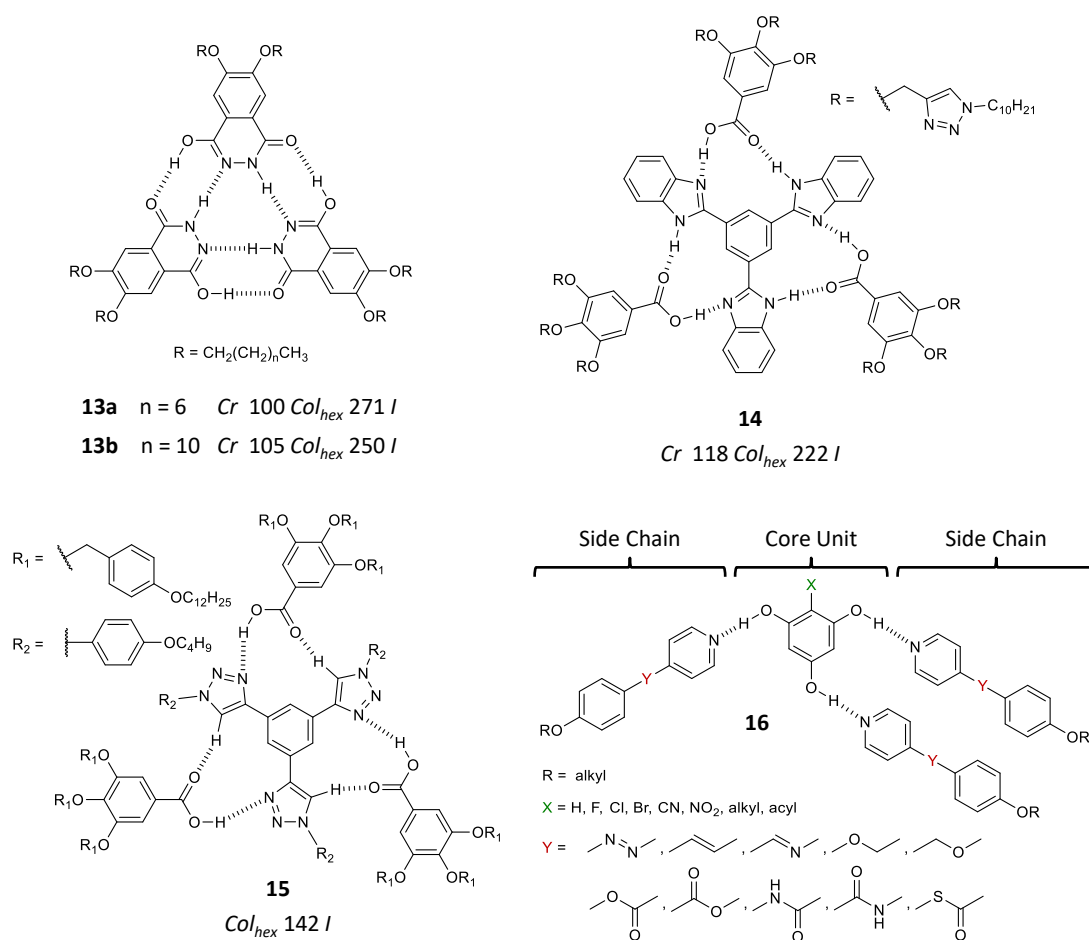


Figure 1.12: Supramolecular hydrogen-bonded liquid crystals.

Another approach was used by *Xiong et al.*<sup>[113]</sup> and *Feringán et al.*<sup>[114]</sup> who used multidentate HB-acceptor molecules which they combined with different benzoic acid derivatives to investigate the mesomorphic properties of the resulting star-shaped mesogens **14** and **15**. A comprehensive study of the structure-property relationships of quaternary supramolecular liquid crystal assembly **16** was performed by *Giese* and coworkers.<sup>[9, 122-123]</sup> Using a modular approach with a divers library of differently functionalized phloroglucinol HB-donors and pyridine-based HB-acceptors, they investigated numerous SMLCs, derived design principles for the supramolecular synthesis of LCs with tailor-made properties, and transferred their findings onto other supramolecular LC systems. They also shed light on the effect of fluorination of core unit and side chain on the mesomorphic properties and found a significant increase of the mesophase stability for core-fluorinated assemblies, whereas side chain fluorinated assemblies showed smaller mesophase ranges.<sup>[124]</sup>

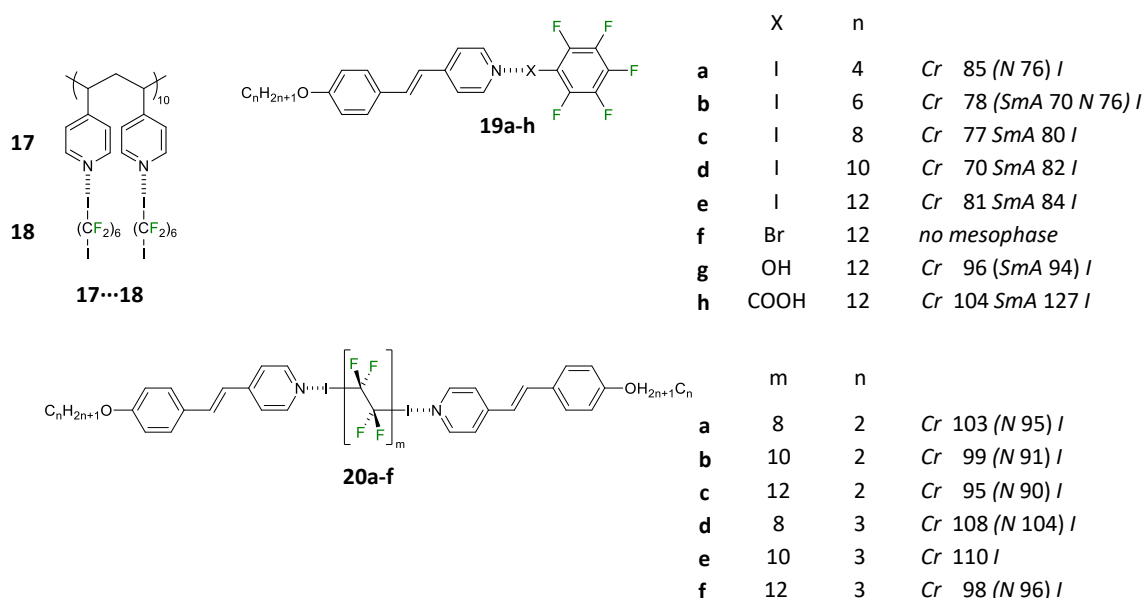


Figure 1.13: First examples of halogen-bonded SMLCs.

The first example of halogen bonding employed as binding motif in supramolecular liquid crystals was reported by *Bertani et al.* who manipulated the thermal properties of comb-like poly(4-vinylpyridine) (**17**) by self-assembly with 1,6-diodoperfluorohexane (**18**) (Figure 1.13).<sup>[125]</sup> They found smectic behavior of the halogen-bonded LC polymer and attributed the observation to the formation of a halogen-bonded assembly and strong nano-segregation of the perfluorinated carbon chains. In 2004, *Nguyen et al.* combined a variety of alkoxy stilbazole acceptors with different pentafluorobenzene HB- and XB-donors and discovered a great similarity in the observed binding characteristics between halogen- and

hydrogen bonds in the supramolecular assembly **19**.<sup>[34]</sup> They also suggested that the absence of a mesophase in **19f** is due to the lower polarization of the bromo substituent and the resulting lower XB-strength which was later confirmed by *Bruce et al.*<sup>[126]</sup> In 2006, *Metrangolo et al.* investigated the impact of halogen bonding on the properties of trimeric liquid crystal **20** and found that the mesophase range and transition temperatures can be influenced by the nature of the spacer and the lengths of the terminal alkyl chains.<sup>[33]</sup> They also discovered that the transition enthalpies are comparable to those of the hydrogen bonded analogues.

The most comprehensive structure-property relationship study on halogen-bonded liquid crystals was published by *Bruce et al.* in 2010 (Figure 1.14).<sup>[29]</sup> They investigated a complete library of different non-mesogenic pyridine-based XB-acceptor and tetrafluoroiodo donors with different terminally attached side chains (*e.g.* achiral or chiral), different linking groups (*e.g.* stilbene or ester), and sizes of the aromatic core. They found a significant correlation between the width or morphology of the mesophase and the length of the attached alkyl chain and that ester derivatives generally lead to remarkably reduced clearing point temperatures below room temperature.

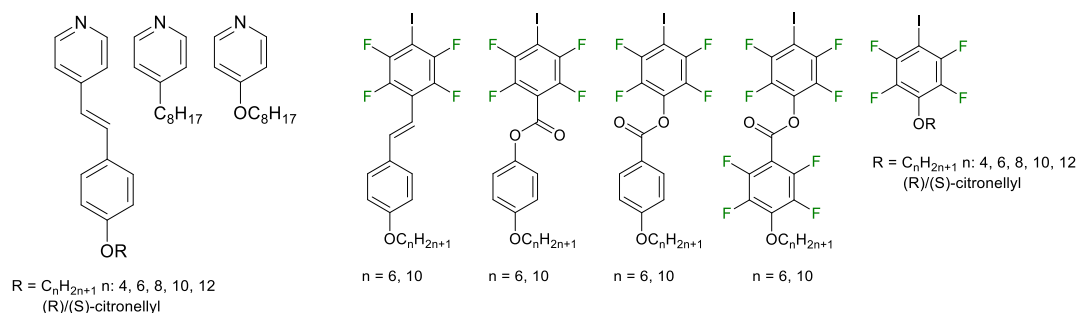


Figure 1.14: Library of XB-acceptors and -donors used by *Bruce et al.*<sup>[29]</sup>

The possibility to induce liquid crystalline behavior by self-assembly of non-mesogenic starting materials to supramolecular bound aggregates has opened the way to new models and approaches to generate advanced LC "smart materials". Especially the introduction of stimuli-responsive moieties into the building blocks has attracted increasing attention in the past as an intermediate step toward commercial applications of such materials. Photo-switchability is just one of many stimuli that have been incorporated into LC materials.

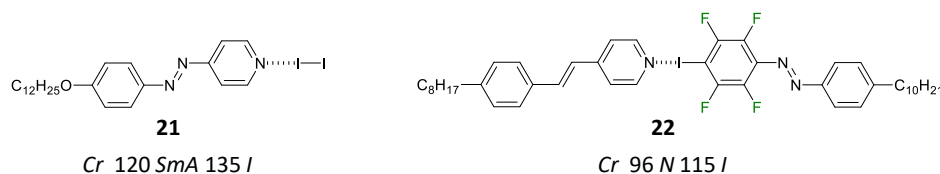


Figure 1.15: Recent examples of photo-switchable halogen-bonded LCs.

*Hecht* and coworkers comprehensively studied the effects of fluorination on the *trans-cis* isomerization of azo benzenes and developed bistable photo-switches.<sup>[127-130]</sup> The first example of a photo-responsive halogen-bonded LC was reported by *Chen et al.* in 2014 (Figure 1.15).<sup>[30]</sup> They found that, upon irradiation with UV light ( $\lambda = 360$  nm), a photo-induced *trans-cis* isomerization of the azo bond in **21** causes a reversible phase transition to the isotropic state. This is due to a destabilization of the ordered LC phase by the formed *cis* isomer. Subsequent irradiation with visible light reverses the process resulting in a recovery of the LC phase. More recently, *Fernandez-Palacio et al.* investigated photo-switchable LC **22** and found that only around 4% *cis* isomer is needed to induce a complete phase transition from the mesophase to the isotropic state.<sup>[31]</sup>

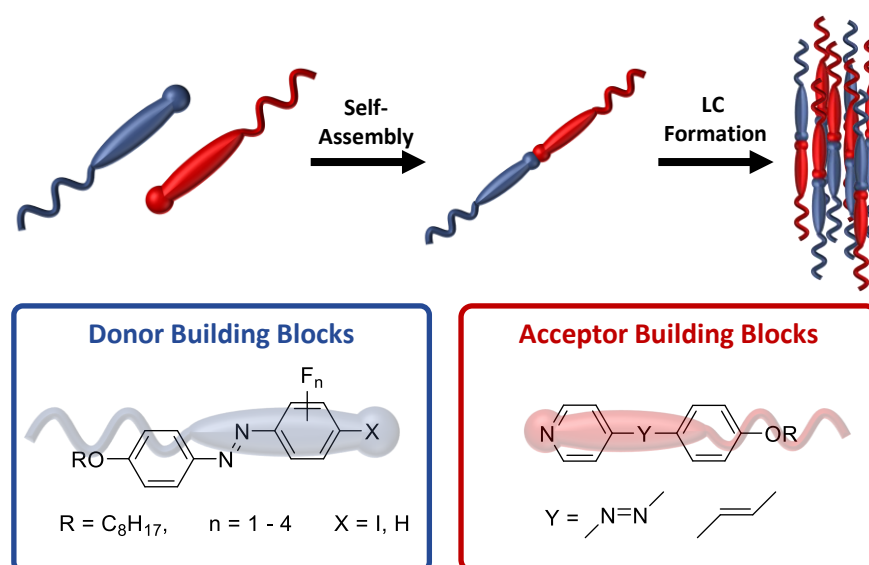
This work aims to fill the gap between the recent findings in halogen-bonded liquid crystals to open up new directions in the design of novel functional materials.

## 2. Idea and Concept

Since supramolecular chemistry and halogen bonding have become a pivotal part of today's research for functional liquid crystalline materials, a comprehensive understanding of the underlying interactions and their synergy is of great interest. The macroscopic properties of such materials are closely related to the mesoscopic structure which makes structure-property relationship studies a versatile tool to shed light on this topic. The studies of *Giese*, *Bruce*, and *Hecht* gave a good impression of the vast possibilities and underlying processes and interactions. [9, 29, 124, 127-130] However, despite the known studies on the effects of fluorination and on halogen-bonded liquid crystals in general, the impact of fluorination on the thermal and photo-physical properties of halogen-bonded LCs continues to be unknown.

This work aims to fill the gap and uses the modular approach employed by *Giese* and *Bruce* to offer valuable clues to how selective fluorination influences the properties of halogen-bonded liquid crystals (Scheme 2.1). Systematic variation of the halogen bond binding motif on the acceptor as well as the donor side, and the supramolecular architecture itself, will provide deeper insight into the individual contributions on the mesomorphic properties with respect to the following key questions:

1. How does the fluorination degree and pattern influence the halogen bond strength?
2. How does the halogen bond strength influence the mesomorphic properties?
3. How does the fluorination influence the photo-physical properties of the materials?



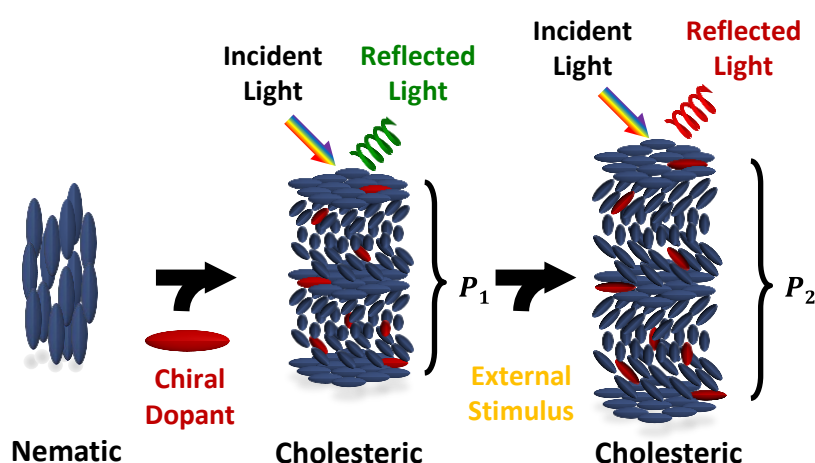
Scheme 2.1: Schematic presentation of the molecular approach used in this project and the possible halogen bond donor (blue) and acceptor molecules (red).

Scheme 2.1 schematically shows the principle behind the approach as well as promising XB acceptor and donor molecules. The modular design allows to combine different XB-acceptors (red) and -donors (blue) to form a series of new supramolecular aggregates which are investigated with respect to their LC properties. Systematic variation of the number of fluorine atoms on the donor side allows the studying of the effects of fluorination on the iodine polarization and thermal properties. Additional incorporation of azo-linking groups enables the external control over the mesomorphic properties by photo-induced *trans-cis* isomerization.

This modular approach is used in a second step to explore the induction of chirality in halogen-bonded liquid crystals as a function of ...

1. ... the fluorination pattern,
2. ... the halogen bond binding strength, and
3. ... the *trans-cis* isomerization.

In the third part, the obtained knowledge is applied to develop a sensor system which uses the principle of structural color for photonic sensing (Scheme 2.2). Promising chiral dopants are identified and investigated with respect to their ability to transfer chirality onto an LC host and to induce structural color. Suitable structurally colored samples are tested regarding their photonic sensing capability by exposure of the systems to different analytes and external stimuli.



Scheme 2.2: Schematic presentation of the induction of structural color using a chiral dopant in a nematic liquid crystal. Reaction to an external stimulus induces a change of the structural color.

### 3. Results and Discussion

#### 3.1 Fluorination of Halogen-Bonded Liquid Crystals

In the past years, tetrafluoroiodobenzene proved to be an excellent halogen bond donor which has been used as supramolecular building block in numerous different systems exhibiting liquid crystalline properties.<sup>[27, 29, 31, 34, 126]</sup> However, the effects of fluorination on the properties of such systems remain obscure and to date especially the effects of the XB-strength on the LC properties have not been investigated in detail. This chapter summarizes the results, which demonstrate the effect of fluorination on the properties of halogen-bonded LCs by synthesis and supramolecular recombination of a series of donor and acceptor molecules. Investigation of the obtained assemblies with respect to their liquid crystalline properties using POM, differential scanning calorimetry (DSC) and x-ray scattering techniques (SAXS, WAXS) allows to correlate the property changes with the individual structural changes of the building blocks.

As both fluorination degree and pattern play a significant role in the complex molecular interplay in such systems (see also Section 1.2), the following XB-donor and -acceptor molecules are good candidates for a comprehensive study (Figure 3.1).

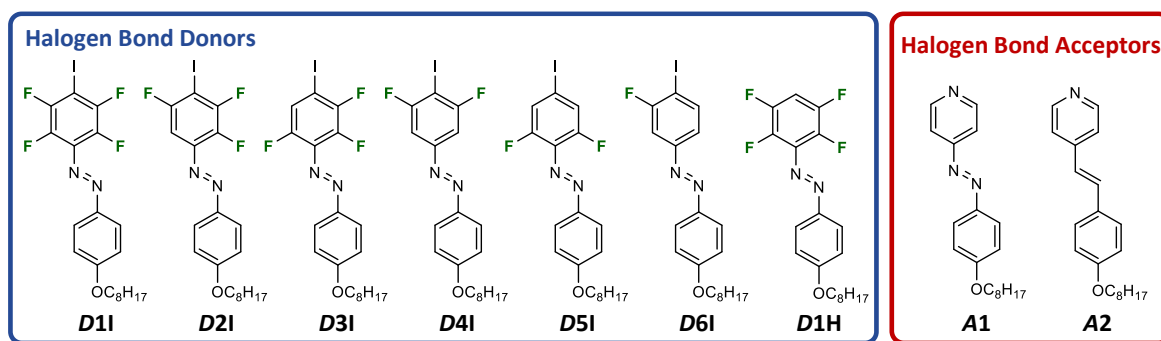


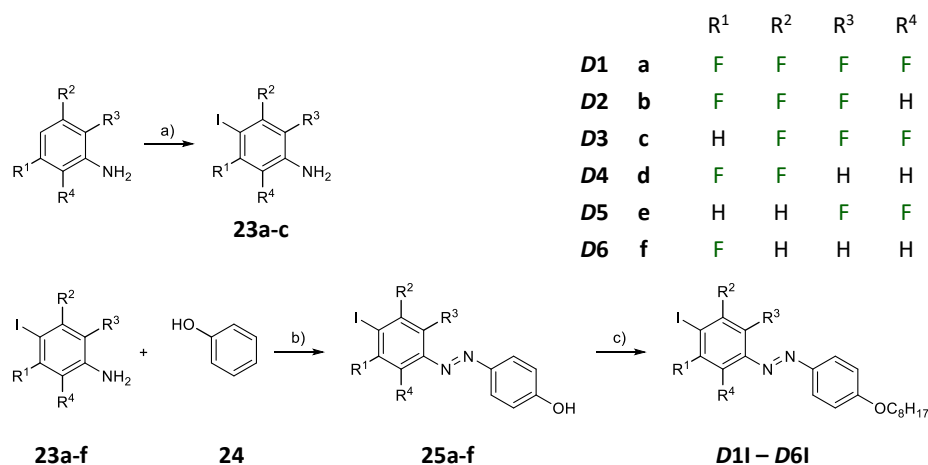
Figure 3.1: Library of XB-donor (blue) and -acceptor molecules (red) used in this study to investigate the impact of fluorination on the LC and photo-physical properties of halogen-bonded liquid crystals.

The varying fluorination pattern (**D1** – **D6**) induces a changing polarization of the halogen atom which has a direct influence on the nature of the formed XB and also affects the photo-physical properties of the azo moiety.<sup>[127-130]</sup> This allows to systematically study the underlying structure-property-relationships. **D1H** is used as reference system to exclude any cross-interactions which are not caused by the formation of the halogen bond. Pyridine building blocks **A1** and **A2** function as XB-acceptors of which **A1** shows reversible photo-responsive properties upon irradiation with UV light (405 nm). This enables the investigation of the

molecular electronic environment on the LC and photo-physical properties. Although the terminal alkyl chain noticeably controls the nature of the formed LC phases, this study focuses on octyloxy derivatives only, as the alkyl chain effects on the LC properties have been comprehensively studied in the past.<sup>[9, 29, 131-135]</sup>

### 3.1.1 Synthesis of XB-Donor and Acceptor Molecules

For the synthesis of the XB-donor and acceptor molecules, modified literature known procedures were used. Acceptors **A1** and **A2** and donator **D1H** (Figure 3.1) were synthesized according to a procedure reported by *Pfletscher et al.*<sup>[9]</sup> Because some of the iodinated amine precursors were commercially available, only precursors **23a-c** were synthesized according to a procedure reported by *Politanskaya et al.* using  $\text{Ag}_2\text{SO}_4$  and  $\text{I}_2$  in ethanol (Scheme 3.1, a)).<sup>[136]</sup> In comparison to other literature known procedures using  $\text{HgO}$  in ethanol or  $\text{NaHCO}_3$  in  $\text{H}_2\text{O}$ , this procedure turned out to be a good compromise in terms of low toxicity, high selectivity for the monoiodinated products (**23b** and **23c**), and retention of moderate to good yields between 60 – 90%.



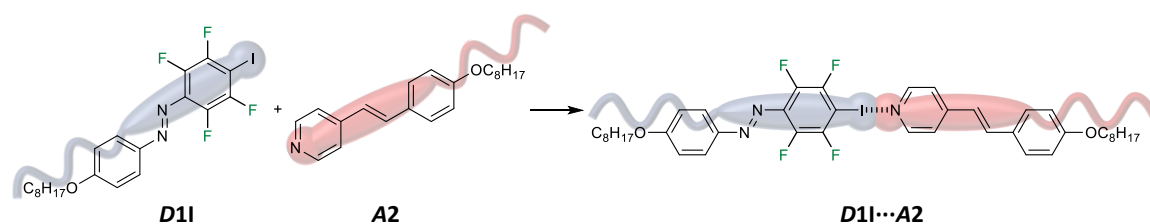
Scheme 3.1: Synthetic route for the synthesis of XB-donors **D11 – D6I**: a)  $\text{Ag}_2\text{SO}_4$ ,  $\text{I}_2$ , ethanol, reflux, 4h; b)  $\text{BF}_4\text{NO}$ , ACN,  $-30\text{ }^\circ\text{C}$ ; c)  $\text{BrC}_8\text{H}_{17}$ ,  $\text{K}_2\text{CO}_3$ , DMF,  $90\text{ }^\circ\text{C}$ .

Due to low solubility of the iodinated amine precursors in 7M HCl and unknown impurities, which could not be removed, the procedure by *Pfletscher et al.* with yields as low as 10 – 20% proved to be unsuitable for the synthesis of azo-precursors **25a-f**.<sup>[9]</sup> Although the yields could be slightly improved by addition of acetone to increase the solubility, the  $^{19}\text{F}$  NMR spectra still showed several peaks not belonging to either the starting material or the product. Eventually, an alternative route was followed using nitrosyl tetrafluoroborate

( $\text{BF}_4\text{NO}$ ) in acetonitrile (ACN) at  $-30^\circ\text{C}$  (Scheme 3.1, b)) which led to isolated yields between 15% (**25f**) and 84% (**25a**).<sup>[137]</sup> The low yield of **25f** can be attributed to technical difficulties during the synthesis and purification steps that led to loss of product. However, since the amount of product was sufficient for the performed experiments, no optimization was performed. Purification was achieved by heating the crude product in deionized water and subsequent hot filtration to remove the excess of remaining phenol. The final Williamson ether synthesis with octylbromide provided the alkylated products in moderate to good yields between 33% (**D3I**) and 93% (**D2I**). All synthesized donor and acceptor molecules were characterized using standard analytical methods (e.g. nuclear magnetic resonance (NMR) and infrared (IR) spectroscopy, and mass spectrometry (MS).

### 3.1.2 Formation of Supramolecular Assemblies

The formation of the supramolecular assemblies was performed by weighing the individual compounds in a 1: 1 molar ratio and subsequent dissolving in small amounts of acetone. The two solutions were combined, and the solvent removed under reduced pressure to obtain the halogen-bonded assemblies as orange solids. In total, 14 supramolecular combinations of the seven XB-donors and two XB-acceptors were prepared. In the following chapters, the supramolecular assemblies are described as **DXY**...**AZ** (Scheme 3.2) where X describes the fluorination pattern 1 – 6 (see also Figure 3.1), Y the substituent in 4-position of the fluorinated arene (iodine [I], hydrogen [H]), and Z describes one of the two acceptor molecules. The formation of the halogen bond was proven by infrared spectroscopy and single crystal analyses.



Scheme 3.2: Formation of the supramolecular halogen-bonded complex **D1I**...**A2** of XB-donor **D1I** and XB-acceptor **A2** as a representative example.

#### 3.1.2.1 IR Spectroscopy

IR Spectroscopy is a powerful tool to investigate the formation of halogen bonds. Due to its decreased strength compared to covalent or ionic bonds, intensity and shift changes of distinct vibrational modes can be used to describe XBs.<sup>[138]</sup> Halogen bonds between pyridyl

units and tetrafluoroiodo moieties lead to a blue shift with an intensity decrease of the pyridyl bands in the region  $3000 - 3050 \text{ cm}^{-1}$  and a red shift of the vibrational modes of the fluorinated arene.<sup>[126, 139]</sup> In fact, these shifts were found for most of the assemblies with **A2** (Figure 7.1). However, for the combinations using acceptor **A1**, the changes were rather small (Figure 7.2). Therefore, the following discussion focuses on the tetrafluoro derivatives as these building blocks and their assemblies showed the most prominent changes in the IR spectra. Figure 3.2 shows representative regions of the IR spectra of **D1I**⋯**A2** (A – C), **D1I**⋯**A1** (D – F), which reveal changes of vibrational modes upon self-assembly of donor (blue) and acceptor (red). **D1H**⋯**A2** (G – I) is displayed as a reference.

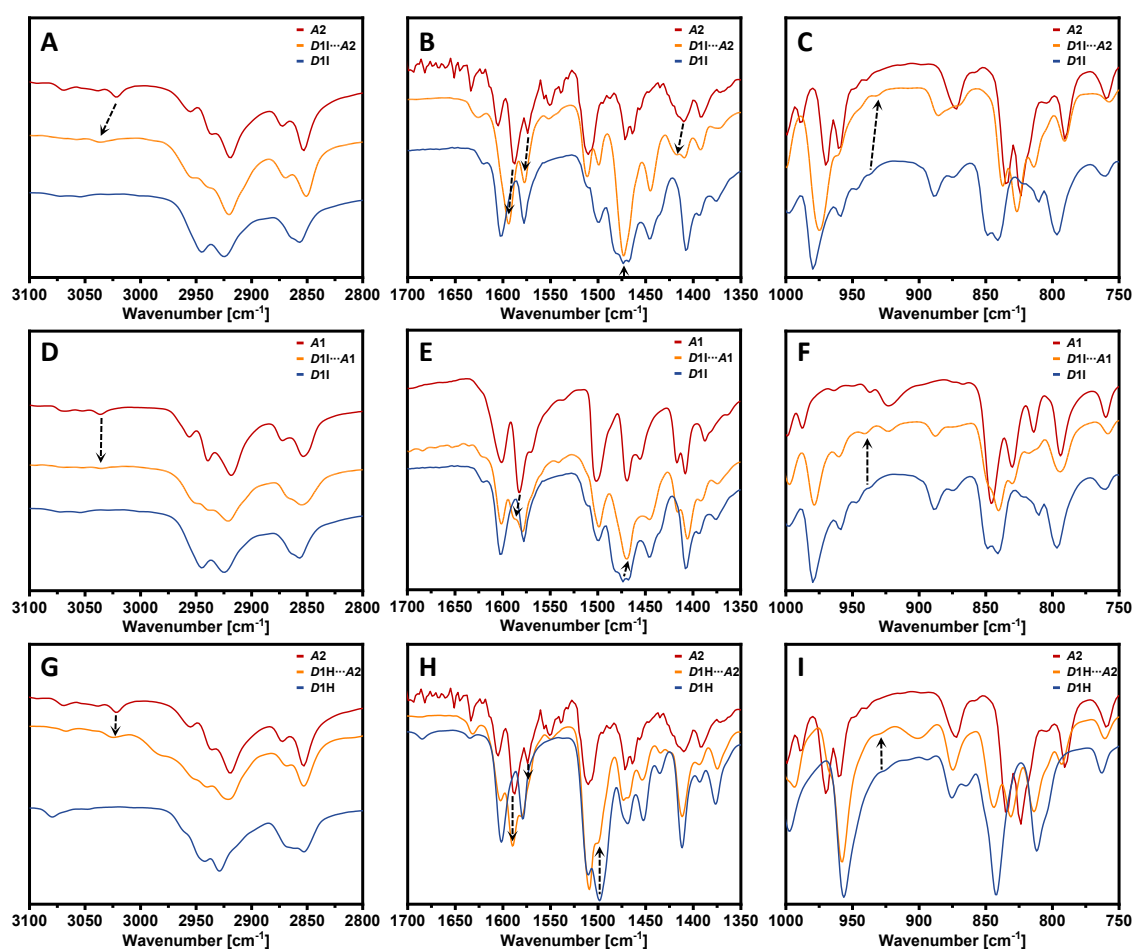


Figure 3.2: IR spectra of **D1I**⋯**A2** (A – C), **D1I**⋯**A1** (D – F), and **D1H**⋯**A2** (G – I) in the regions  $3000 - 3100 \text{ cm}^{-1}$  (left),  $1350 - 1700 \text{ cm}^{-1}$  (middle), and  $1000 - 750 \text{ cm}^{-1}$  (right).

The most distinct changes become evident in **D1I**⋯**A2** (A – C). As a result of the assembly, the electron density on the pyridyl nitrogen atom decreases and the  $\nu_{\text{C-H}}$  absorption band of the pure stilbazole blue shifts to  $3035 \text{ cm}^{-1}$  (A). Simultaneously, a decrease in the vibration band intensity can be seen, as described in the literature.<sup>[139]</sup> Also, the pyridine ring breathing

vibration modes at 1587, 1573, and 1410  $\text{cm}^{-1}$  (B) shift to higher wavenumbers (1593, 1577, and 1417  $\text{cm}^{-1}$ ).<sup>[27, 139-140]</sup> On the other hand, the  $\nu_{\text{C-F}}$  stretching mode at 1473 is only slightly red-shifted to 1471  $\text{cm}^{-1}$ . Similar changes were observed for the  $\nu_{\text{C-F}}$  bending mode at 947  $\text{cm}^{-1}$  (C). Although changes of the  $\nu_{\text{C-F}}$  bending modes at  $\sim 800$   $\text{cm}^{-1}$  have been previously reported in the literature, the shifts are rather vague due to superimposition with other vibrational modes from the stilbazole. Therefore, a reliable correlation of these changes with the formation of the halogen bond was difficult. Similar changes of the pyridyl bands were found for the combinations of **A2** with **D2I**, **D3I**, and **D4I** (see Figure 7.1), but not for the di- and monofluorinated derivatives **D5I** and **D6I**. This suggests that the XB strength gradually decreases with decreasing number of fluorine atom.

Spectra of the corresponding **A1** combinations show noticeably smaller shifts of the vibrational modes (see Figure 7.2). Considerable signal shifts of the pyridyl ring breathing mode at 1583  $\text{cm}^{-1}$  and fluorophenyl  $\nu_{\text{C-F}}$  stretching and bending modes at 1465 and 947  $\text{cm}^{-1}$ , respectively, were only observed for **D1I**···**A1** (see Figure 3.2D – F). The less prominent shifts of the azo pyridyl moiety can be ascribed to the different electronic environment of the adjacent azo group which decreases the electron density on the pyridyl ring. This suggests a lower XB-acceptor capability of the nitrogen atom and thus a weaker bond between XB-donor and azopyridine than between XB-donor and stilbazole.

The proof that the mentioned shifts are induced by the formation of a supramolecular bond between the halogen atom and the pyridine nitrogen and not caused by other non-covalent interactions, is provided by the reference system **D1H**···**A2** (D – F). As expected, no considerable changes in the IR spectra can be observed.

According to the general assumption that the shifts are larger the more involved the pyridine nitrogen is in the supramolecular bond, the IR results indicate that,

- the stilbazole is a better XB-acceptor compared to the azopyridine because of the increased electron density on the pyridine N and
- a minimum number of two *ortho*-fluorine substituents is necessary to form a stable halogen bond with the stilbazole acceptor.

### 3.1.2.2 Computational Analysis

As mentioned above, theoretical investigations on halogen-bonded assemblies are highly suitable for a detailed explanation and understanding of the underlying properties. To get a deeper insight into the findings of the IR studies, the XB-donors **D11** – **D6I** and XB-acceptors **A1** and **A2** were studied using dispersion-corrected density functional theory (DFT-D). Since, the nature of the halogen bond can be described as electrostatic, the ESPs of the XB-donors and -acceptors were calculated. The calculations were performed using the parametrized B97 functional<sup>[141]</sup> and the def2-TZVP basis set<sup>[142-144]</sup> as this is a common configuration for the theoretical investigation of such interactions.<sup>[145-146]</sup> For computational efficiency and because it is not expected to noticeably influence the ESP, the terminal octyloxy group was substituted for a methoxy group. The ESP was calculated on the outer surface  $V_s(\mathbf{r})$  of the molecule at the 0.001 au (electron Bohr<sup>-3</sup>) contour of its electronic density  $\rho(\mathbf{r})$  where it contains roughly 95% of the molecule's or atom's electronic charge.<sup>[147]</sup>

Taking a closer look at the obtained energy values of the acceptors (Figure 3.3A/B), it becomes evident that **A1** (-183.89 kJ/mol) shows in fact a lower (less negative) electronic potential on the pyridyl nitrogen atom than **A2** (-190.59 kJ/mol). This supports the findings of the IR studies, that **A2** is capable of forming a stronger XB due to its higher negative charge on the nitrogen atom.

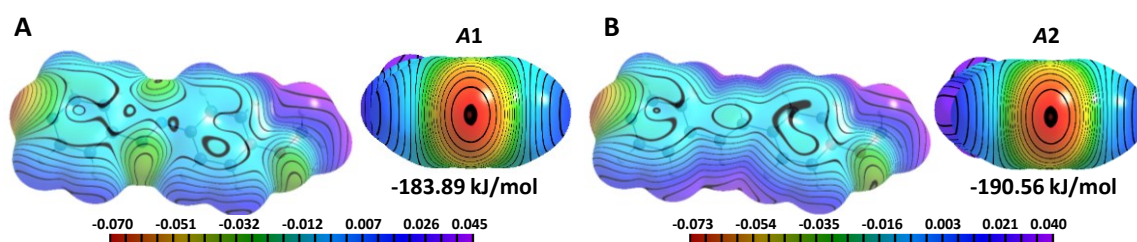


Figure 3.3: ESPs of XB-acceptors **A1** (A) and **A2** (B) (B97-D3/def2-TZVP) on the 0.001 au (electrons Bohr<sup>-3</sup>) contour reveal the increased negative polarization on the pyridyl nitrogen on **A2** compared to **A1** with red being the most negative and purple the most positive areas. Color code in Hartrees.

The ESP energies of the XB-donor molecules (Figure 3.4) clearly reveal the systematic evolution of the iodine polarization. The most positive value was found on the iodine atom of the tetrafluorinated derivative **D11** (A, 126.34 kJ/mol) in elongation of the covalent bond. This value gradually decreases with a decline of the number of electron withdrawing fluorine atoms from **D11** through **D6I** (F, 88.87 kJ/mol). Therefore, a smaller number of fluorine

substituents results in a decrease of the iodine polarization and thus a reduction of the halogen bond strength. This explains, why noticeable shifts in the IR vibrations were only found for the combination **D1I**⋯**A2**, but not for **D2I**⋯**A2** or **D3I**⋯**A2**, because the magnitude of the shift correlates with the strength of the supramolecular interaction.

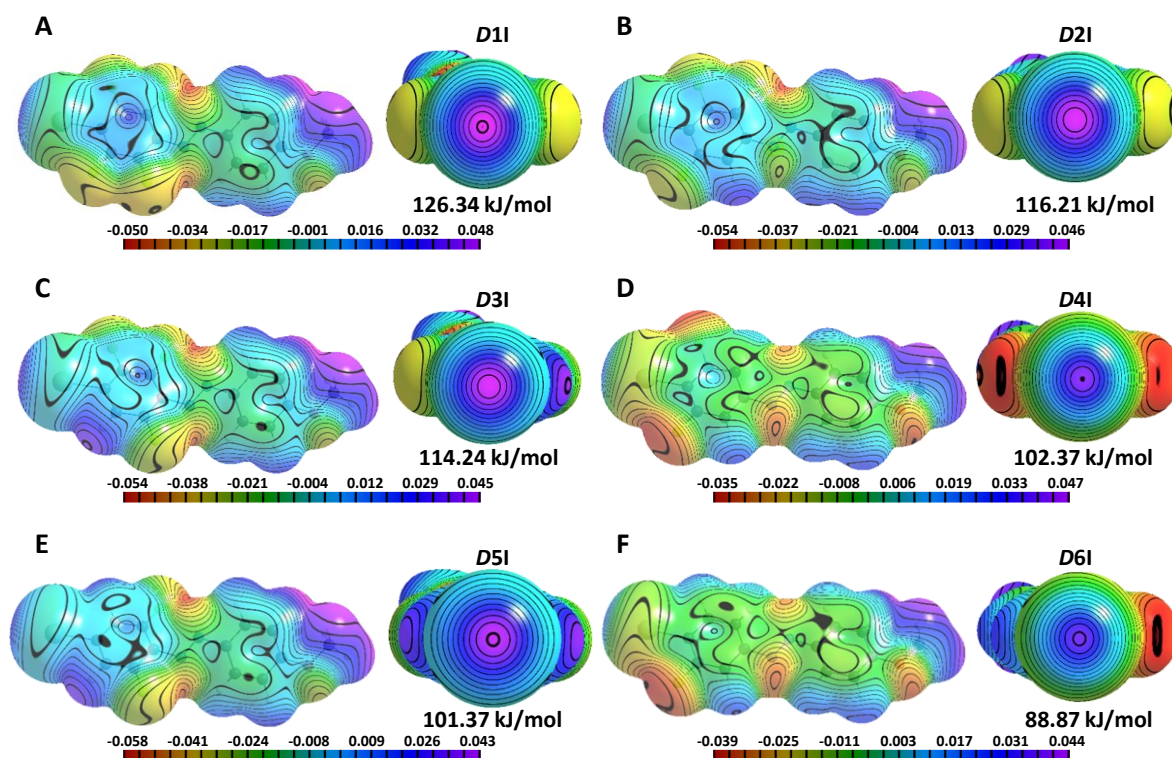


Figure 3.4: Molecular ESPs of XB-acceptors **D1I** (A), **D2I** (B), **D3I** (C), **D4I** (D), **D5I** (E) and **D6I** (F) (B97+D3/def2-TZVP) on the 0.001 au (electrons Bohr<sup>-3</sup>) contour of the electron density show the evolution of the iodine polarization with changing fluorination pattern. Color code in Hartrees.

Moreover, not only the number of attached fluorine substituents influences the iodine polarization, but also the substitution pattern itself. Comparison of the ESP energies of **D2I** (B, 116.21 kJ/mol) and **D3I** (C, 114.24 kJ/mol) shows that, despite having the same number of fluorine atoms, a higher polarization of  $\Delta E = \sim 2$  kJ/mol is achieved for the *ortho*-fluorinated derivative **D2I**. This is due to the fluorine atoms being in closer proximity to the iodine atom compared to **D3I** which in turn causes a stronger polarization. A similar effect can be observed for difluorinated donors **D4I** (D) and **D5I** (E). Interestingly, these findings are in contrast to the findings reported by Riley *et al.*<sup>[56]</sup>. They found a bigger  $\sigma$ -hole with a stronger polarization for the *meta*-difluorinated derivatives. However, they ascribed the stronger XB of the *ortho*-derivatives to additional intermolecular interactions of the fluorine substituents with the hydrogen atoms of the used acetone acceptor molecule.

To get a more detailed impression of the supramolecular processes, the binding energies of the formed assemblies were calculated (Table 7.1). Figure 3.5 summarizes the evolution of the interaction energies as a function of the fluorination degree and used XB-acceptor (**A1** or **A2**). The results reveal a constant decrease of the binding energies starting from tetra-fluoroiodo donor **D1I** in the order  $D1I > D2I > D3I > \text{etc.}$  Moreover, the stilbazole generally forms more stable assemblies than the azo compound due to its higher electron density on the pyridine nitrogen which results in stronger binding energies with each XB-donor (*i.e.*  $D1I \cdots A2 > D1I \cdots A1$ ,  $D2I \cdots A2 > D2I \cdots A1$ , *etc.*). This is coherent with the results of the IR measurements.

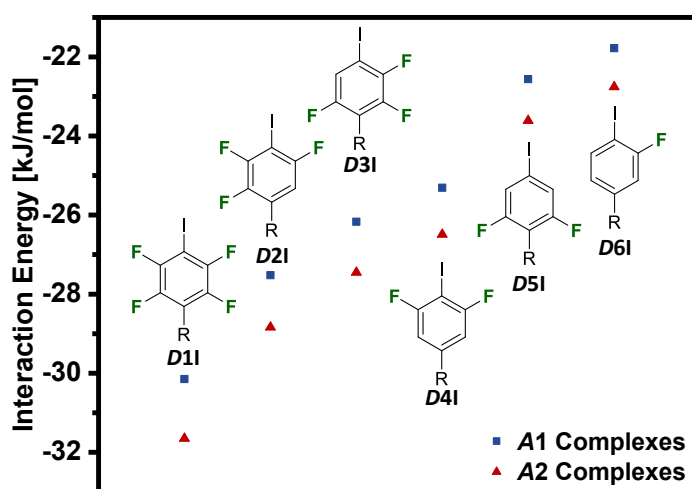


Figure 3.5: Graphical representation of the interaction energies in kJ/mol of XB acceptors **A1** (blue) and **A2** (red) as a function of the XB-donors **D1I** – **D6I**.

### 3.1.2.3 Crystallographic Analysis

Although the analysis of supramolecular interactions between two molecular synthons solely based on geometrical “the-stronger-the-shorter” considerations appears reasonable and has been performed in the past, this approach has been criticized as it often lacks computational support.<sup>[24, 148-150]</sup> Especially for halogen bonding, computational studies are often accompanied by crystallographic structure-property relationship studies and *vice versa*. This approach hence gives a comprehensive view on the underlying processes. Despite the fact that the single crystal packing is a result of numerous attractive and repulsive forces and that the supramolecular arrangement in the liquid crystalline state may differ, single crystal analysis can give a first impression of the supramolecular architecture and intermolecular interactions and is a further proof of the formation of the XB assemblies.<sup>[122]</sup>

By slow evaporation of equimolar ACN solutions of the XB-donors and -acceptors with a propoxy, and methoxy alkyl chain, respectively, three crystal structures of **D1I** (*P1*), **D2I** (*P2<sub>I</sub>*) and **D3I** (*P2<sub>I</sub>*) with **A2** were obtained (Figure 3.6). All these structures show highly directional halogen bonding between the iodine atom and the pyridine nitrogen. The lengths of the N⋯I contacts follow the trends suggested by the calculated binding energies (see Figure 3.5 and Table 7.1) and systematically increase with decreasing degree of fluorination from **D1I**⋯**A2** (A) to **D2I**⋯**A2** (B) to **D3I**⋯**A2** (C) (2.783 Å and 2.894 Å vs. 2.878 Å vs. 2.852 Å and 3.035 Å). Although complexes **D1I**⋯**A2** and **D3I**⋯**A2** show two different N⋯I contact distances, the average distances are still in line with the above mentioned theory. The found XB-distances roughly correspond to a reduction of the sum of the van-der-Waals radii between 25% (for **D1I**⋯**A2**) and 17% (for **D3I**⋯**A2**).<sup>[151]</sup> Taking a look at the individual C–I⋯N angles of **D1I**⋯**A2** (173.55° and 175.25°), **D2I**⋯**A2** (174.85°), and **D3I**⋯**A2** (173.32° and 171.83°) (Figure 3.6), reveals an increasing directionality (*i.e.* the value of the C–I⋯N angle being closer to 180°) with decreasing N⋯I distance. This is in accordance with previous findings.<sup>[152]</sup> However, taking the averaged C–I⋯N angles does not support this theory, which is probably due to the higher degree of disorder in the packing of **D1I**⋯**A2** compared to **D2I**⋯**A2**.

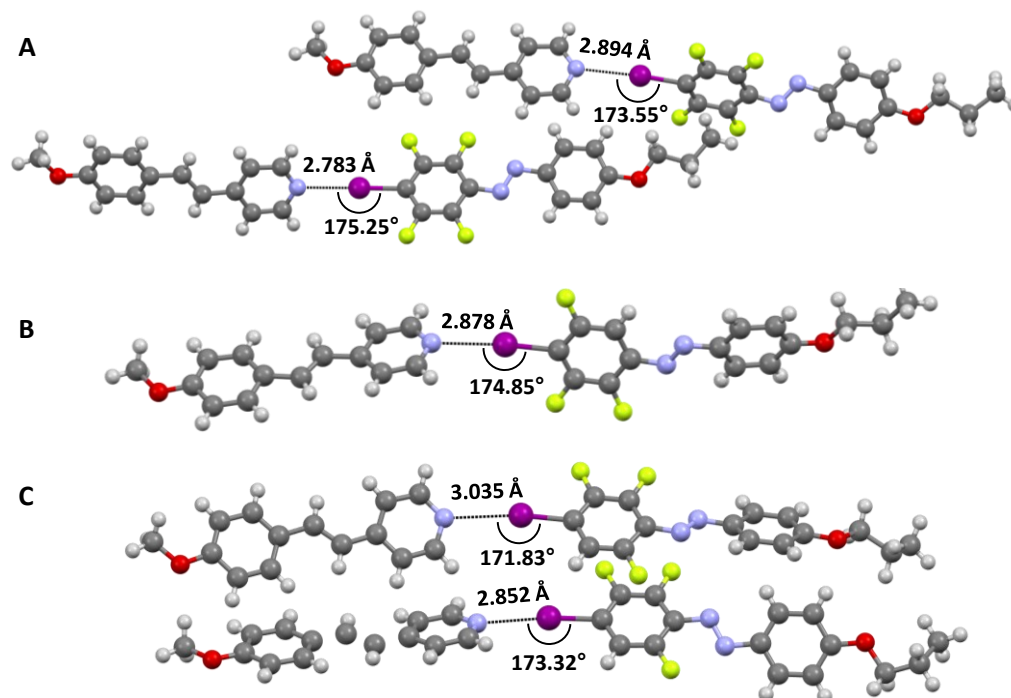


Figure 3.6: Crystal structures of **D1I**⋯**A2** (A, *P1*), **D2I**⋯**A2** (B, *P2<sub>I</sub>*) and **D3I**⋯**A2** (C, *P2<sub>I</sub>*) reveal the highly directional halogen bonds (dotted lines) between the iodine atoms and the pyridine nitrogens and the increasing N⋯I contact distances with decreasing fluorination degree. Ellipsoids are drawn at 50% probability and disordered fragments have been omitted for better understanding. Color code: gray: C; white: H; red: O; blue: N; yellow: F; purple: I.

In contrast to the findings reported by *Fernandez-Palacio et al.*, arene–perfluoroarene interactions do not play a major role in the crystal packing.<sup>[31]</sup> Instead, intermolecular F···H and H···O contacts of the fluoroarene ring support the head to tail alignment of the molecules (see Figure 3.7). Especially in complex **D3I···A2** (C) the asymmetric fluorination pattern plays a significant role in the H···O contacts between the positively polarized H on the trifluoroarene ring with the oxygen of an alkoxy chain of a neighboring stilbazole. Interestingly, the aromatic rings show a significant out of plane tilting along the azo bond, which is due to electrostatic and steric repulsion of the azo nitrogen atoms and the fluorine substituents.<sup>[153]</sup>

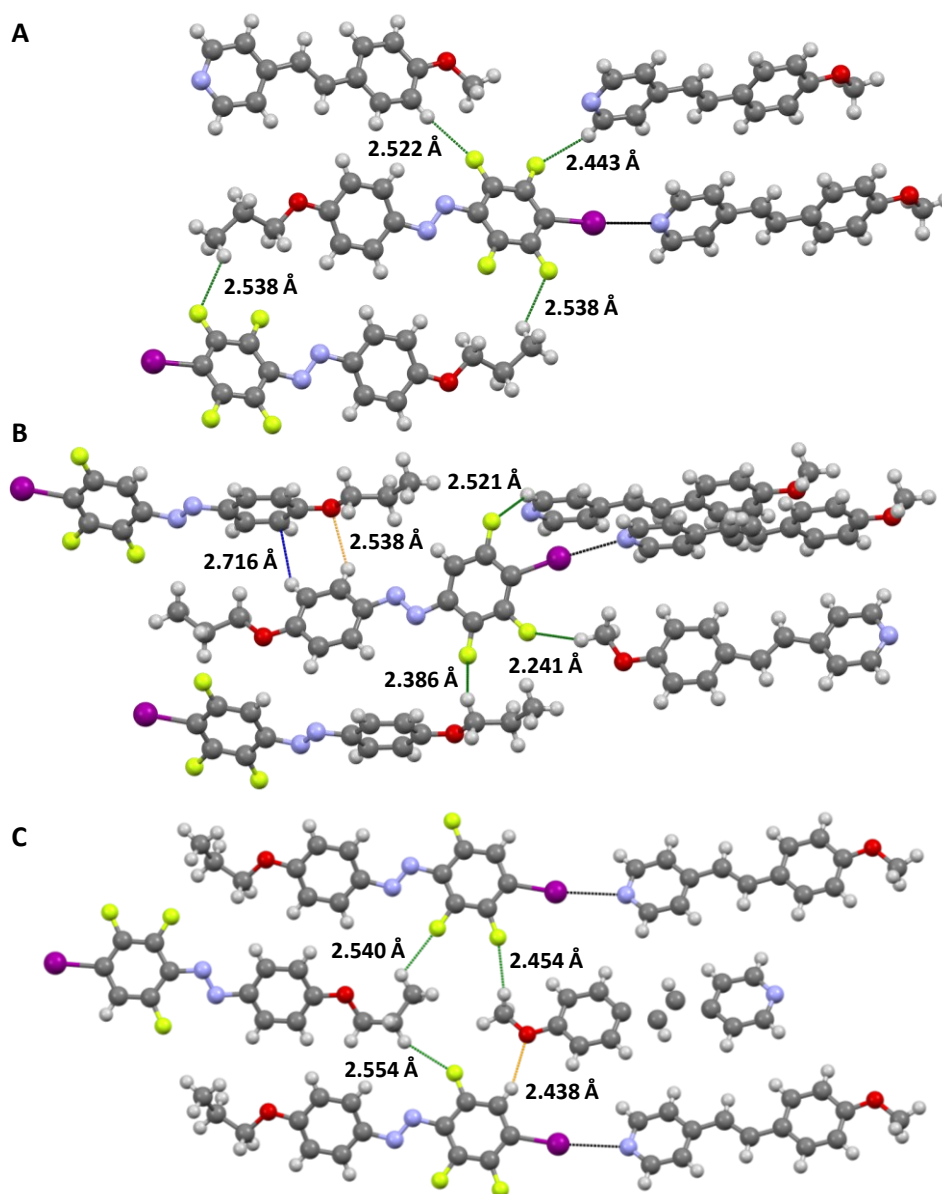


Figure 3.7: Partial view of the crystal packing of **D1I···A2** (A), **D2I···A2** (B) and **D3I···A2** (C). Weak H···O (orange dotted line) C···H (blue dotted line), and H···F contacts (green dotted line) support the head to tail orientation of the molecules. Color code: gray, C; white, H; red, O; blue, N; yellow, F; purple, I.

### 3.1.3 Mesomorphic Behavior

The following chapters deal with a detailed analysis of the thermal and mesomorphic properties of both building blocks and supramolecular assemblies using representative examples. For the investigation, all compounds and assemblies were studied using POM and DSC. All additional data can be reviewed in Chapter 7.2 and will be referenced where necessary. If not otherwise stated, transition temperatures and mesophase ranges were determined using temperature variable POM using untreated glass object and cover slides. It has to be noted that the results discussed in this chapter partly deviate from the ones that have already been published which changes the view on the underlying processes due to more recent observations.<sup>[154]</sup>

#### 3.1.3.1 Thermal Behavior of Building Blocks

Since some of the building blocks pose high structural similarity or are identical to already reported molecules which do not exhibit liquid crystalline properties, only building blocks **D2I** through **D6I** were investigated with respect to their thermal behavior. In accordance with the literature, most of the building blocks did not show liquid crystalline behavior upon heating or cooling. However, a monotropic liquid crystalline phase with a temperature range of  $\Delta T_{\text{meso}} = 17\text{ }^{\circ}\text{C}$  was observed for **D6I** (Figure 3.8A). Upon cooling from the isotropic melt (B), a focal conic texture, which is characteristic for a smectic phase, formed between  $73^{\circ}\text{C}$  and  $56^{\circ}\text{C}$  (C) before transferring to the crystalline state (E). Shearing of the sample in its LC state resulted in a quenching of the birefringent properties (D). This is a typical behavior often observed for nematic or smectic A phases and is caused by a reorientation of the LC domains (Figure 3.9A) to an unidirectional homogeneous alignment of the molecules (parallel) and smectic domains (perpendicular) between the glass slides (B).<sup>[155]</sup>

The formation of a monotropic liquid crystalline phase was also observed in the DSC trace of **D6I** (see Figure 7.3E). The phase transition enthalpy of  $\Delta H_{I-Sm} = -4.4\text{ kJ/mol}$  is in the range of previously reported enthalpies for  $I \rightarrow Sm$  transitions of 4.0 to 6.0 kJ/mol. On the other hand, energies for  $I \rightarrow N$  transitions of such covalent systems are usually between 0.5 and 1.0 kJ/mol.<sup>[156]</sup> The characterization of the LC properties of halogenated and halogen-bonded LCs *via* SAXS experiments will be discussed at a later stage of this thesis.

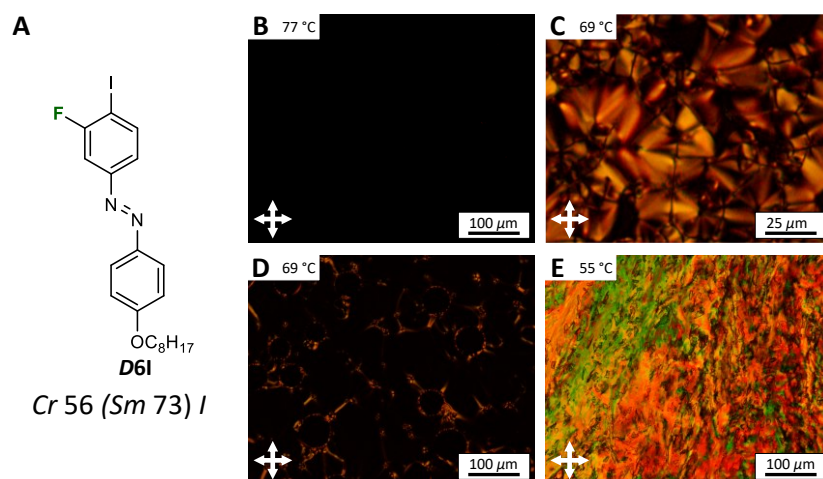


Figure 3.8: Molecular structure and transition sequence of **D6I** (A). POM images reveal the focal conic texture of an *Sm* phase (C) upon cooling from the isotropic melt at 78 °C (B) to the crystalline state at 55 °C (E). Shearing of the sample in its LC state at 69 °C causes a quenching of the birefringence due to homogeneous alignment.

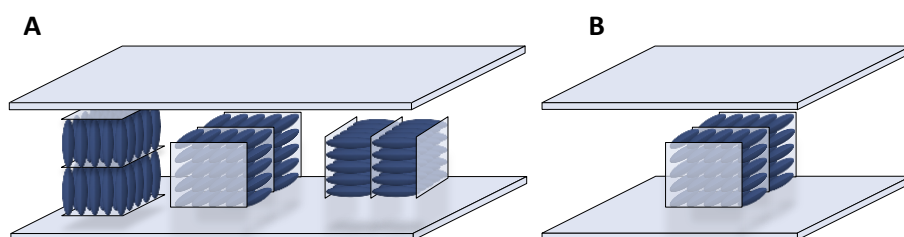


Figure 3.9: Schematic representation of the molecular alignment of an *SmA* phase before shearing (A) and homogeneous alignment after application of shear stress (B).

Compared to **D6I**, the absence of mesomorphic properties of **D2I** – **D5I** can be explained by the increased steric hindrance of the laterally substituted fluorine atoms. These are known to have a tremendous impact on the thermal and mesomorphic properties of covalent and supramolecular liquid crystals.<sup>[157]</sup> *Goodby et al.* could show that lateral fluorine substitution of rod-like mesogens significantly reduces transition temperatures and mesophase ranges.<sup>[158]</sup> More recently, *Giese* and coworkers investigated the impact of fluorination on the LC properties of supramolecular hydrogen bonded LCs and found similar effects for lateral fluorination.<sup>[124]</sup> Therefore, increasing the number of fluorine substituents decreases the mesophase range and leads to an absence of mesomorphic properties for compounds with more than one fluorine substituent.

### 3.1.3.2 Thermal Behavior of the Halogen-Bonded Assemblies

The investigation of the supramolecular assemblies reveals significant changes in the thermal behavior depending on both the used XB-acceptor and the fluorination pattern of the

XB-donors. As the thermal properties of such supramolecular assemblies strongly depend on several inter- and intramolecular interactions, the complex interplay of these interactions makes unambiguous and comprehensive structure-property correlations a challenging task. The changing fluorination pattern, for example, not only alters the electronic nature of the complete  $\pi$ -system but also affects the dielectric anisotropy of the whole assembly. Therefore, the interpretation of the results will be performed in a simplified manner by focusing on the halogen bonds and correlate their strengths with the thermal behavior. In this respect, the interpretation will be made, separately viewed from both the acceptor side and the donor side. To exclude the formation of liquid crystallinity solely by intermolecular interactions instead of the XB formation, the non-iodinated derivative **D1H** was used as reference and combined with the XB-acceptors **A1** and **A2**. In both cases no liquid crystallinity was observed, and the melting and crystallization temperatures were close to the ones of pristine **D1H**. Figure 3.10 shows the mesophase diagram of all investigated assemblies revealing the transition temperatures upon cooling from the isotropic melt as observed under the POM. The thermal behavior upon heating, additional POM images and DSC diagrams are displayed in Figure 7.5, Figure 7.6, and Figure 7.7.

#### *Impact of the halogen bond acceptor*

Comparison of the thermal behavior of assemblies using azopyridine XB-acceptor **A1** with complexes using **A2** reveals an unambiguously lower thermal stability of the **A1** aggregates (Figure 3.10). **A1** only showed enantiotropic nematic behavior in combination with **D1I** ( $\Delta T_{N,h} = 4\text{ }^{\circ}\text{C}$  upon heating,  $\Delta T_{N,c} = 16\text{ }^{\circ}\text{C}$  upon cooling) and monotropic behavior for combination **D2I**...**A1** ( $\Delta T_{N,h} = 4\text{ }^{\circ}\text{C}$ ). In contrast, **A2** exhibited enantiotropic behavior in combination with **D1I** ( $\Delta T_{N,h} = 15\text{ }^{\circ}\text{C}$  and  $\Delta T_{N,c} = 34\text{ }^{\circ}\text{C}$ ) and **D3I** ( $\Delta T_{N,h} = 4\text{ }^{\circ}\text{C}$  and  $\Delta T_{N,c} = 9\text{ }^{\circ}\text{C}$ ), and monotropic behavior with **D2I** ( $\Delta T_{N,c} = 9\text{ }^{\circ}\text{C}$ ). A possible explanation for the noticeably broader temperature ranges upon cooling is a kinetic hindrance of the crystallization due to the out of plane tilting of the aromatic rings of the XB-donor as observed in the crystal structure (Figure 3.11).

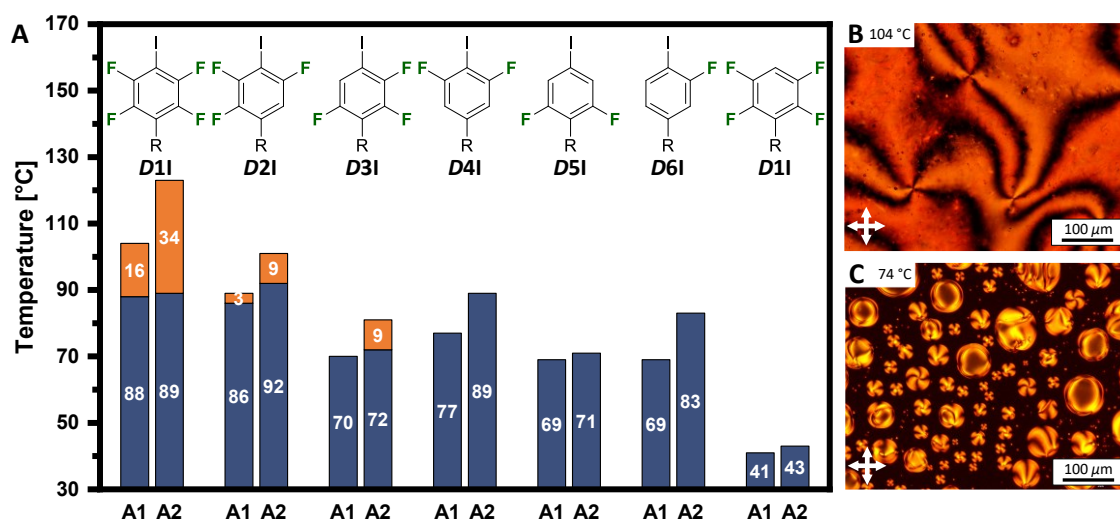


Figure 3.10: Thermal behavior of the halogen-bonded assemblies (A) upon cooling from the isotropic melt as observed under POM: orange, nematic; blue, crystalline phase. Representative POM micrographs of **D11**...**A2** (B) and **D31**...**A2** (C) reveal the characteristic “Schlieren” (B) and droplet texture (C) of a nematic phase upon cooling from the isotropic melt.

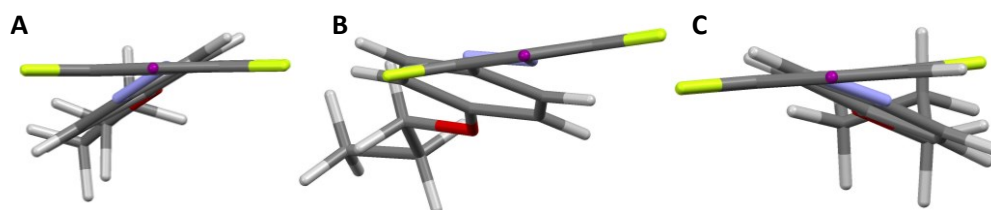


Figure 3.11: Capped sticks representations of **D11** (A), **D21** (B), and **D31** (C) in the crystal structures with **A2**, show the out of plane tilting of the aromatic rings. Molecules viewed along the C–I bond.

The mono- and enantiotropic behavior of the assemblies can be attributed to the lower XB accepting capability of **A1** due to the electron withdrawing property of the azo moiety (see also Section 3.1.2). Combined with electrostatic repulsion of the free electron pairs of the azo bond, this leads to a strong destabilization of the mesophase.<sup>[9, 159]</sup> In fact, considering the calculated interaction energies of **A1** and **A2** with the respective XB-donors (see also Figure 3.5 and Table 7.1) reveals significantly lower (less negative)  $\Delta E_{\text{int}}$  values for all combinations with **A1** (e.g.  $\Delta E_{\text{int}} = -30.15$  kJ/mol for **D11**...**A1** vs.  $\Delta E_{\text{int}} = -31.65$  kJ/mol for **D11**...**A2**). Interestingly, the combination of **D6I** with **A1** or **A2** results in a complete quenching of the LC property of **D6I**. This indicates that no thermally stable XB is formed in this case. Instead, the non-liquid crystalline acceptor molecules act as impurity in the liquid crystalline host system **D6I** and prevent the formation of a mesophase.

---

*Impact of the halogen bond donor*

This discussion mainly focuses on the mesophase behavior of the stilbazole assemblies, as they prevail over their azopyridine counterparts in terms of mesophase range and transition temperatures. By comparison of these parameters, it is possible to correlate the observed changes with the structural modifications and thus the halogen bond strength.

At first glance, the evolution of the mesophase ranges follows the decreasing fluorination degree and pattern (*i.e.* decrease of XB-strength) from tetra- to trifluoro derivatives (Figure 3.10). Decreasing the number of fluorine substituents even further leads to a complete absence of a mesophase suggesting, that no thermally stable XB is present in these combinations. While **D1I**⋯**A2** exhibits a broad nematic mesophase (Figure 3.10B) with a temperature range of  $\Delta T_{N,c} = 34$  °C upon cooling, the temperature range is significantly reduced to  $\Delta T_{N,c} = 9$  °C for **D2I**⋯**A2**. Following this trend, an even narrower nematic mesophase range is expected for **D3I**⋯**A2**. However, **D3I**⋯**A2** not only shows enantiotropic behavior but also has a similar mesophase range as **D2I**⋯**A2** upon cooling ( $\Delta T_{N,c} = 9$  °C). This effect can be attributed to the decreased transition temperatures observed for **D3I**⋯**A2** which prevents the thermal dissociation of the XB and thus an improved mesophase range. An additional effect that plays a role, is the formation of additional intermolecular interactions of the halogenated aromatic ring due to the decreased steric hindrance as observed in the crystal structure of **D3I**⋯**A2** (Figure 3.7C). Such interactions were not observed for **D2I**⋯**A2** (Figure 3.7B). *Präsang et al.* used a similar explanation for their observations on the evolution of N⋯I contact distances between different fluoriodobenzenes and DMAP.<sup>[55]</sup>

The results obtained here show that a minimum of three fluorine atoms on the XB-donor side is needed for the formation of sufficiently strong halogen bonds which can stabilize a mesophase. Therefore, the smallest structural changes can have significant effects on the interaction energies and thus the resulting macroscopic properties. Looking at the evolution of the transition temperatures in order of the fluorination degree reveals that this behavior can indeed be correlated with the decreasing strength of the formed halogen bond. A lower XB strength results in an easier rupture of the supramolecular bond (*i.e.* disassembly of the complex) at elevated temperatures and a quenching of the LC properties. A similar behavior was also observed for the azopyridine assemblies.<sup>[126]</sup>

---

### 3.1.3.3 Mesophase Morphology

As described, the supramolecular assemblies tend to form nematic mesophases, while **D6I** apparently forms a smectic phase. So far, the characterization of the mesophase morphology was solely performed based on interpretation of polarized optical microscopy images and DSC traces. However, a much more sophisticated technique to characterize the formed mesophase and to elucidate the molecular alignment inside the liquid crystalline state are SAXS and WAXS measurements.<sup>[160]</sup> These techniques can provide a detailed view on the molecular alignment inside a liquid crystalline phase. The experiments discussed in this chapter were performed in collaboration with *Prof. Markus Mezger* at the Max Planck Institute for Polymer Research in Mainz. The samples were filled into glass capillaries, heated to the isotropic melt, and subsequently cooled to the mesophase. To increase the alignment inside the capillary, the sample was oriented in a Magnetic field applied parallel to the equator line. The following discussion focuses on the experiments performed with **D11**···**A2**, as it proved to be the combination with the broadest mesophase range and best molecular alignment during the previously performed POM experiments (Figure 3.10B).

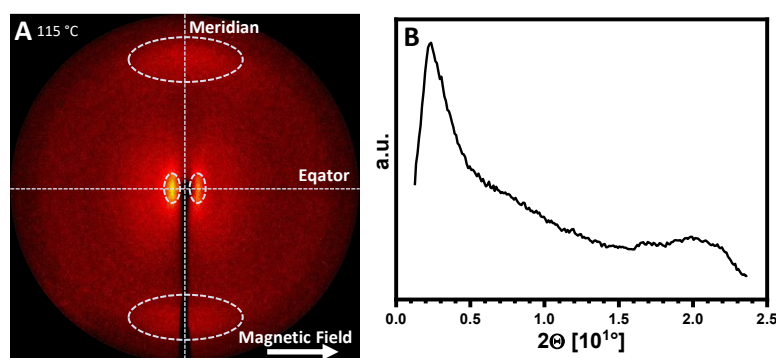


Figure 3.12: 2D diffraction pattern of **D11**···**A2** at 115 °C (A) and the radially averaged 2θ plot (B) reveal two diffuse halos along the meridian and equator line (dashed circles) confirming the formation of a nematic phase.

The 2D diffraction pattern of **D11**···**A2** at 115 °C (Figure 3.12) reveals two sets of diffuse halos at  $2\Theta = 2.2^\circ$  and  $20.0^\circ$  corresponding to real space distances of 39.7 Å and 4.4 Å which confirms the formation of a nematic mesophase.<sup>[9, 161]</sup> However, due to the high electron density of the iodine atom, the intensity of the scattered X-rays was significantly lowered. A fourfold increase of the measuring time and the overlay of four data sets was necessary to obtain the 2D SAXS pattern illustrated in Figure 3.12. Trials to solve the issue by using glass capillaries with a smaller diameter ( $\varnothing = 4$  mm) failed due to insufficient alignment of the sample in the LC phase and due to fast crystallization. Therefore, no further characterization using this technique was conducted.

### 3.1.4 Photo-Physical Properties

The experiments described here were performed in collaboration with *Prof. Arri Priimägi Kim Kuntze*, and *Matti Virkki* at the Tampere University of Applied Sciences in Finland.

Fluorination of azo benzenes is a powerful tool to selectively tweak the photo-physical properties of said entities and has been investigated by numerous researchers in terms of applicability.<sup>[129-130, 162]</sup> Especially *ortho*-fluorination (*ortho* to the azo linkage) proved to be an efficient way to obtain bistable photo-switches. These molecules can only be switched from the *trans*- to the *cis*-isomer and *vice versa* using light with specific different wavelengths and can therefore exhibit *cis* lifetimes of up to several years.<sup>[127-128]</sup> In this context, *cis* lifetime is referred to as the time that it takes to thermally switch half of the photo-induced *cis* isomer back to its *trans* isomer without using light irradiation. This chapter focuses on the photo-responsive properties of the fluorinated XB-donors described above (see Section 3.1.3) and the investigation of the *cis* lifetime behavior of **D11** – **D6I** and **D1H** as a function of the fluorination degree and pattern (see also Figure 3.1). Subsequently, the photo-responsive properties of the liquid crystalline assemblies **D11**··**A2**, **D2I**··**A2**, and **D3I**··**A2** are elucidated.

The *cis* lifetime determination of the building blocks was performed in dilute ( $10^{-5}$  M) solutions of dimethylformamide (DMF) in the dark to prevent disturbance from surrounding light sources. Prior to the actual measurements, the absorption maxima of the respective compounds were measured at room temperature to ensure that the maxima are in the same wavelength region and therefore show a similar reaction to photoirradiation with 365 nm laser light. The determined maxima were found to be in the range of  $\lambda_{\text{max}} = 348$  to 373 nm (see Figure 3.13 and Figure 7.10). Interestingly, the absorption maximum of the  $\pi \rightarrow \pi^*$  transition at  $\sim 360$  nm was more red-shifted for compounds **D2I**, **D4I**, and **D6I** (Group II) having less fluorine atoms in *ortho*-position to the azo linkage than compounds **D1I**, **D3I**, and **D5I** (Group I). This indicates a possible distortion of the planarity of the molecule due to steric hindrance or electrostatic repulsion.<sup>[127]</sup> In addition, the maximum wavelengths gradually blue-shift within these two groups with decreasing number of fluorine substituents from  $\lambda_{\text{max}} = 373$  nm (for **D2I**) to 365 nm (for **D6I**) and from  $\lambda_{\text{max}} = 364$  nm (for **D1I**) to 348 nm (for **D5I**) (Figure 3.13B). This shows the significant impact of the fluorination pattern on the photo-physical properties of the compounds. Comparing the maximum wavelengths of ref-

erence compound **D1H** ( $\lambda_{\max} = 355$  nm) with **D1I** ( $\lambda_{\max} = 364$  nm) reveals, that also the iodine has a significant effect on the  $\pi \rightarrow \pi^*$  transition wavelength and leads to a blue shift of the absorption maximum.

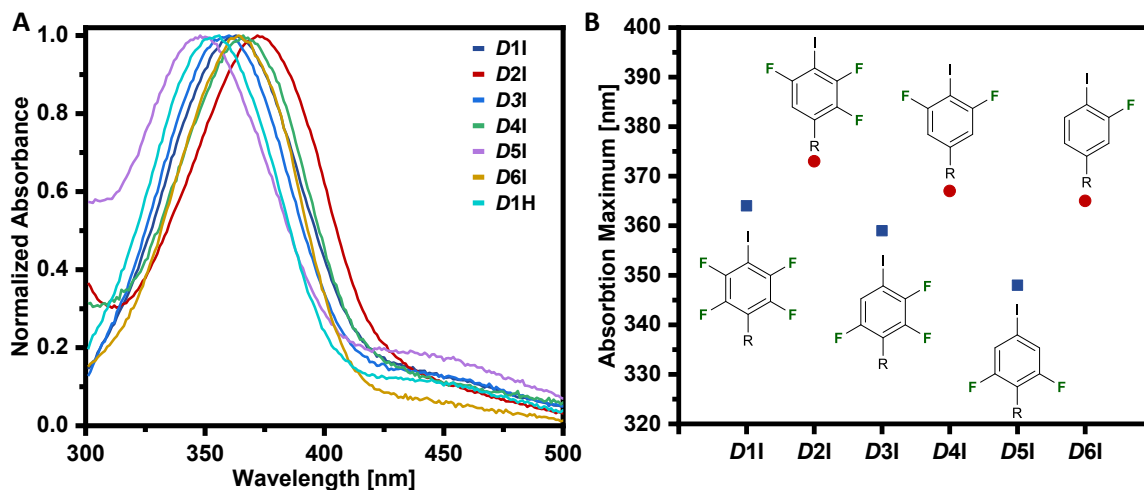


Figure 3.13: UV/Vis absorption spectra of azo photo switches **D1I** – **D6I** and **D1H** (A) and the evolution of the absorption maximum as a function of the fluorination degree and pattern for Group 1 (red circles) and Group 2 (blue squares, B).

#### 3.1.4.1 Photo-responsive Behavior in Solution

For the determination of the *cis* lifetimes, the samples were irradiated with 365 nm UV light ( $\sim 100$  mW/cm<sup>2</sup>) for 30 s. This causes a significant decrease in intensity of the  $\pi \rightarrow \pi^*$  band which slowly recovers after ceasing of irradiation (Figure 3.14A). The evolution of the recovery process was followed over time. Due to the magnitude of the *cis* lifetimes, the measurements were performed at elevated temperatures of 100, 80, and 60 °C. The *cis* lifetimes at 25 °C were extrapolated from the data obtained at elevated temperatures by fitting the kinetic absorbance data at a selected wavelength close to the  $\pi \rightarrow \pi^*$  transition using equation (4)

$$Abs = Abs_{\infty} + (Abs_0 - Abs_{\infty})e^{-kt} \quad (4)$$

where  $Abs_{\infty}$  corresponds to the absorption in the *trans* rich state and  $Abs_0$  to the absorption in the photo-stationary state. The rate constant  $k$  describes the lifetime constant of the *cis-trans* transition and is the inverse of the lifetime  $\tau$ . Linearization of equation (4) gives equation (5):

$$\ln \frac{(Abs - Abs_{\infty})}{(Abs_0 - Abs_{\infty})} = -kt \quad (5)$$

Using the Arrhenius plot

$$\ln(k) = \ln(A) - \frac{E_a}{R} \cdot \frac{1}{T} \quad (6)$$

with the  $k$  values obtained at elevated temperatures allows to linearly plot the inverse of the temperature (in Kelvin) as a function of  $\ln(k)$  and thus extrapolate the lifetime constant  $k$  and lifetime  $\tau$  at 25 °C.<sup>[163]</sup>

Figure 3.14A shows the evolution of the *cis-trans* relaxation of **D1H** after irradiation with 365 nm UV light at 60 °C, as a representative example. Linearization of the data at a selected wavelength of 380 nm using equation (5) yields the lifetime constant of  $k_{60} = 2.918 \cdot 10^{-5} \text{ s}^{-1}$  (B). By plotting the natural logarithm of the lifetime constants ( $\ln(k)$ ) at elevated temperatures in an Arrhenius plot (C), the *cis* lifetime at 25 °C (purple square) can be extrapolated. All additional spectra of the all-*trans* and photo-stationary states of compounds **D1I** – **D6I** and **A2**, and all Arrhenius plots are summarized in Figure 7.10 and Figure 7.11. All experimentally determined  $k$  values can be reviewed in Table 7.2.

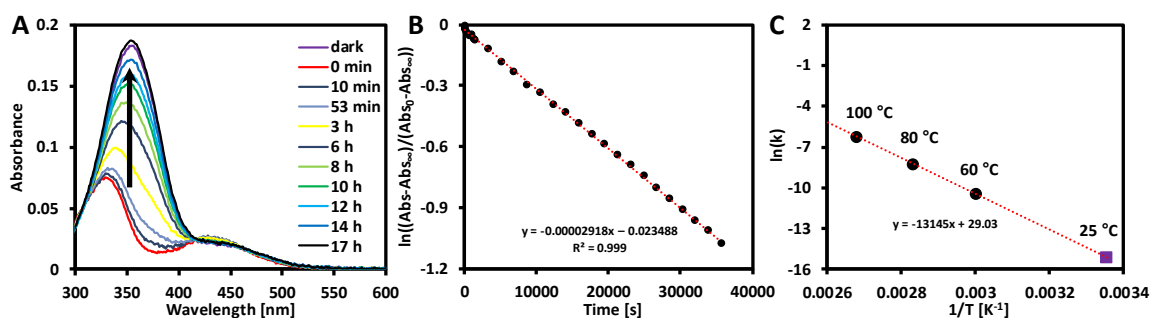


Figure 3.14: *Cis-trans* relaxation spectra of **D1H** at 60 °C after irradiation with 365 nm laser light ( $\sim 100 \text{ mW/cm}^2$ ) (A) and linear plot of the *cis-trans* relaxation (B) at the selected wavelength of 380 nm. The Arrhenius plot of **D1H** (C) shows the lifetime constants at 100, 80, and 60 °C (black circles) and the extrapolated value of  $\tau$  at 25 °C (purple square) using the linear fit (dashed line).

The main trend that can be seen by looking at the *cis* lifetimes (Table 3.1) becomes obvious when comparing the behavior of the two mentioned groups (Group I: **D1I**, **D3I**, and **D5I** and Group II: **D2I**, **D4I**, and **D6I**). Generally, the *cis* lifetimes for Group I, having fluorine substituents in *ortho*-position to the azo linkage, proved to be one order of magnitude longer than those found for Group II.

Table 3.1: Absorption maxima and measured *cis* lifetimes at 100, 80, and 60 °C. Values at 25 °C are extrapolated values. Group I: white; Group II: grey.

	$\lambda_{\max}$ [nm]	$\tau_{100}$ [s]	$\tau_{80}$ [s]	$\tau_{60}$ [s]	$\tau_{25}$ [d]
<b>D1I</b>	364	316.8	2 146	15 429	12.6
<b>D2I</b>	373	48.1	283.8	2 244	1.7
<b>D3I</b>	359	451.7	2 770	22 737	18.7
<b>D4I</b>	367	99.0	556.8	3 484	2.0
<b>D5I</b>	348	549.5	4 095	37 258	42.9
<b>D6I</b>	365	50.1	308.0	2 283	1.7
<b>D1H</b>	355	497.0	3 685	34 270	40.1

Based on the results reported by *Bléger et al.*<sup>[127]</sup> and *Knie et al.*<sup>[128]</sup>, this trend is expected for *ortho*-fluorinated derivatives (Group I) and can be attributed to a stabilization of the *cis* isomer due lower electron density on the nitrogen and thus reduced electronic repulsion of the nonbonding electron pairs. This leads to a lower *cis-trans* relaxation rate and thus longer *cis* lifetime. Interestingly, the lifetimes of the three *ortho*-fluorinated donor molecules systematically increased with decreasing number of fluorine atoms from  $\tau_{25} = 12$  d for **D1I** to  $\tau_{25} = 19$  d for **D3I** to  $\tau_{25} = 43$  d for **D5I**. On the other hand, the *cis* lifetimes of **D2I**, **D4I**, and **D6I** did not significantly change. This shows that both the fluorine in *ortho*-position and the fluorination pattern itself play a significant role.

Comparison of the results of **D1I** and **D1H** reveals, that the substitution of the iodine atom by hydrogen also significantly increases the *cis* lifetime (12 d vs. 40 d). Although the investigations of *Bléger et al.* suggest, that *para*-substituted iodine and bromine do not significantly influence the switching wavelengths of azo benzenes, this finding may be attributed to both steric and favorable electronic contributions of the iodine causing a decrease of the activation energy of the *cis-trans* isomerization which in turn results in lower *cis* lifetimes.<sup>[127]</sup>

#### 3.1.4.2 Photo-responsive behavior in the LC state

The investigation of the photo-responsive behavior in the LC state was conducted as follow-up to previously reported results by *Fernandez-Palacio et al.* on the properties of the system **D1I**...**A2**.<sup>[31]</sup> They found, that only a small portion of *cis*-isomer is necessary to induce a transfer from the liquid crystalline to the isotropic state. The photo-induced *trans-cis* isomerization of the azo compounds in the liquid crystalline state causes a disturbance of the molecular order and thus a collapse of the mesomorphic properties. Upon thermal relaxation

of the system, the liquid crystallinity reappears. Using photo-switches with different *cis* lifetimes allows to tweak the photo-physical properties of the supramolecular assembly and the liquid crystalline properties. The idea of this study is to shed light on the impact of the XB-acceptor (azopyridine *vs.* stilbazole) and the strength of the halogen bond (*i.e.* impact of donor **D1I**, **D2I**, and **D3I**) on the photo-responsive properties of the LC assemblies.

The main difference between the two halogen bond acceptor units **A1** and **A2** is, that **A1** itself is photo-responsive and shows *trans-cis* photoisomerization upon irradiation with UV light (see Figure 7.10H). On the other hand, **A2** is not photo-active under the used experimental conditions but forms stronger XBs and mesophases with broader temperature ranges (Figure 3.5 and Figure 3.10). The *cis* lifetime of **A1** was found to be 3.8 h at room temperature in dilute DMF solution (Figure 7.12A) which is much shorter than any of the investigated donor molecules. The comparison of the impact of the two XB-acceptors was conducted using **D1I** as XB-donor which showed the most stable mesophases with both **A1** and **A2**. First, the samples were irradiated for 30 s in the liquid crystalline state using laser light with a wavelength of 405 nm (40 mW/cm<sup>2</sup>) to cause a photo-induced transition from the liquid crystalline to the isotropic state. Subsequently, the reorganization of the sample and reformation of the LC state were monitored by measuring the change of the birefringence ( $\Delta n$ ) and the optical scattering (Attenuance) as a function of the time (Figure 3.15). To obtain comparable results of assemblies **D1I**···**A1** and **D1I**···**A2**, the experimental temperatures were chosen to be 94 °C and 96 °C, respectively, as they lie as close as possible to each other but yet yield steady mesophases without crystallization. The results reveal a significantly longer photoinduced isotropization of **D1I**···**A1** (red curve) having two photo-isomerizable units than of **D1I**···**A2** (blue curve) where only **D1I** is affected by irradiation (890 s *vs.* 250 s). The photo-induced *trans-cis* isomerization of the azo linkage leads to an instant collapse of the LC properties and loss of birefringence and attenuance for both samples (Figure 3.15A). The small spike in optical scattering that appears upon irradiation is due to local phase separation into *trans*- and *cis*-rich domains causing the attenuance to increase for a short period of time.<sup>[164-165]</sup> The lifetime of the isotropic state is associated with the recovery of birefringence and optical scattering due to thermal *cis-trans* relaxation ultimately resulting in the recovery of the liquid crystalline state.<sup>[31]</sup>

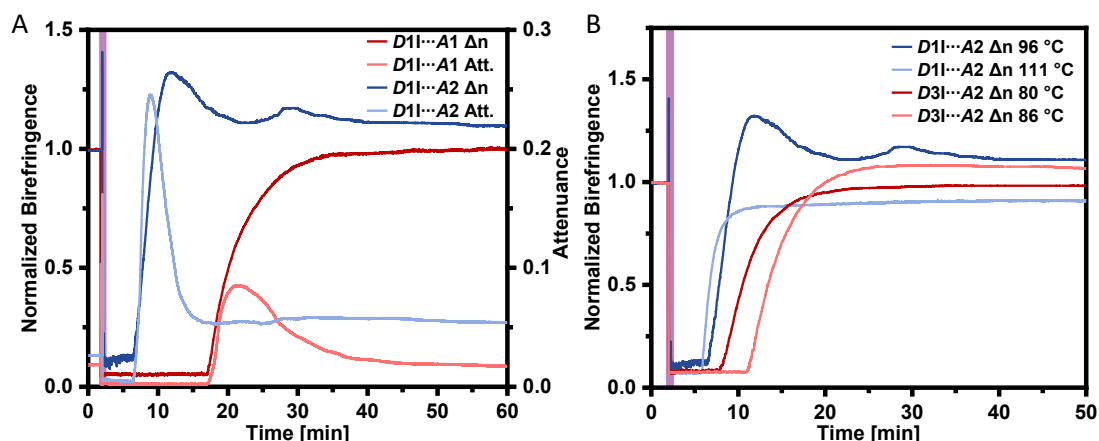


Figure 3.15: Evolution of the normalized birefringence ( $\Delta n$ ) and attenuation ( $Att.$ ) of **D11...A1** at 94 °C (red) and **D11...A2** at 96 °C (blue) (A) and evolution of the normalized birefringence ( $\Delta n$ ) of **D11...A2** at 96 °C and 111 °C (blue) and **D31...A2** at 80 °C and 86 °C (red) (B), both as a function of time upon irradiation with 405 nm laser light (purple bar).

Compared to **D11...A2** (250 s), the extended lifetime of the isotropic state (*i.e.* time until birefringence starts to recover) of **D11...A1** (890 s) seems to be coherent with the fact that it comprises two photo-isomerizable units (donor and acceptor) instead of only one. However, the *cis* lifetimes of the individual building blocks **D11** and **A1** at 94 °C were found to be 545 s and 16.2 s (Figure 7.12B), while having comparable absorption maxima at  $\lambda_{\max} = 364$  and 357 nm. Hence, the different recovery times of the liquid crystalline state are not a matter of the used XB-acceptor but rather a consequence of the different stabilities of the mesophases at the respective temperatures. While **D11...A1** at 94 °C is close to the clearing point, **D11...A2** at 96 °C is close to the crystallization temperature which is a different point in the phase diagram. This allows a larger fraction of *cis* isomer to be present without disturbing the liquid crystalline phase.<sup>[31]</sup> To confirm this assumption, the experiment was repeated at 111 °C which is close to the clearing point of **D11...A2** (Figure 3.15B). Even if the *cis* lifetime of **D11** is significantly decreased at this temperature, the lifetime of the isotropic state is only slightly decreased to 200 s (250 s at 96 °C). However, taking a closer look at the isotropic state lifetimes of **D11...A1** (890 s at 94 °C) and **D11...A2** (200 s at 111 °C) at their upper limits of their LC ranges, it seems reasonable to conclude that the isotropic state lifetime indeed directly depends on the *cis* lifetime differences of the azo moiety at the respective temperatures (545 s *vs.* 128 s). Although, the *cis* lifetimes of the azo units play a significant role in the stability of the photo-induced isotropic state lifetime, it is only possible to compare the effects of photo-responsive units at equivalent points in the phase diagram, *e.g.* either close to the clearing point, or close to the crystallization temperature.

To investigate the impact of the XB-donor moiety (*i.e.* fluorination degree) on the photo-responsive properties of the supramolecular complexes, combinations of **D1I**, **D2I**, and **D3I** with **A2** were investigated. According to the findings described above, the experiments were performed at two different temperatures, with one being close to the crystallization point and the other being close to the clearing point at the upper limit of the LC range. Unfortunately, **D2I**⋯**A2** directly crystallized inside the measuring cell and could not be investigated in the liquid crystalline state. This makes a comparison with the other two assemblies impossible. For **D1I**⋯**A2** and **D3I**⋯**A2** (Figure 3.15B) measuring temperatures of 96 and 111 °C, and 80 and 86 °C, were used. As discussed above, the isotropic state lifetimes of **D1I**⋯**A2** at the two different temperatures were found to be 250 and 200 s, with the recovery time being slightly shorter at higher temperatures. Interestingly, the isotropic state lifetimes of **D3I**⋯**A2** behaved completely different. Instead of being decreased at elevated temperature the lifetime was prolonged by 210 s from 330 s at 80 °C to 540 s at 86 °C. This clearly shows that the difference of the temperatures is a key factor for the analysis of photo-induced phase transitions of such liquid crystalline materials and that its effect on the isotropic state lifetime by far prevails over the impact of the *cis* lifetimes of the individual components.

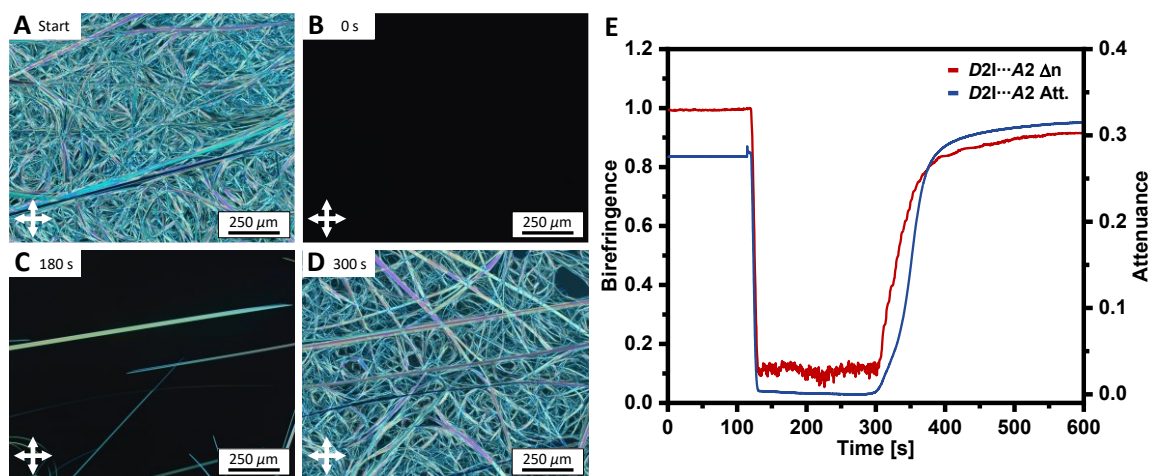


Figure 3.16: POM micrographs of the crystalline state of **D2I**⋯**A2** at 93 °C (A) reveal the photo-induced isotropization upon irradiation with 405 nm laser light (40 mW/cm<sup>2</sup>) for 30 s (B) and the slow recovery of the crystalline state within the subsequent 300 s after irradiation (C, D). *In situ* measurements of the birefringence ( $\Delta n$ ) and attenuance (Att.) (E) show the instant drop in intensity upon irradiation.

Although, **D2I**⋯**A2** crystallized inside the measuring cell during the course of the experiment it was possible to induce a fast and reversible *Cr* → *I* transition by irradiation with 405 nm laser light (40 mW/cm<sup>2</sup>). Upon irradiation of the crystalline sample at 93 °C for 30 s

(Figure 3.16A), the sample immediately transferred to the isotropic state within a few seconds (B) and relaxed to the crystalline state due to thermal *cis-trans* relaxation after 180 s (C), until full recovery after 300 s (D) was achieved. *In situ* measurements of the birefringence and scattering (E) confirmed the POM observations with an instant drop in intensity upon irradiation and subsequent slow recovery after 180 s.

### 3.1.5 Conclusion

The XB-donors **D1I** – **D6I** and acceptors **A1** and **A2**, as well as the reference unit **D1H** were successfully synthesized using modified literature known procedures. Although the synthesis of the XB-donors using sodium nitrite proved to be unsuitable due to solubility issues, moderate to good yields were obtained using an alternative procedure with nitrosyl tetrafluoroborate.

#### 1. Influence of the fluorination degree and pattern on the halogen bond strength.

IR spectroscopic data as well as computational and crystallographic analyses confirmed the formation of supramolecular assemblies between donors **D1I**, **D2I**, and **D3I** and acceptors **A1** and **A2**, and gave a more detailed view of the underlying supramolecular processes. Furthermore, the results show a direct correlation between the decreasing binding strengths between donor and acceptor moieties and the decline of the number of fluorine atoms (**D1I** > **D2I** > *etc.*). The changing fluorination pattern also plays a crucial role. Generally seen, donor molecules with fluorine substituents in *ortho*-position to the iodine tend to form larger  $\sigma$ -holes and therefore stronger XBs (*e.g.* **D2I** > **D3I**).

#### 2. Influence of the halogen bond strength on the mesomorphic properties.

Investigation of the liquid crystalline properties of both building blocks and supramolecular assemblies exposed the significant effects of the number and position of fluorine atoms at the arene moieties. In the case of **D6I** it was shown that the sterical part of the lateral fluorine atom plays an important role for the formation or extinction of LC properties. Increasing the number of lateral fluorine substituents leads to a complete absence of LC properties. The thermal behavior of the assemblies revealed that the mesophase ranges follow the decreasing strength of the XB (*e.g.* **A1** < **A2** and **D1I** > **D2I** > **D3I**) and that at least three fluorine atoms at the donor site are necessary to form XBs with a high enough thermal stability for the exhibition of LC properties.

---

---

3. *Influence of the fluorination on the photo-physical properties of the materials.*

Photo-physical *cis* lifetime measurements of the azo building blocks displayed, that the values can significantly differ and strongly depend on fluorination degree and pattern. Lifetimes for compounds with fluorine atoms in *ortho*-position to the azo-moiety (e.g. **D1I**, **D3I**, **D5I**) are roughly one order of magnitude longer compared to compounds that do not feature this fluorination pattern (e.g. **D2I**, **D4I**, **D6I**). Investigation of the photo-induced *trans-cis* isomerization of halogen-bonded assemblies of **D1I**⋯**A2**, **D1I**⋯**A1**, **D2I**⋯**A2**, and **D3I**⋯**A2** allowed for fast and reversible switching of the mesophase and the crystalline state. However, the results reveal that the experiment temperature plays a much more important role for the isotropic state lifetimes of the assemblies, than the *cis* lifetimes of the individual compounds at the different temperatures.

---

### 3.2 Induction of Chirality using Halogen-Bonded Assemblies

Although research on chiral, doped LCs has been conducted for over three decades, the effects of supramolecular dopants on the chirality transfer remain obscure. In 2010, *Bruce et al.* investigated the liquid crystalline properties of chiral halogen-bonded assemblies of achiral and chiral tetrafluoroiodo stilben and stilbazole building blocks with a terminally attached citronellyl chain (see Figure 3.17, black box).<sup>[29]</sup> Besides the effect of the terminally attached achiral alkyl chain, they focused their investigations on the influence of the position of the chiral side chain (*i.e.* donor side *vs.* acceptor side), but found only minor changes compared to the achiral counterparts. Recently, *Giese et al.* reported on a supramolecular approach to induce chirality in hydrogen-bonded LC systems by addition of different amounts of chiral stilbazole and azobenzene to phloroglucinol to induce broad range blue phases.<sup>[93, 166]</sup> The first study comprising halogen-bonded chiral dopants in commercial liquid crystals was reported by *Wang et al.*<sup>[140]</sup> They developed a photo-switchable chiral unit to selectively switch the structural color of an LC sample by irradiation with laser light and demonstrated that the formation of the halogen bond can change the HTP value of a given dopant. However, they lacked a precise explanation, whether the effect is due to the formation of the supramolecular bond, or due to improved compatibility of the supramolecular dopant with the LC host compared to the non-bonded dopant.

This study aims to provide a deeper understanding of the effects of chiral induction in supramolecular LCs. A series of chiral halogen-bonded liquid crystals is identified, and their thermal properties are investigated depending on the different structural features (*e.g.* fluorination degree/pattern, azo *vs.* stilbene linkage, position of the chiral side chain). Subsequently, specific guest host combinations are chosen based on the obtained results and investigated with respect to the ability to induce chirality regarding the following key questions:

1. *What are the effects of the fluorination pattern on the HTP value?*
  2. *How does the formation of the supramolecular assembly affect the HTP value?*
  3. *How does the halogen bond strength influence the HTP Value?*
-

### 3.2.1 Halogen-Bonded Chiral Liquid Crystals

Because donors **D1I**, **D2I**, and **D3I** proved to be the only XB-donors to form mesophases with XB-acceptors **A1** or **A2**, the molecular library of the preceding study was extended by their chiral counterparts **D1I\*** – **D3I\***, and **A1\*** and **A2\***, respectively (Figure 3.17). The chirality of the systems is conferred by an attached *S*-citronellyl side chain (**R\***). The systematic combination of chiral and achiral acceptor and donor molecules ensures the comprehensive investigation of chiral induction in the halogen-bonded systems.

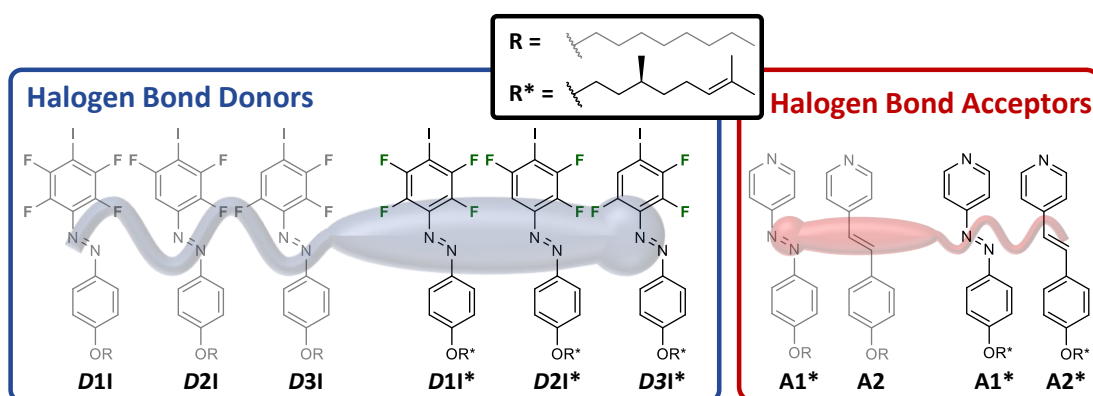


Figure 3.17: Library of achiral (grey) and chiral (\*) XB-donor and XB-acceptor building blocks.

The syntheses of chiral dopants **D1I\*** – **D3I\***, **A1\*** and **A2\***, and all precursors as well as the formation of the supramolecular assemblies was performed based on the approach described in Chapter 3.1.1. As alkylating reagent *S*-citronellylbromide was used, which gave the desired building blocks in isolated yields between minimum 35% (for **D1I\***) and maximum 85% (for **D2I\***). The isolated yields for the acceptor molecules were between 55% (for **A2\***) and 67% (for **A1\***). Based on the number of chiral and achiral donor and acceptor building blocks, the free combination thereof resulted in an overall number of 12 different chiral assemblies which are summarized in Table 3.2. The thermal and mesomorphic properties of the assemblies were characterized using POM and DSC.

Table 3.2: Summary of all chiral supramolecular assemblies using chiral and achiral donors and acceptors.

<b>XB-Donor</b>	<b>XB-Acceptor</b>	<b>Complex</b>
<b>D11*</b>	<b>A1</b>	<b>D11*...A1</b>
<b>D21*</b>	<b>A1</b>	<b>D21*...A1</b>
<b>D31*</b>	<b>A1</b>	<b>D31*...A1</b>
<b>D11*</b>	<b>A2</b>	<b>D11*...A2</b>
<b>D21*</b>	<b>A2</b>	<b>D21*...A2</b>
<b>D31*</b>	<b>A2</b>	<b>D31*...A2</b>
<b>D1I</b>	<b>A1*</b>	<b>D1I...A1*</b>
<b>D2I</b>	<b>A1*</b>	<b>D2I...A1*</b>
<b>D3I</b>	<b>A1*</b>	<b>D3I...A1*</b>
<b>D1I</b>	<b>A2*</b>	<b>D1I...A2*</b>
<b>D2I</b>	<b>A2*</b>	<b>D2I...A2*</b>
<b>D3I</b>	<b>A2*</b>	<b>D3I...A2*</b>

### 3.2.2 Mesomorphic Behavior of Chiral Assemblies

Because the formation of this kind of supramolecular assemblies has already been evidenced and discussed in the chapters above (see also Figure 7.13 and Figure 7.14), the following discussion exclusively focuses on the thermal properties of the supramolecular assemblies and the underlying structure-property relationships. To facilitate the correlation of the structural changes with the thermal behavior, the interpretation of the obtained results will be performed in a simplified manner by separately focusing on three main aspects of the structural features:

1. the effects of the position of the chiral side chain (acceptor side *vs.* donor side),
2. the impact of the acceptor moiety (azo *vs.* stilbene linkage), and
3. the effects of the donor moiety (fluorination degree/pattern).

#### *Impact of the Chiral Side Chain*

With exception of **D3I\*...A1**, all assemblies showed liquid crystallinity. As the chirality is an intrinsic information conferred by the chirality of the molecule itself, all formed mesophases also exhibited chirality in their long-range molecular order. Figure 3.18A summarizes the thermal behavior of all formed assemblies as observed under POM upon cooling from the isotropic melt. In comparison to the achiral equivalents, the results reveal significant changes in both transition temperatures and sequence of the mesophases.

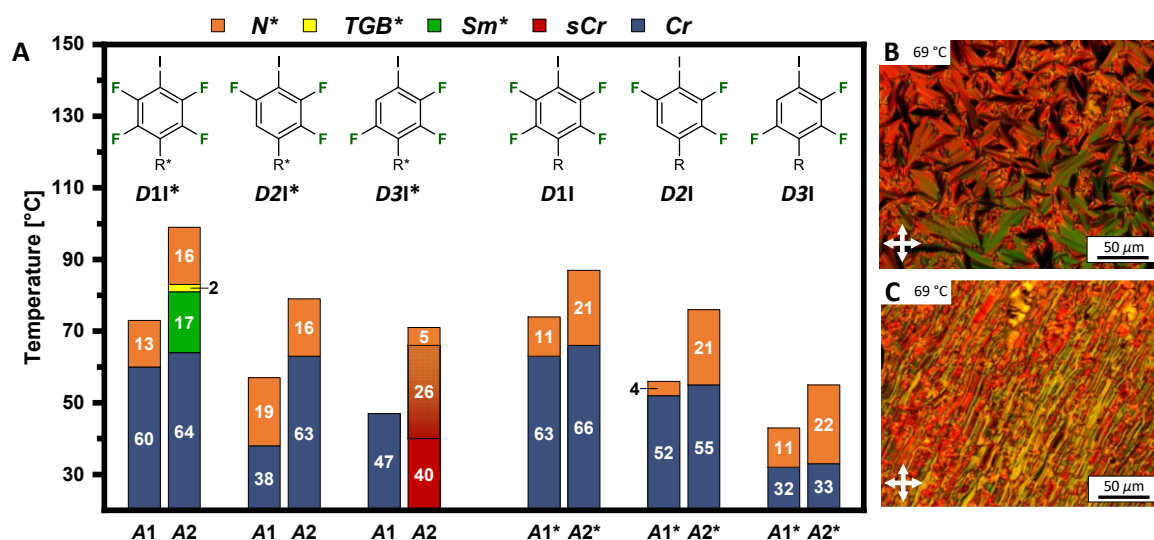


Figure 3.18: Transition temperatures of the formed chiral halogen-bonded assemblies as observed under POM upon cooling from the isotropic melt (A). While all liquid crystalline assemblies show clear transitions between the observed phases, **D31\*...A2** exhibits an indistinctive  $N^* \rightarrow sCr$  (soft crystal) transition. Representative POM images of **D11...A1\*** show the phase transition from the focal conic fan texture of an  $N^*$  phase (B) to an oily streak texture upon shearing of the sample (C).

Complexes formed by self-assembly of an achiral XB-donor (**D11** – **D31**) and a chiral XB-acceptor (**A1\*** or **A2\***) solely exhibited the typical focal conic fan texture of an  $N^*$  phase with a short pitch length (Figure 3.18B, see also). Shearing the sample in its liquid crystalline state caused the formation of an oily streak texture (C) with a planar alignment of the optical axis (*i.e.* helical axis) parallel to the propagation of the light beam. This is a typical behavior for chiral nematic LCs. With  $\Delta T_{N^*,c} = 21$  and  $22$  °C, the stilbazole (**A2\***) assemblies using **D21** and **D31** showed a significantly enhanced LC range compared to their achiral analogues ( $\Delta T_{N,c} = 9$  °C). On the other hand, the temperature range of **D11...A2\*** was decreased ( $\Delta T_{N,c} = 34$  °C *vs.*  $\Delta T_{N^*,c} = 21$  °C). This behavior can be explained by two counteracting effects. The doubly branched geometry and unsaturated link of the citronellyl side chain cause an overall order decrease, a decline of the transition temperatures, and reduction of both melting and clearing points which leads to a decline in the temperature range of the mesophase (see **D11...A2\*** in Figure 3.18A). On the other hand, the reduced transition temperatures prevent the halogen bond from thermal dissociation resulting in an increase of the clearing point temperatures and broader mesophases (see **D21...A2\*** and **D31...A2\***).<sup>[29, 126]</sup>

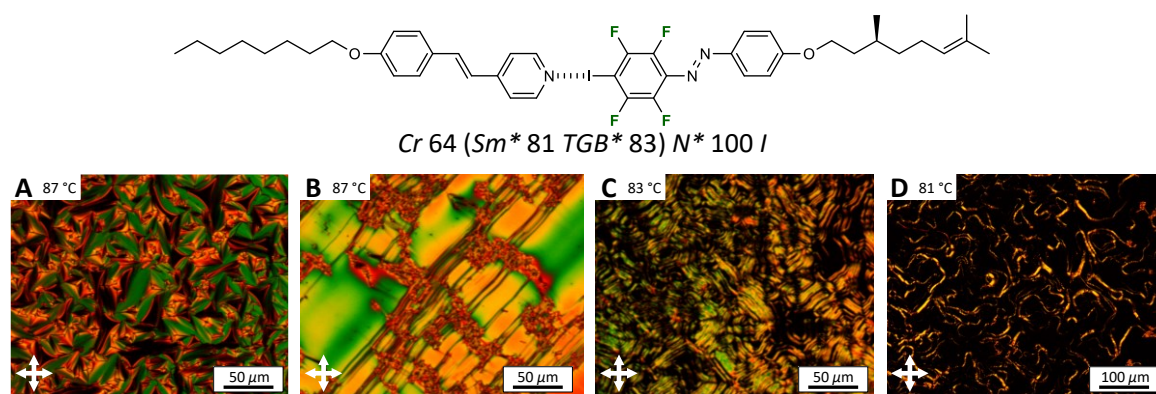


Figure 3.19: Supramolecular structure and mesophase sequence of  $D11^*\cdots A2$ . POM micrographs of  $D11^*\cdots A2$  under crossed polarizers reveal the different textures of the mesophases formed upon cooling from the isotropic melt: focal conic fan texture of an  $N^*$  phase (A); oily streak texture after shearing of the sample (B); filamentary texture of a TGB\* phase (C); texture of a defective homeotropic  $Sm^*$  phase (D).

The results reported by *Bruce et al.* suggest that the position of the chiral side chain does not have a significant effect on the thermal properties of these systems. However, using a chiral XB-donor and an achiral acceptor (*i.e.* donors  $D11^*$ ,  $D21^*$  and  $D31^*$  and acceptors  $A1$  or  $A2$ ) unquestionably broadens the LC range (*e.g.*  $D21^*\cdots A1^*$  vs.  $D21^*\cdots A1$ ), or the phase sequence is completely changed so that new mesophases can be observed (*e.g.*  $D11^*\cdots A2^*$  vs.  $D11^*\cdots A2$ ). In fact,  $D11^*\cdots A2$  not only showed a much higher  $T_C$  compared to its inverted analogue  $D11^*\cdots A2^*$  (100 °C vs. 87 °C) but also exhibited an  $N^* \rightarrow TGB^* \rightarrow Sm^*$  phase sequence upon cooling (Figure 3.19). Upon cooling from the isotropic melt, the typical focal conic fan texture of an  $N^*$  phase is formed (A). This was confirmed by shearing of the sample which yielded the characteristic planar aligned oily streak texture of an  $N^*$  phase (B). Upon further cooling, the filamentary texture of a TGB\* phase was observed (C) ultimately transferring to a mesophase which appears to be a defective homeotropic chiral smectic phase ( $\Delta T_{Sm^*,c} = 17$  °C).<sup>[29, 84, 167]</sup>

### Impact of the Acceptor Moiety

Comparison of the thermal behavior of aggregates using  $A1 / A1^*$  with the ones using  $A2 / A2^*$  reveals, that the unambiguous superiority of the stilbazole is retained for the chiral assemblies. In this respect, the azo assemblies generally exhibited significantly lower transition temperatures and smaller mesophase ranges. Moreover, none of the assemblies using  $A1$  or  $A1^*$  showed enantiotropic behavior, whereas both  $D11^*\cdots A2$  and  $D11^*\cdots A2^*$  revealed an  $N^*$  phase upon heating ( $\Delta T_{N^*,h} = 15$  and 10 °C) and a mesophase with a range of up to 33 °C upon cooling (see also Figure 7.15). As already described for the achiral analogues, this can be traced back to the XB accepting capability of stilbazole, which shows a higher

electron density on the pyridine nitrogen and is therefore capable of forming more stable assemblies with stronger XBs (see also Chapter 3.1.2.2).<sup>[168]</sup>

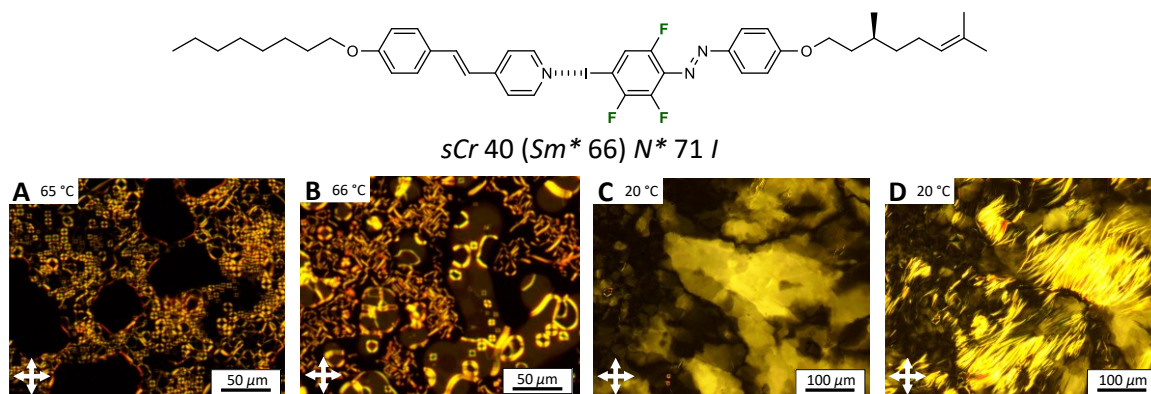


Figure 3.20: Supramolecular structure and proposed mesophase sequence of *D3I*\*...*A2*. POM images of *D3I*\*...*A2* reveal LC properties upon heating (A) and cooling (B). The coexistence of filamentary domains of a *TGB*\* phase and pseudo-isotropic domains upon cooling suggest an *N*\*  $\rightarrow$  *Sm*\* transition. Shearing of the sample at 20 °C (C) reveals a highly viscous behavior and filamentary textures (D) suggesting the existence of a soft-crystal (*sCr*) phase.

Similar to its achiral analogue, *D3I*\*...*A2* also exhibited enantiotropic behavior (Figure 3.20A/B). However, the coexistence of different mesomorphic textures made the unambiguous determination of the temperature ranges difficult. After the formation of droplet-like textures suggesting an *N*\* phase, both filamentary textures similar of a *TGB*\* phase and other pseudo-isotropic domains were observed suggesting an *N*\*  $\rightarrow$  *Sm*\* transition. This assumption is supported by observation of a slow transition to a soft-crystalline (*sCr*) state at lower temperatures (C). Shearing of the sample (D) reveals the highly viscous behavior which is characteristic for such phases. The slow formation of a solid crystalline phase was only observed upon reheating of the sample starting at  $\sim 5$  °C. This suggests a hindrance of the crystallization which can be attributed to the increased disorder conferred by the chiral side chain and a significant molecular rearrangement needed to form crystallites. DSC measurements confirm the observed thermal behavior and reveal two broad peaks upon cooling with a maximum at 70.9 °C ( $\Delta E = -19.6$  kJ/mol) and 4.3 °C ( $\Delta E = -3.0$  kJ/mol) (Figure 7.18H). Although the transitions temperatures differ from the ones observed under the POM due to the different experimental setup, the found transition enthalpies are in the range of values previously reported for *I*  $\rightarrow$  *Sm* transitions with a higher molecular order (e.g. *Sm F*, *Sm I*).<sup>[169]</sup> However, solely based on the POM and DSC results, an unambiguous assignment of mesophases is difficult and cannot be made in this case without further investigations.

In contrast to the general trend that stilbazole assemblies exhibit broader mesophases compared to their azopyridine counterparts, this observation inverts for **D2I\*** which shows a slightly broader mesophase with **A1** than it does in combination with **A2** ( $\Delta T_{N^*,c} = 19\text{ }^\circ\text{C}$  vs.  $\Delta T_{N^*,c} = 16\text{ }^\circ\text{C}$ ). This was observed, even though the stilbazole should form more stable assemblies. At first sight, this seems counter intuitive. However, looking at the clearing point temperatures of  $57\text{ }^\circ\text{C}$  (for **D2I\*...A1**) and  $79\text{ }^\circ\text{C}$  (for **D2I\*...A2**) indicates, that the broader mesophase range is due to the significantly lower  $T_C$  and thus prevented dissociation of the supramolecular bond and quenching of the LC properties.

### *Impact of the Donor Moiety*

Looking at the effect of the donor moiety reveals a similar evolution of the melting and clearing point temperatures as already observed for the achiral counterparts (see Figure 3.10 and Figure 3.18). Both values gradually decrease with decreasing fluorination degree in the order **D1I** > **D2I** > **D3I** or **D1I\*** > **D2I\*** > **D3I\***. However, due to the chiral side chain, the absolute values of the transition temperatures are noticeably reduced compared to the achiral assemblies. As a result of the increased thermal stability of the XB at lower temperatures, especially the trifluoro derivatives exhibit significantly broader mesophases.

Although, the transition temperatures gradually decrease with a decreasing number of fluorine atoms and therefore follow the same trend as observed for the achiral assemblies (*i.e.* **D1I** > **D2I** > **D3I** or **D1I\*** > **D2I\*** > **D3I\***), the evolution of the liquid crystalline ranges of the chiral complexes proved to be much more complex. In fact, the mesophase range for complexes using **A2\*** remained constant and even increased for **A1** complexes from **D1I\*** to **D2I\*** ( $\Delta T_{N^*,c} = 13\text{ }^\circ\text{C}$  vs.  $\Delta T_{N^*,c} = 19\text{ }^\circ\text{C}$ ), while **D3I\*...A1** did not show any liquid crystalline properties at all. On the other hand, its inverted counterpart **D3I...A1\*** exhibited an  $N^*$  phase upon cooling with a temperature range of  $\Delta T_{N^*,c} = 11\text{ }^\circ\text{C}$  despite having a similar transition temperature from the isotropic melt.

In contrast to the achiral assemblies, the main factor that plays a role and explains the evolution of the temperature ranges is the disorder increasing effect of the chiral side chain resulting in lower transition temperatures which in turn prevents the thermal dissociation of the XB. This effect seems to prevail over the mesophase destabilizing effect of the declining fluorination degree and XB-strength.<sup>[126]</sup>

### 3.2.3 Induction of Chirality in Pristine Materials

As the HTP strongly depends on the LC host system and the measuring temperature, the quality of the chiral induction is of major interest. It is thus important to determine the HTPs of chiral dopants under similar conditions (*i.e.* same host and temperature) to ensure comparability of the results. In this respect, the supramolecular assembly **D11**⋯**A2** is a suitable candidate as host system as it provides a broad and uniform nematic mesophase upon cooling between 123 and 89 °C. Furthermore, determination of the HTPs at elevated temperatures reduces the effects of the photo-induced *trans-cis* isomerization of the azo linkage as the *cis* lifetimes are reduced.

Due to the high complexity of the supramolecular system, the following discussion will be made in a simplified manner leaving the fact out of consideration that the formation of the supramolecular bond is reversible and that both chiral and achiral donor can form a halogen bond to acceptor **A2** in a statistic fashion. Therefore, the LC host **D11**⋯**A2** is considered as one single molecular entity which is undisturbed by the presence of the chiral dopant.

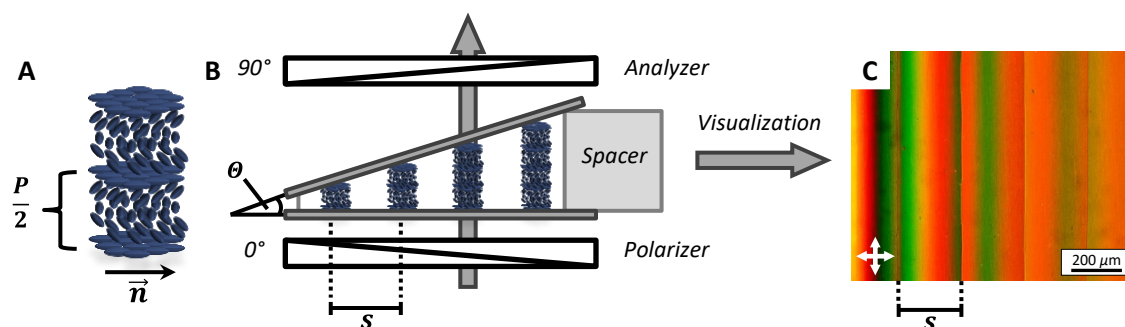


Figure 3.21: Grandjean-Cano wedge cell method: planar alignment of a cholesteric LC (A). Planar alignment inside a wedge cell producing disclination lines in regular distances (B). POM investigations enable to measure the distances between the disclination lines (C).

The HTP values were determined by indirectly measuring the helical pitch ( $P$ ) of the cholesteric system using the Grandjean-Cano wedge cell method (Figure 3.21).<sup>[170-173]</sup> Such a cell consists of two glass slides with a differently sized spacer at each end, producing a specific opening angle ( $\Theta$ ,  $\tan \Theta = 0.01969$ ). Each glass slide is coated with a unidirectionally rubbed polyimide substrate to support planar alignment of the LC molecules (Figure 3.21A). Upon planar alignment of the LC with the director  $\vec{n}$  parallel to the rubbing direction and the helical axis (*i.e.* optical axis) perpendicular to the substrate, discrete disclination lines are formed between areas containing a different number of nematic layers (Figure 3.21B). The difference in thickness between these domains must be  $P/2$  to fulfill the alignment boundary

condition.<sup>[174]</sup> Observation of the sample using polarized optical microscopy enables the measurement of the distance  $s$  between the disclination lines (Figure 3.21C). The pitch is then given by

$$P = 2s \cdot \tan \theta. \quad (7)$$

Assuming that an enantiomerically pure chiral dopant is used, the molar HTP ( $\beta_M$ ) can be calculated using equation (3) and (7) to give

$$\beta_M = \frac{1}{2s \cdot \tan \theta \cdot \omega}. \quad (8)$$

To get an idea of the reliability and accuracy of the measurements, especially of dopants with low HTP values where the error is usually high, a versatile approach is to plot the inverse of the helical pitch as a function of different molar concentrations of the dopant using

$$\frac{1}{P} = \beta \omega. \quad (9)$$

The main assumption of this approach is, that the pitch length for a molar concentration of 0 mol% of dopant is infinite, so that the origin of the linear fit can be set to a fixed value of  $y = 0$ .

In a first step, the nematic host **D11**·**A2** was doped with different molar fractions of **D11**\* of 1.5, 3.0 and 5 mol%, giving an average HTP of  $\beta_M = 1.9 \pm 0.1 \mu\text{m}^{-1}$  for the dopant **D11**\* at a chosen temperature of 110 °C. Figure 3.22 shows the uniform alignment of the disclination lines under the microscope (A – C) and the resulting linear fit (D) as a representative example. Due to reduced compatibility of the chiral dopants **D21**\* and **D31**\* with the host system **D11**·**A2**, the reliable measurement of the HTP values of these dopants was difficult, as a uniform planar alignment and formation of the disclination lines could not be achieved. Also increasing the dopant concentration did not improve the alignment and simply led to a reduced clearing point temperature which made a measurement at the chosen temperature of 110 °C impossible.

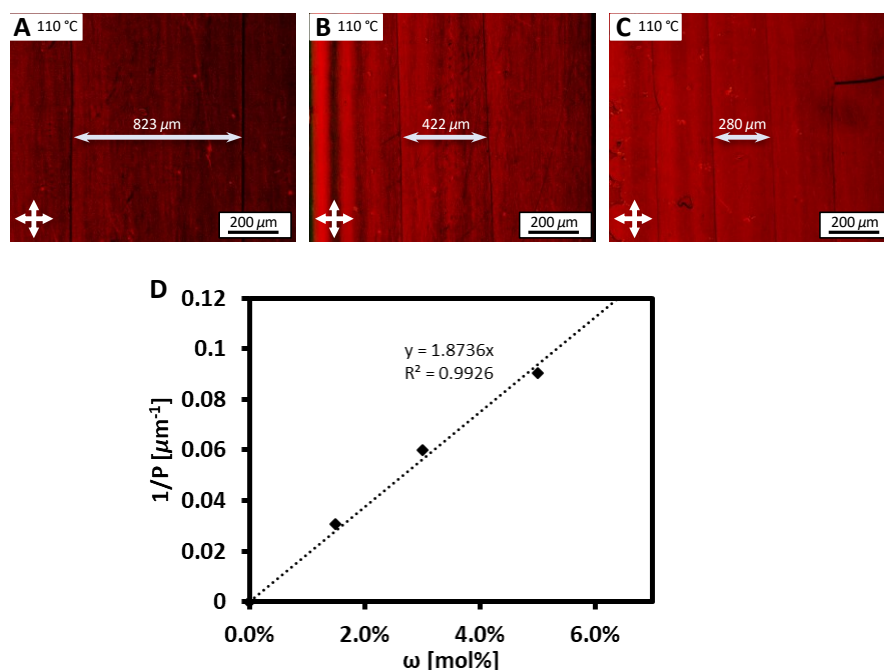


Figure 3.22: POM images of  $D11^*@D11\cdots A2$  reveal the decreasing distance of the disclination lines with increasing dopant concentration from 1.5 % (A), to 3 % (B) and 5% (C). D) linear blot for the determination of the HTP value.

As the reliable determination of the HTPs of dopants  $D11^*$ ,  $D21^*$ , and  $D31^*$  in  $D11\cdots A2$  was not possible, the supramolecular assembly  $D11^*\cdots A2$  was used as dopant to investigate whether the formation of the supramolecular assembly affects the HTP. Therefore the system  $D11^*\cdots A2@D11\cdots A2$  was prepared, with  $D11^*\cdots A2$  being the dopant and  $D11\cdots A2$  being the LC host. The results reveal an HTP of  $\beta_M = 1.9 \pm 0.1 \mu\text{m}^{-1}$  for the complex doped system (Figure 7.20), suggesting that the XB formation does not have a noticeable effect on the chiral transfer in this system. A reliable determination of the HTPs of  $D21^*\cdots A2$  and  $D31^*\cdots A2$  in the host system  $D11\cdots A2$  was not possible as the samples did not properly align inside the wedge cells.

### 3.2.4 Induction of Chirality in 5CB

As the induction of chirality and determination of the HTP values in the pristine material proved to be unsuccessful, a more convenient approach was followed and the HTP values were determined in a commercially available liquid crystal. As LC host, 4-cyano-4'-pentylbiphenyl (5CB) was chosen as it exhibits nematic liquid crystallinity at room temperature with a clearing point at 36 °C <sup>[175]</sup> and is a commonly used LC system for the determination of HTP values (see also Section 1.3.2).<sup>[74, 173, 176-177]</sup>

To get a more comprehensive view on the correlation between structural changes and the efficiency of the chiral transfer, the library of chiral building blocks used for the preceding study was extended by halogen bond donators **D4I\***, **D5I\*** and fluorinated compounds **D1H\***, **D2H\***, and **D3H\*** (Figure 3.23). The latter serve as reference as they lack the capability of forming a halogen bond.

With respect to the three key questions mentioned in the beginning, the chiral dopants can be categorized into three groups (Figure 3.23) enabling the investigation of the effects of different structural features on the chiral transfer:

1. *What are the effects of the fluorination pattern on the HTP value?* (**Group I**, **Group II**)
2. *How does the formation of the supramolecular assembly affect the HTP value?* (**Group I**, **Group III**)
3. *How does the halogen bond strength influence the HTP Value?* (**Group I**, **Group III**)

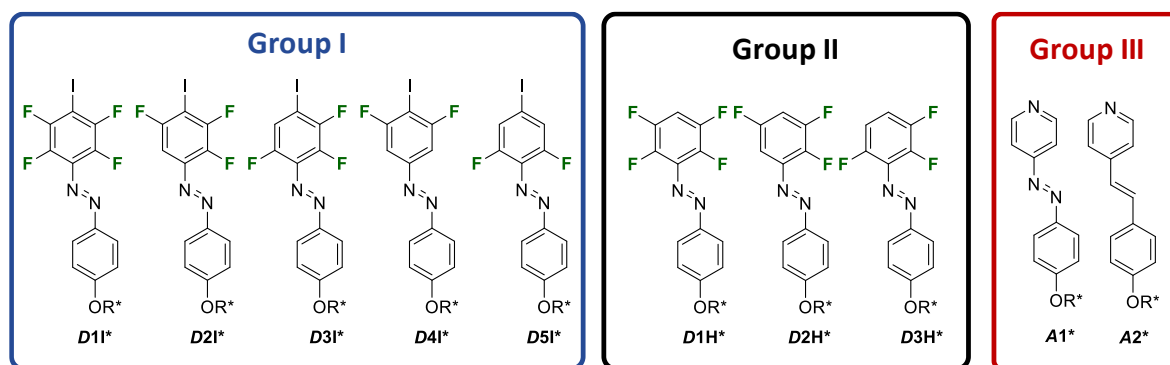


Figure 3.23: Extended library of chiral dopants. Residue R\* corresponds to *S*-citronellyloxy.

The doped 5CB mixtures were prepared as described above by separately weighing and mixing the individual components. The HTP values were determined using the Grandjean-Cano wedge cell method. As the HTP is also influenced by temperature effects, all measurements were uniformly performed at 20 °C to ensure comparability across the whole spectrum of chiral dopants. To reduce the effects of the *trans-cis* isomerization on the HTP, all samples were tempered at 100 °C for 30 min before measuring.

## Impact of the fluorination degree

Figure 3.24 and Table 3.3 summarize the HTPs in 5CB of all investigated compounds. Looking at the measured values emphasizes the importance of the LC host and the measuring temperature. While the measured HTP of **D11\*** (at 110 °C) in the supramolecular host **D11**·**A2** was found to be  $\beta_M = \sim 2 \mu\text{m}^{-1}$ , this value is increased by almost five-fold in 5CB (at 20 °C) to  $\beta_M = \sim 10 \mu\text{m}^{-1}$ . Although the HTPs of the building blocks are significantly higher in 5CB, no obvious systematic trend can be observed. Neither a change of the fluorination pattern (Group I and Group II), nor the replacement of an azo linkage by a C–C double bond (Group III) have a direct effect on the HTP. A possible explanation for the slight variations in the HTPs between  $8.0 \mu\text{m}^{-1}$  and  $9.7 \mu\text{m}^{-1}$  is a different exposure to day light prior to the measurement which led to different fractions of *cis*-isomer inside the mixtures. Due to the different *cis*-lifetimes, this issue could not be completely overcome by heating of the samples prior to the measurement.<sup>[178]</sup>

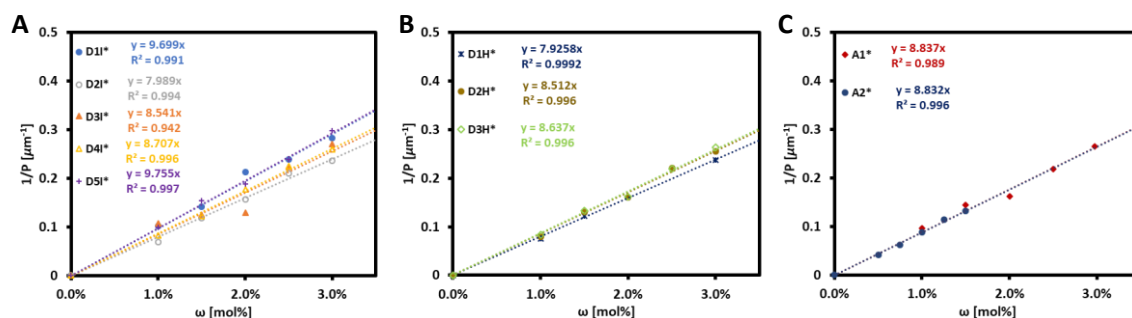


Figure 3.24: Linear plots of the HTP value measurements of Group I (A), Group II (B) and Group III (C) in 5CB at 20°C.

Table 3.3: HTP values of all chiral dopants of Groups I – III in 5CB. All values were determined in 5CB at 20°C using the Grandjean-Cano wedge cell method.

	Dopant	HTP [ $\mu\text{m}^{-1}$ ]
Group I	<b>D11*</b>	$9.7 \pm 0.2$
	<b>D21*</b>	$8.0 \pm 0.1$
	<b>D31*</b>	$8.5 \pm 0.5$
	<b>D41*</b>	$8.7 \pm 0.1$
	<b>D51*</b>	$9.8 \pm 0.1$
Group II	<b>D1H*</b>	$9.0 \pm 0.1$
	<b>D2H*</b>	$8.5 \pm 0.1$
	<b>D3H*</b>	$8.8 \pm 0.2$
Group III	<b>A1*</b>	$8.8 \pm 0.2$
	<b>A2*</b>	$8.8 \pm 0.1$

*Impact of halogen bond strength and position of the chiral side chain*

To get an idea whether the formation of the halogen-bonded assembly and the strength of the formed XB affects the efficiency of the chiral transfer due to increased compatibility of chiral guest and LC host, 5CB was doped with supramolecular complexes of either a chiral acceptor and an achiral donor or *vice versa*. Since the stilbene acceptor generally exhibits the more stable assemblies the following discussion will mainly focus on complexes using **A2** and **A2\***.

However, looking at the measured values (Table 3.4 and Figure 7.21) reveals that the structural changes (*e.g.* fluorination pattern) do not significantly influence the HTP. Although, a slight decrease of the HTP can be observed for donors **D11\*** through **D31\*** in combination with **A2**, this trend could not be confirmed for the assemblies with inverted chirality. As already observed for the experiments described above, differences may be ascribed to a different exposure to daylight prior to the performed measurement. This exposes a major issue of this approach. On the other hand, the HTP of a combination of two chiral components (*e.g.* **D11\*...A2\***) turns out to behave additively ( $\beta_M = 20.1 \mu\text{m}^{-1}$ ) (see Figure 7.21C).

Table 3.4: Summary of the measured HTP values of the supramolecular complexes. All values were determined in 5CB at 20°C using the Grandjean-Cano wedge cell method.

Donor	Acceptor	HTP [ $\mu\text{m}^{-1}$ ]
<b>D11*</b>		$9.8 \pm 0.2$
<b>D21*</b>	<b>A2</b>	$8.3 \pm 0.3$
<b>D31*</b>		$7.5 \pm 0.2$
<b>D41*</b>		$8.6 \pm 0.2$
<b>D11</b>		<b>A1*</b>
<b>D11</b>		$9.5 \pm 0.7$
<b>D21</b>	<b>A2*</b>	$9.3 \pm 0.7$
<b>D31</b>		$9.4 \pm 0.6$
<b>D41</b>		$9.4 \pm 0.5$
<b>D11*</b>	<b>A2*</b>	$20.1 \pm 0.2$

Having observed that the samples show a noticeable reaction to light exposure, a sample of 2 mol% of **D11\*...A2** in 5CB (Figure 3.25) was irradiated with 405 nm laser light upon which an instantaneous and thermally reversible increase of the disclination line distances was observed. The increase of the disclination line distance is equivalent to a decrease of the HTP. This proves, that only an actual change of the molecule's geometry has a significant and direct effect on the chiral induction in such materials, which is in contrast to the initial

assumption, that the supramolecular bond or changing fluorination pattern influences the HTP.

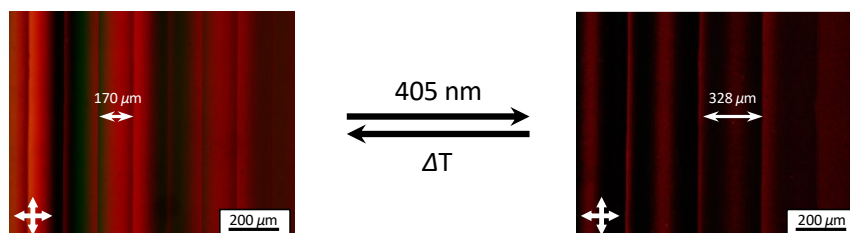


Figure 3.25: POM images of 2 % **D11**\*...**A2** in 5CB reveal the increase of the disclination line distance upon *trans-cis* photo-isomerization.

### 3.2.5 Conclusions

The achiral supramolecular library of XB-donor and acceptor molecules was successfully extended with a series of chiral equivalents with a terminally attached *S*-citronellyl side chain. The investigation of the liquid crystalline properties of the chiral assemblies revealed significant differences compared to the thermal behavior of the achiral equivalents. Not only did the doubly branched side chain generally reduce the transition temperatures upon heating and cooling, it also led to the exhibition of new LC properties (*e.g.* **D31**\*...**A1**\*). Also, the importance of the position of the chiral side chain (acceptor or donor side) could be shown and proved to have a much more pronounced effect on the thermal properties as previously reported findings suggest. This led to the formation of *TGB*\**,* *Sm*\* or *sCr* phases instead of *N*\* (**D11**\*...**A2** vs. **D31**\*...**A2**). The effect of the fluorination pattern turned out to have a similar effect on the LC properties as observed for the achiral counterparts and gradually reduced the transition temperatures with decreasing number of fluorine substituents. Interestingly, the strength of the halogen bond played only a minor role for the exhibition of broad mesophases. In this respect, the broader mesophases were rather a result of the reduced transition temperatures preventing the thermal dissociation of the XB.

Investigations of the HTPs in the pristine LC host **D11**\*...**A2** revealed that chiral donor **D11**\* and supramolecular complex **D11**\*...**A2** both exhibit the same HTPs of  $\beta_M = 1.9 \mu\text{m}^{-1}$  and that the formation of the supramolecular complex does not noticeably influence the efficiency of the chiral transfer. Similar effects were obtained using nematic 5CB which also emphasized the importance of the used LC host and measuring temperature for the magnitude of the HTP. Using the 5CB host and a lower measuring temperature resulted in a five-fold increase of the HTP values. Although no obvious trends of the HTPs depending on

fluorination degree or XB strength were found, the results suggest that an actual conformational change (*e.g. trans-cis* photo-isomerization) of the dopant molecule is necessary to induce a considerable HTP change.

---

### 3.3 Chirality Transfer for Sensing Applications<sup>1</sup>

Sensing applications and specifically environmental gas monitoring have attracted significant attention in the past decade. Especially in urban areas, the concentrations of noxious and climate active gases often exceed critical values. Besides carbon monoxide (CO) and hydrogen sulfide (H<sub>2</sub>S), nitric oxide (NO) and nitrogen dioxide (NO<sub>2</sub>) are two of the most toxic gases which are harmful for both the environment and biological systems.<sup>[179]</sup> The reliable detection of these gases specifically in low concentrations at room temperature is difficult and has been a challenge for scientists. Recent advances in this field are based on semiconducting metal oxides<sup>[180-182]</sup> or metal oxide containing composite materials<sup>[183-187]</sup> which show high sensitivity at low ppm values but often cross-respond to other gases or require elevated temperatures to exhibit their best performance. Phthalocyanine (**26**) (Figure 3.26) as one of the few examples with LC properties has been shown to be suitable for the detection of NO<sub>2</sub> gas already decades ago. Its semiconducting sensing potential has been extensively investigated.<sup>[188-193]</sup> Although phthalocyanines and their metal complexes (Cu<sup>2+</sup>, Zn<sup>2+</sup>) can react to low gas concentrations by showing a change of the semiconducting properties, some examples also cross-respond to other gases or vapors like ammonia or require elevated temperatures to exhibit their full potential. A common problem of all mentioned approaches alike is that the detection itself requires specialized and elaborate technical equipment to detect changes in the current, resistance, or UV/Vis absorption of the sensor system. Examples of simple techniques for *in-situ* detection which can be easily interpreted and are independent of electrical energy sources are sparse. A simple measure for the *in-situ* interpretation of a signal is a change of the structural coloration of a sample due to an external stimulus.

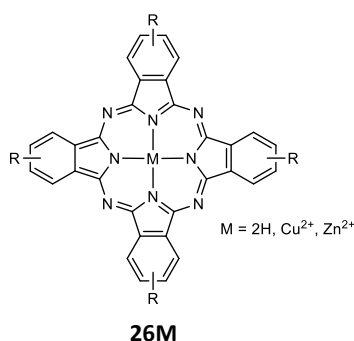


Figure 3.26: Molecular structures of phthalocyanine (**26**) and its metal complexes.

<sup>1</sup> Some sections and paragraphs of this chapter were adapted from a submitted first authored publication and may be identical.

In this respect, cholesteric liquid crystals are excellent candidates. As mentioned above (see Section 1.3.2), TADDOL and binaphthyl dopants are particularly suitable for the chiral induction in liquid crystalline host systems and have been used for stimuli-responsive sensing in the past. In 2010, *Han et al.* reported on the carbon dioxide (CO<sub>2</sub>) sensing capability of hydrogen-bonded TADDOL dopant **27** (Figure 3.27).<sup>[194]</sup> They observed a significant shift of the reflection wavelength upon exposure of the cholesteric LC to CO<sub>2</sub> rich atmosphere. This was due to dissociation of the supramolecular assembly and a change of the dopant's HTP caused by the formation of a carbamate of CO<sub>2</sub> with the diamine. Later, *Pschyklenk et al.* used this approach to further investigate the system's sensing potential by encapsulation of the LC in electro-spun polyvinylpyrrolidone (PVP) fibers.<sup>[195]</sup> Recently, *Li et al.* and *Wang et al.* reported on binaphthyl-based photo switches **28** and **29** as chiral dopants in a nematic LC Host.<sup>[140, 173]</sup> These dopants enabled to actively switch the structural color of the cholesteric LC across the visible light spectrum. Photoirradiation of the sample with specific wavelengths induced a change of the dopant's molecular structure and therefore a change of the HTP and structural color of the sample.

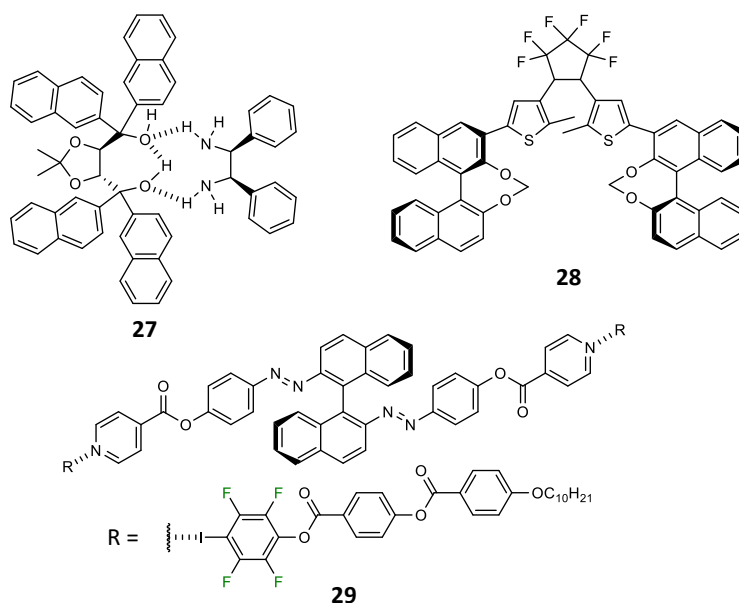
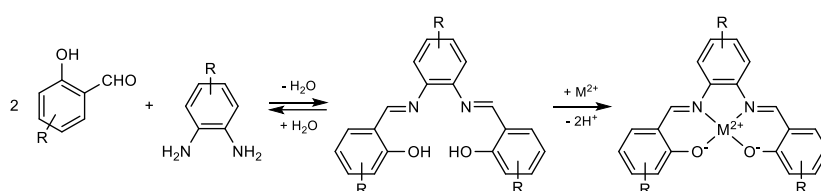


Figure 3.27: Supramolecular TADDOL dopant **27** and binaphthyl-based photo-switches **28** and **29**.

These results and the study on the chiral induction using halogen-bonded LCs (see also Chapter 3.2) suggest that an actual conformational change is necessary to significantly influence the helical twisting power of a given molecule. Therefore, this proof of principle study aims to combine the sensing potential of phthalocyanine copper complexes with the

capability of the binaphthyl core to reliably induce chirality in nematic LCs. The strong affinity of  $\text{NO}_2$  to copper ions and the flexible chirality along the C–C axis of the binaphthyl core provide an excellent combination of functional units for the design of reactive dopants for photonic sensing. In this respect, tetradentate salophen-type compounds (*N,N*-bis(salicylidene)phenylenediamine) (Scheme 3.3) are well suited as they can be easily obtained by conversion of a diamine with salicylaldehyde and form stable complexes with numerous transition metals.<sup>[196-197]</sup> Furthermore, these molecules and their sensing capabilities have been investigated in the past and the synthetic procedures are well-known which makes these molecules easily accessible.<sup>[198-203]</sup>



Scheme 3.3: General synthesis of salophen ligands and their metal complexes.

Figure 3.28 schematically displays the concept of photonic sensing using chiral nematic liquid crystals. The main idea of this concept is that  $\text{NO}_2$  molecules coordinate to the copper ion and induce a conformational change of the reactive dopant. This in turn leads to a change of the HTP and a shift of the wavelength of the reflected light.

Starting from (*S*)-2,2'-binaphthyl diamine (BINAM), tetradentate Schiff-base dopants **L1** – **L3** and their copper complexes **L1Cu** – **L3Cu** are synthesized and used as chiral dopants in a nematic LC. The step wise functionalization in 6,6'-positions of the binaphthyldiimin (BINIM) core and in 4-position of the salicylaldehyde enables the systematic investigation of the helical twisting power, compatibility with the host system, and sensing capabilities regarding the following key questions:

1. How does the functionalization and complex formation influence the HTP value?
2. Is it possible to induce structural color in a liquid crystalline host?
3. Is it possible to detect  $\text{NO}_2$  gas using a cholesteric sensor system of BINIM dopant and LC host by an induced change of the structural color?

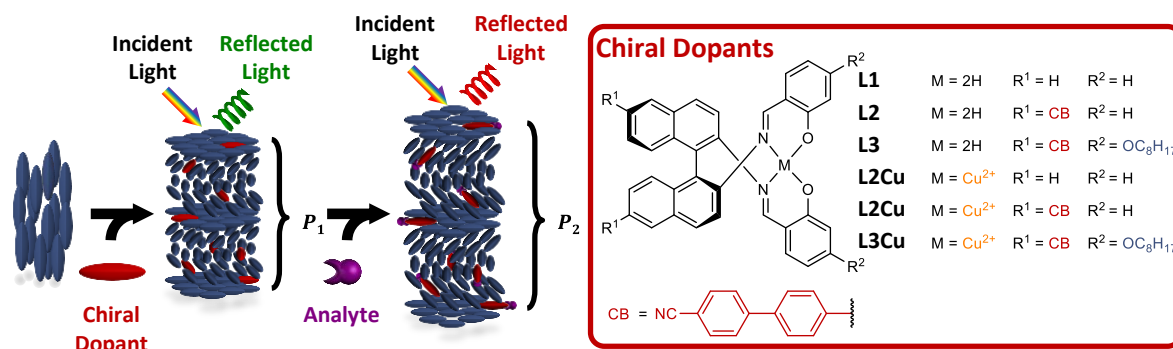
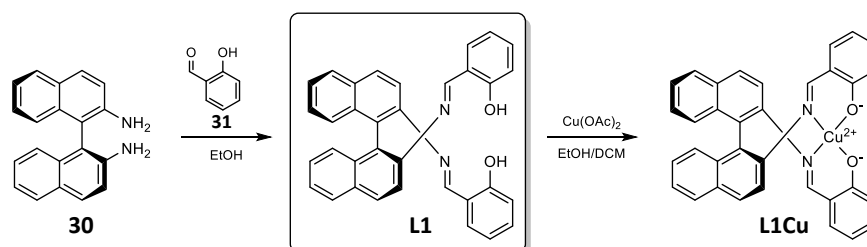


Figure 3.28: Chiral BINIM dopants and schematic representation of the sensing principle: By doping a nematic LC with the reactive chiral dopants, structural coloration can be induced. Exposure of the sample to an analyte changes the HTP value and shifts the wavelength of the reflected light.

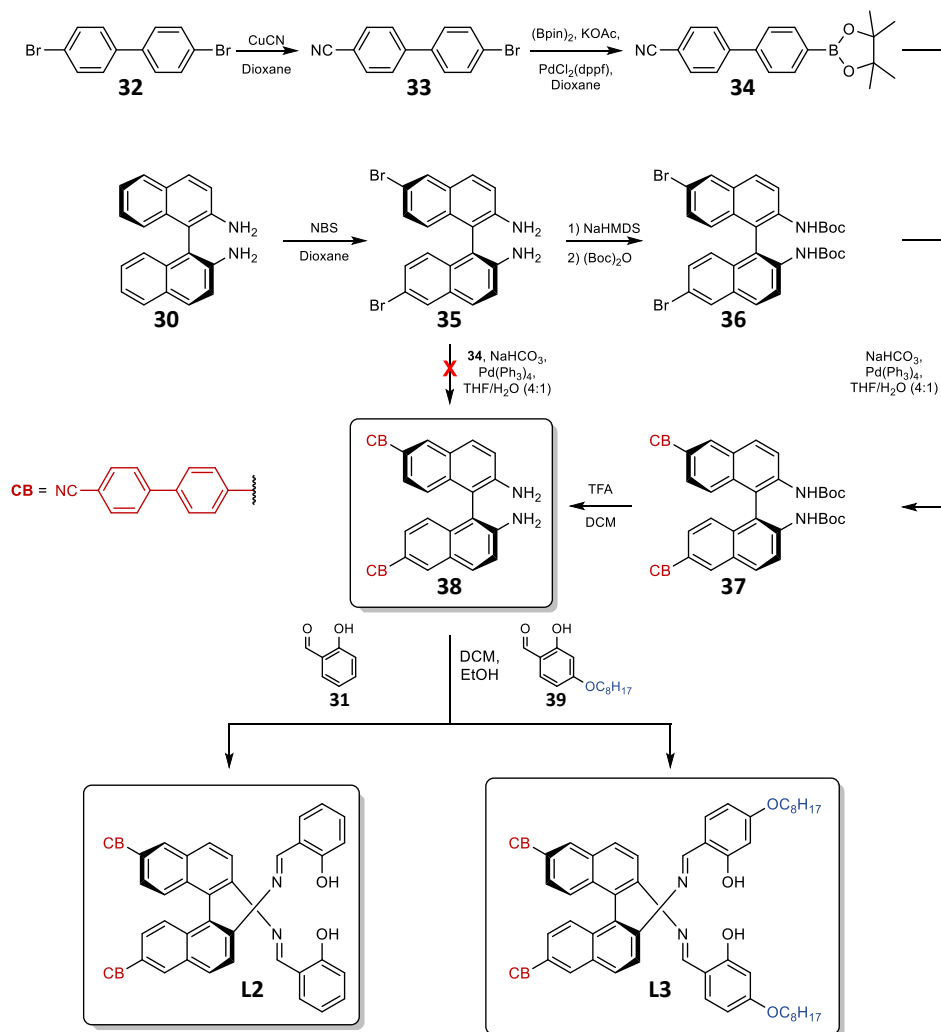
### 3.3.1 Synthesis of the Chiral Dopants

The synthesis of the chiral dopants used in this study was performed starting from commercially available (*S*)-2,2'-binaphthyl diamine (**30**) with 99% *ee* (Scheme 3.4). Ligand **L1** could be readily synthesized according to a literature known procedure in 85% yield by refluxing **30** with salicylaldehyde (**31**) in ethanol followed by filtration and drying. Subsequent treatment with copper(II) acetate (Cu(OAc)<sub>2</sub>) in a mixture of ethanol and DCM yielded dopant **L1Cu** in 88% yield after precipitation from methanol to remove the excess of acetic acid.<sup>[199-200]</sup>



Scheme 3.4: Reaction procedure for the synthesis of **L1** and **L1Cu**.

Pinacol boronic acid precursor **34** was obtained according to the procedure displayed in Scheme 3.5 by conversion of 4,4'-dibromobiphenyl (**32**) with copper cyanide to intermediate **33** in 48% yield and subsequent reaction with bis(pinacolato) diboron in dry dioxane in 99% yield. As the reactants in step 1 were only used in equimolar ratios to ensure the formation of the mono-cyano derivative, remaining starting material could be recovered during column chromatographic purification to be used in a second reaction.



Scheme 3.5: Synthetic route for the preparation of ligands **L2** and **L3**.

The synthesis of the BINAM precursor **38** and the concluding imine synthesis to **L2** and **L3** turned out to be more challenging than initially anticipated (Scheme 3.5). Following the known procedure for the bromination of **30** in 6,6'-positions using NBS in dioxane yielded **35** in 43% yield.<sup>[204]</sup> However, the planned direct conversion of **35** to the Suzuki coupled diamine **38** only yielded an inseparable mixture of unidentifiable byproducts. Therefore, an alternative synthetic route was chosen *via* boc-protection of the free amino groups. As common procedures using di-*tert*-butyl dicarbonate (Boc<sub>2</sub>O) in DCM failed due to low reactivity of the amino groups, activation with sodium hexamethyldisilazide (NaHMDS) was needed. Subsequent reaction with Boc<sub>2</sub>O in dry THF gave boc-protected intermediate **36** in moderate yield of 61% after column chromatographic purification.<sup>[205]</sup> The following Suzuki coupling with boronic acid **34** was performed according to a procedure reported by *Yamakawa et al.* using NaHCO<sub>3</sub> and tetrakis(triphenylphosphine)palladium catalyst in a 4: 1 THF/water mixture.<sup>[206]</sup> Due to the extremely nonpolar character of the molecule, column chromatographic

purification had to be performed twice using cyclohexane/DCM [1: 9] and cyclohexane/ethyl acetate [4: 1] finally giving **37** in excellent yield of 97%. The following boc-deprotection was achieved by treating **37** with an excessive amount of trifluoroacetic acid (TFA) in DCM. Trials where less than 150 eq of TFA were used did not yield the fully deprotected diamine **38**. This is surprising considering that the literature states an amount of 30 eq TFA for the complete deprotection of boc-protected binaphthyl diamines.<sup>[207]</sup>

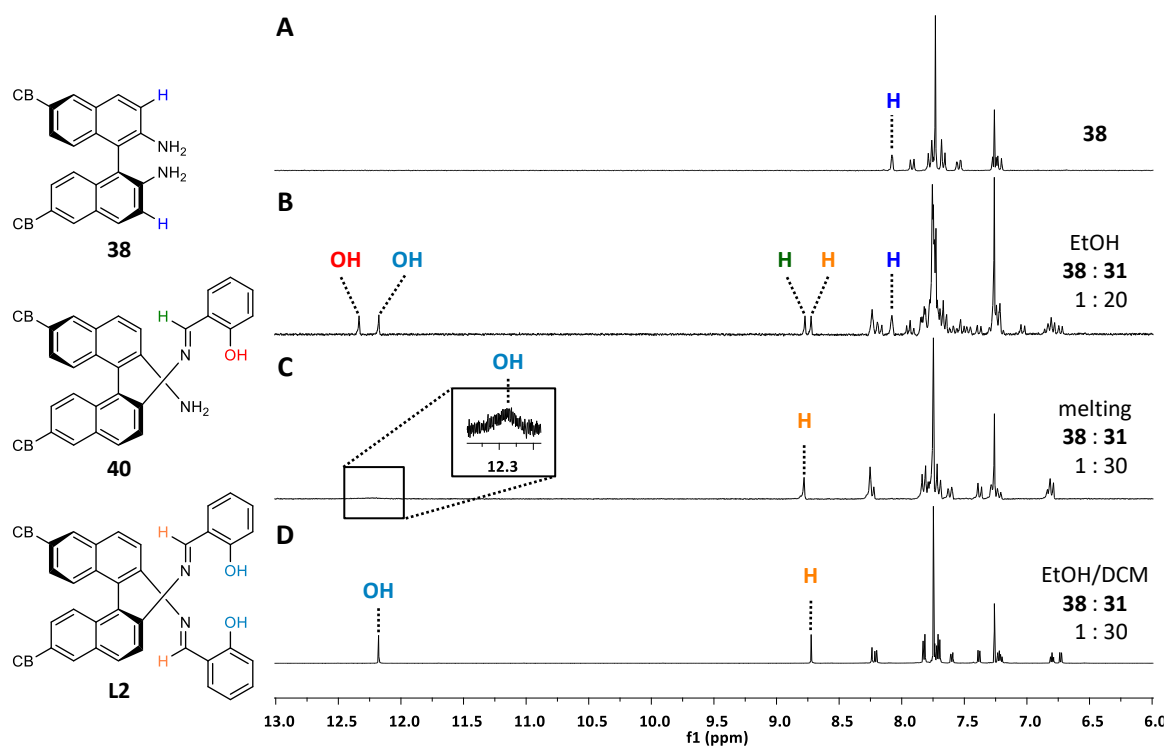


Figure 3.29: NMR Spectra of diamine **38** (A) and the purified products after imine formation using different synthetic methods (B,C and D) and ratios of diamine **38** and salicylaldehyde (**31**). (CDCl<sub>3</sub>; A – C: 300 MHz; D: 400 MHz)

First trials to synthesize **L2** according to the procedure of **L1** by refluxing salicylaldehyde (**31**) and diamine **38** in a 2: 1 molar ratio in ethanol, exclusively yielded a mixture of monoamine **40**, **L2** and amine **38** (Figure 3.29A/B). The remaining aldehyde was removed by filtration of the formed precipitate and subsequent washing with ethanol. Addition of small amounts of DCM to improve the solubility of the precipitating monoamine or addition of catalytic amounts of hydrochloric acid had no positive impact on the resulting product mixture. As separation by column chromatography was not possible due to decomposition of the imine, an alternative route had to be found. The solvent free formation of imines can be achieved by melting together equimolar amounts of amine and aldehyde.<sup>[208]</sup> Since remaining aldehyde can be removed by filtration and washing, this was done with an excess of

aldehyde. Although full conversion to the diimine was achieved (Figure 3.29C), the melting point of diamine **38** by far exceeded the racemization temperature of binaphthyl diamine (150 °C).<sup>[209-210]</sup> Therefore, this approach eventually proved to be unsuitable for the preparation of Ligands **L2** and **L3**. The assumed racemization of the binaphthyl moiety was indirectly proven by repeating the same reaction in a mixture of EtOH and DCM under reflux conditions yielding **L2** in 75% isolated yield and subsequently measuring the HTP value in 5CB (Figure 3.29D). While **L2** synthesized by melting hardly induced any chirality, the HTP of **L2** synthesized in solution was found to be as high as  $\sim 200 \mu\text{m}^{-1}$ . The preparation of **L3** was performed accordingly and the ligand was obtained in 88% yield using 18 eq of 4-oxo-tyloxysalicylaldehyde (**39**).

Copper complexes **L2Cu** and **L3Cu** were synthesized based on the procedure described for **L1Cu** (Scheme 3.4). To confirm the formation of the copper complexes, mass spectrometry was the method of choice as these tetradentate Schiff base complexes proved to be extraordinarily stable and NMR spectroscopy was not possible due to the magnetic spin of the copper ion. All three copper complexes could be evidenced in the mass spectra as displayed in Figure 3.30. Besides the monomer of the complexes, also small portions of dimer could be detected for **L1Cu** and **L2Cu** with  $\text{H}^+$  and  $\text{Na}^+$  as counterions.

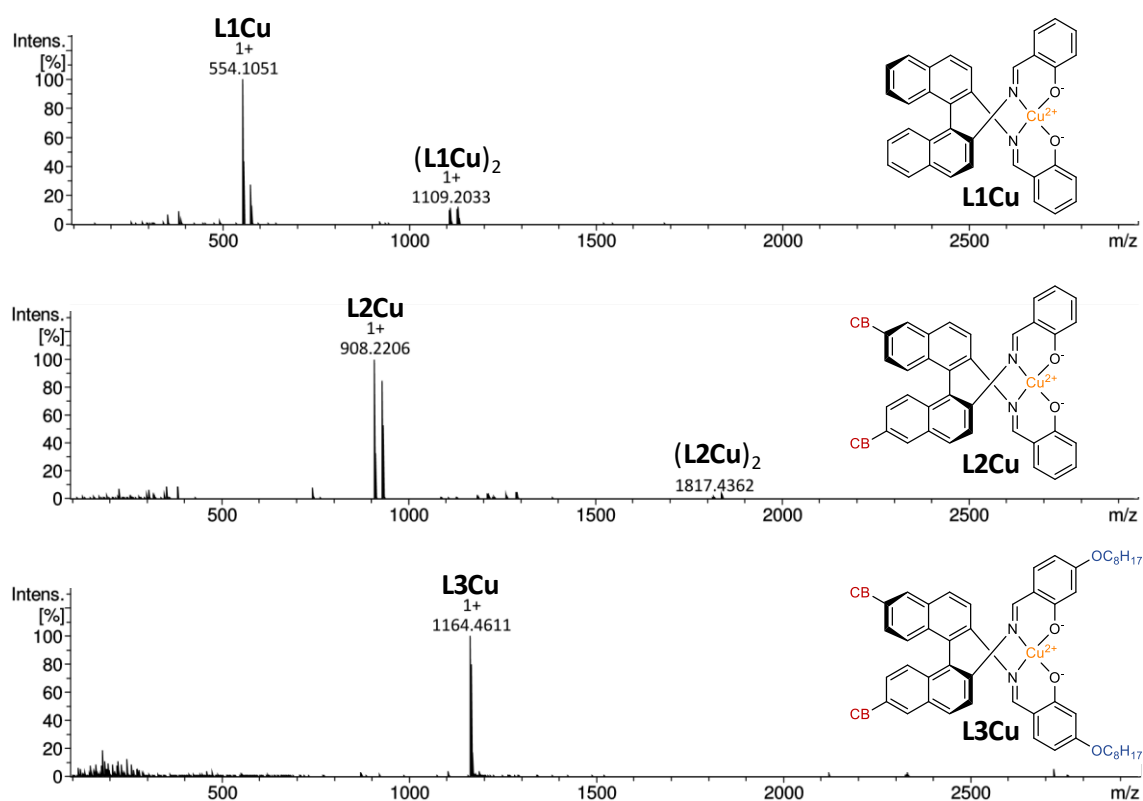


Figure 3.30: Mass spectra of copper complexes **L1Cu**, **L2Cu**, and **L3Cu**.

To further characterize the complexes, IR spectra were collected and compared to the free ligands. Figure 3.31 displays sections of the IR spectra of **L3** (blue) and **L3Cu** (red) as representative examples (see also Figure 7.22). The most significant vibrational changes upon complexation were observed for the characteristic bands of the imine (C=N) which appear at  $\sim 1620\text{ cm}^{-1}$  in the free ligand and shift to lower wavenumbers upon coordination to the copper ion ( $\nu_{\text{C=N}} = \sim 1605\text{ cm}^{-1}$ ).<sup>[200, 211-212]</sup> This indicates a decreasing C=N bond order due to the coordination of the imine nitrogen to the metal ion and back bonding of the copper to the  $\pi^*$ -orbital of the imine. Moreover, the C–O vibration of the phenol generally shifts from  $\sim 1115\text{ cm}^{-1}$  to higher wavenumbers upon coordination to the copper ion ( $\nu_{\text{C-O}} = \sim 1120\text{ cm}^{-1}$ ).

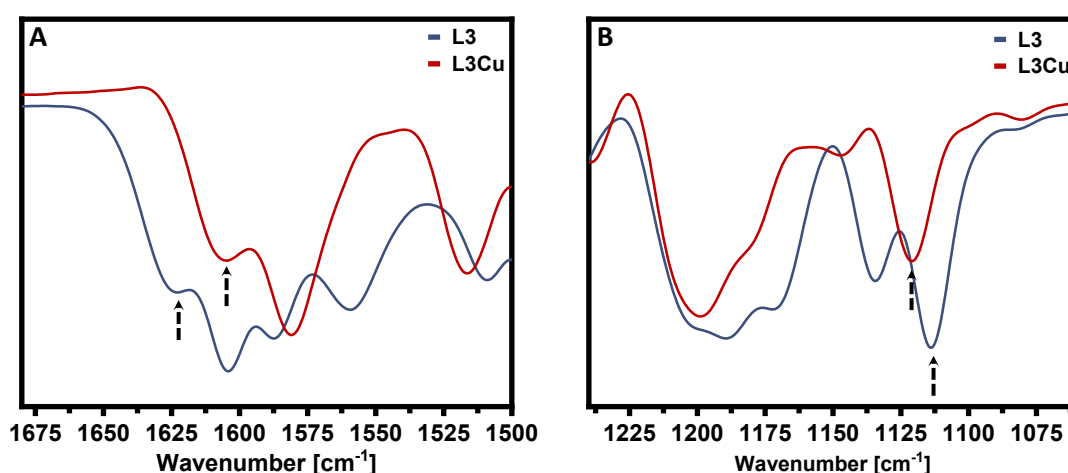


Figure 3.31: Representative IR spectra of **L3** (blue) and **L3Cu** (red) reveal the shifts of the vibrational bands of the imine C=N (A) and the phenolic C–O (B).

### 3.3.2 Determination of HTP Values

Having successfully synthesized the tetradentate BINIM dopants, the next step was to determine the HTP values. These were measured in 5CB using the Grandjean-Cano wedge cell method (see also Chapter 3.2.3). The results of the HTP measurements are summarized in Table 3.5 (see also Figure 7.23) and clearly reveal a remarkable increase of the HTP from  $29\ \mu\text{m}^{-1}$  for **L1** to  $199\ \mu\text{m}^{-1}$  for **L2**. Further enhancement of the HTP was observed for **L3** with  $318\ \mu\text{m}^{-1}$ , which is ten-fold higher than the value of **L1**. Compared to the previously investigated XB-building blocks, these values are extraordinarily high which can be attributed to the intrinsic axial chirality of the binaphthyl moiety.

Table 3.5: Summary of HTPs of ligands and copper complexes in 5CB.

X	HTP ( $\beta_M$ ) [ $\mu\text{m}^{-1}$ ]	
	LX	LXCu
1	$29 \pm 0.5^{\text{a}}$	$32 \pm 0.2$
2	$199 \pm 3$	$230 \pm 3$
3	$318 \pm 8$	$375 \pm 6$

a) determined by measuring a sample with  $\omega = 0.5 \text{ mol}\%$

The remarkable increase of the HTP from **L1** to **L2** can be explained with a different intermolecular interaction between dopant and host molecules. *Gottarelli et al.* proposed a model for the chiral induction in nematic cyanobiphenyl-based LCs with binaphthyl-type dopants (Figure 3.32A). This model suggests that the structural similarity of dopant and LC host plays a decisive role and that the alignment of the biphenyl-based LC molecules occurs along the binaphthyl axis of the dopant.<sup>[106, 213-214]</sup> In case of **L2** the CB substituents in 6,6'-positions increase the structural similarity of dopant and host. This changes the preferred orientation of the LC molecules to an orientation along the substituent's CB axis instead. This leads to significantly larger HTPs and a stronger reaction of the HTP to changes of the dihedral angle (Figure 3.32B).<sup>[215-216]</sup>

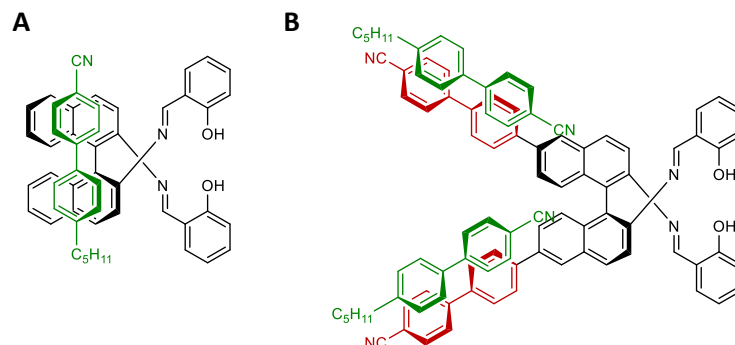


Figure 3.32: Proposed mechanisms for the chiral induction in 5CB using BINIM dopants **L1** (A) and **L2** (B).

This angle  $\theta$  between the aromatic planes of the binaphthyl subunit plays another key role in the efficiency of the chiral transfer and the induction of the helical pitch (Figure 3.33).<sup>[97, 213, 217]</sup> While both *cisoid* ( $\theta < 90^\circ$ ) and *transoid* ( $\theta > 90^\circ$ ) conformation are known to exhibit high HTPs, the values of unsubstituted binaphthyls with a *quasi-orthogonal* conformation ( $\theta \sim 90^\circ$ ) are usually considerably lower. However, also for the 2,2'-substituted derivatives, significant differences can be observed. As experimentally found by *Gottarelli et al.*, 2,2'-binaphthyl diamine (**30**) induces almost no chirality in 5CB due to the orthogonal orientation of the aromatic planes, whereas 2,2'-binaphthol (**5**) exhibits an HTP of

$\beta_M = +32 \mu\text{m}^{-1}$ . In this case, intermolecular hydrogen bonds lead to a stabilization of a rather *cisoid* conformation.<sup>[106]</sup>

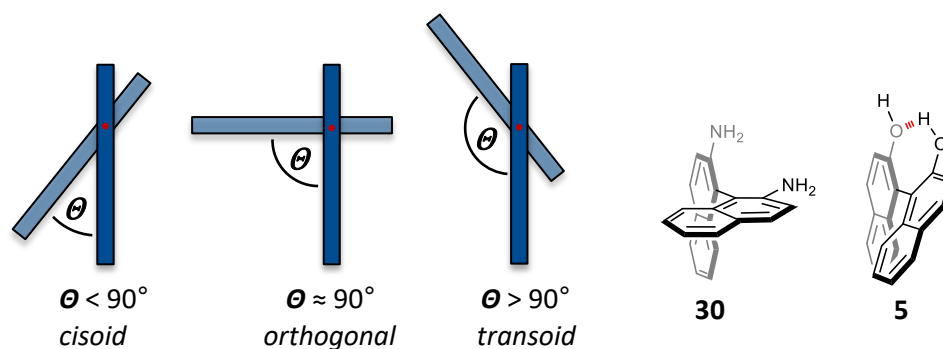


Figure 3.33: Schematic illustration of the *cisoid*, *orthogonal* and *transoid* conformation. Orthogonal conformation of diamine **30** and *cisoid* conformation of **5**.

Taking a closer look at the HTPs, this suggests a noticeable change of the dihedral angle from **L2** to **L3** and upon formation of the copper complexes. Especially the HTPs of **L2Cu** and **L3Cu** are significantly higher than the values of the free ligands (see Table 3.5). With  $\beta_M = 230$  and  $375 \mu\text{m}^{-1}$ , they exhibit helical twisting powers well exceeding previously reported values of metal complex dopants in different nematic host systems.<sup>[218-222]</sup> Therefore, it is reasonable to conclude that the copper ion, being confined in the O–N–N–O cavity of the ligand, geometrically locks the binaphthyl core in a *cisoid* conformation which changes the dihedral angle and reduces the degree of freedom of the binaphthyl bridge.

### 3.3.3 Manipulation of the Photonic Properties

For a reliable induction of structural color in a liquid crystalline host system, the used additives need to exhibit high helical twisting powers and at the same time pose high molecular compatibility (*i.e.* solubility) with the host molecules. The latter becomes even more important for dopants with lower HTPs because higher dopant concentrations are needed to induce the same structural color (*i.e.* helical pitch). However, for a sensor system with a high sensitivity, the dopant concentration should be as high as possible making as many reactive centers accessible for the analyte as possible. At the same time, the dopant should exhibit a strong relative change of the HTP upon interaction with the analyte which results in a detectable shift of the reflected wavelength upon exposure to low concentrations of analyte.

Initial trials to induce structural color in 5CB failed as higher dopant concentrations significantly reduced the clearing point temperature ( $T_C = 36^\circ\text{C}$ ) which made measurements at

room temperature difficult. E7 proved to be a suitable substitute for 5CB (Figure 3.34). As a eutectic mixture of different cyanobiphenyls, it exhibits a higher clearing point ( $T_C = \sim 60^\circ\text{C}$ ) and still has a high structural similarity with 5CB. Therefore, large HTP differences are not expected making it easier to estimate the amount of dopant needed to induce a specific structural color based on the HTPs measured in 5CB.<sup>[223]</sup>

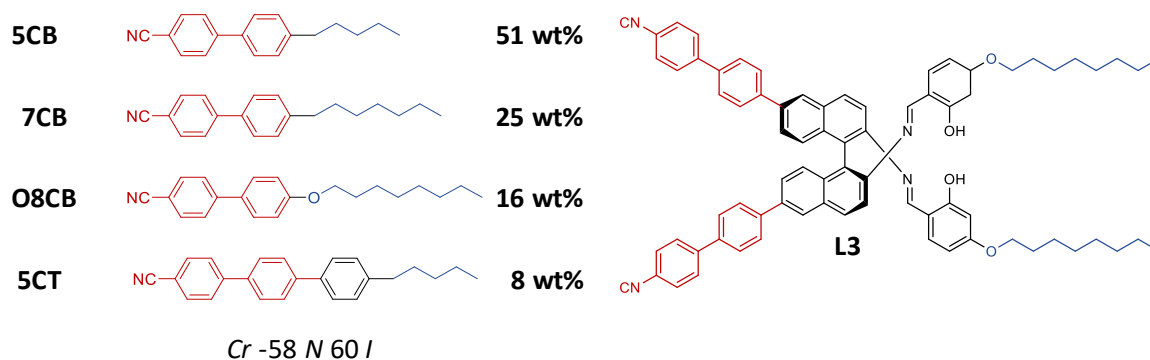


Figure 3.34: Molecular composition of LC mixture E7 and molecular structure of ligand **L3** reveal the shared structural features increasing the solubility.

The nematic LC host was doped with different dopant concentrations between 0.6 mol% and 1.6 mol%. Interestingly, only dopants **L2**, **L3**, and **L3Cu** induced noteworthy structural coloration. Dopants **L1**, **L1Cu**, and **L2Cu** on the other hand, precipitated from the LC host at concentrations below 1.0 mol%, where no noticeable color could be observed. This shows that structural similarity (*i.e.* similar polarity) of dopant and LC host is a crucial variable that needs to be addressed for the successful induction of structural color. This effect becomes even more essential for dopants with lower HTPs. While **L1** shares minor structural features with the biaryl-like host molecules, the attached cyanobiphenyl residues in 6,6'-positions of the binaphthyl core increase the solubility of **L2** (see Figure 3.34). Introduction of an additional alkyl chain in 4-position of the aldehyde (blue) like in **L3**, improves the solubility even more. The alkyl chains also support the molecular alignment of the cyano biphenyl derivatives which, under similar conditions, leads to a stronger intensity and better homogeneity of the structural color compared to samples with **L2**. Figure 3.35 and Figure 3.36A show photographs of the cholesteric LC materials revealing the pronounced structural color and its advancing blue shift with higher dopant concentrations. Based on these results, the compatibility of the dopants can be classified in the order **L1** < **L2** < **L3**. In contrast, the formation of the copper complexes reduces the solubility in E7 due to higher polarity of the molecules (*e.g.* **L1** > **L1Cu**, **L2** > **L2Cu**, and **L3** > **L3Cu**).

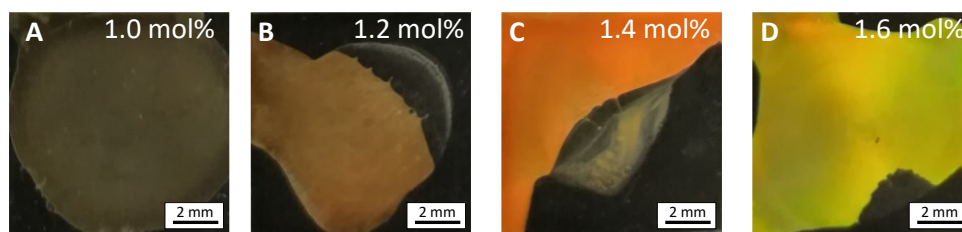


Figure 3.35: Photographs of **L2@E7** in thin films reveal the structural coloration and the remarkable blue shift of the reflected light with increasing dopant concentration.

Interestingly, observing the samples through circularly polarizing light filters exposes an opposite orientation of the cholesteric arrangement of ligand and copper complex-doped systems. In fact, **L3** induces a helical orientation which selectively reflects left circularly polarized light (*L-CPL*) (Figure 3.36B), whereas its copper complex induces an arrangement selectively reflecting right circularly polarized light (*R-CPL*) (C). *Deußen et al.* thoroughly investigated the induction of chirality of 6,6'-disubstituted binaphthol derivatives.<sup>[103]</sup> They found significant correlations between the length of the substituents in 6,6'-positions and the HTPs according to a “the longer the better” approach and confirmed an opposing handedness in cholesteric LCs doped with open-chain (*transoid*) and closed-bridge (*cisoid*) binaphthyl dopants. This indicates the presence of two different conformations of ligand and metal complex. While **L3** is predominantly present in an *S-transoid* conformation inducing the formation of a left-handed helix (Figure 3.36D), the copper ion locks the binaphthyl core in an *S-cisoid* conformation which supports the induction of a right-handed helix (E). The same behavior was observed for the system **L2@E7** (Figure 7.24), however, the following discussion focusses on **L3@E7** and **L3Cu@E7** as representative examples.

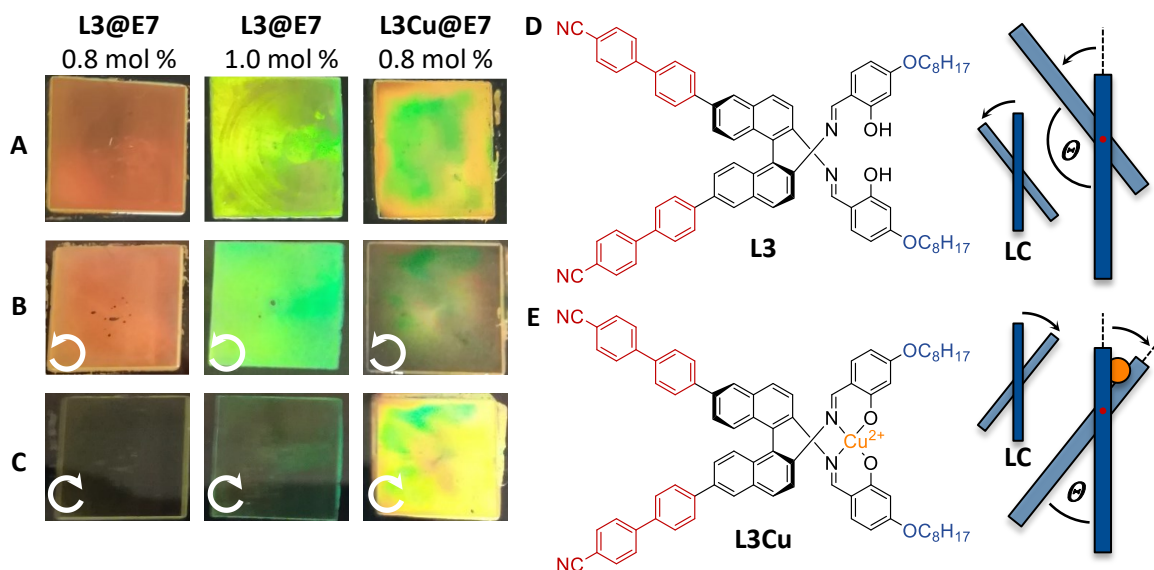


Figure 3.36: Photographs of the structural coloration of cholesteric LC systems **L3@E7** and **L3Cu@E7** under unfiltered light (A), *L*-CPL (B), and *R*-CPL (C). Molecular structure and schematic model of the *S-transoid* conformation of **L3** and locked *S-cisoid* conformation of **L3Cu** and the resulting cholesteric orientation of the LC molecules.

To confirm and quantify these observations, additional experiments of 1.0 mol% **L3@E7** and 0.8 mol% **L3Cu@E7** were performed in thin LC films. Although, the homogeneity of the structural coloration was better in **L3@E7**, reflectance measurements (Figure 7.25) of the two samples reveal similar reflection wavelengths with peak maxima at  $\lambda_{\max} = 598$  for **L3@E7** and 573 nm for **L3Cu@E7**. UV/Vis and CD spectra of the samples show similar values (Figure 3.37). Despite small deviations of the peak maxima caused by different experimental setups and alignment of the samples, both techniques proved the opposing helical arrangement of the two cholesteric samples. While **L3@E7** exhibits a positive CD signal at  $\lambda_{\max} = 548$  nm (A) its copper complex counterpart induces an arrangement which exhibits a negative signal at  $\lambda_{\max} = 577$  nm (B).<sup>[103]</sup>

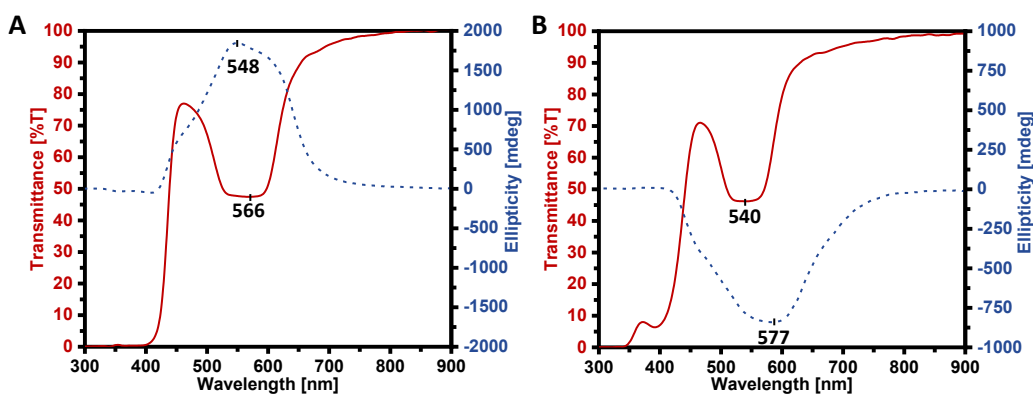


Figure 3.37: UV/Vis (solid line) and CD spectra (dashed line) of thin LC films of E7 doped with 1.0 mol% **L3** (A) and 0.8 mol% **L3Cu** (B).

### 3.3.4 Gas sensing

The experiments described in this section were performed in collaboration with Prof. Peter Kaul and Lukas Pschyklenk from the University of Applied Sciences Bonn-Rhein-Sieg in Rheinbach. The main idea was to investigate the reaction of the cholesteric LC systems described above to different  $\text{NO}_2$  gas concentrations and to evaluate their application potential for photonic sensing devices.

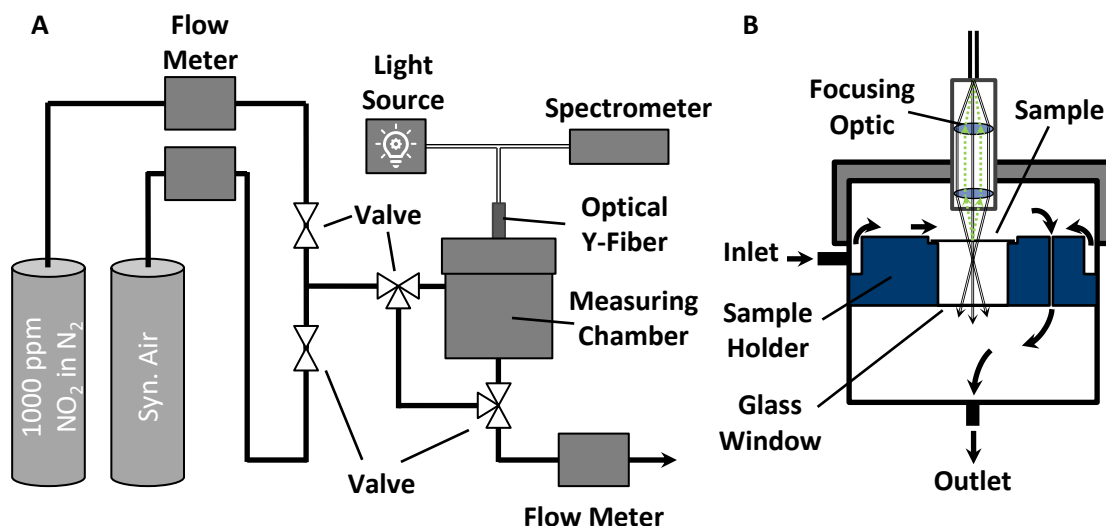


Figure 3.38: A) Schematic representation of the experimental setup used for the gas sensing experiments. B) Schematic representation of the reaction chamber displaying the analyte gas flow (black arrows) and measuring principle of the reflected wavelength using a two-way reflection probe with a focusing optic.

For the execution of the gas sensing, the same experimental setup previously reported by *Pschyklenk et al.* was used (Figure 3.38).<sup>[195]</sup> This setup consists of a custom-built measuring chamber equipped with a two-way fiber optic connected to a light source and a spectrometer (A). The gas concentration was adjusted by proportionate mixing of analyte gas and synthetic air while keeping the overall gas flow at 200 mL/min. To prevent a response of the system due to hydrolysis of the imines, all experiments were performed using dry gas mixtures and dry synthetic air. Prior to the measurement, the sample was spin coated onto an uniaxially rubbed polyvinyl alcohol (PVA) coated microscope cover slip. The polymer substrate supports the planar alignment of the cholesteric LC and yields a more uniform structural color. Subsequently, the sample was placed on the sample holder in the measuring chamber (B) and was purged with synthetic air for several minutes. This setup allowed the continuous recording of the reflection spectra of the sample upon exposure to defined analyte

---

gas concentrations. The response of the system was followed by measuring the shift of the reflectance peak maximum ( $\Delta\lambda_{\max}$ ) as a function of the time.

#### 3.3.4.1 Sensitivity of the Sensor System

Assuming, that the copper functions as the main reactive center in the BINIM dopant, which can strongly interact with  $\text{NO}_2$ , dopant **L3** is not expected to show a significant reaction. Therefore, during first experiments a sample of E7 doped with 1.0 mol% **L3Cu** (**L3Cu@E7**) was investigated. The sample showed a uniform structural color on the PVA substrate with a reflection wavelength of  $\lambda_{\max} = 483 \text{ nm}$  (Figure 7.26).

Because the study of *Pschyklenk et al.* on the sensing of  $\text{CO}_2$  using TADDOL dopant **27** suggested only a small response of a few nm per minute [ $\text{nm}\cdot\text{min}^{-1}$ ], an initial concentration of 1000 ppm  $\text{NO}_2$  was used. However, against all expectations, the reflectance maximum showed an almost instantaneous bathochromic shift beyond 900 nm within a few seconds upon exposure to  $\text{NO}_2$ . As this exceeded the detection limit of the reflection probe, a reliable evaluation of the data was not possible.

Therefore, consecutive experiments were performed with stepwise reduced concentrations of 500, 400, 200, and 100 ppm, which allowed a more detailed investigation of the shift behavior. Figure 3.39 displays the response plots (change of the reflectance maximum as a function of the time) of the measurements which show a significantly different behavior with a reversible and irreversible character depending on the used gas concentration.

---

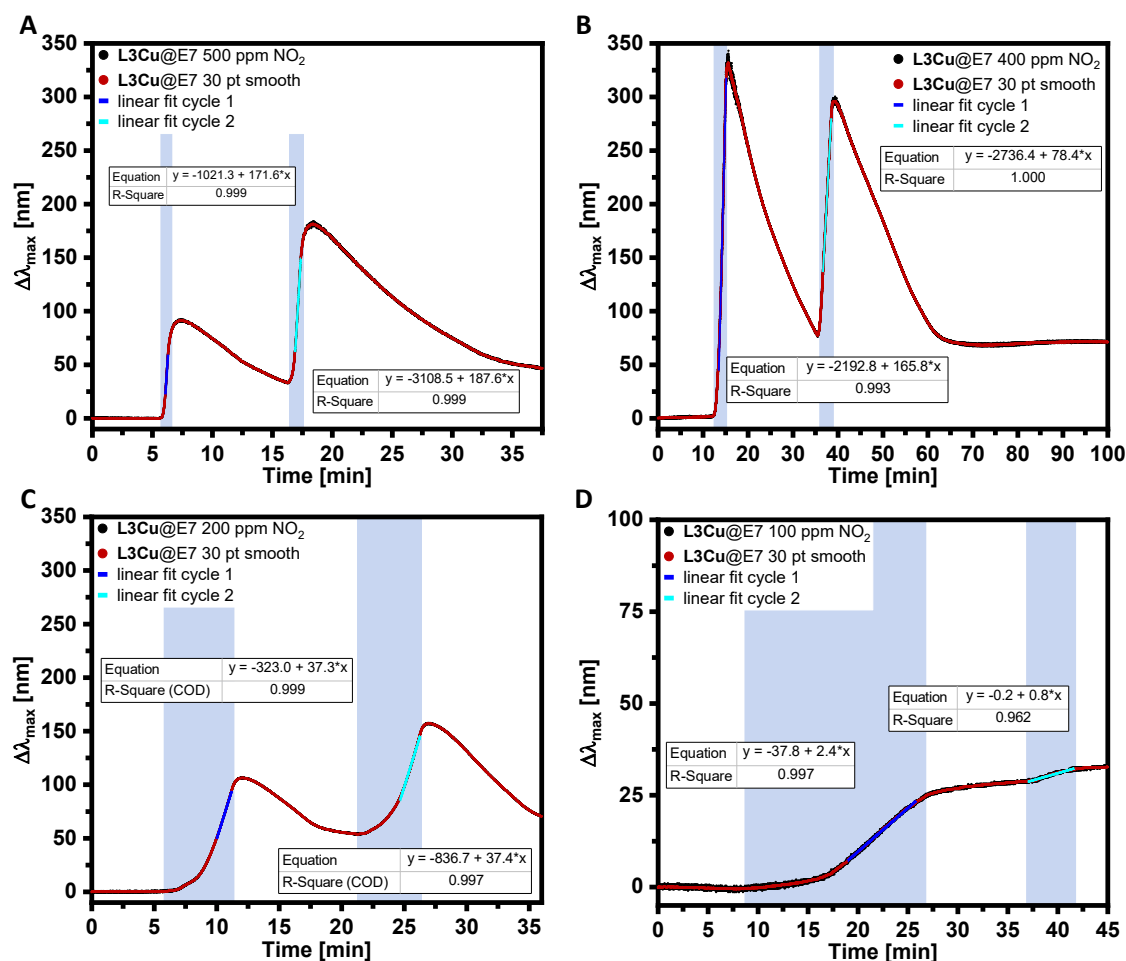


Figure 3.39: Response plots of 1.0 mol% L3Cu@E7 upon exposure to different concentrations of NO<sub>2</sub> gas: A) 500 ppm; B) 400 ppm; C) 200 ppm; D) 100 ppm.

Upon exposure of the sample (blue areas) to higher analyte gas concentrations (Figure 3.39A – C) the reflectance maximum continuously shifted to longer wavelengths until the analyte gas flow was stopped. Interestingly, subsequent purging of the sample with dry synthetic air (white area) shifted the maximum back to shorter wavelengths showing a reversible process over multiple cycles. However, full reversibility of the shift could not be observed. Instead, the reflectance maximum showed a permanent hysteresis which gradually approximated a value of  $\Delta\lambda_{\max} = \sim 70$  nm (*i.e.*  $\lambda_{\max} = \sim 550$  nm) with each exposure cycle. This becomes even more obvious at a gas concentration of 100 ppm where no reversibility of the shift could be observed (Figure 3.39D). Upon NO<sub>2</sub> exposure, the maximum continuously red-shifted and stopped once the sample was purged but did not reverse. This behavior indicates two different processes during the exposure, one being reversible once a certain exposure threshold is exceeded, the other being irreversible. A possible explanation is a reversible and partly irreversible coordination of NO<sub>2</sub> to the copper ion in L3Cu at room temperature.<sup>[189, 193, 224-226]</sup> Lozzi *et al.* found that the interaction of NO<sub>2</sub> with the copper ion in

copper phthalocyanines is strong enough that an irreversible chemisorption can occur. The formation of an ionic bond between the copper ion and  $\text{NO}_2$  and the oxidizing character of  $\text{NO}_2$  lead to strong charge transfer processes which caused the partly irreversible character of their system.<sup>[226]</sup>

For the evaluation of the sensitivity and to allow a later comparison of the results with other gas sensing experiments, the response rates were determined for each measurement. As all experiments (Figure 3.39) showed a linear behavior after a short equilibration time, a determination of the response rate [ $\text{nm}\cdot\text{min}^{-1}$ ] from the slope of the linear fit was reasonable. The results reveal that the shift rates gradually decrease with decreasing gas concentration from  $\sim 170 \text{ nm}\cdot\text{min}^{-1}$  at a concentration of 500 ppm (A) to  $\sim 2 \text{ nm}\cdot\text{min}^{-1}$  at 100 ppm (D). Interestingly, the response is slower during the second cycle of the measurements using concentrations of 400 ppm ( $\sim 166 \text{ nm}\cdot\text{min}^{-1}$  vs.  $\sim 78 \text{ nm}\cdot\text{min}^{-1}$ ; B) and 100 ppm ( $\sim 2 \text{ nm}\cdot\text{min}^{-1}$  vs.  $\sim 1 \text{ nm}\cdot\text{min}^{-1}$ ; D). This can be attributed to a reduced sensitivity due to the irreversible coordination of  $\text{NO}_2$  to the copper ion. Measurements using concentrations of 500 ppm (A) and 200 ppm (C) reveal that the shift rates during the second cycle also depend on the concentration and exposure time (*i.e.* absolute  $\Delta\lambda_{\text{max}}$ ) during the first cycle. While both measurements provide rates of  $\sim 172 \text{ nm}\cdot\text{min}^{-1}$  and  $\sim 38 \text{ nm}\cdot\text{min}^{-1}$  with a shift of  $\Delta\lambda_{\text{max}} = \sim 100 \text{ nm}$  (higher concentration and shorter exposure time at 500 ppm) the second cycle shows a similar or slightly increased shift rate.

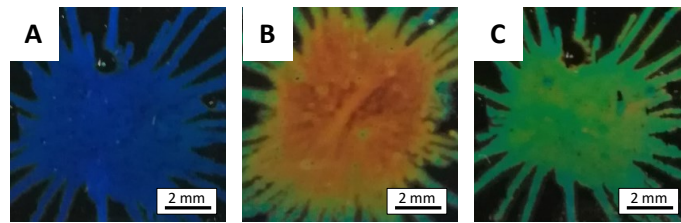


Figure 3.40: Photographs of thin films of **L3Cu@E7** show the reflectance color before (A) and after  $\text{NO}_2$  exposure (500 ppm) and after purging with synthetic air (C).

Thanks to the photonic properties of the material, the reversible and irreversible shift of  $\lambda_{\text{max}}$  can also be observed by the naked eye. Figure 3.40 shows photographs of the structural color of **L3Cu@E7** in a thin film on a PVA substrate. While the sample shows an initial strong blue color (A), the reflected wavelengths red shifts upon exposure to  $\text{NO}_2$  gas (B). Subsequent purging of the sample with dry synthetic air induces a blue shift revealing the permanent green reflectance (C).

To confirm that the response of the system is due to the presence of the chiral dopant and not caused by the LC system itself, a reference experiment was performed using commercially available LC mixture E8 doped with 38.5 mol% liquid crystalline dopant *S*-4-cyano-4'-(2-methylbutyl)biphenyl (CB15@E8) (Figure 3.41A).<sup>[227-228]</sup> This system has a high structural similarity with E7 and 5CB and is not expected to show a response to the NO<sub>2</sub> analyte. The response plot (Figure 3.41B) in fact reveals that the reference system does not react to NO<sub>2</sub> rich atmosphere with concentrations of 500 or 1000 ppm and the reflected wavelength remains at the initial value of 612 nm. This negative experiment indirectly proves that the reaction of **L3Cu**@E7 is due to BINIM dopant **L3Cu**.

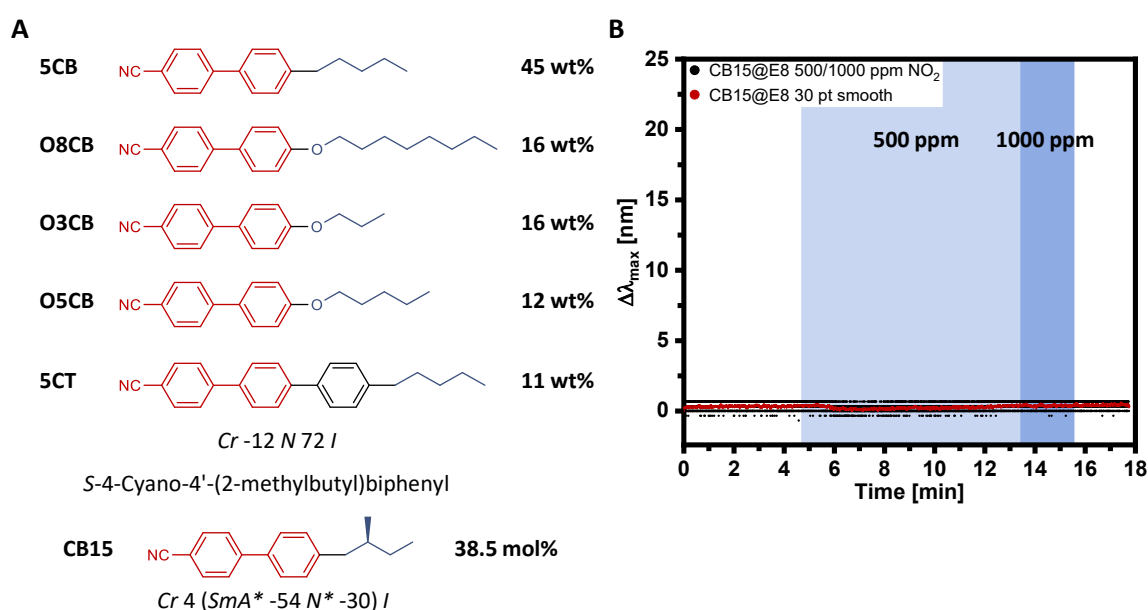


Figure 3.41: A) Molecular structures and thermal properties of LC mixture E8 and chiral dopant CB15.<sup>[227-228]</sup> B) Response plot of E8 doped with 38.5 mol% CB15 upon exposure to 500 and 1000 ppm NO<sub>2</sub> over several minutes shows no shift of the reflectance maximum.

Having confirmed that the response of the system is indeed caused by the used chiral BINIM dopant, the experiments were repeated using the system **L3**@E7. To allow a reliable comparison with the obtained sensitivities of **L3Cu**@E7, the same dopant concentration of 1.0 mol% was used (see also Table 3.6). Due to the lower HTP of BINIM dopant **L3** ( $\beta_M = 318$  vs.  $375 \mu\text{m}^{-1}$ ), the sample expectedly showed a more red-shifted reflectance peak maximum at  $\lambda_{\text{max}} = 612$  nm. The measurements reveal that the sample also responds to NO<sub>2</sub> (Figure 3.41, blue areas). This is interesting, because unlike **L3Cu**, **L3** does not comprise a reactive coordination center for the analyte. Upon exposure to the analyte gas, the reflectance

maximum constantly red shifts until the gas flow is stopped and blue shifts again upon purging with synthetic air which indicates a reversible adsorption of  $\text{NO}_2$  by the system. Measurements at a concentration of 500 ppm (Figure 3.42A and Table 3.6) reveal, however, that the sensitivity is considerably lower compared to the copper derivative ( $\sim 5 \text{ nm}\cdot\text{min}^{-1}$  vs.  $\sim 170 \text{ nm}\cdot\text{min}^{-1}$ ). Although the notably weaker response of **L3@E7** makes this system irrelevant for efficient gas sensing at low concentrations, measurements at higher concentration of 700 and 1000 ppm were conducted to further investigate the behavior of the system (Figure 3.42B/C). As already observed for the system **L3Cu@E7**, the response rates gradually increased with increasing dopant concentration and the process appeared to be partly irreversible resulting in a slight permanent shift of the reflectance peak maximum. As  $\text{NO}_2$  is a strong oxidizer which can take part in various atmospheric reactions, a possible explanation is a partial decomposition of the dopant.<sup>[229-230]</sup> The interaction of  $\text{NO}_2$  with the aromatic system of the dopant or the polar  $\text{HO-N-N-OH}$  cavity of the BINIM ligand is a possible explanation for the reversible behavior.<sup>[231-234]</sup>

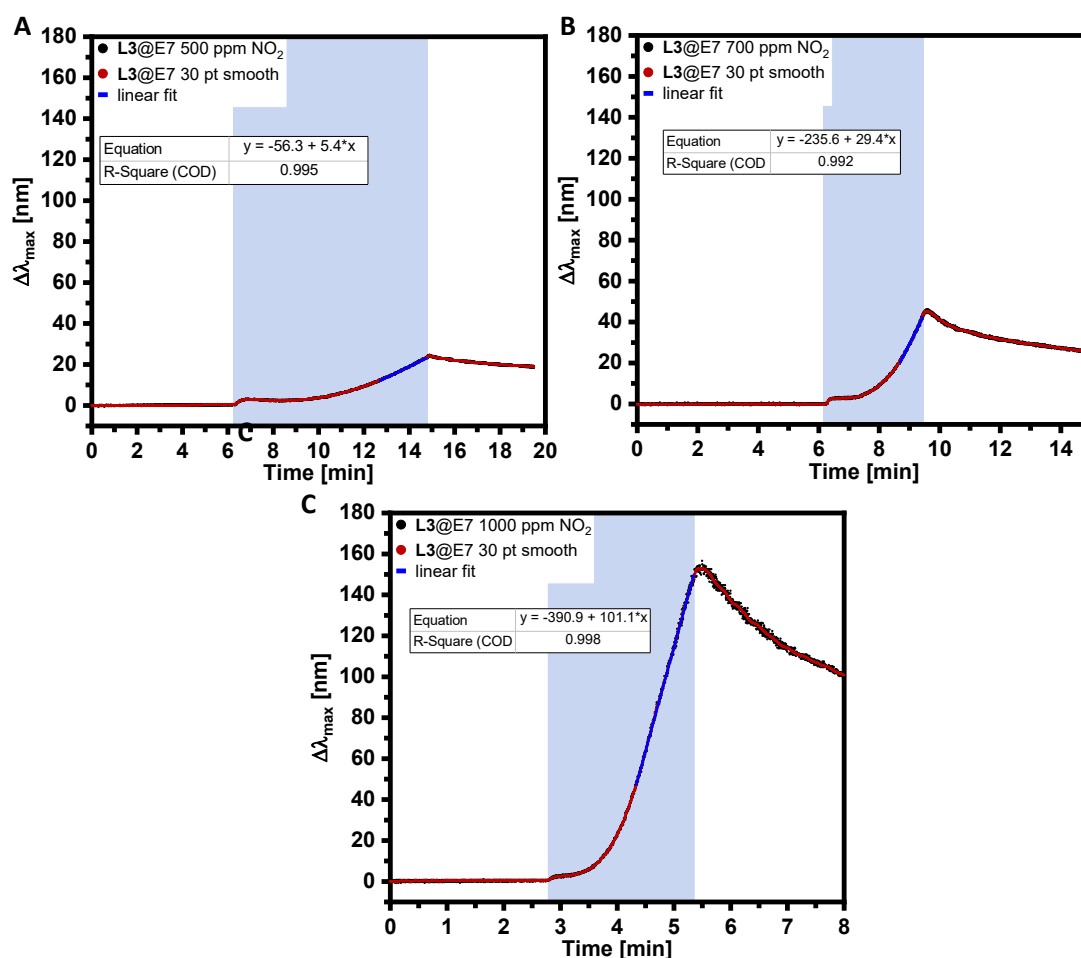


Figure 3.42: Response plots of 1.0 mol% **L3@E7** upon exposure to different concentrations of  $\text{NO}_2$ : A) 500 ppm; B) 700 ppm; C) 1000 ppm.

Table 3.6: Summary of response rates of the two sensor systems upon exposure to different concentrations of NO<sub>2</sub>.

Concentration [ppm]	Shift rate [nm·min <sup>-1</sup> ]	
	L3@E7	L3Cu@E7
100	-	2.4 <sup>a)</sup> / 0.8 <sup>b)</sup>
200	-	37.3 <sup>a)</sup> / 37.4 <sup>b)</sup>
400	-	165.8 <sup>a)</sup> / 78.4 <sup>b)</sup>
500	5.4	171.6 <sup>a)</sup> / 187.6 <sup>b)</sup>
700	29.4	-
1000	101.1	-

<sup>a)</sup> first cycle; <sup>b)</sup> second cycle

### 3.3.4.2 Selectivity of the Sensor System

Having shown that the sensor systems L3@E7 and L3Cu@E7 both show a noticeable reaction to NO<sub>2</sub> gas, additional experiments were conducted using other environmentally hazardous gases like CO, NO, and H<sub>2</sub>S to get an idea of the selectivity of the sensor systems. In this respect, the experiments with NO also function as a reference to confirm that the shifts observed during the experiments with NO<sub>2</sub> are not caused by impurities of NO. To allow a comparison of the results, all measurements were performed with an analyte concentration of 500 ppm. The results are summarized in Table 3.7 and Figure 3.43 and clearly show a remarkable selectivity of the two sensor systems for NO<sub>2</sub>.

Table 3.7: Summary of the responses of L3@E7 and L3Cu@E7 to different analytes with a concentration of 500 ppm.

Analyte	Shift rate [nm·min <sup>-1</sup> ]	
	L3@E7	L3Cu@E7
NO <sub>2</sub>	5.4	171.6
CO	N/D	N/D
NO	0.3	0.4
H <sub>2</sub> S	N/D	1.0

N/D: not determined

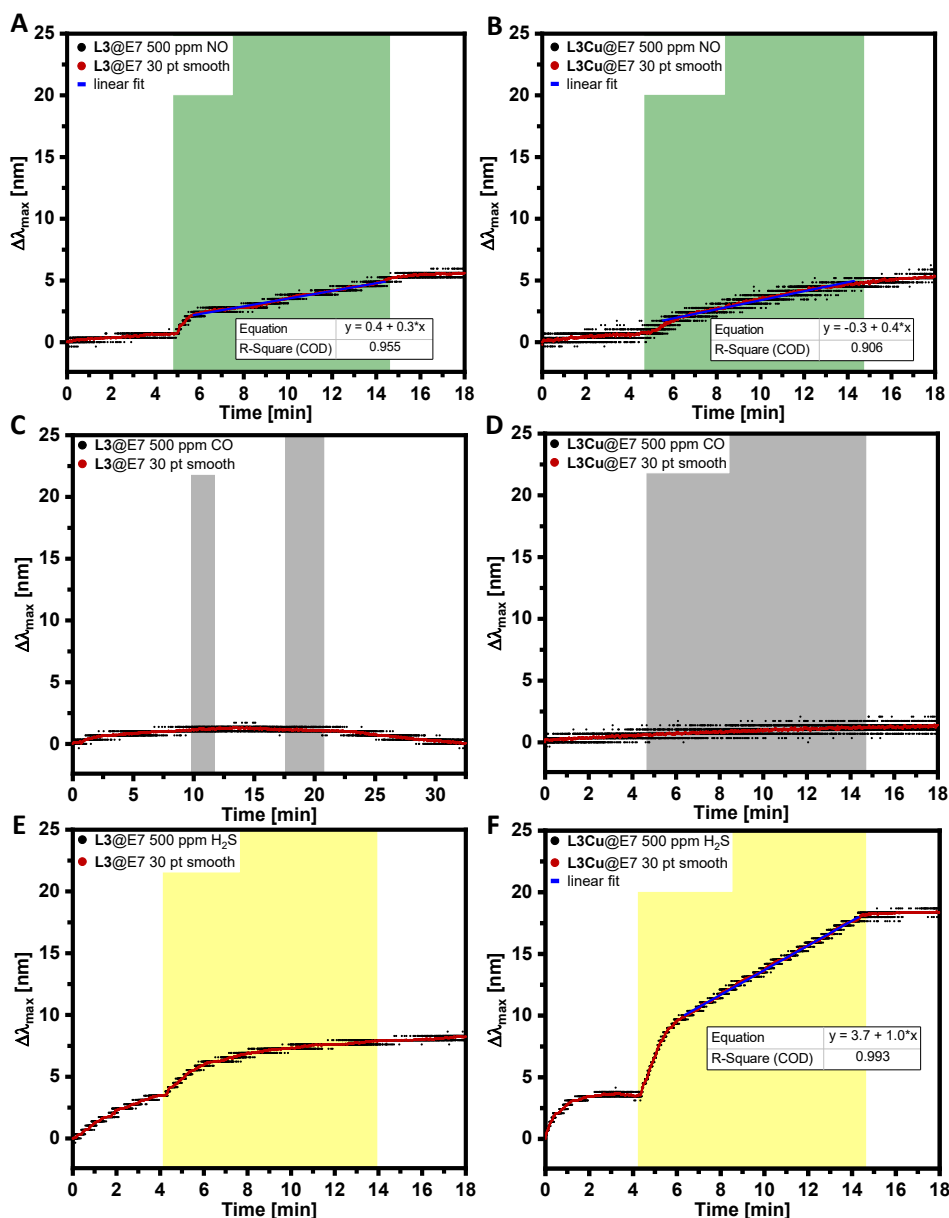
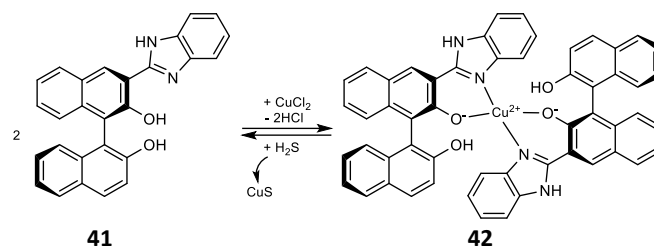


Figure 3.43: Response plots of **L3@E7** and **L3Cu@E7** upon exposure to CO (A/B), NO (C/D), and H<sub>2</sub>S (E/F).

While none of the systems considerably reacted to CO (Figure 3.43A/B), a slow red shift of the reflectance maxima could be observed upon exposure to NO (C/D). However, negligible shift rates of less than  $1 \text{ nm} \cdot \text{min}^{-1}$  prove that the previously observed responses were indeed due to an interaction of NO<sub>2</sub> with the chiral dopant and not caused by NO impurities. A considerable response could only be observed for **L3Cu@E7** upon exposure to H<sub>2</sub>S gas (F) which showed a constant and irreversible linear bathochromic shift of  $1 \text{ nm} \cdot \text{min}^{-1}$  after a short equilibration time. A possible explanation for the response of the system is the interaction of H<sub>2</sub>S with the copper ion.<sup>[235-236]</sup> It is known that, besides NO<sub>2</sub>, H<sub>2</sub>S can also interact with copper ions which makes this combination attractive for sensing applications.<sup>[179, 235, 237-239]</sup>



Scheme 3.6: Displacement of Cu(II) ions by H<sub>2</sub>S.

*Sun et al.* reported on BINOL-benzimidazol copper complex **42** (Scheme 3.6) which reacted to different concentrations of H<sub>2</sub>S, HS<sup>-</sup>, and S<sup>2-</sup> in aqueous media and to different concentrations of H<sub>2</sub>S in the gas phase. By displacement of the copper ion and formation of the free ligand **41**, a permanent shift of the fluorescence signal could be induced.<sup>[236]</sup> Although, colorimetric sensors which respond to low H<sub>2</sub>S concentrations are known, especially LC-based photonic sensors have not been reported yet. A deeper understanding of the underlying processes would allow to selectively functionalize the sensor system to maximize the performance. However, since the focus of this study was the detection of NO<sub>2</sub> gas, the detailed investigation of the underlying processes was not part of this study and will be conducted in concluding investigations.

### 3.3.5 Conclusions

#### 1. Influence of the functionalization and complex formation on the HTP value

HTP measurements of the chiral dopants in 5CB revealed considerable differences in the efficiency of the chiral transfer. A significant increase of the HTP values from **L1** ( $\beta_M = 29 \mu\text{m}^{-1}$ ) through **L2** to **L3** ( $\beta_M = 318 \mu\text{m}^{-1}$ ) was observed, which could be attributed to different induction mechanisms and intermolecular interactions between guest and host caused by the CB functionalization of the binaphthyl core. The formation of the copper complexes enhanced the HTPs even further to up to  $\beta_M = 375 \mu\text{m}^{-1}$  for **L3Cu**. This observation suggests a change of the dihedral angle of the binaphthyl core due to the metal coordination.

#### 2. Induction of structural color in a liquid crystalline host using BINIM Dopants

Experiments to induce structural color in nematic LC host E7 reveal the importance of high HTPs and high structural similarity of guest and host molecules for the exhibition of strong reflectance colors. Only dopants **L2**, **L3**, and **L3Cu** posed high enough solubility in E7 to exhibit structural coloration at concentrations between 0.8 and 1.6 mol%. CD measurements of structurally colored samples of 1.0 mol% **L3@E7** and 0.8 mol% **L3Cu@E7** reveal an

---

opposing helical orientation of the cholesteric LC resulting in selective reflection of *L*-CPL and *R*-CPL, respectively. These findings suggest that the ligand is predominantly present in a *transoid* conformation whereas the copper ion locks the binaphthyl core in a *cisoid* conformation.

### 3. *NO*<sub>2</sub> gas sensing using a cholesteric sensor system of BINIM dopant and LC host

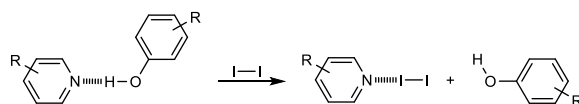
Gas sensing experiments of structurally colored samples revealed a noticeable reaction (red shift) to *NO*<sub>2</sub> rich atmosphere and confirm that the response is caused by interaction of the analyte with the reactive BINIM dopants. Complexation of copper ions by the tetradentate BINIM dopant **L3** significantly improved the sensitivity of the sensor system and allowed the detection of *NO*<sub>2</sub> gas with a concentration of 100 ppm. Both reversible and irreversible processes could be identified.

The unequivocal selectivity of the systems **L3@E7** and **L3Cu@E7** to *NO*<sub>2</sub> was shown by gas sensing experiments with other environmentally hazardous gases like carbon monoxide (CO), hydrogen sulfide (H<sub>2</sub>S), and nitric oxide (NO). Of the investigated combinations only **L3Cu@E7** showed a noticeable and irreversible response when exposed to H<sub>2</sub>S gas. Although the sensitivity was significantly lower compared to *NO*<sub>2</sub>, more detailed follow-up investigations of the mechanistic background may allow the development of a sensitive photonic H<sub>2</sub>S sensor by a tailored functionalization of the reactive dopant.

---

### 3.4 Halogen Bonding for Sensing Applications

Recent findings in our group by *Malotke et al.* revealed the sensing potential of hydrogen-bonded chiral liquid crystals for the detection of iodine and inter halogen vapors. It is thought that the halogen derivatives disturb the pyridyl based hydrogen bond of the assembly by formation of a halogen bond (Scheme 3.7). This changes the helical twisting power of the material which ultimately leads to a shift of the reflected color.<sup>[240]</sup>



Scheme 3.7: Mechanism for the photonic sensing of iodine by disturbance of the hydrogen bond and formation of a halogen bond.<sup>[240]</sup>

Having this in mind, this project aims to use the findings from the previous gas sensing experiments and to combine them with the findings by *Malotke et al.* to develop a binaphthyl-diimine-based sensor system for the detection of iodine vapors. By insertion of a pyridyl unit into the binaphthyl-diimine backbone of the dopant, a halogen bond acceptor site can be added which allows the binding of iodine or other halogen compounds (see Section 3.1). It is thought that the formation of the halogen bond changes the chirality of the dopant and thus induces a change of the structural color (Figure 3.44). *Wang et al.* already showed that the formation of a halogen bond can in fact influence the HTP of a given binaphthyl dopant (see Figure 3.27).<sup>[140]</sup> Based on the results from the previous studies, BINIM dopants **L4** and **L4Cu** are considered to be suitable candidates for this study.

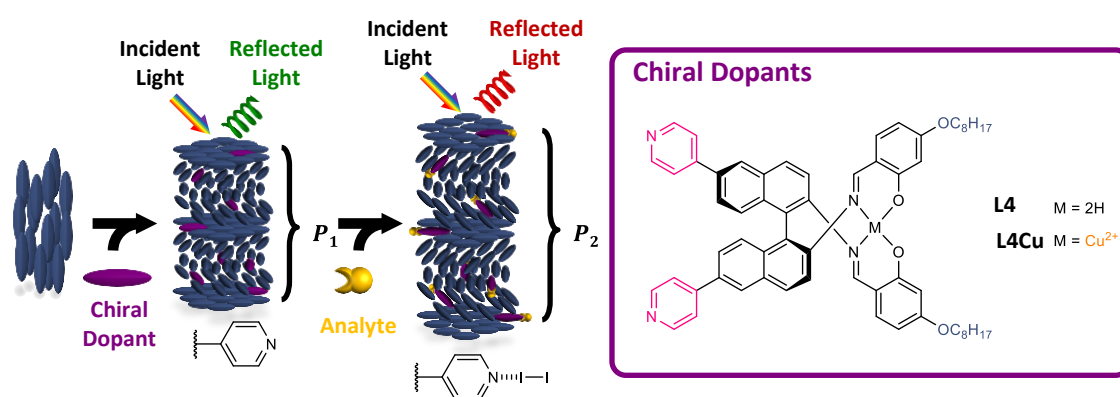
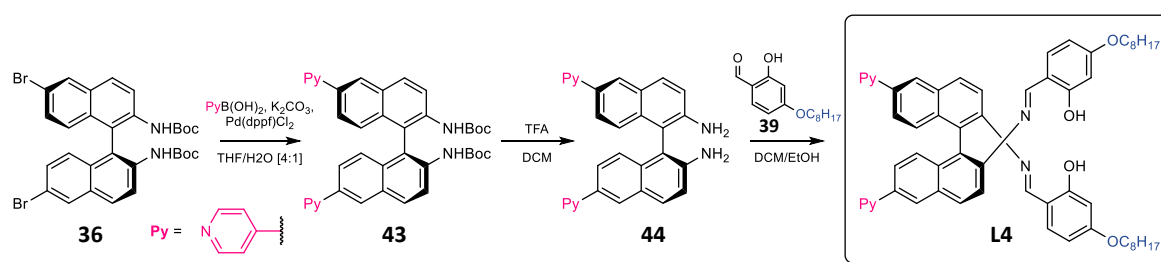


Figure 3.44: Schematic representation of the sensing principle using halogen bond donor dopants **L4** and **L4Cu** for the photonic sensing of iodine vapor.

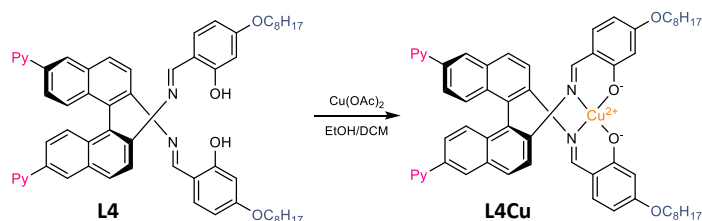
### 3.4.1 Synthesis of Halogen Bond Acceptor Dopants **L4** and **L4Cu**

The synthesis of bipyridine dopants **L4** and **L4Cu** was performed starting from boc-protected precursor **36** which was previously synthesized (see Section 3.3.1). Suzuki coupled intermediate **43** could be readily obtained by reaction of **36** with 4-pyridinylboronic acid in 91% yield (Scheme 3.8). Diamine **44** was synthesized according to the previously described procedure for the boc-deprotection using 180 eq TFA in DCM in 68% yield without further purification. A much more challenging step was the formation of diimine ligand **L4**.



Scheme 3.8: Synthesis of bipyridine dopant **L4**.

Due to the two pyridine units, the formed product was more polar compared to CB ligands **L2** and **L3**. Although only 3 eq 4-octyloxysalicylaldehyde (**39**) were needed for the full conversion to the diimine **L4**, the purification by simple precipitation from methanol and subsequent filtration as performed for **L2** and **L3** was not possible. After several purification trials *via* column chromatography and precipitation from several solvents, fractionate precipitation from a mixture of DCM and methanol turned out to be the method of choice. For this purification method, the crude reaction product was dissolved in a few drops of DCM. Subsequent addition of methanol yielded a yellow emulsion which formed an oily residue upon sonication. The solvent fraction was removed, and the residue washed with a few drops of methanol. This step was repeated until the excess of aldehyde was removed completely. To increase the yield, all solvent fractions were combined, concentrated to dryness and the purification procedure repeated until pure **L4** was isolated in 40% overall yield.



Scheme 3.9: Synthesis of copper complex **L4Cu**.

The synthesis of copper complex **L4Cu** was performed according to the procedure described for **L1Cu** – **L3Cu** and is displayed in Scheme 3.9 (see also Scheme 3.4). After reflux of **L4** with  $\text{Cu}(\text{OAc})_2$  in a mixture of ethanol and DCM, the product could be precipitated from small amounts of methanol in 62% yield. The successful synthesis of ligand **L4** and its copper complex **L4Cu** was confirmed in accordance with the observations made for **L1** – **L3** and their copper complexes *via* NMR spectroscopy (for **L4** only), mass spectrometry and IR spectroscopy (Figure 7.27).

### 3.4.2 HTP and Structural Color

The HTP values of dopants **L4** and **L4Cu** were determined as described earlier using the Grandjean-Cano wedge cell method by doping 5CB with different amounts of dopant (see also Chapter 3.2.3). The  $\beta_M$  values were found to be as high as  $85 \mu\text{m}^{-1}$  for **L4** and  $254 \mu\text{m}^{-1}$  for **L4Cu** revealing a similar trend as observed for the CB ligands **L2** and **L3** and their copper complexes (Figure 7.29 and Table 7.3). This supports the assumption that the significant HTP increase is due to a change of the dihedral angle upon complex formation. A change of the HTP due to compatibility reasons of host and guest can be excluded in this case as the copper complex with the copper ion has a higher polarity compared to the free ligand and therefore a lower compatibility with the nonpolar cyanobiphenyl LC host. This was also observed during trials to induce structural color in E7. While **L4** slowly started to precipitate from E7 at a concentration of 4 mol% without showing noticeable structural coloration (Figure 3.45A), **L4Cu** already precipitated in the vial almost immediately after solvent removal at a dopant concentration of 1 mol% forming small dark crystallites in the LC mixture, as can be seen in the image in Figure 3.45B.

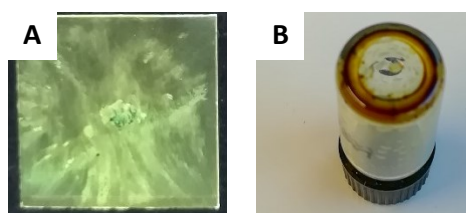


Figure 3.45: A) Real image of 4 mol% **L4@E7** reveals the phase separation in the LC phase without showing structural color. B) Image of 1 mol% **L4Cu@E7** in a vial reveals the precipitating dopant as dark crystallites inside the LC mixture.

### 3.4.2.1 Optimizing the Compatibility of Dopant and LC Host

Having made these observations, it was tried to use the hydrophobicity of the XB to improve the compatibility of the system by capping the polar pyridine groups with a nonpolar halogen bond donator in order to decrease the overall polarity of the systems. As already reported by *Wang et al.*, halogen bonds can be retained in a liquid crystalline host system and may even affect the HTP of a given dopant, however, they lacked a precise explanation whether the observed HTP increase was due to the increased compatibility of the dopant with the LC host (see also Figure 3.27), or due to the formation of the halogen bond itself.<sup>[140]</sup> In Section 3.2 it was shown, that the HTP value is mostly independent of the strength of the halogen bond and that an actual change of the dopants geometry is needed to noticeably influence the HTP. However, besides the dopant's geometry, also the compatibility of the guest with the LC host affects the HTP as it determines how well the host molecules adopt the chiral sense of the dopant.

In this respect, pyridine units **L4** and **L4Cu** are excellent candidates to investigate this process. With **L4Cu** being geometrically locked and **L4** having a higher rotational freedom along the binaphthyl C–C axis, a change of the HTP due to the XB formation can occur in two general ways (Figure 3.46):

1. The HTPs of **L4** and **L4Cu** are affected in the same manner indicating that the increased compatibility with the host primarily determines the HTP value in this case or
2. Only the HTP of **L4** is affected which indicates that an actual change of the dihedral angle of the binaphthyl core is changed due to the formation of the halogen bond and increased intermolecular interactions.

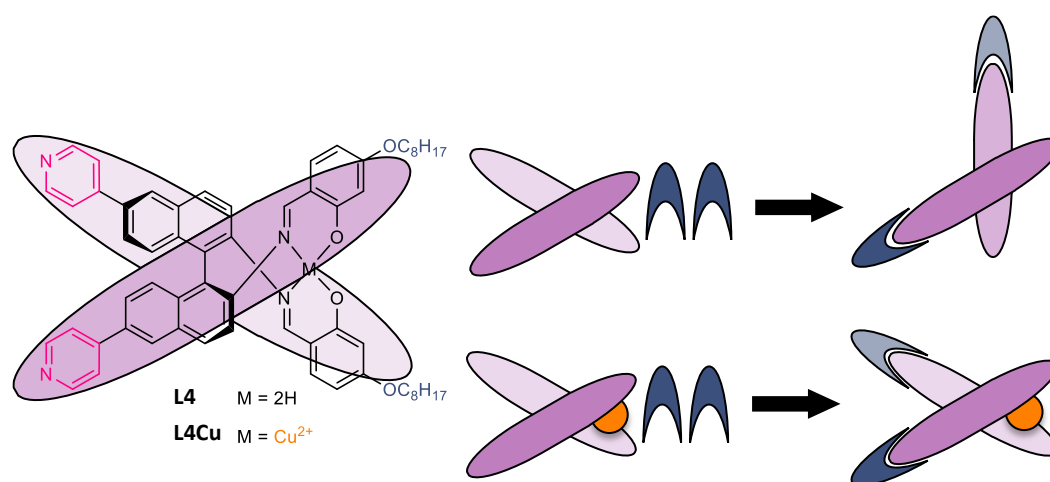
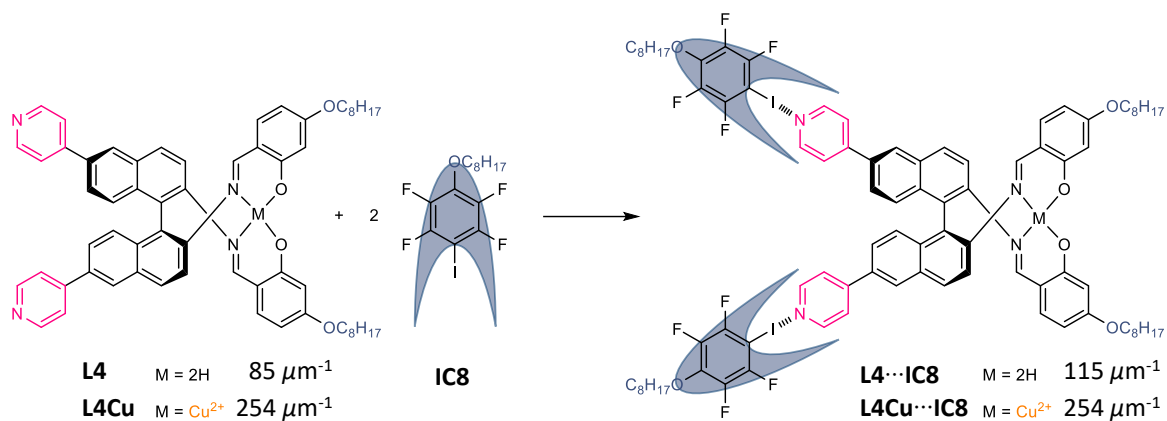


Figure 3.46: Schematic illustration of a change of the HTP change due to formation of the halogen bond and a change of the dihedral angle.

In Section 3.1 it was shown, that of the classic alkylated fluoro-iodo donors, building blocks comprising a tetrafluoroiodo unit form the most stable XBs with pyridine moieties. To exclude the influence of light on the HTP, XB-donor 4-octyloxy-2,3,5,6-tetrafluoroiodo benzene (**IC8**) was chosen to cap the pyridyl groups (Scheme 3.10). This donor does not include a photoisomerizable azo- or stilbene linkage but still significantly increases the overall compatibility with the LC host due to its aromatic system and long alkyl chain. The synthesis of **IC8** was performed according to the literature and the desired product was obtained in an overall yield of 71%.<sup>[29]</sup>

The formation of the halogen-bonded dopants **L4**⋯**IC8** and **L4Cu**⋯**IC8** was achieved according to the procedure described in Section 3.1.2. The individual components were separately weighed in a 2: 1 molar ratio of donor and acceptor (Scheme 3.10) and subsequently dissolved in DCM. The solutions were combined, and the solvent removed under reduced pressure. IR measurements confirmed the formation of the supramolecular bond (Figure 7.28).<sup>[139]</sup>



Scheme 3.10: Formation of the halogen-bonded dopants **L4...IC8** and **L4Cu...IC8** and their HTPs in 5CB.

The subsequent determination of the HTP values in 5CB, in fact revealed an increase of the HTP to  $\beta_M = 115 \mu\text{m}^{-1}$  for **L4...IC8** compared to its free pyridine pendant **L4** ( $\beta_M = 85 \mu\text{m}^{-1}$ ) (see also Figure 7.29 and Table 7.3). On the other hand, the HTP of **L4Cu...IC8** was not affected upon formation of the halogen bond and gave the same value as found for the free pyridine analogue ( $\beta_M = 254 \mu\text{m}^{-1}$ ). These findings support the assumption that the formation of the halogen bond induces a small change of the dihedral angle and therefore an increase of the HTP which most likely was the case during the formation of azo donor **29** by Wang *et al.* (see also Figure 3.27).

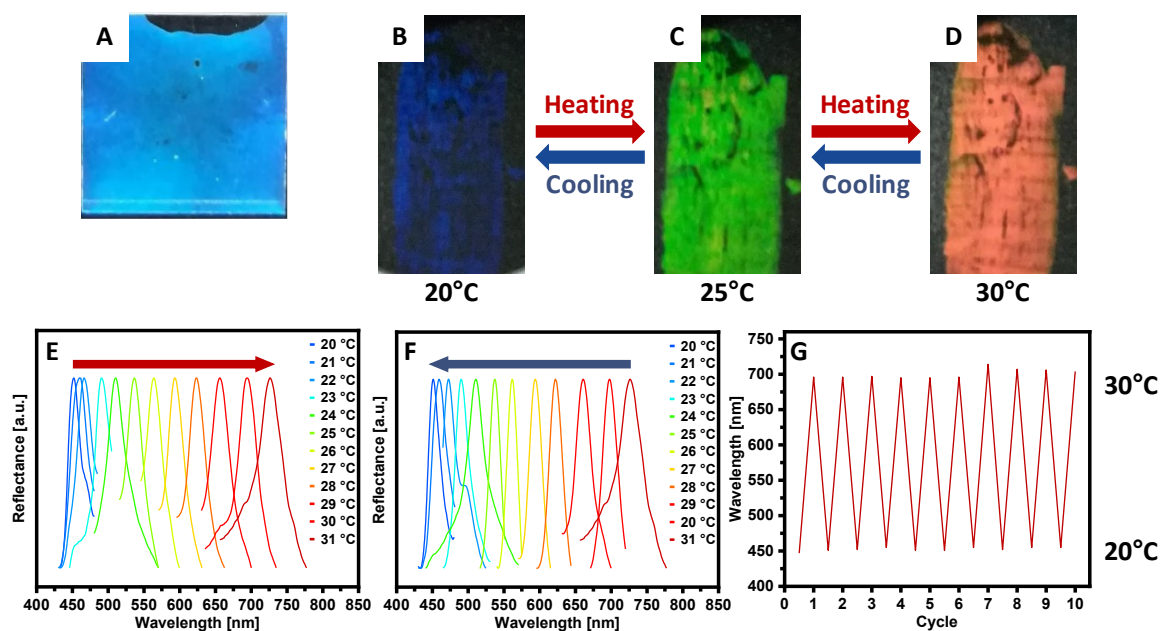


Figure 3.47: Photographs of the structural coloration of E7 doped with 4 mol% **L4...IC8** show the impressive blue reflection color between microscope cover slides (A) and at different temperatures on a black polypropylene substrate (B – D). Temperature variable reflection measurements confirm the full reversibility of the color change (E/F) over several heating and cooling cycles (G).

Doping of E7 with the halogen-bonded dopants revealed the remarkable impact of the XB-capping on the performance of the dopants and the differences between **L4**···**IC8** and **L4Cu**···**IC8**. Despite the improved compatibility of **L4Cu**···**IC8** with the LC host, it was still not possible to successfully induce noticeable structural color as the dopant still precipitated from the LC. On the other hand, halogen-bonded dopant **L4**···**IC8** exhibited an intense blue structural color at room temperature using the same dopant concentration of 4 mol% as previously used for the free pyridine dopant **L4** (Figure 3.47A). Surprisingly, the system also showed a strong temperature dependence of the structural color in a small temperature range which was not observed for the CB dopants. Upon heating from 20 °C, the reflection color shifted across the visible light spectrum from blue (B) through green (C) to a strong red color (D) at 30 °C. Temperature-variable reflectance measurements confirmed the full reversibility of the shift over several heating and cooling cycles (Figure 3.47E–G) making this system an interesting candidate for a small range temperature sensor. Although the temperature dependency of the HTP in general and of binaphthyl dopants in particular is a known phenomenon, such a strong sensitivity was not expected for **L4**···**IC8** and was not observed for binaphthyl dopants **L2** and **L3**.<sup>[102-103, 140, 176, 215, 241]</sup>

### 3.4.2.2 Temperature dependence of the HTP

For biaryl dopants the temperature dependence of the HTP is often described in terms of a conformational equilibrium between two or more local energetic minima<sup>[242]</sup> *Deußen et al.* and *Kakisaka et al.* investigated the temperature dependency of a great variety of binaphthyl derivatives. Their studies revealed that the relative changes of the HTPs were significantly higher for open chain (*transoid*) than for closed-bridge (*cisoid*) derivatives and suggested that the temperature sensitivity of the HTP of binaphthyl dopants is determined by the rotational freedom along the chiral C–C axis. In closed-bridge derivatives, this freedom is significantly reduced.<sup>[103, 241]</sup> In some cases however, the temperature dependence of the HTP could not be explained in this view. Findings reported by *Proni et al.* suggest a more complex process and that the temperature dependence can not only be attributed to the rotation around the chiral C–C axis but rather to all conformational changes of the molecule and the temperature dependent alignment of the dopant with respect to the host molecules.<sup>[242]</sup> Although *Wang et al.* also reported on the temperature dependence of the HTP of halogen-bonded photo-switch **29** (see Figure 3.27), their reported temperature range of almost 25 °C to switch from blue to red was significantly broader than the range of  $\Delta T = 10$  °C found in this study.<sup>[140]</sup>

To get a better understanding of the observed behavior and to understand why this effect is so pronounced for **L4**··**IC8**, the HTP was determined as a function of the reduced temperature (*i.e.* temperature below the clearing point) in 5CB and compared to **L2**, **L3**, and **L4** (Figure 3.48A). Interestingly, **L3** (blue rhombs) showed a completely different behavior as observed for the other dopants. Upon heating, the value constantly increased until it reached a maximum and finally dropped again before transferring to the isotropic state. A possible explanation is the temperature dependent conformational change of the alkyl chain which leads to a changed alignment of the CB host molecules with respect to the dopant.<sup>[242]</sup>

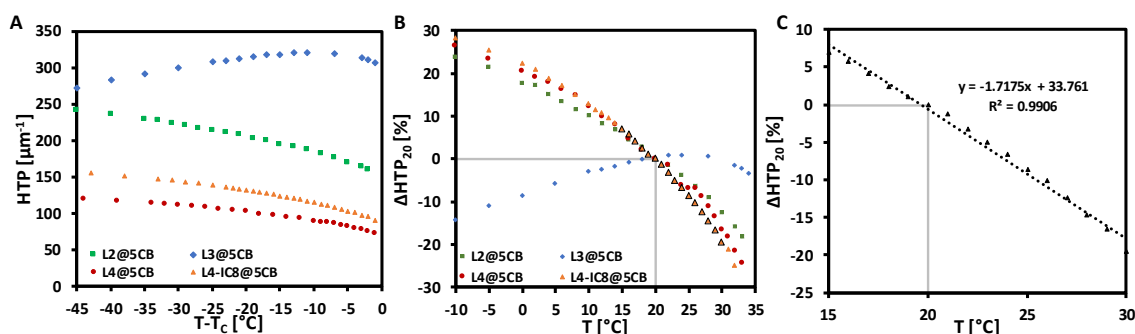


Figure 3.48: Temperature dependence of the HTP values of **L2**, **L3**, **L4**, and **L4**··**IC8** as a function of the reduced temperature (A). Relative changes of the HTP values normalized to 20 °C as a function of the temperature (B). *Quasi*-linear plot of the temperature dependence of **L4**··**IC8** between 15 and 30 °C allows to determine the temperature sensitivity from the slope of the linear fit (C).

On the other hand, the HTPs of **L2**, **L4**, and **L4**··**IC8** constantly decreased with decreasing reduced temperature. The change of the HTP close to the clearing point ( $T - T_c = 0^\circ\text{C}$ ) is due to the collapse of the chiral super structure of the LC material before transferring to the isotropic state and was observed for all investigated samples alike. To reliably compare the temperature sensitivity of dopants **L2**, **L4**, and **L4**··**IC8**, the relative change of the HTP values ( $\Delta\text{HTP}_{20}$ ; normalized to HTP at 20 °C) as a function of the temperature was calculated (Figure 3.48B). In contrast to some literature reports, the results show that the temperature dependent HTP changes are clearly not linear. However, the behavior seems to be quasi-linear over a short temperature range between 15 and 30 °C (black triangles in Figure 3.48B). Such a quasi-linear behavior is an essential factor for the development of reliable high sensitivity photonic temperature sensors. The determination of the slope of the linear fit in this temperature region gives the relative normalized temperature dependence ( $\Delta\text{HTP}_{t,d}$ ). This value indicates the relative HTP change upon a temperature change of the sample of one degree Celsius (°C). The sign and magnitude of  $\Delta\text{HTP}_{t,d}$  determine the efficiency of the system (*e.g.* large value small temperature range) and how it reacts to a temperature change

(e.g. a negative value indicates a red shift upon heating/blue shift upon cooling and *vice versa*) The obtained values of  $\Delta\text{HTP}_{\text{t,d}} = -1.71 \text{ \%}\cdot\text{°C}^{-1}$  for **L4**··**IC8**,  $-1.48 \text{ \%}\cdot\text{°C}^{-1}$  for **L4**, and  $-1.26 \text{ \%}\cdot\text{°C}^{-1}$  for **L2** (see also Figure 7.30A/B and Table 7.4) show that **L4**··**IC8** has the largest (relative) change of the HTP and therefore exhibits the highest temperature sensitivity of the three systems.

### 3.4.3 Conclusions

Halogen bond acceptor dopants **L4** and **L4Cu** have been successfully synthesized. Investigation of the helical twisting powers revealed a similar trend as observed for CB dopants **L2** and **L3** and a significant increase of the HTP upon copper complex formation from  $85 \mu\text{m}^{-1}$  to  $254 \mu\text{m}^{-1}$ . However, during trials to induce structural color in E7 the dopants precipitated due to low solubility in the LC host material.

By capping the polar pyridine moieties with nonpolar halogen bond donator **IC8**, the overall compatibility of the systems could be improved. While dopant **L4Cu**··**IC8** still phase separated in the LC host despite the improved compatibility, 4.0 mol% **L4**··**IC8**@E7 showed a prominent blue structural color. Moreover, the formation of the halogen bond gave a deeper insight into the effects that influence the HTP, suggesting that the formation of the XB leads to a change of the dihedral angle of the binaphthyl core.

Interestingly, the system **L4**··**IC8**@E7 showed a remarkable temperature sensitivity which enabled the shifting of the reflected wavelength across the complete visible light spectrum in a small temperature range between 20 and 30 °C. Although the high temperature sensitivity makes the system irrelevant for the detection of iodine vapors, this may be a new approach for the systematic tweaking of the temperature dependence by halogen bonding. Using a library of XB-donors allows for the manipulation of the temperature sensitivity and the development of novel photonic temperature sensors based on binaphthyl diimine dopants.

These results show that for the development of a reliable photonic temperature sensor based on binaphthyl diimine dopants, not only high HTP values are needed but also a good compatibility with the liquid crystalline host. Moreover, a high relative change of the HTP value in a given temperature range is necessary to exhibit a high sensitivity to small temperature changes.

## 4. Summary and Outlook

The present work provides a deeper understanding of halogen bonding in supramolecular assemblies and its application potential in liquid crystal-based photonic sensors. The systematic investigation of the underlying processes demonstrates that the properties of these materials strongly correlate with the structural changes of the building blocks.

Fluorination of the XB-donor moiety in halogen-bonded liquid crystals considerably influences the polarization of the iodine atom and strength of the formed halogen bond. These both equally follow the trend of the receding number of fluorine substituents ( $D_{11} > D_{21} > \text{etc.}$ ) (Figure 4.1). Computational analyses demonstrate that also the fluorination pattern plays a crucial role. Accordingly, building blocks with an equal number but more fluorine substituents in *ortho*-position show a stronger iodine polarization (e.g.  $D_{21} > D_{31}$ ).

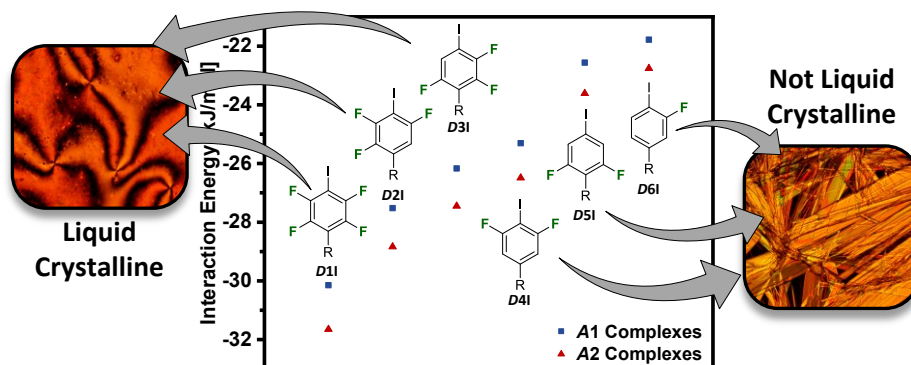


Figure 4.1: Fluorination of the donor moiety in halogen-bonded assemblies leads to a decreasing iodine polarization and XB strength which follow the receding number of fluorine substituents resulting in liquid crystalline properties for assemblies with a minimum number of three fluorine atoms

This polarization and the fluorination pattern itself also affect the thermal properties of the assemblies and can directly be correlated with the decreasing mesophase ranges. Although the stilbazole acceptor prevails over the azo pyridine in terms of XB strength and mesophase stability, the observed mesophase ranges of the assemblies generally decrease with decreasing fluorination degree (*i.e.* XB strength). The results show that at least three fluorine atoms on the donor side are necessary to form XBs with a high enough thermal stability to exhibit liquid crystalline properties at elevated temperatures.

The fluorination of the azo compounds also affects the photo-physical properties of the building blocks. The *cis* lifetimes of building blocks with fluorine atoms in *ortho*-position to the azo linkage turned out to be one order of magnitude longer compared to the lifetimes



possible mechanisms for the chiral induction provide a deeper understanding of the remarkable HTP increase from **L1** to **L2** and **L3**. The transition from a *transoid* to a *cisoid* conformation upon copper complexation of dopants **L2** and **L3** explains the opposing reflection of circularly polarized light of structurally colored samples (Figure 4.2B).

Gas sensing experiments of structurally colored samples of **L3** and **L3Cu** in E7 reveal a noticeable and partly reversible red shift of the reflectance maximum as response to NO<sub>2</sub> gas (Figure 4.2C). The incorporation of a copper ion significantly enhances the sensitivity of the system which allows to detect NO<sub>2</sub> with a concentration of 100 ppm. Reference experiments with other toxic gases prove the remarkable selectivity of the system for NO<sub>2</sub>.

These experiments reveal the application potential of reactive BINIM dopants for photonic gas sensing. The flexibility of the approach allows to selectively manipulate the performance of the sensor system. Future investigations could focus on further improvement of the system's properties by manipulation of the reactive center or compatibility with the host system by selective functionalization (Figure 4.3A). The employment of a series of related transition metal complexes enables the development of a high sensitivity photonic sensor array for the detection of different analytes (Figure 4.3B).

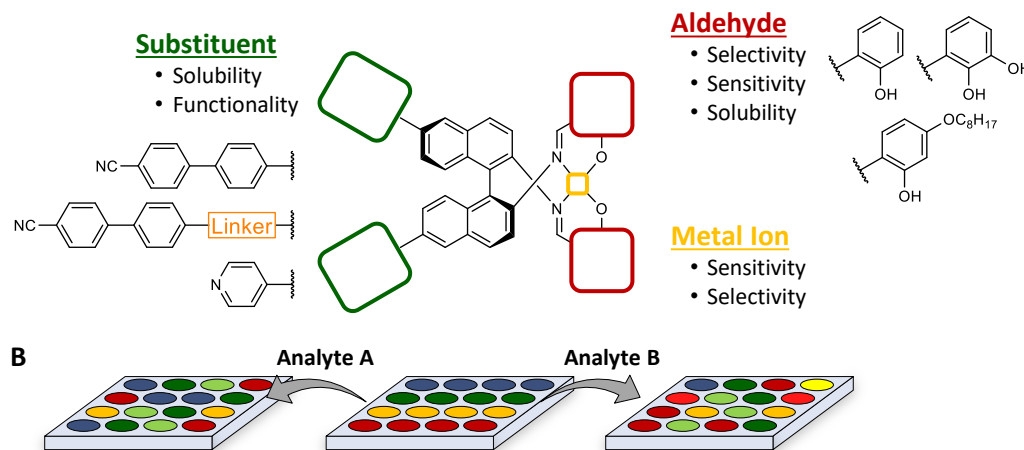


Figure 4.3: Manipulation of the dopant's properties by selective functionalization (A). Sensor array for the selective analyte detection using a series of reactive dopants and samples with different structural colors (B).

The last project of this work combines the findings of the previous studies in the development and investigation of a halogen-bonded binaphthyl-based temperature sensor (Figure 4.4A). The study provides a deeper understanding of the effects of structural changes and supramolecular modifications of a binaphthyl dopant on its helical twisting power and emphasizes the importance of molecular compatibility of dopant and host for the successful

induction of structural color. The results suggest that the HTP of BINIM dopant **L4** is influenced by the dihedral angle of the binaphthyl core which can be manipulated by supramolecular binding of a halogen bond donor to the free pyridine groups. Investigation of the temperature dependence of the HTP and structural color of **L4**⋯**IC8**@E7 provides a deeper understanding of the processes and confirms the complete reversibility of the process over multiple heating and cooling cycles (Figure 4.4B).

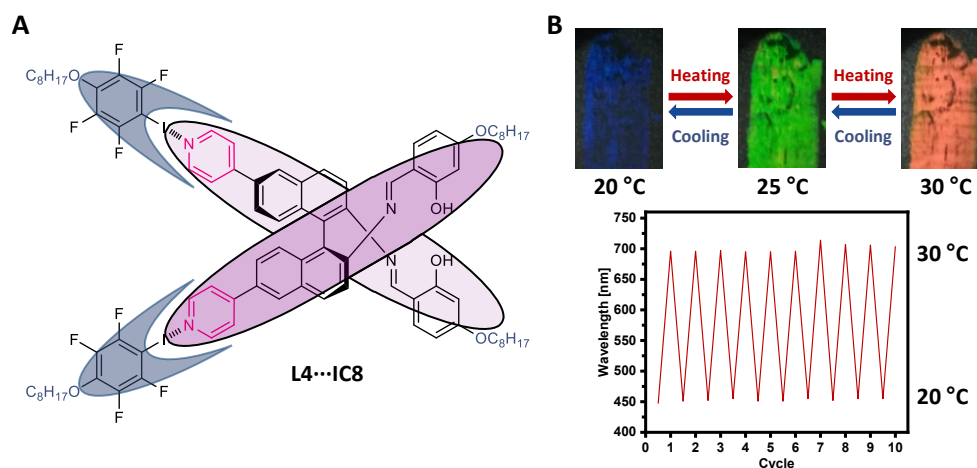


Figure 4.4: Halogen-bonded chiral dopant **L4**⋯**IC8** (A) and temperature dependency of the structural color (B).

These findings pave the way for novel photonic temperature sensors based on halogen-bonded chiral dopants. The use of different XB-donor moieties allows to selectively manipulate the temperature dependence and sensitivity. Suppression of the temperature dependent change of the HTP by bridging dihalogen or dihydrogen bond donors would allow to use this system for the detection of gaseous analytes like iodine vapors

## 5. Zusammenfassung und Ausblick

Die hier vorliegende Arbeit trägt zu einem tieferen Verständnis von Halogenbindungen in supramolekularen Aggregaten bei und offenbart deren Anwendungspotenzial für flüssigkristallbasierte photonische Sensoren. Die systematische Untersuchung der zugrunde liegenden Prozesse zeigt, dass die Eigenschaften dieser Materialien stark mit den strukturellen Veränderungen der Bausteine korrelieren.

Die Fluorierung der XB-Donorbausteine in halogengebundenen Flüssigkristallen führt zu einer erheblichen Beeinflussung der Polarisation des Jodatoms und der Stärke der gebildeten Halogenbindung. Beide folgen gleichermaßen dem Trend der abnehmenden Anzahl an Fluorsubstituenten in der Reihenfolge  $D1I > D2I > \text{etc.}$  (Abbildung 5.1). Theoretische Berechnungen zeigen, dass auch das Fluorierungsmuster dabei eine entscheidende Rolle spielt. Dementsprechend zeigen Bausteine mit einer größeren Anzahl an Fluorsubstituenten in *ortho*-Position eine stärkere Polarisation des Iodatoms (e.g.  $D2I > D3I$ ).

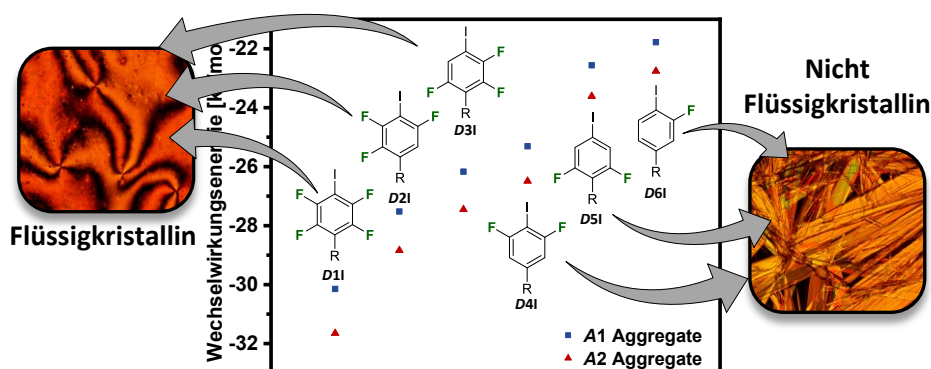


Abbildung 5.1: Die Fluorierung von XB-Donorbausteinen in halogengebundenen Aggregaten führt zu einer schrittweise abnehmenden Polarisation des Iodatoms und der Halogenbindungsstärke. Diese folgen der abnehmenden Anzahl an Fluorsubstituenten, was eine Mindestanzahl von drei Fluoratomen voraussetzt, um flüssigkristalline Eigenschaften auszubilden.

Die sich ändernde Polarisation und das Fluorierungsmuster selbst beeinflussen auch die thermischen Eigenschaften der Aggregate und können direkt mit den abnehmenden Temperaturbereichen der beobachteten Mesophasen in Zusammenhang gebracht werden. Obwohl der Stilbazol-Akzeptor gegenüber dem Azopyridin in Bezug auf XB-Stärke und Mesophasenstabilität besser ist, nehmen die beobachteten Mesophasenbreiten der Aggregate im Allgemeinen mit abnehmendem Fluorierungsgrad (d. h. XB-Stärke) ab. Die Ergebnisse zeigen, dass mindestens drei Fluoratome auf der Donorseite erforderlich sind, damit Halogenbindungen mit einer ausreichend hohen thermischen Stabilität ausgebildet werden, die flüssigkristalline Eigenschaften bei erhöhten Temperaturen ermöglichen.

Das unterschiedliche Fluorierungsmuster der Azoverbindungen hat auch einen entscheidenden Einfluss auf die photo-physikalischen Eigenschaften der Bausteine. So zeigte die Untersuchung der *cis*-Halbwertszeiten der Bausteine, dass Fluoratome in *ortho*-Position zur Azobindung zu Halbwertszeiten führen, die um eine Größenordnung länger sind als die der Komponenten, die dieses Fluorierungsmuster nicht besitzen. Jedoch spielen die *cis*-Lebensdauern der einzelnen Verbindungen für die Lebensdauer der photo-induzierten isotropen Phase der flüssigkristallinen Aggregate nur eine untergeordnete Rolle. Die Ergebnisse deuten darauf hin, dass der Einfluss der Messtemperatur (d. h. Punkt im Phasendiagramm) den Einfluss der einzelnen *cis*-Halbwertszeiten bei den entsprechenden Temperaturen überwiegt.

In einem zweiten Projekt wurde die Induktion von Chiralität in halogengebundenen Flüssigkristallen untersucht. Die thermischen Eigenschaften der chiralen Flüssigkristalle zeigen ähnliche Auswirkungen der Halogenbindungsstärke auf die LC-Eigenschaften, wie sie schon im Fall der achiralen Aggregate beobachtet wurden. Die Absenkung der Übergangstemperaturen durch die chirale Seitenkette führt jedoch zu einem Anstieg der Mesophasenbreiten und zur Ausbildung verschiedener chiraler Mesophasen wie *N\**-, *TGB\**- oder *Sm\**-Phasen. Die Bestimmung der HTP-Werte zeigt, dass die Effizienz des chiralen Transfers nicht vom Fluorierungsgrad oder der Stärke der Halogenbindung beeinflusst wird. Stattdessen ist eine erhebliche Konformationsänderung (z.B. *trans-cis*-Isomerisierung der Azobindung) notwendig, um eine merkliche Änderung des HTP-Wertes herbeizuführen.

Das Wissen, dass eine tatsächliche Konformationsänderung des Moleküls nötig ist, wurde in einer Machbarkeitsstudie verwendet, um ein binaphthylidiimin-basiertes photonisches Sensorsystem (BINIM) für den selektiven Nachweis von NO<sub>2</sub>-Gas zu entwickeln. Die Ergebnisse zeigen, dass BINIM-Dopanden mit ihrer intrinsischen Chiralität als reaktive Dotierstoffe ausgezeichnete Kandidaten sind (Abbildung 5.2A). Die HTP-Werte dieser Additive hängen stark von der Molekülstruktur, dem Diederwinkel des Binaphthylkerns und der strukturellen Ähnlichkeit mit dem LC-Wirt ab. Die Identifizierung zweier möglicher Mechanismen für die chirale Induktion liefern ein tieferes Verständnis des bemerkenswerten HTP-Anstiegs von **L1** zu **L2** und **L3**. Der Übergang von einer *transoiden* zu einer *cisoiden* Konformation des Binaphthylkerns bei der Kupferkomplexierung der Dopanden **L2** und **L3** erklärt die entgegengesetzte Reflexion von links und rechts zirkular polarisiertem Licht (*L*-CPL / *R*-CPL) strukturell farbiger Proben (Abbildung 5.2B).

---

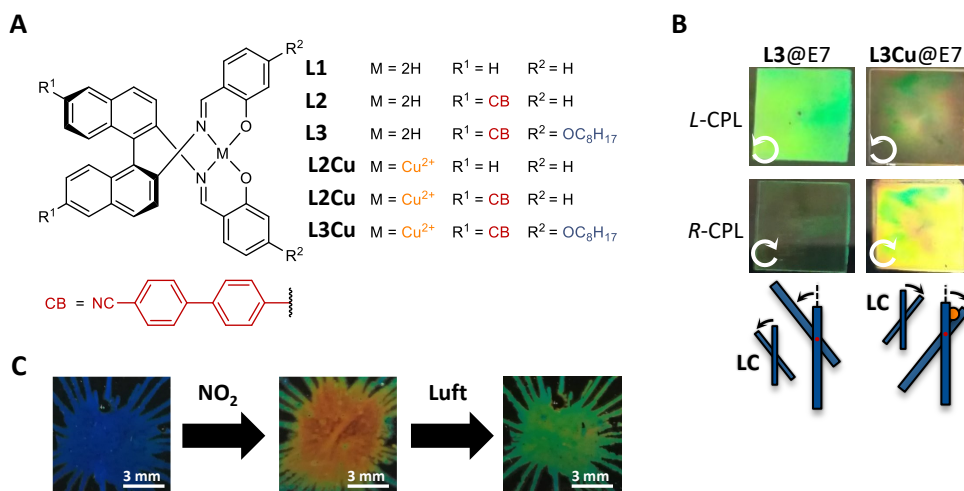


Abbildung 5.2: Molekülstruktur der BINIM-Dopanden (A). Selektive Reflexion von *L*-CPL und *R*-CPL strukturell farbiger Proben von E7 dotiert mit **L3** und **L3Cu** (B). Verschiebung der Reflexionsfarbe bei NO<sub>2</sub>-Exposition und anschließendem Spülen mit Luft (C).

Experimente zur Gasdetektion mit strukturell farbigen Proben von **L3** und **L3Cu** in E7 zeigen eine markante und teilweise reversible Rotverschiebung des Reflexionsmaximums als Reaktion auf NO<sub>2</sub>-Gas (Abbildung 5.2C). Durch den Einbau eines Kupferions wird die Empfindlichkeit des Systems deutlich erhöht, was es ermöglicht NO<sub>2</sub> mit einer Konzentration von 100 ppm selektiv nachzuweisen. Referenzexperimente mit weiteren giftigen Gasen offenbaren die herausragende Selektivität der Systeme für NO<sub>2</sub>.

Diese Experimente zeigen das Anwendungspotenzial dieser reaktiven BINIM-Dopanden für die photonische Gassensorik. Die Flexibilität des Ansatzes erlaubt es, die Leistung des Sensorsystems gezielt zu manipulieren. Zukünftige Untersuchungen könnten sich auf die weitere Verbesserung der Eigenschaften des Systems durch Manipulation des reaktiven Zentrums oder die Kompatibilität mit dem Wirtssystem durch selektive Funktionalisierung konzentrieren (Abbildung 5.3A). Der Einsatz einer Reihe verwandter Übergangsmetallkomplexe ermöglicht die Entwicklung eines hochempfindlichen photonischen Sensorarrays für die Detektion verschiedener Analyte (Abbildung 5.3B).

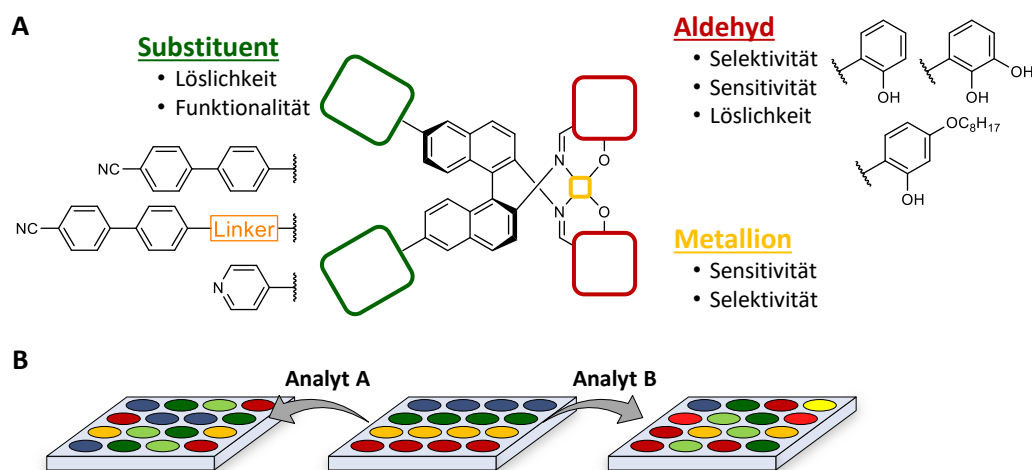


Abbildung 5.3: Manipulation der Eigenschaften des Dopanden durch selektive Funktionalisierung (A). Sensorarray für den selektiven Nachweis von Analyten unter Verwendung einer Reihe von reaktiven Dotierstoffen und Proben mit unterschiedlicher struktureller Färbung (B).

Das letzte Projekt dieser hier vorliegenden Arbeit kombiniert die Ergebnisse der vorangegangenen Studien bei der Entwicklung und Untersuchung eines halogengebundenen Temperatursensors auf Binaphthylbasis (Abbildung 5.4A). Die Studie liefert ein tieferes Verständnis der Auswirkungen von strukturellen Veränderungen und supramolekularen Modifikationen eines Binaphthyl-Dopanden auf die Fähigkeit, Chiralität in einem flüssigkristallinen Wirtssystem zu induzieren. Darüber hinaus wird die Bedeutung der molekularen Kompatibilität von Dotierungsstoff und Wirt für die erfolgreiche Induktion der Strukturfarbe verdeutlicht. Die Ergebnisse deuten darauf hin, dass der HTP-Wert des BINIM-Dopanden **L4** vom Diederwinkel des Binaphthylkerns beeinflusst wird, der durch supramolekulare Bindung eines Halogenbindungsdonators an die freien Pyridingruppen manipuliert werden kann. Die temperaturabhängige Untersuchung des HTP-Wertes und der strukturellen Farbe des Systems **L4**·**IC8@E7** offenbart ein tieferes Verständnis der Prozesse und bestätigt die vollständige Reversibilität des Prozesses über mehrere Heiz- und Kühlzyklen (Abbildung 5.4B).

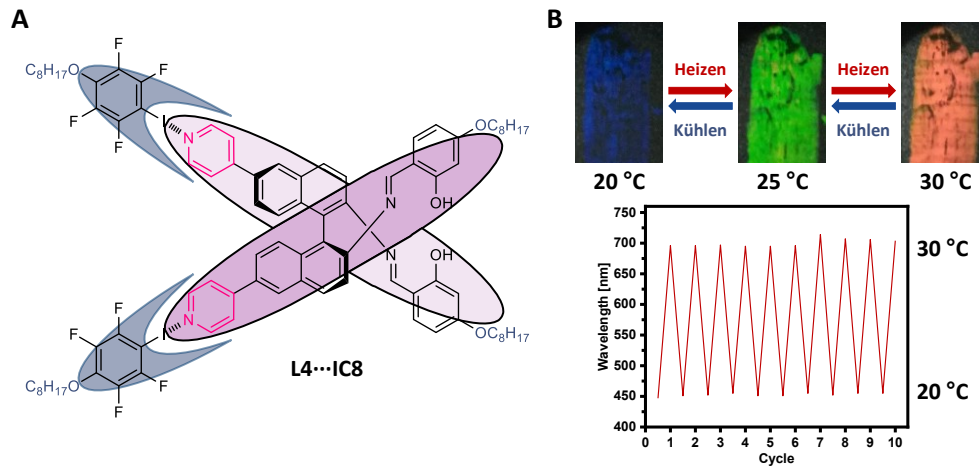


Abbildung 5.4: Molekülstruktur des halogengebundenen, chiralen Dotierstoffs **L4...IC8** (A) und Temperaturabhängigkeit der strukturellen Färbung (B).

Diese Erkenntnisse ebnen den Weg für neuartige photonische Temperatursensoren auf Basis halogengebundener, chiraler Dotierstoffe. Die Verwendung verschiedener XB-Donatoren könnte es ermöglichen, die Empfindlichkeit der Temperaturabhängigkeit zu manipulieren. Die Unterdrückung der temperaturabhängigen Änderung des HTP-Wertes durch die Überbrückung der Pyridine durch Halogen- oder Wasserstoffbrückenbindungsdonatoren würde es erlauben, dieses System z.B. für den Nachweis von Joddämpfen zu verwenden.



---

## 6. Experimental Section

---

### 6.1 Materials and Methods

If not otherwise stated, all reagents used throughout this work were used as obtained by the suppliers. Fluorinated anilines 3-fluoro-4-iodoaniline, 3,5-difluoro-4-iodoaniline, 2,6-difluoro-4-iodoaniline, 2,3,5-trifluoroaniline, 4-bromo-2,3,5,6-tetrafluoroaniline, 4-aminopyridine, (*S*)-(-)-1,1'-binaphthyl-2,2'-diamine, tetrakis(triphenylphosphine-palladium(0)) (Pd(Ph<sub>3</sub>)<sub>4</sub>), and [1,1'-bis(diphenylphosphino)ferrocene]dichloropalladium(II) (Pd(dppf)Cl<sub>2</sub>) were purchased from Fluorochem Ltd.

Gas mixtures of NO<sub>2</sub> (1000 ppm in N<sub>2</sub>), CO (500 ppm in N<sub>2</sub>), H<sub>2</sub>S (500 ppm in N<sub>2</sub>), NO (500 ppm in synthetic air), and synthetic air (20.5% O<sub>2</sub>, 79.5% N<sub>2</sub>) for gas sensing were purchased from Westfalen AG.

2,3,5,6-Tetrafluoroaniline, nitrosyl tetrafluoroborate (BF<sub>4</sub>NO), phenol, sodium nitrite, and silver sulfate (Ag<sub>2</sub>SO<sub>4</sub>) were purchased from abcr GmbH Deutschland.

Magnesium sulfate (MgSO<sub>4</sub>), ammonium chloride (NH<sub>4</sub>Cl), sodium thiosulfate (Na<sub>2</sub>S<sub>2</sub>O<sub>3</sub>), and potassium carbonate were used as received from Bernd Kraft GmbH.

1-Bromooctane, *R*-(-)-citronellylbromide, copper acetate, 4,4'-dibromobiphenyl, 4-pyridinylboronic acid, and pure DMF (99.8%) were purchased from Sigma Aldrich Inc.

4-Cyano-4'-pentylbiphenyl, *N*-bromosuccinimide (NBS), sodium nitrite and TADDOL were purchased from TCI Deutschland GmbH and liquid crystal mixture E7 was ordered from Synthon Chemicals.

2,3,6-Trifluoroaniline and 2,3-dihydroxybenzaldehyd were purchased from Alfa Aeser.

Hydrochloric acid (HCl), sodium chloride (NaCl), and sodium hydrogen carbonate (NaHCO<sub>3</sub>) were purchased from Carl Roth GmbH & Co. Kg.

For thin-layer chromatography (TLC) pre-coated TLC plates POLYGRAM<sup>®</sup> SIL G/UV<sub>254</sub> (40 × 80 mm sheets, 0.2 mm) with fluorescent indicator were used. For purification by flash column chromatography silica gel 60M (40 – 63 μm) or neutral aluminum oxide (ALOX) was used. Both TLC plates and silica gel were purchased from Macherey-Nagel GmbH & Co. KG. For detection of UV active compounds, ultraviolet light with a wavelength of

---

$\lambda_1 = 254$  nm or  $\lambda_2 = 366$  nm was used. Column chromatographic purification was generally performed under aluminum foil.

All analytical grade solvents and triethylamine were used as received from Fisher Scientific™. Technical grade ethyl acetate and cyclohexane were distilled prior to use and stored in brown glass bottles. THF was dried by refluxing over sodium and benzophenone for several hours and was freshly distilled prior to use. Dry DCM was obtained by refluxing over P<sub>2</sub>O<sub>5</sub> for several hours. The dried DCM was distilled and stored over activated molecular sieves (4Å) under argon in brown glass bottles.

## 6.2 Analytical Methods

### 6.2.1 Fourier Transform Infrared Spectroscopy (FT-IR)

IR data were collected using a Bruker Alpha Platinum-ATR spectrometer. Peak positions are denoted in cm<sup>-1</sup>.

### 6.2.2 Mass Spectrometry (MS)

Massspectral data were collected using a Bruker amazon SL for low resolution mass spectra (LRMS) and a MaXis 4G Q-TOF-mass spectrometer for high resolution mass spectra (HRMS). All samples were prepared as ~1 μM solutions in a suitable solvent. All Mass data are denoted as m/z ratios. The respective experiment ID is given as a *italic* digit number for each data set (*e.g.* MS (ESI-pos, *10439*)...).

### 6.2.3 Elemental Analysis (EA)

Elemental analysis data were collected using a Euro EA - CHNSO Elemental Analyser by HEKAtech GmbH.

### 6.2.4 NMR Spectroscopy

NMR Spectra were collected using a Bruker DRX 300 (<sup>1</sup>H: 300 MHz, <sup>19</sup>F: 282 MHz, <sup>13</sup>C: 75 MHz), a Bruker Avance Neo 400 (<sup>1</sup>H, 400 MHz, <sup>19</sup>F: 376 MHz, <sup>13</sup>C: 101 MHz), and a Bruker DRX 600 (<sup>1</sup>H: 600 MHz, <sup>19</sup>F: 565 MHz, <sup>13</sup>C: 151 MHz), respectively. If not otherwise stated, all spectra were recorded at room temperature in deuterated solvents (DMSO-*d*<sub>6</sub>, chloroform-*d*<sub>1</sub> or methanol-*d*<sub>4</sub>). Chloroform-*d*<sub>1</sub> which was used for the measurements of imine compounds was filtered through activated aluminum oxide prior to sample

---

preparation to remove residues of hydrochloric acid. Chemical shifts are stated in parts per million (ppm) referenced to the solvent peak in the  $^1\text{H}$  NMR spectrum (DSMO:  $\delta$  (ppm) = 2.50 ppm,  $\text{CDCl}_3$ :  $\delta$  (ppm) = 7.26 ppm,  $\text{CD}_3\text{OD}$ :  $\delta$  (ppm) = 3.31 ppm) or the solvent peak in the  $^{13}\text{C}$  NMR spectrum (DSMO:  $\delta$  (ppm) = 39.52 ppm,  $\text{CDCl}_3$ :  $\delta$  (ppm) = 77.16 ppm,  $\text{CD}_3\text{OD}$ :  $\delta$  (ppm) = 49.00 ppm). All signals are characterized as singlet (s), doublet (d) triplet (t) quartet (q) or multiplet (m) with their corresponding coupling constants (Hz).

### 6.2.5 UV-Visible Absorption Spectroscopy (UV/Vis)

UV/Vis absorption spectra were collected using a Thermo Fisher Evolution 201. For measurements in solution 400  $\mu\text{L}$  115-QS cuvettes from Hellma Analytics ( $d = 10$  mm) were used. UV/Vis measurements of LC samples were performed by placing a drop of the LC mixture between two quartz glass slides which were then placed in a 100-QS cuvette from Hellma Analytics ( $d = 10$  mm) perpendicular to the light beam.

### 6.2.6 Circular Dichroism Spectroscopy (CD)

CD spectra were collected using a JASCO V-660 CD Spectrometer. Measurements in solution and in the LC phase were performed as described for the UV/Vis measurements

### 6.2.7 Reflection Spectroscopy

Reflection Spectra were collected in the dark, using a LTS420 hotstage from Linkam Scientific Instruments Ltd and an OceanOptics Flame-S-XR1-ES spectrometer equipped with an OceanOptics DH-2000-BAL UV-VIS-NIR light source and an OceanOptics fiberoptic (727-7358-2447). For temperature variable reflection measurements, the liquid crystal sample was coated on a black polypropylene foil.

### 6.2.8 Melting Point (mp.)

Melting points were determined using open end glass tubes in a Büchi B-450 apparatus.

### 6.2.9 Photophysical Properties

The measurements of the photophysical properties were performed by Kim Kuntze, and Matti Virkki in collaboration with the group of Arri Priimägi at the Tampere University of Applied Sciences in Tampere, Finland.

---

*Cis* lifetimes in solution were determined using an Agilent Cary 60 Spectrometer equipped with a custom-built cavity with an Ocean Optics qpod 2e cuvette holder for temperature control and a Prior Scientific Lumen-1600 light source.

The investigation of the photo-switching properties of the liquid crystalline materials was performed using an Avantes AvaSpec-2048L fiber optic spectrometer and an Avantes AvaLight-DH-S-BAL balanced deuterium-halogen light source which was connected to a vertical beam custom-built cavity equipped with a Linkam LinkPad temperature controller and a Thorlabs M405FP1 photoexcitation light source.

For measurements of the birefringence a 676 nm Thorlabs CPS670F laser equipped with a photodiode was used. The LC sample was placed in a planar cell between crossed polarizers and a 676 nm band pass before the diode. The birefringence  $\Delta n$  was calculated using the measured voltage  $U$  and equation

$$\Delta n = \frac{\lambda}{\pi l} \cdot a \cdot \sin \frac{U}{U_0} \quad (10)$$

where  $\lambda$  is the wavelength 676 nm,  $l$  indicates the thickness of the planar cell (2.3  $\mu\text{m}$ ), and  $U_0$  is the voltage with parallelly oriented polarizers (1.29 V). The calculated values of  $\Delta n$  were subsequently normalized as the absolute birefringence of the samples was too high with the used cells.

#### 6.2.10 Differential Scanning Calorimetry (DSC)

DSC data were collected using a DSC3+ 700/866/Argon by Mettler Toledo equipped with a sample robot. Prior to measurement, the samples were ground into powder, placed in 40  $\mu\text{L}$  standard aluminum crucibles and sealed with an aluminum lid. If not otherwise stated, measurements were performed under argon with a heating and cooling rate of 10K/min. Each heating and cooling cycle was repeated three times in order to confirm reproducibility. Plotted data are extracted from the complete data set and display the second heating and cooling cycle of the complete measurement.

#### 6.2.11 Polarized Optical Microscopy (POM)

Polarized optical microscopy images were recorded using a Nikon Eclipse *Ni* optical microscope equipped with an OptixCam Summit K2 OCS-D3K4-14-52X microscope camera and

---

a LTS420 hot stage from Linkam Scientific Instruments Ltd for temperature control. If not otherwise stated all images were taken on untreated glass object and cover slides.

### 6.2.12 Helical Twisting Power (HTP)

The helical twisting power (HTP) of the chiral complexes was determined using the Grandjean-Cano wedge method. The helical pitch  $P$  of the cholesteric liquid crystals was determined by measuring the average disclination line distance in KCRK-07 Cano wedge cells ( $\tan \Theta = 0.01969$ ) purchased from E.H.C. Co., LTD. using the setup for POM measurements (see Chap. 6.2.11). The wedge cells were filled from the side at the bottom of the cell using 2 – 3  $\mu\text{L}$  of LC mixture. If not otherwise stated, all measurements were performed at 20°C. The helical twisting power  $\beta$  was calculated using the equation

$$\beta = \frac{1}{P \cdot \omega} = \frac{1}{2s \cdot \tan\Theta \cdot \omega} \quad (11)$$

where  $\omega$  represents the molar fraction of the chiral dopant,  $s$  represents the experimentally measured distance between the Grandjean lines, and  $\Theta$  indicates the opening angle of the Cano wedge cell (see also Figure 6.1). For weighing of the respective compounds, a Mettler Toledo MX5 microbalance was used.

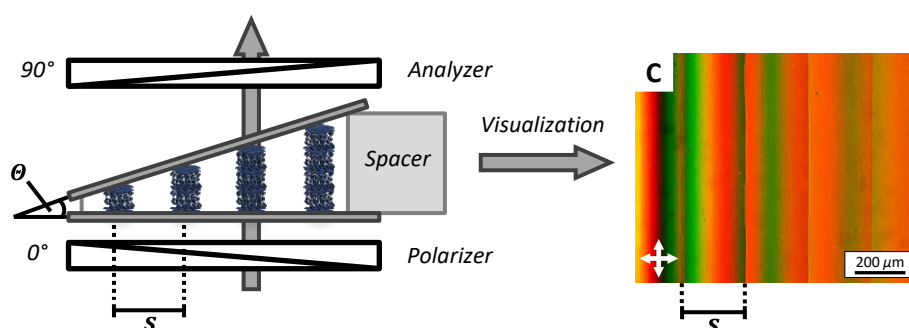


Figure 6.1: Schematic representation of a Grandjean-Cano wedge cell between the two polarizer of a POM and the resulting visual observation of the Grandjean lines under the microscope.

For the preparation of the chiral nematic liquid crystal mixtures for both the determination of the HTP Values and the induction of structural color, the dopant and the nematic liquid crystalline host were weighed separately, subsequently dissolved in DCM and the resulting solutions quantitatively combined. Concluding removal of the solvent by rotary evaporation at 40°C for 10 min yielded the solvent free doped cholesteric liquid crystal mixtures.

For the calculation of the molar ratios of dopant and host, the averaged molar masses of the host mixtures 249.357 g/mol (5CB, CB15), 271.751 g/mol (E7), and 267.012 (E8), respectively, were used.

### **6.2.13 Gassensing**

Gas sensing experiments were performed in collaboration with Professor Peter-Michael Kaul and Lukas Pschyklenk at the University of Applied Sciences Bonn-Rhein-Sieg in Rheinbach.

The experiments were performed at room temperature using a custom-built gas flow reactor equipped with a 3D-printed sample holder for glass cover slides and a reflection probe attached to a Thorlabs SLS301 light source and an OceanOptics Flame S-VIS-NIR-ES spectrometer. The gas flow was measured using a Mesalabs Definer 220 gas flow detector. The gas concentration was adjusted by proportionally adjusting the flow rates of the analyte gas and synthetic air, respectively, using two MKS GE50 A digital mass flow controller (013103RBV020 1000 sccm) from Kurt J. Lesker Company Ltd. while keeping the combined flow rate at 200 mL/min. The gases were mixed prior to entering of the reactor.

The liquid crystal samples were spin coated onto polyvinylalcohol coated and uniaxially wiped microscope cover slides using a Spin 150 spincoater (3000 rpm for 70s) by SPS-Europe B.V. yielding LC films with  $\sim 10\mu\text{m}$  thickness.

### **6.2.14 X-Ray Diffraction (XRD)**

Single crystal x-ray analyses were performed in collaboration with Dr. Christoph Wölper from the Department of Inorganic Chemistry at the Universität Duisburg-Essen using a Bruker D8 Venture and a Bruker D8 Kappa APEX2.

### **6.2.15 Small Angle x-Ray Scattering (SAXS)**

Small angle x-ray scattering measurements were performed in collaboration with Professor Markus Mezger at the Max-Planck-Institute for Polymer Research in Mainz using a Rigaku MicroMax 007 x-ray generator ( $\text{CuK}\alpha$ ) equipped with an Osmic Confocal Max-Flur multi-layer optic. For temperature control a Cryostream 700 from Oxford Cryosystems was used. The samples were melted into glass capillaries ( $\text{Ø} = 0.7\text{ mm}$ ) and placed in a magnetic field using an ALNiCo permanent magnet (2000 Gauss) which was oriented perpendicular to the x-ray beam, to support a better alignment of the liquid crystalline phase. Scattering data was

---

recorded using a Mar345 online image plate detector by MarResearch GmbH with a sample-detector distance of 350 mm and was analyzed using the analysis software Datasqueeze developed by Professor Paul Heiney.

### 6.3 Synthetic Procedures and Analytical Data

#### 6.3.1 Synthesis of Amine Precursor 23

The syntheses were performed according to a modified literature known procedure.<sup>[136]</sup>

##### 6.3.1.1 Synthesis of 2,3,5,6-Tetrafluoro-4-iodoaniline (23a)

Described experiment: ms-172, repeated: ms-138, ms-158, ms-164



To a stirred solution of silver sulfate (8.91 g, 28.6 mmol) and iodine (7.25 g, 28.6 mmol) in ethanol (50 mL), 2,3,5,6-tetrafluoroaniline (3.63 g, 22.0 mmol) dissolved in ethanol (20 mL) was added dropwise over 15 min. The reaction mixture was refluxed for 4 h and the reaction progress followed by TLC. Upon

full conversion, the reaction mixture was filtered, the solvent evaporated, and the obtained residue dissolved in  $\text{CHCl}_3$  (100 mL). The dark solution was washed with saturated  $\text{Na}_2\text{S}_2\text{O}_3$  solution (3x50 mL),  $\text{NaCl}$  (50 mL), and deionized water (50 mL) and dried over  $\text{MgSO}_4$ . Column chromatographic purification (Cy:EA [9:1]) after solvent removal yielded 2,3,5,6-tetrafluoro-4-iodoaniline (**23a**) as pale brown solid (5.12 g, 17.6 mmol, 80%).

Analytical data was in accordance with the literature.<sup>[243]</sup>

$^1\text{H}$  NMR (300 MHz, DMSO):  $\delta$  (ppm) = 6.16 (s, 2H).

$^{19}\text{F}$  NMR (282 MHz, DMSO):  $\delta$  (ppm) = -125.95 – -126.26 (m, 2F), -158.29 – -158.55 (m, 2F).

$^{13}\text{C}$  NMR (151 MHz,  $\text{CDCl}_3$ ):  $\delta$  (ppm) = 152.57 – 150.78 (m), 140.59 (dddd,  $J$  = 240.8, 18.1, 6.9, 3.2), 134.02 (tt,  $J$  = 14.6, 3.9), 58.64 (t,  $J$  = 29.4).

IR:  $\nu$  ( $\text{cm}^{-1}$ ) = 3480, 3387, 2987, 1651, 1615, 1598, 1480, 1408, 1346, 1325, 1305, 1266, 1170, 1152, 1091, 1073, 1047, 972, 913, 828, 798, 712, 641, 600, 433.

MS (APCI-neg, 25079):  $m/z$  (%) = 289.9 (100,  $[\text{M}-\text{H}]^-$ ,  $[\text{C}_6\text{H}_2\text{F}_4\text{IN}-\text{H}]^-$ ; calc.:  $m/z$  = 289.9).

### 6.3.1.2 Synthesis of 2,3,5-Trifluoro-4-iodoaniline (**23b**)

Described experiment: ms-102, repeated: ms-004, ms-013, ms-143



To a stirred solution of silver sulfate (583 mg, 1.87 mmol) and iodine (485 mg, 1.90 mmol) in ethanol (10 mL), 2,3,5-trifluoroaniline (250 mg, 180  $\mu$ L, 1.70 mmol) was added dropwise. The mixture was refluxed for 5.5 h and the reaction progress was monitored by TLC until full conversion. The reaction was quenched with 20 mL of saturated  $\text{Na}_2\text{S}_2\text{O}_3$  solution and ethanol was evaporated. The resulting solution was extracted with  $\text{CHCl}_3$  (4x 10 mL) and dried over  $\text{MgSO}_4$ . Column chromatographic purification (Cy:EA [9:1],  $R_f=0.18$ ) yielded 2,3,5-trifluoro-4-iodoaniline (**23b**) as a pale brown solid (408 mg, 1.5 mmol, 88%).

mp: 79 – 80 °C

$^1\text{H}$  NMR (300 MHz, DMSO):  $\delta$  (ppm) = 6.51 (ddd,  $J = 10.0, 6.9, 2.2$  Hz, 1H), 6.01 (s, 2H).

$^{19}\text{F}$  NMR (282 MHz, DMSO):  $\delta$  (ppm) = -101.79 (t,  $J = 10.0$  Hz, 1F), -120.27 (d,  $J = 22.7$  Hz, 1F), -162.13 (ddd,  $J = 22.7, 9.8, 7.1$  Hz, 1F).

$^{13}\text{C}$  NMR (151 MHz, DMSO):  $\delta$  (ppm) = 157.52 (ddd,  $J = 235.8, 8.4, 2.5$  Hz), 150.14 (ddd,  $J = 238.1, 11.7, 11.1$  Hz), 139.21 (ddd,  $J = 13.7, 11.8, 4.4$  Hz), 135.36 (ddd,  $J = 238.2, 16.9, 3.5$  Hz), 97.78 – 97.45 (m), 52.84 (dd,  $J = 33.6, 27.5$  Hz).

IR:  $\nu$  ( $\text{cm}^{-1}$ ) = 3509, 3410, 3203, 3080, 2960, 2920, 2852, 1641, 1617, 1588, 1505, 1448, 1384, 1312, 1273, 1224, 1181, 1109, 1062, 1011, 824.

MS (APCI-neg, 19168):  $m/z$  (%) = 271.8 (100,  $[\text{M}-\text{H}]^-$ ,  $[\text{C}_6\text{H}_3\text{F}_3\text{IN}-\text{H}]^-$ ; calc.:  $m/z = 271.9$ ).

### 6.3.1.3 Synthesis of 2,3,6-Trifluoro-4-iodoaniline (**23c**)

Described experiment: ms-113



2,3,6-trifluoroaniline (200 mg, 0.14 mL, 1.36 mmol), silver sulfate (555 mg, 1.78 mmol), and iodine (452 mg, 1.78 mmol) were dissolved in ethanol (6 mL) and refluxed for 4 h. The reaction progress was monitored by TLC (Cy:EA [9:1],  $R_f=0.24$ ). The reaction mixture was subsequently cooled to room temperature, filtered, and concentrated to dryness. The resulting precipitate was dissolved in  $\text{CHCl}_3$  (50 mL), washed with  $\text{Na}_2\text{S}_2\text{O}_3$  (sat.) (3x25 mL), brine (25 mL), and  $\text{H}_2\text{O}$  (25 mL) and dried over  $\text{MgSO}_4$ . Column chromatographic purification using (Cy:EA [95:5];  $R_f = 0.35$ ) yielded the *para* iodinated product **23c** (222 mg, 0.81 mmol, 60%).

mp: 60 – 61 °C

$^1\text{H}$  NMR (600 MHz, DMSO):  $\delta$  (ppm) (ppm) = 7.33 (ddd,  $J = 10.2, 5.2, 2.4$  Hz, 1H), 5.78 (s, 2H).

$^{19}\text{F}$  NMR (282 MHz, DMSO):  $\delta$  (ppm) = -125.14 (ddd,  $J$  = 22.9, 10.6, 5.2 Hz, 1F), -134.45 (dd,  $J$  = 22.0, 10.9, 1F), -152.39 (ddd,  $J$  = 22.9, 12.0, 1.5 Hz, 1F).

$^{13}\text{C}$  NMR (151 MHz, DMSO):  $\delta$  (ppm) = 147.44 (ddd,  $J$  = 239.4, 6.9, 2.1 Hz), 147.25 (ddd,  $J$  = 235.0, 11.4, 3.0 Hz), 138.33 (ddd,  $J$  = 243.0, 18.5, 9.0 Hz), 127.93 (ddd,  $J$  = 18.2, 13.4, 2.6 Hz), 118.14 (dt,  $J$  = 22.5, 2.7 Hz), 60.84 (dd,  $J$  = 25.4, 9.4 Hz).

IR:  $\nu$  ( $\text{cm}^{-1}$ ) = 3460, 3375, 1639, 1594, 1497, 1468, 1342, 1326, 1307, 1256, 1202, 1162, 1136, 1069, 936, 846, 793, 714.

MS (APCI-neg, 19169):  $m/z$  (%) = 271.8 (100,  $[\text{M}-\text{H}]^-$ ,  $[\text{C}_6\text{H}_3\text{F}_3\text{IN}-\text{H}]^-$ , calc.:  $m/z$  = 271.9).

### 6.3.2 Synthesis of XB-Donator and XB-Acceptor Precursors

All azo compounds were synthesized according to modified literature known syntheses by *Weiss et al.*<sup>[137]</sup> or *Pfletscher et al.*<sup>[9]</sup>

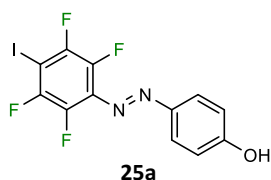
#### 6.3.2.1 General Procedure for the Azo Coupling using $\text{BF}_4\text{NO}$

A solution of the respective fluoro-aniline (1 eq) in acetonitrile (3 mL / mmol aniline) was added dropwise to a solution of nitrosonium tetrafluoroborate (1.2 eq) in acetonitrile (3 mL / mmol aniline) at  $-30\text{ }^\circ\text{C}$  over 15 min. The reaction mixture was stirred at  $-30\text{ }^\circ\text{C}$  for 1 h and a solution of phenol (4 eq) in acetonitrile (2 mL / mmol aniline) was added dropwise over 30 min. After stirring over night at room temperature, water was added, and the mixture was extracted using dichloromethane (6 x 3 mL / mmol aniline). The combined organic layers were dried over  $\text{MgSO}_4$  and the solvent removed under reduced pressure. The residue was taken up in DI water (35 mL / mmol aniline) and refluxed for 15 min. Hot filtration, washing with water, and drying at  $60\text{ }^\circ\text{C}$  overnight yielded the desired product as orange solid

##### 6.3.2.1.1 Synthesis of (*E*)-4'-((2,3,5,6-Tetrafluoro-4-iodophenyl)diazenyl)phenol

###### (25a)

Described experiment: ms-173, repeated: ms-140, ms-159, ms-165



2,3,5,6-tetrafluoro-4-iodoaniline (**23a**) (2.00 g, 6.87 mmol) gave the desired product (*E*)-4'-((2,3,5,6-trifluorophenyl)diazenyl)phenol (**25a**) (2.29 g, 5.78 mmol, 84%).

$^1\text{H}$  NMR (600 MHz, DMSO):  $\delta$  (ppm) = 10.72 (s, 1H), 7.85 – 7.76 (m, 2H), 7.00 – 6.93 (m, 2H).

$^{19}\text{F}$  NMR (282 MHz, DMSO):  $\delta$  (ppm) = -122.09 – -122.38 (m, 2F), -150.41 – -150.69 (m, 2F).

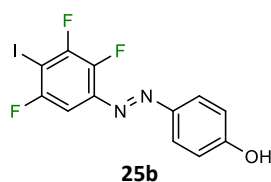
$^{13}\text{C}$  NMR (151 MHz, DMSO):  $\delta$  (ppm) = 163.02 (s), 147.92 – 146.08 (m), 146.00 (s), 140.27 – 138.11 (m), 131.69 (t,  $J$  = 8.9 Hz), 125.73 (s), 116.32 (s), 75.65 (t,  $J$  = 29.8 Hz).

IR:  $\nu$  ( $\text{cm}^{-1}$ ) = 3347, 1590, 1480, 1457, 1425, 1357, 1232, 1203, 1144, 1099, 1072, 1046, 1008, 976, 888, 838, 793, 738, 682, 614, 523, 481, 414.

MS (ESI-pos, 11166):  $m/z$  (%) = 396.9454 (100,  $[\text{M}+\text{H}]^+$ ,  $[\text{C}_{12}\text{H}_5\text{F}_4\text{IN}_2\text{O}+\text{H}]$ , calc.:  $m/z$  = 369.9456).

### 6.3.2.1.2 Synthesis of (*E*)-4'-((2,3,5-Trifluoro-4-iodophenyl)diazenyl)phenol (**25b**)

Described experiment: ms-104, repeated: ms-011, ms-038, ms-043, ms-144



2,3,5-Trifluoro-4-iodoaniline (**23a**) (300 mg, 1.10 mmol) gave the desired product (*E*)-4'-((2,3,5-trifluoro-4-iodophenyl)diazenyl)-phenol (**25b**) as a dark solid (323 mg, 1.4 mmol, 78%) with a reaction time of 3.5 h after addition of phenol (**24**).

mp: 147 – 148 °C

$^1\text{H}$  NMR (600 MHz, DMSO):  $\delta$  (ppm) = 10.65 (s, 1H), 7.88 – 7.80 (m, 2H), 7.38 (ddd,  $J$  = 8.0, 5.6, 2.0 Hz, 1H), 7.00 – 6.94 (m, 2H).

$^{19}\text{F}$  NMR (282 MHz, DMSO):  $\delta$  (ppm) = -98.57 (dd,  $J$  = 12.2, 8.7 Hz, 1F), -115.59 (d,  $J$  = 23.4 Hz, 1F), -151.89 (ddd,  $J$  = 18.3, 12.5, 5.1 Hz, 1F).

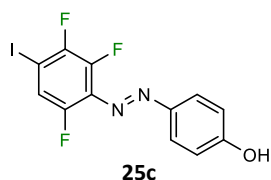
$^{13}\text{C}$  NMR (151 MHz, DMSO):  $\delta$  (ppm) = 162.63 (s), 157.44 (d,  $J$  = 244.5 Hz), 151.34 (ddd,  $J$  = 242.3, 13.1, 8.2 Hz), 145.17 (s), 143.61 (ddd,  $J$  = 256.4, 16.2, 4.2 Hz), 141.22 – 141.07 (m), 125.99 (s), 116.31 (s), 98.54 (dd,  $J$  = 28.3, 3.2 Hz), 76.68 (dd,  $J$  = 34.4, 27.4 Hz).

IR:  $\nu$  ( $\text{cm}^{-1}$ ) = 3348, 3235, 1593, 1523, 1499, 1461, 1440, 1421, 1372, 1334, 1229, 1201, 1143, 1099, 1027, 902, 869, 838, 807, 764, 729, 677.

MS (ESI-neg, 9433):  $m/z$  (%) = 376.9419 (100,  $[\text{M}-\text{H}]^-$ ,  $[\text{C}_{12}\text{H}_6\text{F}_3\text{IN}_2\text{O}-\text{H}]^-$ , calc.:  $m/z$  = 376.9393).

### 6.3.2.1.3 Synthesis of (*E*)-4'-((2,3,6-Trifluoro-4-iodophenyl)diazenyl)phenol (**25c**)

Described experiment: ms-114, repeated: ms-139



2,3,6-Trifluoro-4-iodoaniline (**23a**) (150 mg, 0.55 mmol) gave the desired product (*E*)-4'-((2,3,6-trifluoro-4-iodophenyl)diazenyl)-phenol (**25c**) as a dark solid (172 mg, 0.45 mmol, 83%) with a reaction time of 1 h after each addition step.

mp: 80 °C (decomposition)

$^1\text{H}$  NMR (600 MHz, DMSO):  $\delta$  (ppm) = 10.64 (s, 1H), 7.89 (ddd,  $J$  = 9.8, 4.6, 1.8 Hz, 1H), 7.80 (d,  $J$  = 8.8, 2H), 6.96 (d,  $J$  = 8.8 Hz, 2H).

$^{19}\text{F}$  NMR (282 MHz, DMSO):  $\delta$  (ppm) = -121.92 (ddd,  $J$  = 22.2, 13.1, 4.4 Hz, 1F), -126.63 (dd,  $J$  = 12.4, 10.7 Hz, 1F), -144.49 (d,  $J$  = 22.4 Hz, 1F).

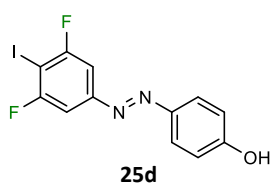
$^{13}\text{C}$  NMR (151 MHz, DMSO):  $\delta$  (ppm) = 162.61 (s), 150.93 (dt,  $J$  = 257.1, 3.1 Hz), 147.65 (ddd,  $J$  = 239.2, 12.5, 3.8 Hz), 146.04 (s), 141.86 (ddd,  $J$  = 262.9, 17.8, 5.6 Hz), 131.34 (dd,  $J$  = 12.2, 7.7 Hz), 125.50 (s), 120.84 (dd,  $J$  = 24.2, 2.8 Hz), 116.24 (s), 83.34 (dd,  $J$  = 25.8, 9.6 Hz).

IR:  $\nu$  ( $\text{cm}^{-1}$ ) = 3526, 3333, 2923, 1604, 1587, 1500, 1475, 1452, 1436, 1374, 1266, 1242, 1206, 1175, 1142, 1088, 1062, 1034, 1008, 971, 841, 799, 738, 660.

MS (ESI-pos, 9606):  $m/z$  (%) = 378.9554 (100,  $[\text{M}+\text{H}]^+$ ,  $[\text{C}_{12}\text{H}_6\text{F}_3\text{IN}_2\text{O}+\text{H}]^+$ , calc.:  $m/z$  = 378.9550).

#### 6.3.2.1.4 Synthesis of (*E*)-4'-((3,5-Difluoro-4-iodophenyl)diazenyl)phenol (**25d**)

Described experiment: ms-099, repeated: ms-027, ms-185



3,5-Difluoro-4-iodoaniline (**23d**) (510 mg, 2.00 mmol) gave the desired product (*E*)-4'-((3,5-difluoro-4-iodophenyl)diazenyl)phenol (**25d**) as a dark solid (300 mg, 0.83 mmol, 42%) with a reaction time of 1 h after each addition step.

mp: 130 °C (decomposition)

$^1\text{H}$  NMR (300 MHz, DMSO):  $\delta$  (ppm) = 10.54 (s, 1H), 7.86 – 7.75 (m, 2H), 7.55 – 7.46 (m, 2H), 7.01 – 6.91 (m, 2H).

$^{19}\text{F}$  NMR (282 MHz, DMSO):  $\delta$  (ppm) = -92.30 (d,  $J$  = 7.2 Hz).

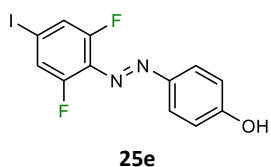
$^{13}\text{C}$  NMR (75 MHz, DMSO):  $\delta$  (ppm) = 162.55 (dd,  $J$  = 244.2, 7.7 Hz), 162.09 (s), 154.06 (t,  $J$  = 8.7 Hz), 144.68 (s), 125.58 (s), 116.13 (s), 105.03 (dd,  $J$  = 26.9, 2.8 Hz), 74.76 (t,  $J$  = 31.4 Hz).

IR:  $\nu$  ( $\text{cm}^{-1}$ ) = 3129, 3098, 1599, 1577, 1503, 1464, 1433, 1404, 1356, 1324, 1281, 1211, 1187, 1143, 1115, 1101, 1042, 1020, 998, 949, 873, 840, 811, 754, 724, 689.

MS (ESI-neg, 9385):  $m/z$  (%) = 358.9510 (100,  $[\text{M}-\text{H}]^-$ ,  $[\text{C}_{12}\text{H}_7\text{F}_2\text{IN}_2\text{O}-\text{H}]^-$ , calc.:  $m/z$  = 358.9487).

#### 6.3.2.1.5 Synthesis of (*E*)-4'-((2,6-Difluoro-4-iodophenyl)diazenyl)phenol (**25e**)

Described experiment: ms-097, repeated: ms-053, ms-196



3,6-Difluoro-4-iodoaniline (**23e**) (510 mg, 2.00 mmol) gave the desired product (*E*)-4'-((2,6-difluoro-4-iodophenyl)diazenyl)phenol (**25e**) (260 mg, 0.72 mmol, 36%) with a reaction time of 3 h after addition of phenol (**24**).

mp: 90 °C (decomposition)

$^1\text{H}$  NMR (300 MHz, DMSO):  $\delta$  (ppm) = 10.54 (s, 1H), 7.74 (dd,  $J$  = 11.6, 8.6 Hz, 4H), 6.92 (t,  $J$  = 11.1 Hz, 2H).

$^{19}\text{F}$  NMR (282 MHz, DMSO):  $\delta$  (ppm) = -121.84 (d,  $J$  = 8.5 Hz).

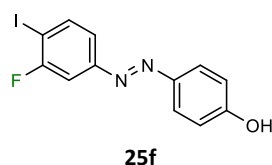
$^{13}\text{C}$  NMR (75 MHz, DMSO):  $\delta$  (ppm) = 162.15 (s), 154.37 (dd,  $J$  = 260.3, 4.8 Hz), 150.01 – 149.74 (m), 146.04 (s), 125.18 (s), 122.37 – 121.47 (m), 116.07 (s), 77.04 – 76.23 (m).

IR:  $\nu$  ( $\text{cm}^{-1}$ ) = 3088, 3044, 1598, 1573, 1503, 1469, 1428, 1408, 1370, 1280, 1224, 1203, 1185, 1139, 1101, 1081, 1038, 923, 887, 837, 756, 729.

MS (ESI-pos, 9386):  $m/z$  (%) = 358.9513 (100,  $[\text{M}+\text{H}]^+$ ,  $[\text{C}_{12}\text{H}_7\text{F}_2\text{IN}_2\text{O}]^+$ , calc.:  $m/z$  = 358.9487).

#### 6.3.2.1.6 Synthesis of (*E*)-4'-((3-Fluoro-4-iodophenyl)diazenyl)phenol (**25f**)

Described experiment: ms-123, repeated: ms-063



3-Fluoro-4-iodoaniline (**23f**) (202 mg, 0.85 mmol) gave the desired product (*E*)-4'-((3-fluoro-4-iodophenyl)diazenyl)phenol (**25f**) as a brown solid (45 mg, 0.13 mmol, 15%) with a reaction time of 3 h after addition of phenol (**24**).

mp: 113 – 114 °C

$^1\text{H}$  NMR (300 MHz, DMSO):  $\delta$  (ppm) = 10.46 (s, 1H), 8.04 (dd,  $J$  = 8.3, 6.9 Hz, 1H), 7.85 – 7.79 (m, 2H), 7.60 (dd,  $J$  = 9.1, 2.1 Hz, 1H), 7.49 (dd,  $J$  = 8.3, 2.1 Hz, 1H), 6.99 – 6.92 (m, 2H).

$^{19}\text{F}$  NMR (282 MHz, DMSO):  $\delta$  (ppm) = -93.65 (dd,  $J$  = 8.6, 7.4).

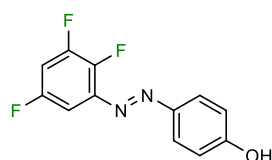
$^{13}\text{C}$  NMR (151 MHz, DMSO):  $\delta$  (ppm) = 161.81 (d,  $J$  = 243.8 Hz), 161.73 (s), 153.72 (d,  $J$  = 6.4 Hz), 144.91 (s), 139.91 (d,  $J$  = 2.5 Hz), 125.36 (s), 120.88 (d,  $J$  = 2.9 Hz), 116.10 (s), 107.66 (d,  $J$  = 25.6 Hz), 84.76 (d,  $J$  = 26.7 Hz).

IR:  $\nu$  ( $\text{cm}^{-1}$ ) = 3243, 3084, 3028, 1589, 1523, 1503, 1486, 1459, 1431, 1397, 1227, 1144, 1101, 1025, 980, 964, 868, 839, 813, 750, 719, 688.

MS (ESI-neg, 9654):  $m/z$  (%) = 340.9609 (100,  $[\text{M}-\text{H}]^-$ ,  $[\text{C}_{12}\text{H}_8\text{FIN}_2\text{O}]^-$ , calc.:  $m/z$  = 340.9582).

#### 6.3.2.1.7 Synthesis of (*E*)-4'-((2,3,5-Trifluorophenyl)diazenyl)phenol

Described experiment: ms-216



2,3,5-trifluoroaniline (250 mg, 1.70 mmol) gave the desired product (*E*)-4'-((2,3,5-trifluorophenyl)diazenyl)phenol as a brown solid (226 mg, 1.00 mmol, 59%) with a reaction time of 1 h after addition of phenol (**24**).

mp: >140°C (decomposition)

$^1\text{H}$  NMR (400 MHz, DMSO):  $\delta$  (ppm) = 10.63 (s, 1H), 7.88 – 7.79 (m, 2H), 7.73 – 7.62 (m, 1H), 7.34 – 7.25 (m, 1H), 7.00 – 6.94 (m, 2H).

$^{19}\text{F}$  NMR (282 MHz, DMSO):  $\delta$  (ppm) = -113.59 – -114.28 (m, 1F), -133.62 (dd,  $J$  = 21.0, 10.6 Hz, 1F), -154.07 – -155.14 (m, 1F).

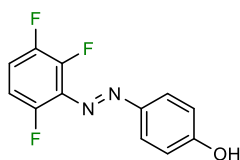
$^{13}\text{C}$  NMR (101 MHz, DMSO):  $\delta$  (ppm) = 162.53 (s), 157.21 (ddd,  $J$  = 245.0, 12.1, 3.2 Hz), 150.63 (dt,  $J$  = 248.0, 13.6 Hz), 145.20 (s), 144.23 (ddd,  $J$  = 252.5, 13.9, 4.1 Hz), 141.62 – 141.24 (m), 125.94 (s), 116.27 (s), 107.04 (dd,  $J$  = 29.5, 21.9 Hz), 99.45 (dd,  $J$  = 25.3, 3.5 Hz).

IR:  $\nu$  ( $\text{cm}^{-1}$ ) = 3266, 3185, 3099, 3066, 3004, 1622, 1591, 1493, 1454, 1407, 1361, 1332, 1276, 1203, 1142, 1104, 1015, 997, 852, 839, 816, 774, 655, 582, 534, 517, 495, 444.

MS (ESI-pos, 14505):  $m/z$  (%) = 253.0589 (100,  $[\text{M}+\text{H}]^+$ ,  $[\text{C}_{12}\text{H}_7\text{F}_3\text{N}_2\text{O}+\text{H}]^+$ , calc.:  $m/z$  = 253.0583).

### 6.3.2.1.8 Synthesis of (*E*)-4'-((2,3,6-Trifluorophenyl)diazenyl)phenol

Described experiment: se-057



2,3,6-trifluoroaniline (200 mg, 1.36 mmol) gave the desired product (*E*)-4'-((2,3,6-trifluorophenyl)diazenyl)phenol as a brown solid (243 mg, 0.96 mmol, 67%) with a reaction time of 1 h after addition of phenol (**24**).

mp: 124 – 125 °C

$^1\text{H}$  NMR (400 MHz,  $\text{CDCl}_3$ ):  $\delta$  (ppm) = 7.94 – 7.87 (m, 2H), 7.14 (tdd,  $J$  = 9.4, 8.2, 4.7 Hz, 1H), 7.02 – 6.92 (m, 3H), 5.45 (s, 1H).

$^{19}\text{F}$  NMR (376 MHz,  $\text{CDCl}_3$ ):  $\delta$  (ppm) = -126.91 – -127.15 (m, 1F), -141.10 – -141.34 (m, 1F), -145.67 – -145.91 (m, 1F).

$^{13}\text{C}$  NMR (101 MHz,  $\text{CDCl}_3$ ):  $\delta$  (ppm) = 159.65 (s), 152.95 – 150.18 (m), 147.92 (s), 147.75 (ddd,  $J$  = 246.1, 12.0, 3.7 Hz), 143.93 (dd,  $J$  = 260.3, 5.2 Hz), 132.99 – 132.46 (m), 125.70 (s), 116.26 (dd,  $J$  = 20.1, 10.3 Hz), 116.07 (s), 111.33 (ddd,  $J$  = 22.6, 6.9, 4.5 Hz).

IR:  $\nu$  ( $\text{cm}^{-1}$ ) = 3569, 3320, 3023, 1585, 1492, 1462, 1442, 1412, 1388, 1276, 1249, 1228, 1195, 1135, 1105, 1021, 957, 872, 843, 808, 751, 713, 640, 609, 553, 512, 485, 465, 420.

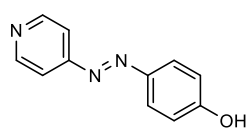
MS (ESI-pos, 12435):  $m/z$  (%) = 253.0579 (100,  $[\text{M}+\text{H}]^+$ ,  $[\text{C}_{12}\text{H}_7\text{F}_3\text{N}_2\text{O}+\text{H}]^+$ , calc.:  $m/z$  = 253.0583).

### 6.3.2.2 General procedure for the azo coupling using NaNO<sub>2</sub>

The respective amine (1.2 eq) was dissolved in 7 M HCl (1.5 mL / mmol amine) and cooled to -20 °C. A solution of phenol (1 eq) and sodium nitrite (1.1 eq) in of 10% NaOH (1.5 mL / mmol amine) added dropwise to the cooled solution over 20 min. To prevent freezing, the temperature was gradually increased to -15 °C during addition of the phenol solution. After additional stirring at room temperature for 1 h, the reaction mixture was neutralized using 10% NaOH yielding the desired crude product. Which was further purified using reflux in water or column chromatography.

#### 6.3.2.2.1 Synthesis of (*E*)-4-(Pyridinyl)-diazenylphenol

Described experiment: ms-121



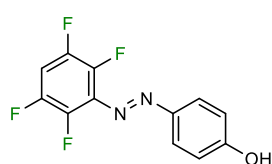
4-Aminopyridine (1.00 g, 10.63 mmol) gave the desired product (*E*)-4-(pyridinyl)-diazenylphenol as an orange solid (1.52 g, 7.63 mmol, 86%) without further purification.

Analytical data was in accordance with the literature.<sup>[9]</sup>

<sup>1</sup>H NMR (300 MHz, DMSO): δ (ppm) = 10.58 (s, 1H), 8.81 – 8.71 (m, 2H), 7.91 – 7.81 (m, 2H), 7.71 – 7.63 (m, 2H), 7.02 – 6.92 (m, 2H).

#### 6.3.2.2.2 Synthesis of (*E*)-4-((2,3,5,6-Tetrafluorophenyl)diazenyl)phenol

Described experiment: ms-050



2,3,5,6-Tetrafluoroaniline (1.00 g, 6.05 mmol) gave the desired product (*E*)-4-((2,3,5,6-tetrafluorophenyl)diazenyl)phenol as brown solid (335 mg, 1.24 mmol, 21%) after column chromatographic purification using (Cy:EA [9:1] R<sub>f</sub> = 0.3) on silica.

mp: 120 – 121 °C

<sup>1</sup>H NMR (600 MHz, DMSO): δ (ppm) = 10.72 (s, 1H), 7.99 – 7.91 (m, 1H), 7.85 – 7.79 (m, 2H), 7.00 – 6.95 (m, 2H).

<sup>19</sup>F NMR (565 MHz, DMSO): δ (ppm) = -139.36 – -139.50 (m), 2F, -152.55 (ddd, *J* = 21.7, 11.9, 8.2 Hz, 2F).

<sup>13</sup>C NMR (151 MHz, DMSO, 70 °C): δ (ppm) = 163.00 (s), 145.88 (s), 146.68 – 144.82 (m), 140.54 – 138.61 (m), 132.30 (t, *J* = 8.9 Hz), 125.73 (s), 116.30 (s), 106.08 (t, *J* = 23.6 Hz).

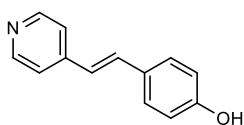
IR:  $\nu$  (cm<sup>-1</sup>) = 3566, 3398, 3086, 1587, 1508, 1496, 1462, 1442, 1424, 1375, 1352, 1277, 1230, 1202, 1176, 1147, 1117, 1100, 1069, 1036, 992, 956, 874, 835, 808, 738, 719.

MS (ESI-neg, 8853):  $m/z$  (%) = 269.0332 (100, [M-H]<sup>-</sup>, [C<sub>12</sub>H<sub>6</sub>F<sub>4</sub>N<sub>2</sub>O-H]<sup>-</sup>, calc.:  $m/z$  = 269.0333).

### 6.3.2.3 Synthesis of (*E*)-(2-(4-Pyridinyl)ethenyl)phenol

Described experiment: ms-155

The Synthesis of (*E*)-(2-(4-pyridinyl)ethenyl)phenol was performed according to a literature known procedure.<sup>[244]</sup>



To a solution of 4-hydroxybenzaldehyde (8.2 g, 67.1 mmol) in 30 mL acetic anhydride, 4-methylpyridine (5.00 g, 53.7 mmol) was added dropwise. The mixture was refluxed for 24 h, cooled to room temperature, poured into 250 mL of ice water, and stirred for 2 h. The obtained precipitate was filtered off and refluxed in an ethanolic solution (100 mL) of potassium hydroxide (5.0 g). Adjusting the pH to 5-6 using acetic acid yielded a yellow precipitate which was filtered off. Column chromatographic purification (Cy:EA, [9:1],  $R_f$  = 0.3) yielded (*E*)-(2-(4-pyridinyl)ethenyl)phenol as pale yellow solid (578 mg, 2.67 mmol, 5%).

Analytical data was in accordance with the literature.

<sup>1</sup>H NMR (300 MHz, DMSO):  $\delta$  (ppm) = 9.74 (s, 1H), 8.52 – 8.46 (m, 2H), 7.53 – 7.47 (m, 4H), 7.43 (d,  $J$  = 16.5 Hz, 1H), 7.00 (d,  $J$  = 16.5 Hz, 1H), 6.83 – 6.76 (m, 2H).

### 6.3.3 Synthesis of XB-Donator and XB-Acceptor Molecules

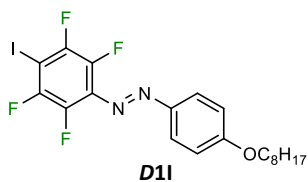
#### General Procedure for the alkylation of phenols

The appropriate phenol (1 eq) and K<sub>2</sub>CO<sub>3</sub> (1.5 eq) were dissolved in DMF (5–10mL). 1-Bromooctane or (*S*)-citronellylbromide (1 eq) was added, and the mixture was stirred at 90 °C for overnight until full conversion was observed by TLC (Cy:EA). The hot solution was subsequently poured into deionized water (50 mL/mmol) yielding an orange precipitate. The Mixture was extracted with EA (5x25 mL/mmol bromide) and the combined organic layers washed with 5% NaHCO<sub>3(aq)</sub> (25 mL/mmol bromide) and brine (25 mL/mmol bromide). Drying over MgSO<sub>4</sub> and evaporation to dryness yielded the crude product which was purified by column chromatography.

### 6.3.3.1 Synthesis of Achiral XB-Donator and XB-Acceptor Molecules

#### 6.3.3.1.1 (*E*)-1-(4'-(Octyloxy)phenyl)-2-(2,3,5,6-tetrafluoro-4-iodophenyl)diazene (**D11**)

Described experiment: ms-166, repeated: ms-142, ms-160, ms-ST020



(*E*)-4'-((2,3,5,6-tetrafluoro-4-iodophenyl)diazenyl)phenol (**25a**) (600 mg, 1.51 mmol) gave (*E*)-1-(4'-(octyloxy)phenyl)-2-(2,3,5,6-tetrafluoro-4-iodophenyl)diazene (**D11**) (610 mg, 1.20 mmol, 80%) using *n*-hex ( $R_f = 0.4$ ) as eluent and ALOX as stationary phase.

mp: 78 – 79 °C

$^1\text{H NMR}$  (300 MHz,  $\text{CDCl}_3$ ):  $\delta$  (ppm) = 7.98 – 7.89 (m, 2H), 7.06 – 6.97 (m, 2H), 4.06 (t,  $J = 6.6$  Hz, 2H), 1.89 – 1.72 (m, 2H), 1.54 – 1.20 (m, 10H), 0.90 (t,  $J = 6.8$  Hz, 3H).

$^{19}\text{F NMR}$  (282 MHz,  $\text{CDCl}_3$ ):  $\delta$  (ppm) = -120.58 – -120.87 (m, 2F), -149.47 – -149.76 (m, 2F).

$^{13}\text{C NMR}$  (151 MHz,  $\text{CDCl}_3$ ):  $\delta$  (ppm) = 163.64 (s), 147.59 (s), 147.57 (ddt,  $J = 245.4, 13.9, 4.7$ ), 139.87 (ddt,  $J = 261.3, 16.8, 3.8$ ), 133.25 (t,  $J = 9.0$ ), 125.84 (s), 122.57 (s), 115.04 (s), 71.66 (t,  $J = 28.0$ ), 68.73 (s), 31.95 (s), 29.47 (s), 29.37 (s), 29.24 (s), 26.12 (s), 22.80 (s), 14.25 (s).

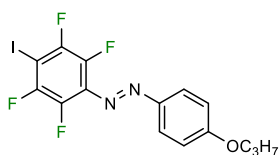
IR:  $\nu$  ( $\text{cm}^{-1}$ ) = 3073, 3055, 2945, 2924, 2857, 1601, 1578, 1499, 1472, 1447, 1408, 1375, 1329, 1300, 1250, 1213, 1177, 1144, 1111, 1042, 1028, 997, 980, 958, 889, 841, 810, 797, 762, 741, 723.

MS (ESI-pos, 11138):  $m/z$  (%) = 509.0703 (100,  $[\text{M}+\text{H}]^+$ ,  $[\text{C}_{20}\text{H}_{21}\text{F}_4\text{IN}_2\text{O}+\text{H}]^+$ , calc.:  $m/z = 509.0708$ ).

CHN: calc. (%)  $\text{C}_{20}\text{H}_{21}\text{F}_4\text{IN}_2\text{O}$ : C 47.3, H 4.16, N 5.51; found (%): C 48.1, H 4.44, N 6.18.

#### 6.3.3.1.2 (*E*)-1-(4'-(Propyloxy)phenyl)-2-(2,3,5,6-tetrafluoro-4-iodophenyl)diazene

Described experiment: ms-095



(*E*)-4'-((2,3,5,6-tetrafluoro-4-iodophenyl)diazenyl)phenol (**25a**) (140 mg, 0.35 mmol) and iodopropane (35  $\mu\text{L}$ , 0.36 mmol) gave (*E*)-1-(4'-(propyloxy)phenyl)-2-(2,3,5,6-tetrafluoro-4-iodophenyl)-

diazene (49 mg, 0.11 mmol, 31%) using *n*-hexane as eluent ( $R_f = 0.35$ ) for flash column chromatographic purification on silica.

$^1\text{H NMR}$  (300 MHz,  $\text{CDCl}_3$ ):  $\delta$  (ppm) = 7.99 – 7.89 (m, 2H), 7.08 – 6.96 (m, 2H), 4.03 (t,  $J = 6.6$  Hz, 2H), 1.94 – 1.74 (m, 2H), 1.07 (t,  $J = 7.4$  Hz, 3H).

$^{19}\text{F NMR}$  (282 MHz,  $\text{CDCl}_3$ ):  $\delta$  (ppm) = -120.59 – -120.85 (m, 2F), -149.52 – -149.78 (m, 2F).

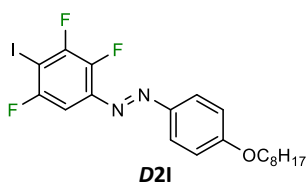
$^{13}\text{C}$  NMR (101 MHz,  $\text{CDCl}_3$ ):  $\delta$  (ppm) = 163.63 (s), 147.60 (s), 149.24 – 145.56 (m), 141.51 – 138.08 (m), 133.26 (t,  $J = 9.4$  Hz), 125.85 (s), 115.05 (s), 71.68 (t,  $J = 27.8$  Hz), 70.17 (s), 22.60 (s), 10.60 (s).

MS (ESI-pos, 9382):  $m/z$  (%) = 438.9935 (100,  $[\text{M}+\text{H}]^+$ ,  $[\text{C}_{15}\text{H}_{11}\text{F}_4\text{IN}_2\text{O}+\text{H}]^+$ , calc.:  $m/z = 438.9925$ ).

CHN: calc. (%)  $\text{C}_{15}\text{H}_{11}\text{F}_4\text{IN}_2\text{O}$ : C 41.1, H 2.53, N 6.39; found (%): C 45.0, H 3.69, N 6.53.

### 6.3.3.1.3 (*E*)-1-(4'-(Octyloxy)phenyl)-2-(2,3,5-trifluoro-4-iodophenyl)diazene (**D2I**)

Described experiment: ms-145, repeated: ms-015, ms-045, ms-124



(*E*)-4'-((2,3,5-trifluoro-4-iodophenyl)diazenyl)phenol (**25b**)

(910 mg, 2.41 mmol) gave 1.10 g (2.24 mmol, 93%)

(*E*)-1-(4'-(octyloxy)-phenyl)-2-(2,3,5-trifluoro-4-iodophenyl)diazene (**D2I**) using DCM: Cy ([99:1]  $R_f = 0.3$ ) on silica for column chromatographic purification.

mp: 76 – 77 °C

$^1\text{H}$  NMR (600 MHz, DMSO):  $\delta$  (ppm) = 7.95 – 7.90 (m, 2H), 7.44 – 7.38 (m, 1H), 7.17 – 7.12 (m, 2H), 4.12 (t,  $J = 6.5$  Hz, 2H), 1.80 – 1.73 (m, 2H), 1.49 – 1.41 (m, 2H), 1.39 – 1.18 (m, 8H), 0.88 (t,  $J = 7.0$ , 3H).

$^{19}\text{F}$  NMR (282 MHz, DMSO):  $\delta$  (ppm) = -98.45 (dd,  $J = 12.7, 8.5$ ), -115.43 (dd,  $J = 23.5, 1.4$ ), -151.67 (ddd,  $J = 23.3, 12.7, 5.5$ ).

$^{13}\text{C}$  NMR (151 MHz, DMSO):  $\delta$  (ppm) = 162.66 (s), 145.89 (s), 125.22 (s), 115.13 (s), 98.58 (dd,  $J = 28.5, 3.3$  Hz), 68.06 (s), 30.82 (s), 28.29 (s), 28.21 (s), 28.19 (s), 25.06 (s), 21.63 (s), 13.45 (s).

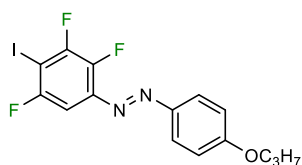
IR:  $\nu$  ( $\text{cm}^{-1}$ ) = 3093, 3073, 2992, 2856, 1738, 1599, 1577, 1499, 1466, 1429, 1407, 1390, 1338, 1317, 1297, 1250, 1207, 1141, 1110, 1030, 999, 943, 898, 872, 838, 808, 758, 722, 679.

MS (ESI-pos, 9652):  $m/z$  (%) = 491.0807 (100,  $[\text{M}+\text{H}]^+$ ,  $[\text{C}_{20}\text{H}_{22}\text{F}_3\text{IN}_2\text{O}+\text{H}]^+$ , calc.:  $m/z = 491.0802$ ).

CHN: calc. (%)  $\text{C}_{20}\text{H}_{22}\text{F}_3\text{IN}_2\text{O}$ : C 49.0, H 4.52, N 5.71; found (%): C 49.7, H 4.81, N 6.43.

### 6.3.3.1.4 (*E*)-1-(4'-(Propyloxy)phenyl)-2-(2,3,5-trifluoro-4-iodophenyl)diazene

Described experiment: ms-108



(*E*)-4'-((2,3,5-trifluoro-4-iodophenyl)diazenyl)phenol (**25b**)

(150 mg, 0.40 mmol) and iodopropane (39  $\mu\text{L}$ , 0.40 mmol) gave

(*E*)-1-(4'-(propyloxy)phenyl)-2-(2,3,5-trifluoro-4-iodophenyl)diazene (121 mg, 0.28 mmol, 73%) using Cy:DCM ([1:1]  $R_f = 0.3$ ) as eluent for column chromatographic purification on silica.

$^1\text{H}$  NMR (300 MHz,  $\text{CDCl}_3$ ):  $\delta$  (ppm) = 7.99 – 7.91 (m, 2H), 7.36 (ddd,  $J$  = 8.3, 5.6, 2.3 Hz, 1H), 7.05 – 6.97 (m, 2H), 4.02 (t,  $J$  = 6.6 Hz, 2H), 1.93 – 1.78 (m, 2H), 1.07 (t,  $J$  = 7.4 Hz, 3H).

$^{19}\text{F}$  NMR (282 MHz,  $\text{CDCl}_3$ ):  $\delta$  (ppm) = -98.13 (dd,  $J$  = 12.2, 8.6, 1F), -113.89 (d,  $J$  = 21.4, 1F), -150.88 (ddd,  $J$  = 21.3, 12.4, 5.5, 1F).

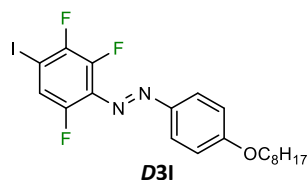
$^{13}\text{C}$  NMR (101 MHz,  $\text{CDCl}_3$ ):  $\delta$  (ppm) = 163.28 (s), 159.27 – 156.15 (m), 153.36 – 150.68 (m), 146.80 (s), 146.17 – 143.23 (m), 142.38 – 142.00 (m), 126.02 (s), 115.08 (s), 98.61 (dd,  $J$  = 27.6, 3.6 Hz), 74.17 – 73.40 (m), 70.12 (s), 22.62 (s), 10.62 (s).

MS (ESI-pos, 9491):  $m/z$  (%) = 421.0027 (100,  $[\text{M}+\text{H}]^+$ ,  $[\text{C}_{15}\text{H}_{12}\text{F}_3\text{IN}_2\text{O}+\text{H}]^+$ , calc.:  $m/z$  = 421.0019).

CHN: calc. (%)  $\text{C}_{15}\text{H}_{12}\text{F}_3\text{IN}_2\text{O}$ : C 42.9, H 2.88, N 6.67; found (%): C 43.2, H 3.13, N 7.25.

### 6.3.3.1.5 (*E*)-1-(4'-(Octyloxy)phenyl)-2-(2,3,6-trifluoro-4-iodophenyl)diazene (**D3I**)

Described experiment: ms-141, repeated: ms-026, ms-042



(*E*)-4'-((2,3,6-trifluoro-4-iodophenyl)diazenyl)phenol (**25c**)

(700 mg, 1.85 mmol) gave (*E*)-1-(4'-(octyloxy)phenyl)-2-(2,3,6-trifluoro-4-iodophenyl)diazene (**D3I**) (305 mg, 0.62 mmol, 33%) after column chromatographic purification using DCM:EA ([99:1]

$R_f$  = 0.3) on silica and recrystallization from MeOH:water [9:1] (~140 mL).

mp: 55 – 56 °C

$^1\text{H}$  NMR (600 MHz, DMSO, @70 °C):  $\delta$  (ppm) = 7.92 – 7.79 (m, 3H), 7.18 – 7.09 (m, 2H), 4.12 (t,  $J$  = 6.5 Hz, 2H), 1.80 – 1.73 (m, 2H), 1.48 – 1.41 (m, 2H), 1.37 – 1.26 (m, 8H), 0.87 (t,  $J$  = 6.9 Hz, 3H).

$^{19}\text{F}$  NMR (565 MHz, DMSO):  $\delta$  (ppm) = -121.64 – -121.77 (m, 1F), -126.43 (dd,  $J$  = 13.1, 10.1 Hz, 1F), -144.25 (dd,  $J$  = 21.9, 1.9 Hz, 1F).

$^{13}\text{C}$  NMR (151 MHz, DMSO, @70 °C):  $\delta$  (ppm) = 162.66 (s), 146.70 (s), 124.73 (s), 120.86 – 120.76 (m), 120.62 (dd,  $J$  = 24.1, 3.0 Hz), 115.07 (s), 68.06 (s), 30.82 (s), 28.24 (d,  $J$  = 14.3 Hz), 25.05 (s), 21.63 (s), 13.44 (s).

IR:  $\nu$  ( $\text{cm}^{-1}$ ) = 3069, 2944, 2920, 2856, 1601, 1577, 1500, 1465, 1441, 1404, 1330, 1297, 1253, 1214, 1185, 1141, 1110, 1090, 1059, 1029, 1000, 968, 896, 850, 838, 810, 799, 759, 748, 723, 656.

MS (ESI-pos, 8516):  $m/z$  (%) = 491.0800 (100,  $[\text{M}+\text{H}]^+$ ,  $[\text{C}_{20}\text{H}_{23}\text{F}_3\text{IN}_2\text{O}+\text{H}]^+$ , calc.:  $m/z$  = 491.0802).

CHN: calc. (%)  $\text{C}_{20}\text{H}_{23}\text{F}_3\text{IN}_2\text{O}$ : C 49.0, H 4.52, N 5.71; found (%): C 49.3, H 4.69, N 6.61.

### 6.3.3.1.6 (*E*)-1-(4'-(Propyloxy)phenyl)-2-(2,3,5-trifluoro-4-iodophenyl)diazene

Described experiment: ms-116



(*E*)-4'-((2,3,6-trifluoro-4-iodophenyl)diazenyl)phenol (**25c**)

(120 mg, 0.32 mmol) and iodopropane (31  $\mu$ L, 0.32 mmol) gave

(*E*)-1-(4'-(propyloxy)phenyl)-2-(2,3,6-trifluoro-4-iodophenyl)-  
diazene (75 mg, 0.18 mmol, 57%) using Cy:DCM ([9:1]

$R_f = 0.35$ ) as eluent for column chromatographic purification on silica.

$^1\text{H}$  NMR (600 MHz,  $\text{CDCl}_3$ ):  $\delta$  (ppm) = 7.95 – 7.90 (m, 2H), 7.43 (ddd,  $J = 9.4, 4.7, 2.3$  Hz, 1H), 7.04 – 6.99 (m, 2H), 4.02 (t,  $J = 6.6$  Hz, 2H), 1.89 – 1.83 (m, 2H), 1.07 (t,  $J = 7.4$  Hz, 3H).

$^{19}\text{F}$  NMR (565 MHz,  $\text{CDCl}_3$ ):  $\delta$  (ppm) = -120.35 (ddd,  $J = 20.5, 12.5, 4.7$ , 1F), -126.19 (dd,  $J = 12.4, 9.4$ , 1F), -142.61 (dd,  $J = 20.5, 1.9$ , 1F).

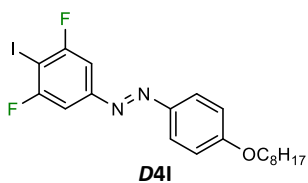
$^{13}\text{C}$  NMR (151 MHz,  $\text{CDCl}_3$ ):  $\delta$  (ppm) = 163.29 (s), 160.69 – 160.54 (m), 151.52 (dt,  $J = 259.4, 3.6$  Hz), 147.69 (s), 144.05 – 141.99 (m), 125.60 (s), 120.75 (dd,  $J = 24.5, 4.2$  Hz), 114.98 (s), 80.06 (dd,  $J = 25.0, 9.8$  Hz), 70.12 (s), 22.62 (s), 10.61 (s).

MS (ESI-pos, 949I):  $m/z$  (%) = 421.0025 (100,  $[\text{M}+\text{H}]^+$ ,  $[\text{C}_{15}\text{H}_{12}\text{F}_3\text{IN}_2\text{O}+\text{H}]^+$ , calc.:  $m/z = 421.0019$ ).

CHN: calc. (%)  $\text{C}_{15}\text{H}_{12}\text{F}_3\text{IN}_2\text{O}$ : C 42.9, H 2.88, N 6.67; found (%): C 42.8, H 3.17, N 7.25.

### 6.3.3.1.7 (*E*)-1-(4'-(Octyloxy)phenyl)-2-(3,5-difluoro-4-iodophenyl)diazene (**D4I**)

Described experiment: ms-184, repeated: ms-028



(*E*)-4'-((3,5-difluoro-4-iodophenyl)diazenyl)phenol (**25d**)

(119 mg, 0.55 mmol) gave (*E*)-1-(4'-(octyloxy)phenyl)-2-(3,5-  
difluoro-4-iodophenyl)diazene (**D4I**) (110 mg, 0.23 mmol, 46%)

using *n*-hex:DEE [9:1]  $R_f = 0.25$ ) on silica for column chromato-

graphic purification.

mp: <30  $^\circ\text{C}$

$^1\text{H}$  NMR (300 MHz, DMSO, *cis*):  $\delta$  (ppm) = 7.30 – 7.20 (m, 2H), 6.93 – 6.84 (m, 4H), 3.92 (t,  $J = 6.5$  Hz, 2H), 1.75 – 1.58 (m, 2H), 1.46 – 1.15 (m, 10H), 0.84 (d,  $J = 6.9$  Hz, 3H).

$^{19}\text{F}$  NMR (282 MHz, DMSO, *cis*):  $\delta$  (ppm) = -92.20 (d,  $J = 7.2$  Hz, 2F).

$^{13}\text{C}$  NMR (151 MHz, DMSO, *cis*):  $\delta$  (ppm) = 162.55 (dd,  $J = 244.4, 7.7$  Hz), 162.43 (s), 158.59 (s), 153.97 (t,  $J = 8.8$  Hz), 129.29 (s), 114.33 (s), 105.26 – 104.87 (m), 75.01 (t,  $J = 31.6$ ), 67.20 (s), 31.08 (s), 28.59 (s), 28.58 (s), 28.50 (s), 25.40 (s), 21.92 (s), 13.78 (s).

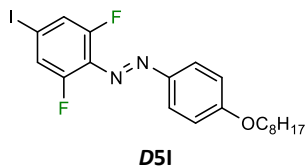
IR:  $\nu$  ( $\text{cm}^{-1}$ ) = 2923, 2854, 1599, 1586, 1496, 1468, 1389, 1299, 1242, 1171, 1144, 1078, 1022, 997, 879, 838, 814, 751, 723, 690.

MS (ESI-pos, 8510):  $m/z$  (%) = 473.0900 (100,  $[M+H]^+$ ,  $[C_{20}H_{23}F_2IN_2O+H]^+$ , calc.:  $m/z$  = 490.0896).

CHN: calc. (%)  $C_{20}H_{23}F_2IN_2O$ : C 50.9, H 4.91, N 5.93; found (%): C 50.8, H 5.03, N 6.15.

### 6.3.3.1.8 (*E*)-1-(4'-(Octyloxy)phenyl)-2-(2,6-difluoro-4-iodophenyl)diazene (**D5I**)

Described experiment: ms-055, repeated ms-162, ms-197



(*E*)-4'-((2,6-difluoro-4-iodophenyl)diazenyl)phenol (**25e**)

(265 mg, 0.74 mmol) gave (*E*)-4'-((2,6-trifluorophenyl)-diazenyl)-

phenol (**D5I**) (252 mg, 0.53 mmol, 72%) using *n*-hex:EA ([99:1]

$R_f$  = 0.3) on silica for column chromatographic purification.

mp: 74 – 75 °C

$^1H$  NMR (500 MHz, DMSO, 70 °C):  $\delta$  (ppm) = 7.87 – 7.79 (m, 2H), 7.75 – 7.67 (m, 2H), 7.15 – 7.08 (m, 2H), 4.11 (t,  $J$  = 6.5 Hz, 2H), 1.80 – 1.72 (m, 2H), 1.49 – 1.40 (m, 2H), 1.40 – 1.21 (m, 8H), 0.88 (t,  $J$  = 7.0 Hz, 3H).

$^{19}F$  NMR (565 MHz, DMSO):  $\delta$  (ppm) = -121.64 (d,  $J$  = 8.7 Hz, 2F).

$^{13}C$  NMR (126 MHz, DMSO, 70 °C):  $\delta$  (ppm) = 162.30 (s), 154.10 (dd,  $J$  = 261.1, 4.9 Hz), 146.74 (s), 130.10 (t,  $J$  = 10.4 Hz), 124.45 (s), 121.98 – 121.49 (m), 114.96 (s), 93.24 (t,  $J$  = 7.9 Hz), 67.98 (s), 30.77 (s), 28.25 (s), 28.17 (s), 28.14 (s), 25.02 (s), 21.58 (s), 13.39 (s).

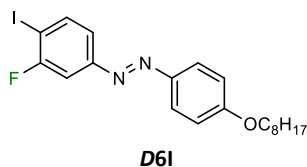
IR:  $\nu$  ( $cm^{-1}$ ) = 3076, 2945, 2919, 2855, 1725, 1595, 1578, 1566, 1500, 1471, 1419, 1401, 1322, 1298, 1263, 1201, 1140, 1109, 1049, 1000, 904, 839, 810, 800, 759, 723.

MS (ESI-pos, 9062):  $m/z$  (%) = 473.0898 (100,  $[M+H]^+$ ,  $[C_{20}H_{22}F_3IN_2O+H]^+$ , calc.:  $m/z$  = 490.0896).

CHN: calc. (%)  $C_{20}H_{23}F_2IN_2O$ : C 50.9, H 4.91, N 5.93; found (%): C 51.7, H 5.23, N 6.58.

### 6.3.3.1.9 (*E*)-1-(4'-(Octyloxy)phenyl)-2-(3-fluoro-4-iodophenyl)diazene (**D6I**)

Described experiment: ms-068, repeated: ms-062



(*E*)-4'-((3-fluoro-4-iodophenyl)diazenyl)phenol (**25f**) (132 mg,

0.38 mmol) gave (*E*)-4'-((3-fluorophenyl)diazenyl)phenol (**D6I**)

(112 mg, 0.24 mmol, 64%) using Cy:EA ([99:1]  $R_f$  = 0.2) on sil-

ica for column chromatographic purification.

mp: 61 – 63 °C

$^1H$  NMR (500 MHz, DMSO, @70 °C):  $\delta$  (ppm) = 8.05 (dd,  $J$  = 8.3, 6.9 Hz, 1H), 7.91 – 7.87 (m, 2H), 7.61 (dd,  $J$  = 9.0, 2.1 Hz, 1H), 7.51 (dd,  $J$  = 8.3, 2.1 Hz, 1H), 7.15 – 7.10 (m, 2H), 4.11 (t,  $J$  = 6.5 Hz, 2H), 1.80 – 1.72 (m, 2H), 1.49 – 1.41 (m, 2H), 1.38 – 1.23 (m, 8H), 0.88 (t,  $J$  = 6.9 Hz, 3H).

$^{19}\text{F}$  NMR (282 MHz, DMSO):  $\delta$  (ppm) = -93.56 (dd,  $J$  = 8.4, 7.4 Hz, 1F).

$^{13}\text{C}$  NMR (126 MHz, DMSO, @70 °C):  $\delta$  (ppm) = 161.88 (s), 161.51 (d,  $J$  = 244.4 Hz), 153.57 (d,  $J$  = 6.3 Hz), 145.66 (s), 139.61 (d,  $J$  = 2.4 Hz), 124.59 (s), 120.46 (d,  $J$  = 3.1 Hz), 114.93 (s), 107.44 (d,  $J$  = 25.7 Hz), 84.06 (d,  $J$  = 26.2 Hz), 67.93 (s), 30.77 (s), 28.25 (s), 28.20 (s), 28.15 (s), 25.03 (s), 21.58 (s), 13.39 (s).

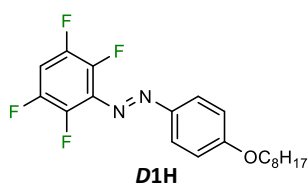
IR:  $\nu$  ( $\text{cm}^{-1}$ ) = 3069, 2944, 2918, 2852, 1603, 1582, 1501, 1469, 1398, 1318, 1296, 1259, 1234, 1145, 1130, 1106, 10433, 1024, 1000, 961, 925, 876, 840, 820, 754, 724, 694, 665.

MS (ESI-pos, 9067):  $m/z$  (%) = 455.0998 (100,  $[\text{M}+\text{H}]^+$ ,  $[\text{C}_{20}\text{H}_{24}\text{FIN}_2\text{O}+\text{H}]^+$ , calc.:  $m/z$  = 455.0990).

CHN: calc. (%)  $\text{C}_{20}\text{H}_{24}\text{FIN}_2\text{O}$ : C 52.9, H 5.32, N 4.18; found (%): C 53.5, H 5.56, N 6.93.

### 6.3.3.1.10 (*E*)-1-(4'-(Octyloxy)phenyl)-2-(2,3,5,6-tetrafluorophenyl)diazene (**D1H**)

Described experiment: ms-059



(*E*)-4'-((2,3,5,6-tetrafluorophenyl)diazenyl)phenol (150 mg, 0.56 mmol) yielded (*E*)-1-(4'-(octyloxy)phenyl)-2-(4-bromo-2,3,5,6-tetrafluorophenyl)diazene (**D1H**) (147 mg 0.38 mmol, 69%) using Cy:EA ([9:1]  $R_f$  = 0.3) for column chromatographic purification.

mp: 49 – 50 °C

$^1\text{H}$  NMR (500 MHz, DMSO, @70 °C):  $\delta$  (ppm) = 7.95 – 7.82 (m, 3H), 7.18 – 7.12 (m, 2H), 4.13 (t,  $J$  = 6.5 Hz, 2H), 1.81 – 1.72 (m, 2H), 1.49 – 1.40 (m, 2H), 1.38 – 1.25 (m, 8H), 0.88 (t,  $J$  = 7.0 Hz, 3H).

$^{19}\text{F}$  NMR (282 MHz,  $\text{CDCl}_3$ ):  $\delta$  (ppm) = -139.20 – -139.49 (m, 1F), -151.75 – -152.02 (m, 1F).

$^{13}\text{C}$  NMR (126 MHz, DMSO, @70 °C):  $\delta$  (ppm) = 162.92 (s), 146.52 (s), 124.89 (s), 115.09 (s), 105.87 (t,  $J$  = 23.8 Hz), 68.08 (s), 30.77 (s), 28.25 (s), 28.15 (s), 25.01 (s), 21.58 (s), 13.38 (s).

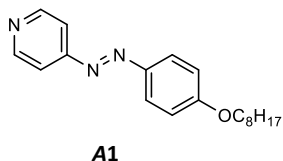
IR:  $\nu$  ( $\text{cm}^{-1}$ ) = 3079, 2944, 2929, 2853, 1684, 1601, 1579, 1509, 1498, 1468, 1452, 1434, 1411, 1393, 1376, 1322, 1299, 1274, 1249, 1210, 1175, 1143, 1109, 1067, 1037, 1025, 997, 956, 875, 841, 811, 762, 738, 722, 701.

MS (ESI-pos, 9064):  $m/z$  (%) = 383.1742 (100,  $[\text{M}+\text{H}]^+$ ,  $[\text{C}_{20}\text{H}_{22}\text{F}_4\text{N}_2\text{O}+\text{H}]^+$ , calc.:  $m/z$  = 383.1741).

CHN: calc. (%)  $\text{C}_{20}\text{H}_{22}\text{F}_4\text{N}_2\text{O}$ : C 62.8, H 5.80, N 7.33, O 4.18; found (%): C 63.3, H 6.18, N 7.06.

**6.3.3.1.11 (*E*)-4-((4'-(Octyloxy)phenyl)diazenyl)pyridine (**A1**)**

Described experiment: ms-122, repeated: se-004



(*E*)-4-(pyridinyl)-diazenylphenol (763 mg, 3.83 mmol) yielded 1.08 g (3.5 mmol, 91%) (*E*)-4-((4'-(octyloxy)phenyl)diazenyl)-pyridine (**A1**) using Cy:EA ([8:2],  $R_f = 0.3$ ) for column chromatographic purification.

Analytical data was in accordance with the literature.<sup>[244]</sup>

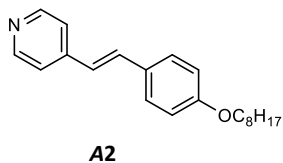
$^1\text{H NMR}$  (300 MHz,  $\text{CDCl}_3$ ):  $\delta$  (ppm) = 8.78 (dd,  $J = 4.8, 1.6$  Hz, 2H), 8.02 – 7.91 (m, 2H), 7.78 – 7.71 (m, 2H), 7.06 – 6.97 (m, 2H), 4.07 (t,  $J = 6.5$  Hz, 2H), 1.90 – 1.77 (m, 2H), 1.54 – 1.24 (m,  $J = 42.7, 13.1$  Hz, 10H), 0.89 (t, 3H).

$^{13}\text{C NMR}$  (75 MHz,  $\text{CDCl}_3$ ):  $\delta$  (ppm) = 163.59 (s), 158.53 (s), 149.71 (s), 146.95 (s), 126.12 (s), 116.88 (s), 115.17 (s), 68.77 (s), 31.95 (s), 29.47 (s), 29.36 (s), 29.27 (s), 26.14 (s), 22.80 (s), 14.23 (s), 12.46 (s).

CHN: calc. (%)  $\text{C}_{19}\text{H}_{25}\text{N}_3\text{O}$ : C 73.3, H 8.09, N 13.49; found (%): C 73.7, H 8.62, N 15.0.

**6.3.3.1.12 (*E*)-4-(4'-(octyloxy)styryl)pyridine (**A2**)**

Described experiment: ms-179



(*E*)-(2-(4-pyridinyl)ethenyl)phenol (1.0 g, 5.07 mmol) yielded (*E*)-4-(4'-(octyloxy)styryl)pyridine (923 mg, 2.98 mmol, 60%) after column chromatographic purification using Cy:EA ([1:1],  $R_f = 0.3$ ) and recrystallization from methanol (~15 mL).

Analytical data was in accordance with the literature.<sup>[244]</sup>

$^1\text{H NMR}$  (300 MHz,  $\text{CDCl}_3$ ):  $\delta$  (ppm) = 8.54 (d,  $J = 5.8$  Hz, 2H), 7.51 – 7.44 (m, 2H), 7.37 (d,  $J = 5.9$  Hz, 2H), 7.28 (d,  $J = 16.0$  Hz, 1H), 6.90 (dd,  $J = 12.4, 9.6$  Hz, 3H), 3.99 (t,  $J = 6.6$  Hz, 2H), 1.86 – 1.73 (m, 2H), 1.53 – 1.18 (m, 10H), 0.89 (t,  $J = 6.8$  Hz, 3H).

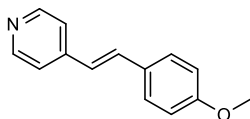
IR:  $\nu$  ( $\text{cm}^{-1}$ ) = 3069, 3021, 2918, 2872, 2853, 1632, 1605, 1587, 1549, 1510, 1470, 1408, 1391, 1346, 1310, 1281, 1256, 1213, 1190, 1175, 1130, 1113, 1065, 1044, 1024, 999, 968, 872, 824, 789, 758, 719, 665, 638, 627.

CHN: calc. (%)  $\text{C}_{21}\text{H}_{27}\text{NO}$ : C 81.5, H 8.79, N 4.53; found (%): C 81.3, H 9.24, N 5.80.

**6.3.3.1.13 (E)-4-(4'-methoxystyryl)pyridine**

Described experiment: ms-096

(E)-4-(4'-methoxystyryl)pyridine was synthesized according to a literature known procedure.<sup>[245]</sup>



4-Methylpyridine (1.05 mL, 11.0 mmol) and 4-methoxybenzaldehyde (1.30 mL, 11.0 mmol) were dissolved in dry DMF under argon. Potassium *tert*-butoxide was added in one portion and the mixture was stirred for 2 h at 80 °C. The reaction progress was monitored by TLC using Cy:EA [4:1] ( $R_f = 0.15$ ). Upon full conversion, the mixture was cooled to room temperature, added to 200 mL DCM and washed with ice water (200 mL) and 1M KOH (3 x 200 mL). Drying over MgSO<sub>4</sub> evaporation of the solvent and recrystallization from cyclohexane yielded the product as pale-yellow crystals (947 mg, 4.5 mmol, 42%).

Analytical data was in accordance with the literature.<sup>[245]</sup>

<sup>1</sup>H NMR (300 MHz, CDCl<sub>3</sub>):  $\delta$  (ppm) = 8.57 – 8.50 (m, 1H), 7.52 – 7.44 (m, 2H), 7.35 – 7.29 (m, 2H), 7.25 (d,  $J = 16.3$  Hz, 1H), 6.96 – 6.81 (m, 3H), 3.84 (s, 1H).

<sup>13</sup>C NMR (75 MHz, CDCl<sub>3</sub>):  $\delta$  (ppm) = 160.33 (s), 150.17 (s), 145.19 (s), 132.90 (s), 129.05 (s), 128.53 (s), 123.87 (s), 120.77 (s), 114.44 (s), 55.48 (s).

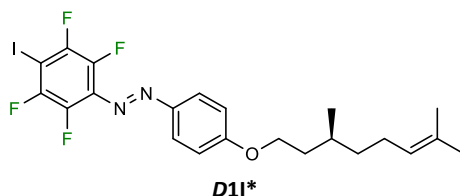
MS (ESI-pos, 9388):  $m/z$  (%) = 212.1075 (100, [M+H]<sup>+</sup>, [C<sub>14</sub>H<sub>13</sub>NO+H]<sup>+</sup>, calc.:  $m/z = 212.1070$ ).

CHN: calc. (%) C<sub>21</sub>H<sub>27</sub>NO: C 79.59, H 6.20, N 6.63; found (%): C 80.2, H 6.55, N 7.49.

### 6.3.3.2 Synthesis of chiral XB-donator and XB-acceptor molecules

#### 6.3.3.2.1 (*S,E*)-1-[4'-((3,7-Dimethyloct-6-en-1-yl)oxy)phenyl]-2-(2,3,5,6-tetrafluoro-4-iodophenyl)diazene (**D11\***)

Described experiment: ms-163, repeated: ms-161, ms-171, se-001



(*E*)-4'-((2,3,5,6-tetrafluoro-4-iodophenyl)diazenyl)phenol (**25a**) (218 mg, 0.55 mmol) yielded (*S,E*)-1-[4'-((3,7-dimethyloct-6-en-1-yl)oxy)phenyl]-2-(2,3,5,6-tetrafluoro-4-iodophenyl)diazene (**D11\***) (104 mg, 0.19 mmol, 35%) using *n*-hex:EA ([99:1],  $R_f = 0.4$ ) as eluent and ALOX as stationary phase.

mp: 50 – 51 °C

$^1\text{H NMR}$  (600 MHz,  $\text{CDCl}_3$ ):  $\delta$  (ppm) = 8.00 – 7.92 (m, 2H), 7.08 – 6.97 (m, 2H), 5.19 – 5.07 (m, 1H), 4.15 – 4.05 (m, 2H), 2.10 – 1.96 (m, 2H), 1.92 – 1.85 (m, 1H), 1.77 – 1.59 (m, 8H), 1.46 – 1.38 (m, 1H), 1.34 – 1.18 (m, 1H), 0.98 (d,  $J = 6.6$  Hz, 3H).

$^{19}\text{F NMR}$  (565 MHz,  $\text{CDCl}_3$ ):  $\delta$  (ppm) = -120.61 – -120.79 (m, 2F), -149.44 – -149.65 (m, 2F).

$^{13}\text{C NMR}$  (151 MHz,  $\text{CDCl}_3$ ):  $\delta$  (ppm) = 163.59 (s), 147.59 (s), 147.56 (ddt,  $J = 245.4, 14.1, 4.8$  Hz), 139.86 (ddt,  $J = 261.3, 16.9, 3.8$  Hz), 133.22 (t,  $J = 8.9$  Hz), 131.59 (s), 125.83 (s), 124.68 (s), 115.04 (s), 71.67 (t,  $J = 28.0$  Hz), 67.01 (s), 37.23 (s), 36.07 (s), 29.63 (s), 25.87 (s), 25.58 (s), 19.67 (s), 17.82 (s).

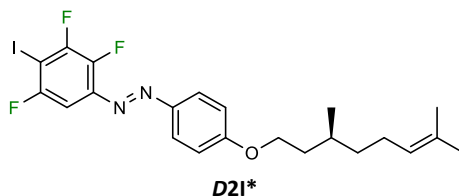
IR:  $\nu$  ( $\text{cm}^{-1}$ ) = 2956, 2926, 2915, 2873, 2846, 1599, 1577, 1500, 1479, 1470, 1446, 1408, 1378, 1325, 1300, 1276, 1249, 1210, 1144, 1110, 1044, 1003, 979, 948, 889, 844, 811, 800, 784, 737, 628, 619, 572, 556, 527, 477, 438, 410.

MS (ESI-pos, 10402):  $m/z$  (%) = 535.0845 (100,  $[\text{M}+\text{H}]^+$ ,  $[\text{C}_{22}\text{H}_{23}\text{F}_4\text{IN}_2\text{O}+\text{H}]^+$ , calc.:  $m/z = 535.0864$ ).

CHN: calc. (%)  $\text{C}_{22}\text{H}_{23}\text{F}_4\text{IN}_2\text{O}$ : C 49.5, H 4.34, N 5.24; found (%): C 50.4, H 4.65, N 5.92.

**6.3.3.2.2 (S,E)-1-[4'-((3,7-Dimethyloct-6-en-1-yl)oxy)phenyl]-2-(2,3,5-trifluoro-4-iodophenyl)diazene (D2I\*)**

Described experiment: se-002



(E)-4'-((2,3,5-trifluoro-4-iodophenyl)diazenyl)phenol (**25b**) (500 mg, 1.32 mmol) yielded (S,E)-1-[4'-((3,7-dimethyloct-6-en-1-yl)oxy)phenyl]-2-(2,3,5-trifluoro-4-iodophenyl)diazene (**D2I\***) (579 mg, 1.12 mmol, 85%) using *n*-hex:EA ([99:1],  $R_f = 0.2$ ) on silica for column chromatography.

mp: 44 – 44 °C

$^1\text{H}$  NMR (300 MHz,  $\text{CDCl}_3$ ):  $\delta$  (ppm) = 7.99 – 7.91 (m, 2H), 7.40 – 7.33 (m, 1H), 7.04 – 6.97 (m, 2H), 5.16 – 5.07 (m, 1H), 4.14 – 4.06 (m, 2H), 2.12 – 1.96 (m,  $J = 14.8, 7.3$  Hz, 2H), 1.93 – 1.81 (m, 1H), 1.71 – 1.59 (m, 8H), 1.52 – 1.33 (m,  $J = 12.0, 11.4, 6.0$  Hz, 1H), 1.33 – 1.12 (m,  $J = 20.8, 11.3, 6.9$  Hz, 1H), 0.98 (d,  $J = 6.4$  Hz, 3H).

$^{19}\text{F}$  NMR (282 MHz,  $\text{CDCl}_3$ ):  $\delta$  (ppm) = -98.14 (dd,  $J = 12.2, 8.5$  Hz), -113.89 (d,  $J = 21.3$  Hz), -150.90 (ddd,  $J = 21.3, 12.4, 5.5$  Hz).

$^{13}\text{C}$  NMR (151 MHz,  $\text{CDCl}_3$ ):  $\delta$  (ppm) = 163.23 (s), 158.67 – 156.89 (m), 152.88 – 151.06 (m), 146.78 (s), 144.86 (ddd,  $J = 231.9, 14.6, 8.5$  Hz), 142.18 (s), 131.56 (s), 125.99 (s), 124.67 (s), 115.07 (s), 98.59 (dd,  $J = 27.7, 3.5$  Hz), 73.76 (dd,  $J = 33.2, 26.3$  Hz), 66.95 (s), 37.22 (s), 36.08 (s), 29.61 (s), 25.86 (s), 25.56 (s), 19.67 (s), 17.81 (s).

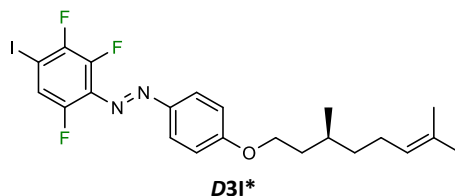
IR:  $\nu$  ( $\text{cm}^{-1}$ ) = 3090, 3053, 2950, 2941, 2916, 2874, 2847, 1601, 1578, 1501, 1470, 1451, 1410, 1379, 1339, 1298, 1252, 1207, 1142, 1109, 1053, 1028, 1007, 951, 901, 864, 841, 808, 787, 731, 679, 638, 628.

MS (ESI-pos, 10439):  $m/z$  (%) = 517.0959 (100,  $[\text{M}+\text{H}]^+$ ,  $[\text{C}_{22}\text{H}_{24}\text{F}_3\text{IN}_2\text{O}+\text{H}]^+$ , calc.:  $m/z = 517.0958$ ).

CHN: calc. (%)  $\text{C}_{22}\text{H}_{24}\text{F}_3\text{IN}_2\text{O}$ : C 51.2, H 4.69, N 5.43; found (%): C 51.7, H 4.89, N 6.13.

### 6.3.3.2.3 (*S,E*)-1-[4'-((3,7-Dimethyloct-6-en-1-yl)oxy)phenyl]-2-(2,3,6-trifluoro-4-iodophenyl)diazene (**D3I\***)

Described experiment: ms-182, repeated: ms-180, se-018



(*E*)-4'-((2,3,6-trifluoro-4-iodophenyl)diazenyl)phenol (**25c**) (302 mg, 0.80 mmol) yielded (*S,E*)-1-[4'-((3,7-dimethyloct-6-en-1-yl)oxy)phenyl]-2-(2,3,6-trifluoro-4-iodophenyl)diazene (**D3I\***) (278 mg, 0.53 mmol, 67%) using *n*-hex:EA ([99:1],  $R_f = 0.25$ ) for column chromatography on silica.

mp: <25 °C

$^1\text{H}$  NMR (400 MHz,  $\text{CDCl}_3$ , *trans*):  $\delta$  (ppm) = 7.96 – 7.89 (m, 2H), 7.44 (ddd,  $J = 9.5, 4.7, 2.4$  Hz, 1H), 7.05 – 6.97 (m, 2H), 5.15 – 5.06 (m, 1H), 4.13 – 4.05 (m, 2H), 2.11 – 1.95 (m, 2H), 1.93 – 1.78 (m, 1H), 1.76 – 1.58 (m, 8H), 1.47 – 1.35 (m, 1H), 1.32 – 1.18 (m, 1H), 0.98 (d,  $J = 6.5$  Hz, 3H).

$^{19}\text{F}$  NMR (376 MHz,  $\text{CDCl}_3$ , *trans*):  $\delta$  (ppm) = -120.33 (ddd,  $J = 20.6, 12.0, 4.6$  Hz), -126.19 (dd,  $J = 12.4, 9.6$  Hz), -142.60 (dd,  $J = 20.5, 2.4$  Hz).

$^{13}\text{C}$  NMR (101 MHz,  $\text{CDCl}_3$ )  $\delta$  (ppm) = 163.27 (s), 152.88 – 150.12 (m,  $J = 259.1$  Hz), 149.86 – 146.85 (m), 147.69 (s), 144.78 – 141.35 (m), 133.08 – 132.23 (m), 131.59 (s), 125.60 (s), 124.69 (s), 120.75 (dd,  $J = 24.5, 4.3$  Hz), 115.00 (s), 80.06 (dd,  $J = 25.1, 9.7$  Hz), 66.96 (s), 37.24 (s), 36.09 (s), 29.63 (s), 25.88 (s), 25.58 (s), 19.68 (s), 17.83 (s).

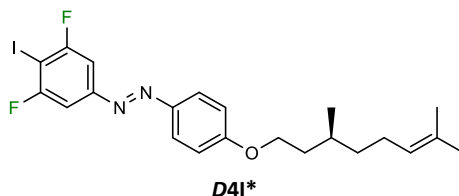
IR:  $\nu$  ( $\text{cm}^{-1}$ ) = 2955, 2915, 2872, 2853, 1597, 1578, 1499, 1468, 1449, 1414, 1377, 1311, 1298, 1250, 1140, 1107, 1086, 1059, 1013, 972, 882, 837, 799, 739, 698, 629, 611.

MS (ESI-pos, 14835):  $m/z$  (%) = 517.0982 (100,  $[\text{M}+\text{H}]^+$ ,  $[\text{C}_{22}\text{H}_{24}\text{F}_3\text{IN}_2\text{O}+\text{H}]^+$ , calc.:  $m/z = 517.0958$ ).

CHN: calc. (%)  $\text{C}_{22}\text{H}_{24}\text{F}_3\text{IN}_2\text{O}$ : C 51.2, H 4.69, N 5.43; found (%): C 55.0, H 5.80, N 5.35.

**6.3.3.2.4 (*S,E*)-1-[4'-((3,7-Dimethyloct-6-en-1-yl)oxy)phenyl]-2-(3,5-difluoro-4-iodophenyl)diazene (*D4I*\*)**

Described experiment: ms-186



(*E*)-4'-((3,5-difluoro-4-iodophenyl)diazenyl)phenol (**25d**) (500 mg, 1.38 mmol) yielded (*S,E*)-1-[4'-((3,7-dimethyloct-6-en-1-yl)oxy)phenyl]-2-(3,5-difluoro-4-iodophenyl)diazene (*D4I*\*) (232 mg, 0.47 mmol, 34%) using *n*-hex:DEE ([99:1],  $R_f = 0.25$ ) and *n*-hex:toluene ([95:5],  $R_f = 0.2$ ) on silica for column chromatography.

mp: 56 – 57 °C

$^1\text{H}$  NMR (400 MHz,  $\text{CDCl}_3$ ):  $\delta$  (ppm) = 7.94 – 7.89 (m, 2H), 7.47 – 7.42 (m, 2H), 7.04 – 6.98 (m, 2H), 5.15 – 5.08 (m, 1H), 4.13 – 4.06 (m, 2H), 2.12 – 1.94 (m, 2H), 1.93 – 1.83 (m, 1H), 1.79 – 1.56 (m, 8H), 1.48 – 1.36 (m, 1H), 1.31 – 1.20 (m, 1H), 0.98 (d,  $J = 6.5$  Hz, 3H).

$^{19}\text{F}$  NMR (282 MHz,  $\text{CDCl}_3$ ):  $\delta$  (ppm) = -91.67 (d,  $J = 7.1$  Hz, 2F).

$^{13}\text{C}$  NMR (101 MHz,  $\text{CDCl}_3$ ):  $\delta$  (ppm) = 163.05 (dd,  $J = 247.3, 6.7$  Hz), 162.87 (s), 154.87 (t,  $J = 8.5$  Hz), 146.35 (s), 131.58 (s), 125.61 (s), 124.70 (s), 115.05 (s), 105.54 (dd,  $J = 26.3, 3.0$  Hz), 72.77 (t,  $J = 30.3$  Hz), 66.92 (s), 37.24 (s), 36.11 (s), 29.64 (s), 25.88 (s), 25.58 (s), 19.69 (s), 17.83 (s).

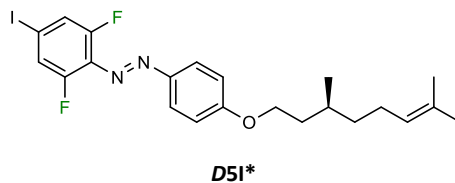
IR:  $\nu$  ( $\text{cm}^{-1}$ ) = 3078, 2963, 2908, 2854, 1728, 1597, 1577, 1499, 1470, 1443, 1403, 1324, 1298, 1247, 1178, 1146, 1102, 1068, 1014, 939, 868, 833, 788, 737, 724, 688, 634, 559, 519, 454, 427.

MS (ESI-pos, 12436):  $m/z$  (%) = 499.1065(100,  $[\text{M}+\text{H}]^+$ ,  $[\text{C}_{22}\text{H}_{25}\text{F}_2\text{IN}_2\text{O}+\text{H}]^+$ , calc.:  $m/z = 499.1052$ ).

CHN: calc. (%)  $\text{C}_{22}\text{H}_{25}\text{F}_2\text{IN}_2\text{O}$ : C 53.0, H 5.06, N 5.62; found (%): C 53.4, H 5.41, N 6.13.

**6.3.3.2.5 (S,E)-1-[4'-((3,7-Dimethyloct-6-en-1-yl)oxy)phenyl]-2-(2,6-difluoro-4-iodophenyl)diazene (D5I\*)**

Described experiment: ms-198



(*E*)-4'-((3,5-difluoro-4-iodophenyl)diazanyl)phenol (**25e**) (1.00 g, 2.78 mmol) yielded (*S,E*)-1-[4'-((3,7-dimethyloct-6-en-1-yl)oxy)phenyl]-2-(2,6-difluoro-4-iodophenyl)diazene (**D5I\***) (736 mg, 1.47 mmol, 53%) using Cy:DCM ([9:1],  $R_f = 0.2$ )  $\rightarrow$  ([2:1],  $R_f = 0.6$ ) on silica for column chromatography.

mp: &lt;25 °C

$^1\text{H NMR}$  (400 MHz,  $\text{CDCl}_3$ ):  $\delta$  (ppm) = 7.94 – 7.88 (m, 2H), 7.45 – 7.38 (m, 2H), 7.02 – 6.97 (m, 2H), 5.15 – 5.08 (m, 1H), 4.14 – 4.03 (m, 2H), 2.11 – 1.93 (m, 2H), 1.93 – 1.82 (m, 1H), 1.78 – 1.58 (m, 8H), 1.46 – 1.36 (m, 1H), 1.32 – 1.16 (m, 1H), 0.98 (d,  $J = 6.5$  Hz, 3H).

$^{19}\text{F NMR}$  (282 MHz,  $\text{CDCl}_3$ ):  $\delta$  (ppm) = -120.69 (d,  $J = 7.9$  Hz, 2F).

$^{13}\text{C NMR}$  (101 MHz,  $\text{CDCl}_3$ ):  $\delta$  (ppm) = 162.92 (s), 155.38 (dd,  $J = 263.2, 4.7$  Hz), 150.59 (t,  $J = 4.1$  Hz), 147.77 (s), 131.57 (s), 125.35 (s), 124.71 (s), 122.65 – 121.98 (m), 114.93 (s), 91.40 (t,  $J = 10.4$  Hz), 66.91 (s), 37.24 (s), 36.11 (s), 29.63 (s), 25.88 (s), 25.58 (s), 19.69 (s), 17.83 (s).

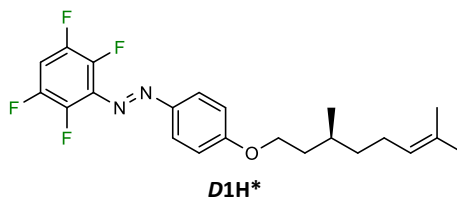
IR:  $\nu$  ( $\text{cm}^{-1}$ ) = 3078, 3049, 2959, 2914, 2873, 2853, 1597, 1572, 1499, 1470, 1451, 1407, 1379, 1313, 1298, 1249, 1202, 1138, 1105, 1046, 1013, 979, 912, 836, 751, 637, 600, 574, 526, 512.

MS (ESI-pos, 14474):  $m/z$  (%) = 499.1049 (100,  $[\text{M}+\text{H}]^+$ ,  $[\text{C}_{22}\text{H}_{25}\text{F}_2\text{IN}_2\text{O}+\text{H}]^+$ , calc.:  $m/z = 499.1052$ ).

CHN: calc. (%)  $\text{C}_{22}\text{H}_{25}\text{F}_2\text{IN}_2\text{O}$ : C 53.0, H 5.06, N 5.62; found (%): C 53.5, H 5.41, N 6.35.

**6.3.3.2.6 (*S,E*)-1-[4'-((3,7-Dimethyloct-6-en-1-yl)oxy)phenyl]-2-(2,3,5,6-tetrafluorophenyl)diazene (*D1H*\*)**

Described experiment: ms-187



(*E*)-4'-((2,3,5,6-tetrafluorophenyl)diazenyl)phenol (100 mg, 0.37 mmol) yielded (*S,E*)-1-[4'-((3,7-dimethyloct-6-en-1-yl)oxy)phenyl]-2-(2,3,5,6-tetrafluorophenyl)diazene (*D1H*\*) (57 mg, 0.14 mmol, 37%) using Cy:EA ([9:1],  $R_f = 0.2$ ) for column chromatographic purification.

mp: 38 – 40 °C

$^1\text{H}$  NMR (600 MHz,  $\text{CDCl}_3$ ):  $\delta$  (ppm) = 7.96 – 7.92 (m, 2H), 7.06 (tdd,  $J = 7.1, 5.7, 2.6$  Hz, 1H), 7.03 – 7.00 (m, 2H), 5.14 – 5.07 (m, 1H), 4.14 – 4.06 (m, 2H), 2.10 – 1.96 (m, 2H), 1.92 – 1.85 (m, 1H), 1.76 – 1.59 (m, 8H), 1.45 – 1.38 (m, 1H), 1.28 – 1.22 (m, 1H), 0.98 (d,  $J = 6.6$  Hz, 3H).

$^{19}\text{F}$  NMR (565 MHz,  $\text{CDCl}_3$ ):  $\delta$  (ppm) = -139.25 – -139.40 (m, 2F), -151.80 – -151.93 (m, 2F).

$^{13}\text{C}$  NMR (151 MHz,  $\text{CDCl}_3$ ):  $\delta$  (ppm) = 163.46 (s), 147.51 (s), 147.30 – 145.38 (m), 141.25 – 139.35 (m), 133.63 (t,  $J = 8.8$  Hz), 131.59 (s), 125.75 (s), 124.69 (s), 115.03 (s), 104.97 (t,  $J = 22.9$  Hz), 67.00 (s), 37.24 (s), 36.08 (s), 29.63 (s), 25.88 (s), 25.58 (s), 19.68 (s), 17.83 (s).

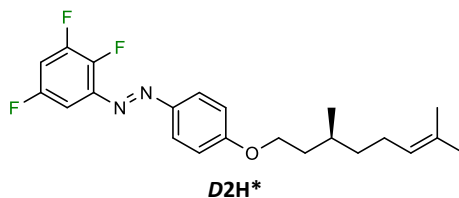
IR:  $\nu$  ( $\text{cm}^{-1}$ ) = 3070, 2954, 2927, 2907, 2877, 2847, 1599, 1577, 1499, 1468, 1453, 1435, 1414, 1380, 1320, 1297, 1276, 1253, 1176, 1144, 1104, 1036, 1005, 956, 874, 836, 814, 792, 751, 737, 718, 700, 629, 570, 550, 516, 482, 444.

MS (ESI-pos, 12437):  $m/z$  (%) = 409.1905 (100,  $[\text{M}+\text{H}]^+$ ,  $[\text{C}_{22}\text{H}_{24}\text{F}_4\text{IN}_2\text{O}+\text{H}]^+$ , calc.:  $m/z = 409.1898$ ).

CHN: calc. (%)  $\text{C}_{22}\text{H}_{24}\text{F}_4\text{N}_2\text{O}$ : C 64.7, H 5.92, N 6.86; found (%): C 65.1, H 6.38, N 7.34.

### 6.3.3.2.7 (*S,E*)-1-[4'-((3,7-Dimethyloct-6-en-1-yl)oxy)phenyl]-2-(2,3,5-trifluorophenyl)diazene (**D2H\***)

Described experiment: ms-217



(*E*)-4'-((2,3,5-trifluorophenyl)diazenyl)phenol (120 mg, 0.47 mmol) yielded (*S,E*)-1-[4'-((3,7-dimethyloct-6-en-1-yl)oxy)phenyl]-2-(2,3,5-trifluorophenyl)diazene (**D2H\***) (112 mg, 0.29 mmol, 60%) using Cy:EA ([4:1],  $R_f = 0.4$ ) for column chromatographic purification.

mp: 53 – 54 °C

$^1\text{H}$  NMR (400 MHz,  $\text{CDCl}_3$ ):  $\delta$  (ppm) = 8.24 – 8.18 (m, 2H), 7.57 – 7.50 (m, 1H), 7.30 – 7.21 (m, 3H), 5.41 – 5.33 (m, 1H), 4.41 – 4.30 (m, 2H), 2.38 – 2.19 (m, 2H), 2.19 – 2.09 (m, 1H), 2.04 – 1.84 (m, 8H), 1.73 – 1.62 (m, 1H), 1.57 – 1.45 (m, 1H), 1.24 (d,  $J = 6.5$  Hz, 3H).

$^{19}\text{F}$  NMR (376 MHz,  $\text{CDCl}_3$ ):  $\delta$  (ppm) = -114.69 – -114.86 (m, 1F), -133.25 – -133.41 (m, 1F), -153.86 – -154.05 (m, 1F).

$^{13}\text{C}$  NMR (101 MHz,  $\text{CDCl}_3$ ):  $\delta$  (ppm) = 163.05 (s), 157.66 (ddd,  $J = 246.7, 10.8, 3.3$  Hz), 151.37 (dt,  $J = 26.4, 13.0$  Hz), 146.84 (s), 145.36 (ddd,  $J = 255.7, 13.9, 4.6$  Hz), 142.55 – 142.16 (m), 131.59 (s), 125.88 (s), 124.70 (s), 115.04 (s), 106.49 (dd,  $J = 28.7, 21.2$  Hz), 99.50 (dd,  $J = 25.0, 3.6$  Hz), 66.94 (s), 37.24 (s), 36.11 (s), 29.63 (s), 25.88 (s), 25.58 (s), 19.69 (s), 17.83 (s).

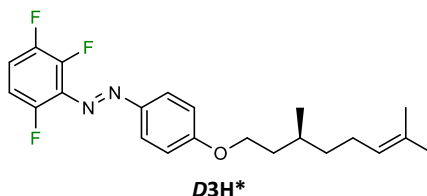
IR:  $\nu$  ( $\text{cm}^{-1}$ ) = 3089, 2968, 2952, 2907, 2873, 2846, 1600, 1578, 1499, 1467, 1452, 1414, 1378, 1339, 1295, 1254, 1206, 1145, 1112, 999, 943, 866, 836, 774, 751, 731, 711, 652, 600, 572, 551, 517, 441.

MS (ESI-pos, 14710):  $m/z$  (%) = 391.2003 (100,  $[\text{M}+\text{H}]^+$ ,  $[\text{C}_{22}\text{H}_{25}\text{F}_3\text{N}_2\text{O}+\text{H}]^+$ , calc.:  $m/z = 391.1992$ ).

CHN: calc. (%)  $\text{C}_{22}\text{H}_{25}\text{F}_3\text{N}_2\text{O}$ : C 67.7, H 6.45, N 7.17; found (%): C 68.3, H 6.99, N 7.64.

**6.3.3.2.8 (S,E)-1-[4'-((3,7-Dimethyloct-6-en-1-yl)oxy)phenyl]-2-(2,3,6-trifluorophenyl)diazene (D3H\*)**

Described experiment: ms-188



(E)-4'-((2,3,6-trifluorophenyl)diazenyl)phenol (200 mg, 0.79 mmol) yielded (S,E)-1-[4'-((3,7-dimethyloct-6-en-1-yl)oxy)phenyl]-2-(2,3,6-trifluorophenyl)diazene (**D3H\***) (82 mg (0.21 mmol, 26%) using Cy:EA ([95:5],  $R_f = 0.2$ ) for column chromatographic purification.

mp: <25 °C

$^1\text{H}$  NMR (400 MHz,  $\text{CDCl}_3$ ):  $\delta$  (ppm) = 8.24 – 8.18 (m, 2H), 7.57 – 7.50 (m, 1H), 7.30 – 7.21 (m, 3H), 5.41 – 5.33 (m, 1H), 4.41 – 4.30 (m, 2H), 2.38 – 2.19 (m, 2H), 2.19 – 2.09 (m, 1H), 2.04 – 1.84 (m, 8H), 1.73 – 1.62 (m, 1H), 1.57 – 1.45 (m, 1H), 1.24 (d,  $J = 6.5$  Hz, 3H).

$^{19}\text{F}$  NMR (376 MHz,  $\text{CDCl}_3$ ):  $\delta$  (ppm) = -114.69 – -114.86 (m, 1F), -133.25 – -133.41 (m, 1F), -153.86 – -154.05 (m, 1F).

$^{13}\text{C}$  NMR (101 MHz,  $\text{CDCl}_3$ ):  $\delta$  (ppm) = 163.05 (s), 157.66 (ddd,  $J = 246.7, 10.8, 3.3$  Hz), 151.37 (dt,  $J = 26.4, 13.0$  Hz), 146.84 (s), 145.36 (ddd,  $J = 255.7, 13.9, 4.6$  Hz), 142.55 – 142.16 (m), 131.59 (s), 125.88 (s), 124.70 (s), 115.04 (s), 106.49 (dd,  $J = 28.7, 21.2$  Hz), 99.50 (dd,  $J = 25.0, 3.6$  Hz), 66.94 (s), 37.24 (s), 36.11 (s), 29.63 (s), 25.88 (s), 25.58 (s), 19.69 (s), 17.83 (s).

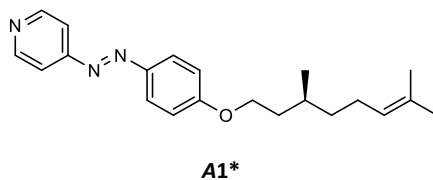
IR:  $\nu$  ( $\text{cm}^{-1}$ ) = 2959, 2921, 2874, 2854, 1599, 1580, 1497, 1456, 1416, 1379, 1312, 1299, 1252, 1138, 1107, 1050, 1024, 980, 955, 878, 838, 805, 750, 716, 633, 607, 556, 517, 447.

MS (ESI-pos, 12438):  $m/z$  (%) = 391.2004 (100,  $[\text{M}+\text{H}]^+$ ,  $[\text{C}_{22}\text{H}_{25}\text{F}_3\text{N}_2\text{O}+\text{H}]^+$ , calc.:  $m/z = 391.1992$ ).

CHN: calc. (%)  $\text{C}_{22}\text{H}_{25}\text{F}_3\text{N}_2\text{O}$ : C 67.7, H 6.45, N 7.17; found (%): C 69.2, H 6.46, N 8.05.

### 6.3.3.2.9 (*S,E*)-4-[(4'-((3,7-Dimethyloct-6-en-1-yl)oxy)phenyl)diazenyl]pyridine (**A1\***)

Described experiment: se-003



(*E*)-4-(pyridinyl)-diazenylphenol (2.21 g, 11.08 mmol) yielded (*S,E*)-4-[(4'-((3,7-dimethyloct-6-en-1-yl)oxy)phenyl)diazenyl]pyridine (**A1\***) (2.51 g, 7.43 mmol, 67%) using Cy:EA ([8:2],  $R_f = 0.2$ ) on silica for column chromatographic purification.

Analytical data was in accordance with the literature.<sup>[93]</sup>

$^1\text{H}$  NMR (300 MHz,  $\text{CDCl}_3$ ):  $\delta$  (ppm) = 8.84 – 8.71 (m, 2H), 8.02 – 7.89 (m, 2H), 7.72 – 7.65 (m, 2H), 7.06 – 6.93 (m, 2H), 5.17 – 5.04 (m, 1H), 4.18 – 4.01 (m, 2H), 2.12 – 1.95 (m, 2H), 1.93 – 1.80 (m, 1H), 1.78 – 1.54 (m, 8H), 1.49 – 1.34 (m, 1H), 1.33 – 1.17 (m, 1H), 0.98 (d,  $J = 6.4$  Hz, 3H).

$^{13}\text{C}$  NMR (75 MHz,  $\text{CDCl}_3$ ):  $\delta$  (ppm) = 163.27 (s), 158.04 (s), 150.63 (s), 146.92 (s), 131.59 (s), 125.91 (s), 124.70 (s), 116.55 (s), 115.11 (s), 67.01 (s), 37.25 (s), 36.12 (s), 29.67 (s), 25.87 (s), 25.59 (s), 19.70 (s), 17.83 (s).

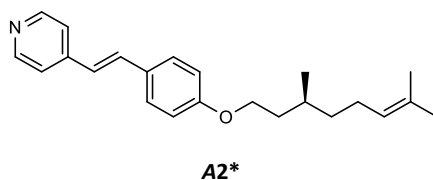
IR:  $\nu$  ( $\text{cm}^{-1}$ ) = 3044, 2965, 2903, 2874, 2845, 1597, 1584, 1565, 1499, 1472, 1452, 1408, 1379, 1319, 1296, 1256, 1227, 1142, 1101, 1005, 988, 939, 924, 839, 797, 787, 739, 719, 662, 631.

MS (ESI-pos, 10403):  $m/z$  (%) = 338.2228 [100 %] ( $[\text{C}_{21}\text{H}_{27}\text{N}_3\text{O}] + \text{H}^+$ , calc.:  $m/z = 338.2227$ ).

CHN: calc. (%)  $\text{C}_{21}\text{H}_{27}\text{N}_3\text{O}$ : C 74.8, H 8.06, N 12.45; found (%): C 75.8, H 8.57, N 13.8.

### 6.3.3.2.10 (*S,E*)-4-(4-((3,7-dimethyloct-6-en-1-yl)oxy)styryl)pyridine (**A2\***)

Described experiment: se-012



(*E*)-(2-(4-pyridinyl)ethenyl)phenol (1.08 g, 5.48 mmol) yielded (*S,E*)-4-(4-((3,7-dimethyloct-6-en-1-yl)oxy)styryl)pyridine (**A2\***) (1.02 g, 3.02 mmol, 55%) after column chromatographic purification using Cy:EA ([1:1],  $R_f = 0.2$ ) and recrystallization from methanol.

Analytical data was in accordance with the literature.<sup>[29]</sup>

$^1\text{H}$  NMR (300 MHz,  $\text{CDCl}_3$ ):  $\delta$  8.54 (dd,  $J = 4.7, 1.5$  Hz, 2H), 7.51 – 7.44 (m, 2H), 7.36 (d,  $J = 5.9$  Hz, 2H), 7.27 (d,  $J = 16.3$  Hz, 1H), 6.94 – 6.81 (m, 3H), 5.15 – 5.06 (m, 1H), 4.07 – 3.98 (m, 2H), 2.12 – 1.94 (m, 2H), 1.90 – 1.78 (m, 1H), 1.76 – 1.54 (m, 8H), 1.50 – 1.31 (m, 1H), 1.31 – 1.13 (m, 1H), 0.96 (d,  $J = 6.4$  Hz, 3H).

$^{13}\text{C}$  NMR (75 MHz,  $\text{CDCl}_3$ ):  $\delta$  159.08 (s), 149.66 (s), 131.48 (s,  $J = 1.8$  Hz), 130.30 (s), 128.62 (s,  $J = 17.6$  Hz), 125.87 (s), 124.77 (s), 123.71 (s,  $J = 16.5$  Hz), 120.86 (s), 115.04 (s), 114.55 (s), 66.45 (s,  $J = 11.1$  Hz), 37.27 (s), 36.23 (s), 29.69 (s), 25.86 (s), 25.60 (s), 19.71 (s), 17.81 (s).

IR:  $\nu$  ( $\text{cm}^{-1}$ ) = 3025, 2959, 2930, 2882, 2849, 1587, 1547, 1510, 1474, 1455, 1412, 1389, 1327, 1306, 1281, 1252, 1175, 1113, 1057, 1009, 970, 937, 878, 853, 831, 814, 772, 739, 665, 633.

MS (ESI-pos, 10441):  $m/z$  (%) = 336.2330 (100,  $[\text{M}+\text{H}]^+$ ,  $[\text{C}_{23}\text{H}_{29}\text{NO}+\text{H}]^+$ , calc.:  $m/z = 336.2322$ ).

CHN: calc. (%)  $\text{C}_{23}\text{H}_{29}\text{NO}$ : C 82.3, H 8.71, N 4.18; found (%): C 78.1, H 8.37, N 4.64.

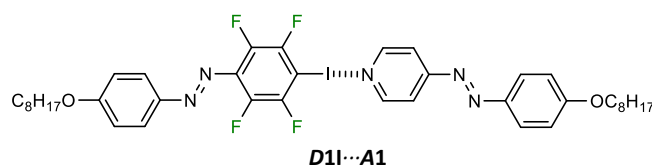
### 6.3.4 Formation of Halogen-Bonded Complexes

For the formation of the XB-bonded complexes the respective XB-acceptor and XB-donor were weighed separately in an equimolar ratio, dissolved in DCM and the solutions combined. Upon solvent removal and drying under vacuum, the halogen-bonded complexes were obtained in quantitative yields.

#### 6.3.4.1 Complexes with A1

##### 6.3.4.1.1 $D11 \cdots A1$

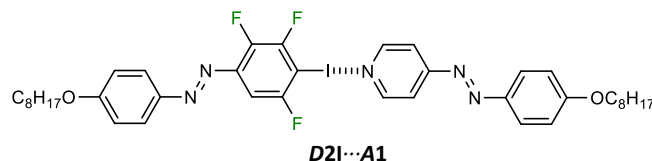
Experiment number: msLC-049, MSC-XB6, A-P



IR:  $\nu$  ( $\text{cm}^{-1}$ ) = 2922, 2855, 1602, 1579, 1499, 1469, 1446, 1406, 1318, 1298, 1252, 1176, 1138, 1110, 1042, 1025, 997, 979, 923, 888, 841, 795, 759, 738, 720.

**6.3.4.1.2 D2I...A1**

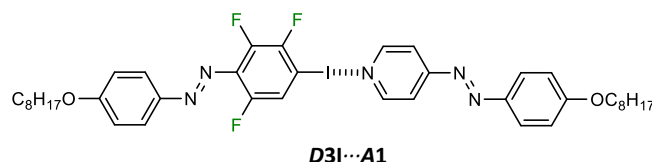
Experiment number: msLC-074, MSC-XB9, D-P



IR:  $\nu$  (cm<sup>-1</sup>) = 2921, 2854, 1602, 1582, 1499, 1466, 1408, 1335, 1317, 1299, 1251, 1176, 1140, 1110, 1027, 997, 940, 923, 900, 864, 840, 810, 796, 759, 722, 680.

**6.3.4.1.3 D3I...A1**

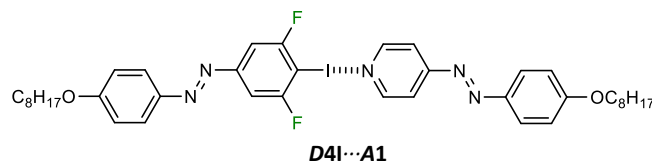
Experiment number: MSC-XB7, B-P



IR:  $\nu$  (cm<sup>-1</sup>) = 3050, 2922, 2852, 1602, 1580, 1500, 1468, 1405, 1318, 1298, 1252, 1177, 1141, 1108, 1092, 1060, 1030, 996, 970, 923, 875, 837, 795, 761, 723.

**6.3.4.1.4 D4I...A1**

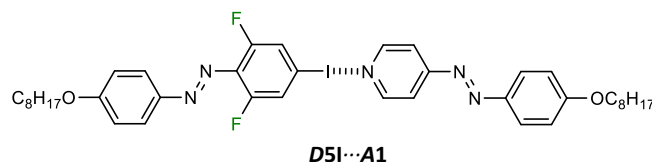
Experiment number: msLC-073, C-P, MSC-XB8



IR:  $\nu$  (cm<sup>-1</sup>) = 3069, 3035, 2921, 2853, 1601, 1582, 1499, 1469, 1418, 1405, 1318, 1298, 1252, 1174, 1140, 1109, 1043, 1021, 997, 924, 867, 843, 815, 795, 758, 722, 697.

**6.3.4.1.5 D5I...A1**

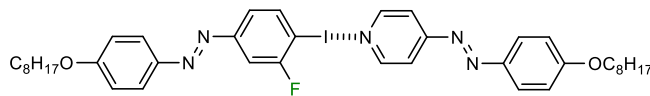
Experiment number: MSC-XB10, E-P



IR:  $\nu$  (cm<sup>-1</sup>) = 3074, 3047, 2939, 2920, 2853, 1599, 1578, 1500, 1469, 1418, 1403, 1319, 1304, 1260, 1202, 1142, 1109, 1048, 1026, 996, 923, 841, 796, 759, 723.

**6.3.4.1.6 D6I...A1**

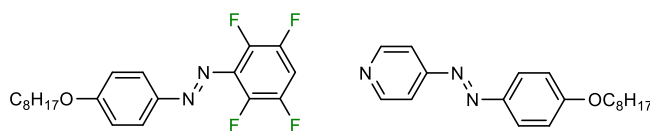
Experiment number: MSC-XB11, G-P

**D6I...A1**

IR:  $\nu$  (cm<sup>-1</sup>) = 3071, 3035, 2920, 2852, 2579, 2489, 2160, 2034, 1978, 1602, 1582, 1498, 1467, 1416, 1404, 1318, 1298, 1250, 1139, 1108, 1043, 1025, 995, 877, 841, 817, 796, 756, 722, 695, 661.

**6.3.4.1.7 D1H...A1**

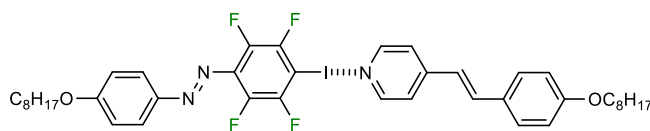
Experiment number: F-P

**D1H...A1**

IR:  $\nu$  (cm<sup>-1</sup>) = 2923, 2854, 1580, 1509, 1409, 1300, 1252, 1206, 1139, 1025, 997, 958, 901, 876, 844, 796, 761, 721.

**6.3.4.2 Complexes with A2****6.3.4.2.1 D1I...A2**

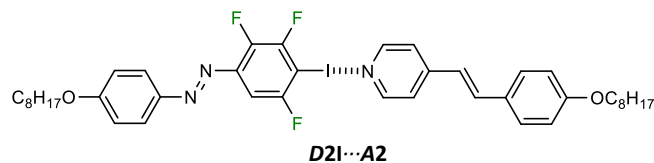
Experiment number: msLC-027, msLC-048, A-S

**D1I...A2**

IR:  $\nu$  (cm<sup>-1</sup>) = 3035, 2921, 2851, 1626, 1594, 1577, 1511, 1473, 1445, 1410, 1392, 1374, 1321, 1281, 1245, 1209, 1196, 1176, 1141, 1106, 1040, 1000, 975, 885, 826, 791, 758, 723.

**6.3.4.2.2 D2I...A2**

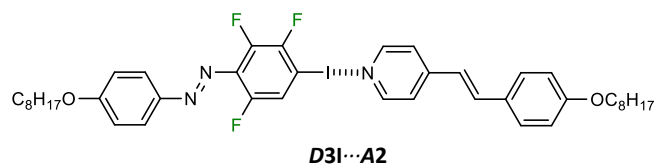
Experiment number: msLC-026, MSC-XB3, D-S



IR:  $\nu$  (cm<sup>-1</sup>) = 3072, 3039, 2922, 2852, 1595, 1500, 1467, 1410, 1391, 1335, 1315, 1298, 1281, 1245, 1177, 1142, 1109, 1067, 1026, 999, 970, 900, 854, 826, 810, 758, 723, 680.

**6.3.4.2.3 D3I...A2**

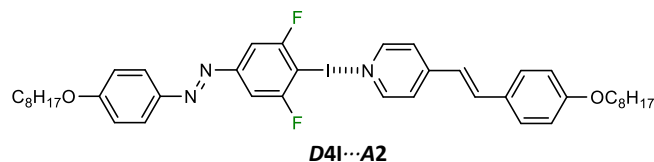
Experiment number: msLC-025, MSC-XB1, B-S



IR:  $\nu$  (cm<sup>-1</sup>) = 3075, 3039, 2921, 2852, 1631, 1591, 1500, 1466, 1444, 1427, 1392, 1313, 1282, 1251, 1194, 1174, 1142, 1107, 1090, 1059, 1029, 997, 968, 874, 825, 793, 745, 723.

**6.3.4.2.4 D4I...A2**

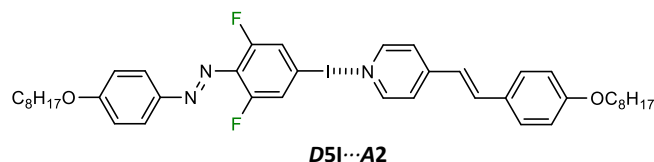
Experiment number: msLC-072, MSC-XB2, C-S



IR:  $\nu$  (cm<sup>-1</sup>) = 3075, 3039, 2921, 2850, 1594, 1578, 1512, 1500, 1469, 1418, 1405, 1312, 1281, 1246, 1210, 1176, 1145, 1105, 1065, 1017, 999, 965, 861, 824, 793, 758, 723, 690.

**6.3.4.2.5 D5I...A2**

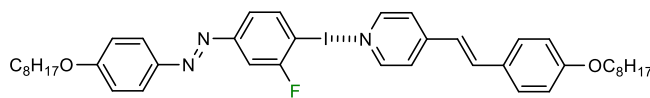
Experiment number: MSC-XB4, E-S



IR:  $\nu$  (cm<sup>-1</sup>) = 3069, 3026, 2919, 2853, 1590, 1512, 1469, 1417, 1403, 1282, 1254, 1174, 1141, 1109, 1047, 1028, 994, 966, 874, 845, 827, 760, 724.

**6.3.4.2.6 D6I...A2**

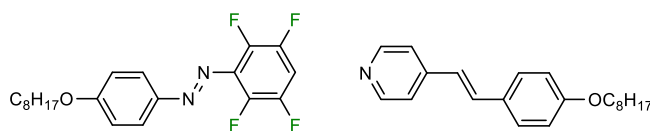
Experiment number: MSC-XB5, G-S

**D6I...A2**

IR:  $\nu$  (cm<sup>-1</sup>) = 3072, 3050, 2952, 2923, 2868, 2853, 1593, 1581, 1513, 1498, 1463, 1415, 1394, 1317, 1281, 1241, 1194, 1178, 1147, 1111, 1029, 995, 968, 873, 845, 825, 791, 758, 724, 698, 662.

**6.3.4.2.7 D1H...A2**

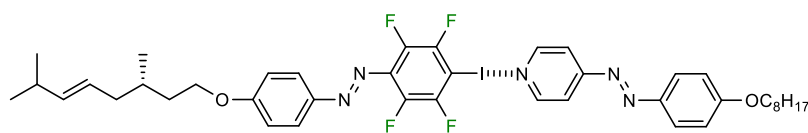
Experiment number: F-S

**D1H...A2**

IR:  $\nu$  (cm<sup>-1</sup>) = 3072, 3024, 2922, 2853, 1631, 1590, 1550, 1509, 1472, 1454, 1412, 1375, 1302, 1281, 1253, 1207, 1176, 1146, 1112, 1066, 1025, 994, 957, 902, 875, 844, 831, 814, 761, 722, 703.

**6.3.4.3 Chiral Complexes with A1****6.3.4.3.1 D11\*...A1**

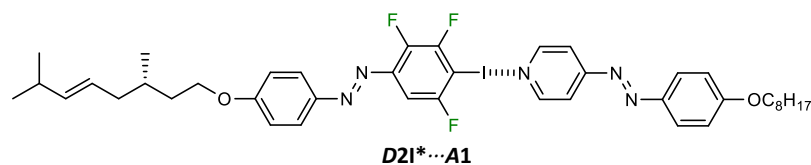
Experiment number: msLC-035, se-015

**D11\*...A1**

IR:  $\nu$  (cm<sup>-1</sup>) = 3073, 3048, 3031, 2953, 2918, 2853, 1599, 1580, 1499, 1474, 1447, 1406, 1387, 1316, 1298, 1246, 1175, 1136, 1109, 1044, 999, 978, 920, 887, 872, 837, 795, 773, 737, 721, 633, 619.

**6.3.4.3.2 D2I\*...A1**

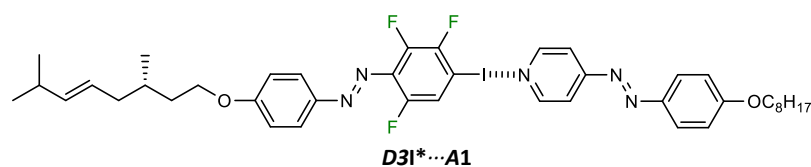
Experiment number: se-007



IR:  $\nu$  (cm<sup>-1</sup>) = 3046, 2951, 2922, 2870, 2853, 1599, 1580, 1499, 1466, 1406, 1333, 1317, 1296, 1248, 1179, 1138, 1107, 1028, 997, 980, 941, 924, 860, 833, 797, 723, 681, 633.

**6.3.4.3.3 D3I\*...A1**

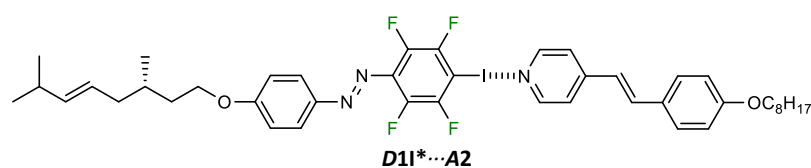
Experiment number: msLC-036



IR:  $\nu$  (cm<sup>-1</sup>) = 3036, 2951, 2917, 2867, 2854, 1597, 1579, 1499, 1466, 1447, 1414, 1403, 1375, 1317, 1296, 1242, 1139, 1106, 1090, 1058, 1018, 995, 970, 857, 835, 797, 736, 723, 631, 597, 548, 526, 497, 478, 432.

**6.3.4.4 Chiral Complexes with A2****6.3.4.4.1 D1I\*...A2**

Experiment number: msLC-031



IR:  $\nu$  (cm<sup>-1</sup>) = 3043, 2959, 2920, 2871, 2851, 1592, 1502, 1470, 1455, 1418, 1390, 1379, 1309, 1296, 1282, 1250, 1208, 1195, 1176, 1147, 1113, 1102, 1065, 1044, 1023, 997, 969, 891, 876, 832, 787, 775, 724, 616, 579, 563, 547, 527, 479, 456, 424.

### 6.3.4.4.2 *D2I\*...A2*

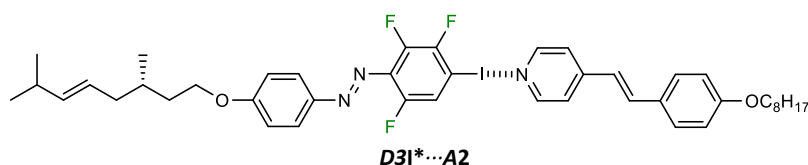
Experiment number: msLC-138, se-016



IR:  $\nu$  ( $\text{cm}^{-1}$ ) = 3077, 3040, 2926, 2868, 2853, 1595, 1574, 1512, 1499, 1466, 1424, 1406, 1379, 1337, 1314, 1283, 1246, 1204, 1175, 1140, 1107, 1069, 1026, 999, 968, 953, 855, 826, 806, 731, 679, 631, 610.

### 6.3.4.4.3 *D3I\*...A2*

Experiment number: msLC-032

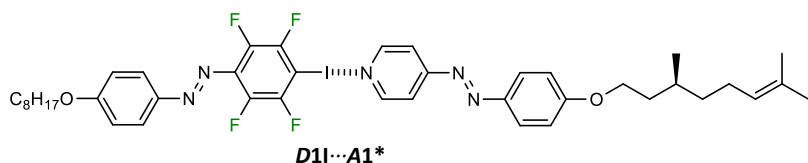


IR:  $\nu$  ( $\text{cm}^{-1}$ ) = 3071, 3029, 2917, 2852, 1602, 1589, 1575, 1550, 1512, 1499, 1463, 1427, 1406, 1394, 1377, 1313, 1281, 1251, 1207, 1193, 1176, 1142, 1108, 1060, 1032, 1017, 996, 966, 939, 873, 852, 833, 821, 792, 760, 727, 657, 641, 629, 615, 545, 523, 479, 437.

## 6.3.4.5 Chiral Complexes with *A1\**

### 6.3.4.5.1 *D1I...A1\**

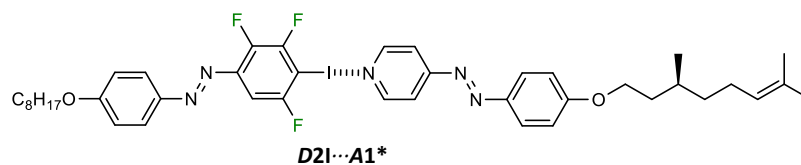
Experiment number: se-008



IR:  $\nu$  ( $\text{cm}^{-1}$ ) = 2924, 2853, 1601, 1580, 1499, 1472, 1447, 1408, 1379, 1321, 1298, 1246, 1142, 1105, 1044, 1015, 997, 976, 887, 833, 795, 739, 723, 631, 619.

### 6.3.4.5.2 D2I...A1\*

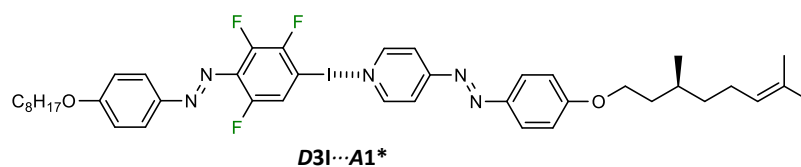
Experiment number: se-009



IR:  $\nu$  (cm<sup>-1</sup>) = 3080, 3048, 2922, 2869, 2851, 1601, 1582, 1499, 1468, 1408, 1335, 1317, 1298, 1246, 1202, 1142, 1107, 1028, 1017, 997, 941, 862, 835, 810, 739, 723, 679, 633.

### 6.3.4.5.3 D3I...A1\*

Experiment number: msLC-037, se-010

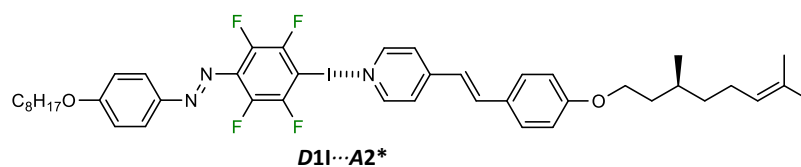


IR:  $\nu$  (cm<sup>-1</sup>) = 2922, 2868, 2853, 1601, 1580, 1497, 1468, 1443, 1406, 1379, 1319, 1298, 1246, 1180, 1140, 1105, 1090, 1057, 1030, 1015, 997, 968, 941, 835, 793, 739, 721, 658, 635, 615.

### 6.3.4.6 Chiral Complexes with A2\*

#### 6.3.4.6.1 D1I...A2\*

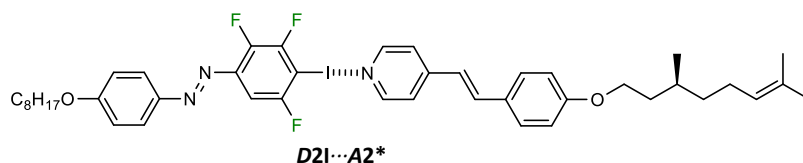
Experiment number: se-024



IR:  $\nu$  (cm<sup>-1</sup>) = 3036, 2920, 2869, 2853, 1626, 1593, 1577, 1510, 1499, 1474, 1447, 1420, 1393, 1316, 1279, 1244, 1196, 1175, 1142, 1105, 1020, 999, 974, 885, 837, 827, 792, 737, 723, 631, 619.

### 6.3.4.6.2 D2I...A2\*

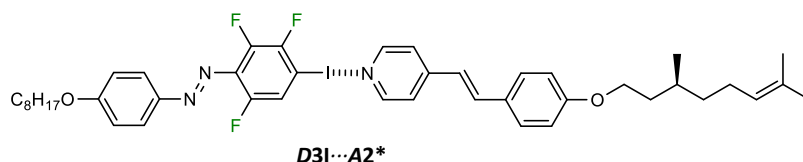
Experiment number: msLC-039



IR:  $\nu$  (cm<sup>-1</sup>) = 3071, 3035, 2924, 2869, 2854, 1595, 1576, 1512, 1500, 1466, 1424, 1409, 1392, 1378, 1334, 1315, 1298, 1280, 1246, 1178, 1142, 1108, 1067, 1027, 998, 969, 855, 837, 826, 809, 782, 758, 723, 679, 640, 630, 582, 568, 542, 523, 446, 434.

### 6.3.4.6.3 D3I...A2\*

Experiment number: msLC-038, se-027



IR:  $\nu$  (cm<sup>-1</sup>) = 3028, 2946, 2918, 2867, 2853, 1591, 1574, 1510, 1501, 1462, 1444, 1416, 1310, 1254, 1215, 1175, 1140, 1088, 1055, 1030, 1019, 997, 966, 877, 833, 793, 739, 725, 633, 611.

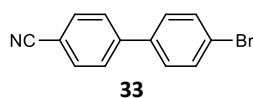
## 6.3.5 Synthesis of Chiral Dopants for Sensing Applications

### 6.3.5.1 Synthesis of 4-Cyanobiphenyl-4'-boronic acid pinacol ester (**34**)

4-Cyanobiphenyl-4'-boronic acid pinacol ester was synthesized according to a modified procedure which was already reported in the literature.<sup>[206]</sup>

#### 6.3.5.1.1 4'-Bromo-[1,1'-biphenyl]-4-carbonitrile (**33**)

Described experiment: ms-249, repeated: ms-254



4,4'-Dibromo-1,1'-biphenyl (**32**) (3.30 g, 10.50 mmol) and copper(I) cyanide (0.94 g, 10.50 mmol) were refluxed in DMF (30 mL) for 6 h.

The reaction progress was followed by TLC using Cy:DCM [1:1];  $R_f = 0.3$ . After 3h the reaction was quenched with aq. FeSO<sub>4</sub> solution. The mixture was extracted with CHCl<sub>3</sub> (6x30 mL) and the combined organic layers dried over MgSO<sub>4</sub>. Purification by silica gel column chromatography (Cy:DCM [2:1],  $R_f = 0.2$ ) yielded **33** in 48% yield (1.19 g, 4.61 mmol).



$^1\text{H}$  NMR (300 MHz,  $\text{CDCl}_3$ ):  $\delta$  (ppm) = 11.47 (s, 1H), 9.70 (s, 1H), 7.41 (d,  $J = 8.7$ , 1H), 6.53 (dd,  $J = 8.6, 2.3$ , 1H), 6.41 (d,  $J = 2.3$ , 1H), 4.00 (t,  $J = 6.6$ , 2H), 1.85 – 1.73 (m, 2H), 1.50 – 1.23 (m, 10H), 0.89 (t,  $J = 6.8$ , 3H).

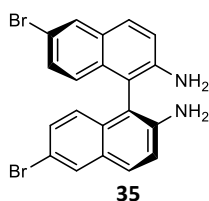
$^{13}\text{C}$  NMR (75 MHz,  $\text{CDCl}_3$ ):  $\delta$  (ppm) = 194.43 (s), 166.64 (s), 164.70 (s), 135.34 (s), 115.19 (s), 108.94 (s), 101.24 (s), 68.78 (s), 31.93 (s), 29.41 (s), 29.33 (s), 29.08 (s), 26.07 (s), 22.79 (s), 14.22 (s).

### 6.3.5.3 Synthesis of boc-Protected Precursors 37 and 43

#### 6.3.5.3.1 (*S*)-6,6'-Dibromo-[1,1'-binaphthalene]-2,2'-diamine (35)

Described experiment: SS1, repeated: ms-250, ms-264, ms-277

(*S*)-6,6'-dibromo-[1,1'-binaphthalene]-2,2'-diamine **35** was synthesized according to a literature known procedure.<sup>[204]</sup>



To a solution of (*S*)-**30** (2.00 g, 7.03 mmol) in 1,4-dioxane (70 mL) was added *N*-bromosuccinimide (3.73 g, 21.10 mmol), and the mixture was stirred at ambient temperature for 2 h. The Reaction progress was monitored by TLC (Cy:EA [2:1],  $R_f = 0.3$ ). The reaction was quenched with sat.  $\text{Na}_2\text{S}_2\text{O}_3$  solution (70 mL), and the aqueous layer extracted with EA (6 x 50 mL). The combined organic layers and extracts were washed with  $\text{H}_2\text{O}$  (2 x 50 mL) and brine (2 x 50 mL), dried over  $\text{MgSO}_4$ , and concentrated to dryness. The residue was purified by column chromatography on silica gel using DCM as eluent ( $R_f = 0.3$ ), to give **35** in 43% yield (1.34 g, 3.03 mmol).

The analytical data was in accordance with the literature.<sup>[204]</sup>

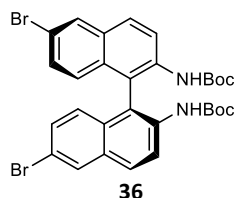
$^1\text{H}$  NMR (300 MHz,  $\text{CDCl}_3$ ):  $\delta$  (ppm) = 7.94 (s, 2H), 7.72 (d,  $J = 8.7$ , 2H), 7.32 – 7.24 (m, 2H), 7.17 (d,  $J = 8.8$ , 2H), 6.88 (d,  $J = 9.0$ , 2H), 3.67 (s, 4H).

$^{13}\text{C}$  NMR (75 MHz,  $\text{CDCl}_3$ ):  $\delta$  (ppm) = 143.02 (s), 132.28 (s), 130.31 (s), 129.78 (s), 129.01 (s), 125.80 (s), 119.47 (s), 116.33 (s), 112.14 (s).

### 6.3.5.3.2 (*S*)-Di-tert-butyl-(6,6'-dibromo-[1,1'-binaphthalene]-2,2'-diyl)dicarbamate (**36**)

Described experiment: SS2, repeated: ms-266, ms-280

(*S*)-di-tert-butyl-(6,6'-dibromo-[1,1'-binaphthalene]-2,2'-diyl)dicarbamate (**36**) was synthesized according to a modified literature known procedure.<sup>[205]</sup>



To a solution of **35** (1.05 g, 2.23 mmol) in dry THF (25 mL) was added 2M NaHMDS solution in THF (5.7 mL, 11.42 mmol) at rt and the reaction mixture was stirred at rt for 1 h. The reaction progress was followed by TLC (Cy:DCM [1:2]). Subsequently, a solution of Boc<sub>2</sub>O (1.49 g, 6.48 mmol) in THF (25 mL) was added dropwise at 0°C. The resulting mixture was stirred at rt and the reaction progress again followed by TLC (Cy:DCM [1:2]). Upon full conversion, the solvent was removed under reduced pressure, the dark residue was dissolved in dichloromethane (35 mL) and washed with water (70 mL). The organic layer was separated, and the aqueous layer was extracted with dichloromethane (5 x 25 mL). The combined organic layers were washed with brine (20 mL), dried over MgSO<sub>4</sub> and concentrated under reduced pressure to give a dark residue. The obtained crude product was purified by silica gel column chromatography using Cy:DCM ([1:2], R<sub>f</sub> = 0.3) as eluent to obtain **36** in 61% yield (0.94 g, 1.46 mmol) as a pale brown solid.

<sup>1</sup>H NMR (300 MHz, CDCl<sub>3</sub>): δ (ppm) = 8.57 (d, *J* = 9.2, 2H), 8.07 (d, *J* = 2.0, 2H), 7.94 (d, *J* = 9.2, 2H), 7.31 (dd, *J* = 9.0, 2.0, 2H), 6.78 (d, *J* = 9.0, 2H), 6.07 (s, 2H), 1.39 (s, 18H).

<sup>13</sup>C NMR (75 MHz, CDCl<sub>3</sub>): δ (ppm) = 152.92 (s), 136.32 (s), 131.73 (s), 131.15 (s), 130.79 (s), 130.47 (s), 129.41 (s), 126.64 (s), 121.06 (s), 119.14 (s), 117.34 (s), 81.50 (s), 28.29 (s).

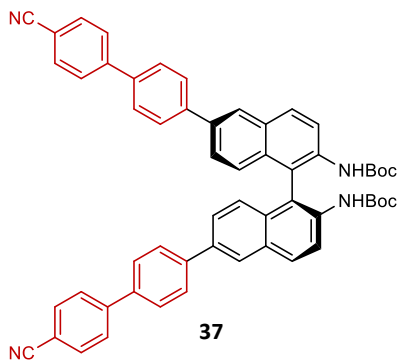
IR:  $\nu$  (cm<sup>-1</sup>) = 3408., 3007, 2982, 2933, 1728, 1587, 1487, 1448, 1388, 1364, 1327, 1287, 1225, 1144, 1080, 959, 913, 882, 818, 763, 677, 603, 578, 475, 425.

MS (ESI-pos, 14117): *m/z* (%) = 665.0450 (100, [M+Na]<sup>+</sup>, [C<sub>30</sub>H<sub>30</sub>Br<sub>2</sub>N<sub>2</sub>O<sub>2</sub>+Na]<sup>+</sup>, calc.: *m/z* = 665.0447).

### 6.3.5.3.3 (*S*)-Di-boc-BINAM-CB (**37**)<sup>[246]</sup>

Described experiment: SS3A, repeated: ms-263, ms-270, ms-282

(*S*)-di-boc-BINAP-CB (**37**) was synthesized according to a modified literature known procedure.<sup>[246]</sup>



**36** (316 mg, 0.49 mmol), **34** (350 mg, 1.14 mmol) and NaHCO<sub>3</sub> (257 mg, 3.06 mmol) were dissolved in 20 mL degassed THF/H<sub>2</sub>O (4:1) and Pd(TPP)<sub>4</sub> (120 mg, 0.10 mmol) was added. The mixture was refluxed overnight at 75 °C and the reaction progress was monitored by TLC (Cy:DCM [1:3] R<sub>f</sub> = 0.2). Upon full conversion, the mixture was cooled to room temperature and extracted with DCM (3 x 20 mL). The organic layer was washed with brine (20 mL) and dried over MgSO<sub>4</sub>. Purification by silica gel column chromatography (Cy:DCM [1:9] R<sub>f</sub> = 0.15 and Cy:EA [4:1] R<sub>f</sub> = 0.5) afforded **37** in 97% Yield (409 mg, 0.48 mmol) as a pale brown powder.

<sup>1</sup>H NMR (600 MHz, CDCl<sub>3</sub>): δ (ppm) = 8.61 (d, *J* = 9.1, 2H), 8.20 (d, *J* = 1.8, 2H), 8.14 (d, *J* = 9.2, 2H), 7.82 – 7.79 (m, 4H), 7.75 (s, 8H), 7.72 – 7.69 (m, 4H), 7.57 (dd, *J* = 8.8, 1.9, 2H), 7.10 (d, *J* = 8.8, 2H), 6.23 (s, 2H), 1.41 (s, 18H).

<sup>13</sup>C NMR (151 MHz, CDCl<sub>3</sub>): δ (ppm) = 153.09 (s), 145.19 (s), 141.10 (s), 138.22 (s), 136.67 (s), 136.24 (s), 132.83 (s), 132.22 (s), 130.94 (s), 130.59 (s), 127.97 (s), 127.91 (s), 127.71 (s), 126.67 (s), 126.34 (s), 125.86 (s), 120.56 (s), 119.07 (s), 116.19 (s), 111.14 (s), 81.34 (s), 28.33 (s).

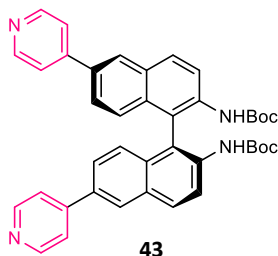
IR: ν (cm<sup>-1</sup>) = 3409, 3323, 2976, 2930, 2225, 1719, 1599, 1484, 1456, 1392, 1365, 1315, 1266, 1226, 1150, 1094, 1059, 1002, 964, 922, 883, 813, 762, 730, 692, 616, 592, 556, 519, 456, 430.

MS (ESI-pos, 13619): *m/z* (%) = 861.3415, (100, [M+Na]<sup>+</sup>, [C<sub>56</sub>H<sub>46</sub>N<sub>4</sub>O<sub>4</sub>+Na]<sup>+</sup>, calc.: *m/z* = 861.3411).

### 6.3.5.3.4 (*S*)-Di-boc-BINAM-Py (**43**)

Described experiment: SS3B, repeated: ms-286

(*S*)-Di-boc-BINAP-Py (**43**) was synthesized according to a modified literature known procedure.<sup>[247]</sup>



**36** (405 mg, 0.63 mmol), 4-pyridinylboronic acid (404 mg, 3.29 mmol) and  $K_2CO_3$  (442 mg, 3.20 mmol) were dissolved in 20 mL degassed THF/ $H_2O$  (4:1) and  $Pd(dppf)Cl_2$  (94 mg, 0.12 mmol) was added. The mixture was refluxed for overnight at 70 °C and the reaction progress was monitored by TLC (Cy:EA:NEt<sub>3</sub> [3:6:1]  $R_f=0.2$ ). Upon full conversion, the mixture was

cooled to room temperature and extracted with DCM (3 x 50 mL). The organic layer was washed with brine (20 mL) and dried over  $MgSO_4$ . Purification by silica gel column chromatography (Cy:EA:NEt<sub>3</sub> [3:6:1]  $R_f=0.2$ ) afforded **43** in 91% Yield (361 mg, 0.56 mmol) as a pale brown powder.

<sup>1</sup>H NMR (300 MHz,  $CDCl_3$ ):  $\delta$  (ppm) = 8.77 – 8.61 (m, 6H), 8.26 (s, 2H), 8.17 (d,  $J = 9.1$ , 2H), 7.70 (s, 4H), 7.55 (d,  $J = 8.1$ , 2H), 7.09 (d,  $J = 8.3$ , 2H), 6.21 (s, 2H), 1.40 (s, 18H).

<sup>13</sup>C NMR (151 MHz,  $CDCl_3$ ):  $\delta$  (ppm) = 152.85 (s), 148.22 (s), 137.41 (s), 133.50 (s), 133.25 (s), 131.23 (s), 130.62 (s), 127.76 (s), 126.24 (s), 125.92 (s), 122.44 (s), 120.93 (s), 116.95 (s), 81.69 (s), 28.29 (s).

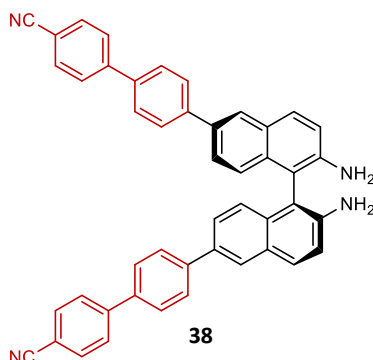
IR:  $\tilde{\nu}$  ( $cm^{-1}$ ) = 3409, 3063, 3025, 2974, 2929, 2873, 1715, 1592, 1518, 1487, 1456, 1414, 1391, 1366, 1334, 1269, 1225, 1149, 1061, 994, 964, 926, 884, 810, 771, 738, 704, 687, 616, 556, 524, 460, 427.  
MS (ESI-pos, 14199):  $m/z$  (%) = 320.1522 (16.9,  $[M+H]^{2+}$ ,  $[C_{40}H_{38}N_4O_4+2H]^{2+}$ , calc.:  $m/z = 320.1519$ ).

### 6.3.5.4 Synthesis of (*S*)-BINAM-CB (**38**) and (*S*)-BINAM-Py (**43**)

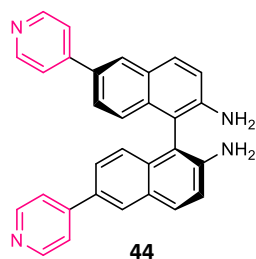
To a solution of the respective boc-protected amine (**37** or **43**) in DCM was added  $CF_3COOH$  (180 eq) at 0°C. The reaction mixture was stirred at rt and the reaction progress monitored by TLC (Cy:EA [1:2] (**38**); EA [100%] (**44**)). Upon full conversion, the reaction mixture was basified using aqueous  $K_2CO_3$  solution followed by extraction with DCM. The organic layers were dried over  $MgSO_4$  and concentrated to dryness. The crude products of **38** and **44** were used as obtained without further purification.

**6.3.5.4.1 (S)-BINAM-CB (38)**

Described experiment: ms-305, repeated: ms-276, ms-285

**37** (364 mg, 0.43 mmol) yielded the desired product **38** (246 mg, 0.38 mmol, 89%). $^1\text{H}$  NMR (300 MHz,  $\text{CDCl}_3$ ):  $\delta$  (ppm) = 8.08 (d,  $J$  = 1.5, 2H), 7.92 (d,  $J$  = 8.8, 2H), 7.81 – 7.64 (m, 18H), 7.54 (dd,  $J$  = 8.8, 1.9, 2H), 7.26 (d,  $J$  = 8.7, 2H), 7.22 (d,  $J$  = 8.8, 2H), 3.20 (s, 4H). $^{13}\text{C}$  NMR (151 MHz,  $\text{CDCl}_3$ ):  $\delta$  (ppm) = 145.29 (s), 143.23 (s), 141.68 (s), 137.59 (s), 134.21 (s), 133.30 (s), 132.76 (s), 130.20 (s), 128.83 (s), 127.77 (s,  $J$  = 4.7), 127.74 (s), 127.60 (s), 126.44 (s,  $J$  = 18.7), 126.32 (s), 124.79 (s), 119.09 (s), 112.36 (s), 110.91 (s).IR:  $\nu$  ( $\text{cm}^{-1}$ ) = 3472, 3370, 3197, 3033, 2922, 2852, 2224, 1910, 1777, 1601, 1524, 1490, 1434, 1384, 1359, 1286, 1267, 1247, 1178, 1118, 1096, 1024, 1001, 964, 930, 888, 857, 814, 724, 691, 559, 534, 423.MS (ESI-pos, 14197):  $m/z$  (%) = 639.2546 (100,  $[\text{M}+\text{H}]^+$ ,  $\text{C}_{46}\text{H}_{30}\text{N}_4+\text{H}^+$ , calc.:  $m/z$  = 639.2543).**6.3.5.4.2 (S)-BINAM-Py (44)**

Described experiment: ms-306, repeated: ms-289

**43** (374 mg, 0.58 mmol) yielded the desired product **44** (173 mg, 0.39 mmol, 68%). $^1\text{H}$  NMR (300 MHz,  $\text{CDCl}_3$  :  $\text{CD}_3\text{OD}$  [10: 1]):  $\delta$  (ppm) = 8.55 (d,  $J$  = 6.1, 4H), 8.08 (d,  $J$  = 1.7, 2H), 7.89 (d,  $J$  = 8.8, 2H), 7.59 (d,  $J$  = 6.2, 4H), 7.47 (dd,  $J$  = 8.8, 1.9, 2H), 7.21 (d,  $J$  = 8.8, 2H), 7.16 (d,  $J$  = 8.8, 2H).

$^1\text{H}$  NMR (300 MHz,  $\text{CDCl}_3$ ):  $\delta$  (ppm) = 8.66 (d,  $J$  = 5.2, 4H), 8.12 (d,  $J$  = 1.7, 2H), 7.93 (d,  $J$  = 8.8, 2H), 7.63 (d,  $J$  = 5.1, 4H), 7.52 (dd,  $J$  = 8.8, 1.9, 2H), 7.24 (d,  $J$  = 8.9, 2H), 7.19 (s, 2H), 3.66 (s, 4H).

$^{13}\text{C}$  NMR (151 MHz,  $\text{CDCl}_3$ ):  $\delta$  (ppm) = 149.39 (s), 144.01 (s), 134.15 (s), 131.43 (s), 130.52 (s), 128.48 (s), 127.11 (s), 125.45 (s), 124.93 (s), 121.75 (s), 119.22 (s), 111.80 (s).

IR:  $\nu$  ( $\text{cm}^{-1}$ ) = 3438, 3289, 3157, 3024, 1919, 1616, 1589, 1545, 1488, 1475, 1414, 1385, 1361, 1295, 1251, 1220, 1187, 1122, 1067, 1034, 994, 956, 931, 890, 845, 809, 732, 687, 657, 628, 601, 565, 514, 490, 427.

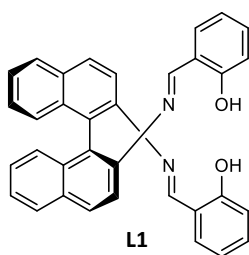
MS (ESI-pos, 14198):  $m/z$  (%) = 220.0999 (100,  $[\text{M}+\text{H}]^{2+}$ ,  $[\text{C}_{30}\text{H}_{22}\text{N}_4+2\text{H}]^{2+}$ , calc.:  $m/z$  = 220.0995).

### 6.3.6 Synthesis of BINIM Dopants L1 – L4

#### 6.3.6.1 L1

Described experiment: ms-291

**L1** was synthesized according to a previously reported procedure.<sup>[199]</sup>



To a suspension of (*S*)-**30** (150 mg, 0.52 mmol) in ethanol (1.5 mL) was added a solution of salicylaldehyde (161 mg, 1.3 mmol) in ethanol (1.5 mL). The reaction mixture was refluxed for 3h, the formed yellow precipitate was filtered off, washed with ethanol (5 mL) and dried. The desired dopant **L1** was obtained as bright yellow precipitate (218 mg, 0.44 mmol, 85%).

Analytical data was in accordance with the literature.<sup>[199]</sup>

$^1\text{H}$  NMR (300 MHz,  $\text{CDCl}_3$ ):  $\delta$  (ppm) = 12.09 (s, 3H), 8.66 (s, 3H), 8.11 (d,  $J$  = 8.8 Hz, 3H), 7.97 (d,  $J$  = 8.2 Hz, 3H), 7.64 (d,  $J$  = 8.8 Hz, 3H), 7.46 (ddd,  $J$  = 8.1, 6.2, 1.9 Hz, 3H), 7.32 – 7.27 (m, 2H), 7.25 – 7.15 (m, 7H), 6.78 (td,  $J$  = 7.6, 1.1 Hz, 3H), 6.71 (d,  $J$  = 7.9 Hz, 3H).

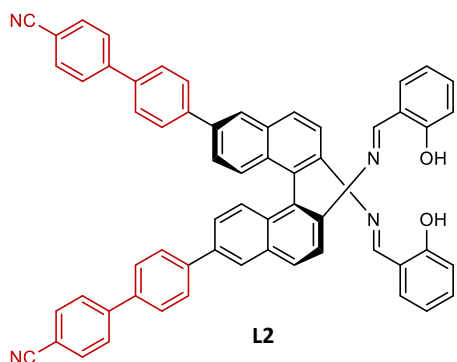
$^{13}\text{C}$  NMR (75 MHz,  $\text{CDCl}_3$ ):  $\delta$  (ppm) = 162.01 (s), 160.95 (s), 143.95 (s), 133.37 (s), 132.89 (s), 132.66 (s), 132.30 (s), 130.17 (s), 129.65 (s), 128.44 (s), 127.14 (s), 126.60 (s), 126.04 (s), 119.47 (s), 118.79 (s), 117.21 (s), 117.06 (s).

IR:  $\nu$  ( $\text{cm}^{-1}$ ) = 3053, 2701, 1624, 1605, 1590, 1560, 1492, 1461, 1452, 1431, 1400, 1385, 1345, 1281, 1193, 1150, 1115, 1073, 1030, 973, 955, 925, 901, 860, 811, 796, 765, 744, 731, 692, 682, 674, 641, 626, 594, 563, 551, 523, 514, 476, 454, 446, 428.

HTP (5CB) = 29  $\mu\text{m}^{-1}$ .

### 6.3.6.2 L2

Described experiment: ms-298, repeated: ms-279, ms-287, ms-307



To a solution of **38** (25.3 mg, 0.04 mmol) in DCM (1.5 mL) was added a solution of salicylaldehyde (**31**) (147.4 mg, 1.2 mmol) in methanol (1.5 mL). After reflux overnight, the solvent was removed, and the residue dissolved in 0.2 mL DCM. Upon addition of methanol (5 mL) dopant **L2** formed as a bright yellow precipitate which was filtered off and dried under vacuum. (Yield: 26 mg, 0.03 mmol, 75%).

$^1\text{H}$  NMR (600 MHz,  $\text{CDCl}_3$ ):  $\delta$  (ppm) = 12.18 (s,  $J = 5.7$  Hz, 2H), 8.72 (s, 2H), 8.24 (d,  $J = 1.8$  Hz, 2H), 8.21 (d,  $J = 8.7$  Hz, 2H), 7.84 – 7.80 (m, 4H), 7.77 – 7.69 (m, 14H), 7.60 (dd,  $J = 8.8, 1.9$  Hz, 2H), 7.38 (d,  $J = 8.8$  Hz, 2H), 7.21 (ddd,  $J = 8.8, 8.2, 1.6$  Hz, 4H), 6.80 (td,  $J = 7.6, 1.0$  Hz, 2H), 6.73 (d,  $J = 8.2$  Hz, 2H).

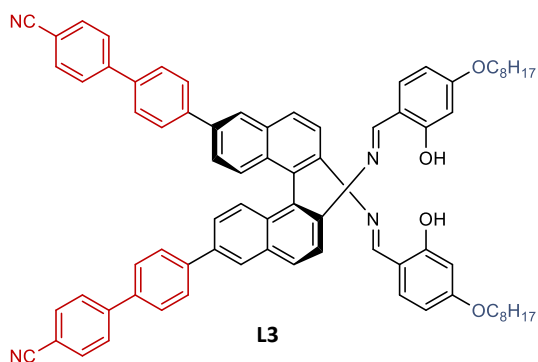
$^{13}\text{C}$  NMR (151 MHz,  $\text{CDCl}_3$ ):  $\delta$  (ppm) = 162.16 (s), 160.97 (s), 145.22 (s), 144.26 (s), 141.21 (s), 138.23 (s), 137.62 (s), 133.10 (s), 132.94 (s), 132.82 (s), 132.76 (s), 132.41 (s), 130.62 (s), 129.52 (s), 128.12 (s), 127.85 (s), 127.71 (s), 127.35 (s), 126.56 (s), 126.49 (s), 119.46 (s), 119.09 (s), 118.94 (s), 117.69 (s), 117.22 (s), 111.12 (s).

IR:  $\nu$  ( $\text{cm}^{-1}$ ) = 3034, 2924, 2853, 2225, 1605, 1568, 1489, 1392, 1339, 1279, 1194, 1150, 1114, 1031, 1003, 976, 933, 900, 815, 753, 689, 646, 561, 534, 467, 425.

MS (ESI-pos, 13742):  $m/z$  (%) = 847.3072 (100,  $[\text{M}-\text{H}]^-$ ,  $[\text{C}_{60}\text{H}_{38}\text{N}_4\text{O}_2+\text{H}]^+$ , calc.:  $m/z = 847.3068$ ).  
HTP (5CB) = 199  $\mu\text{m}^{-1}$ .

### 6.3.6.3 L3

Described experiment: ms-299, repeated: ms-290, ms-308



To a solution of **38** (23.7 mg, 0.04 mmol) in DCM (1.5 mL) was added a solution of 4-octyloxysalicylaldehyde (**39**) (185.6 mg, 0.74 mmol) in methanol (1.5 mL). After reflux overnight, the solvent was removed, and the residue dissolved in 0.2 mL DCM. Upon addition of methanol (5 mL) dopant **L3** formed as a

bright yellow precipitate which was filtered off and dried under vacuum (36.4 mg, 0.03 mmol, 88%).

$^1\text{H}$  NMR (300 MHz,  $\text{CDCl}_3$ ):  $\delta$  (ppm) = 12.69 (s, 2H), 8.61 (s, 2H), 8.22 (s, 2H), 8.18 (d,  $J$  = 8.8 Hz, 2H), 7.84 – 7.68 (m, 18H), 7.58 (dd,  $J$  = 8.8, 1.8 Hz, 2H), 7.36 (d,  $J$  = 8.8 Hz, 2H), 7.10 (d,  $J$  = 8.7 Hz, 2H), 6.34 (dd,  $J$  = 8.6, 2.4 Hz, 2H), 6.21 (d,  $J$  = 2.3 Hz, 2H), 3.85 (t,  $J$  = 6.6 Hz, 4H), 1.75 – 1.65 (m, 4H), 1.26 (s, 20H), 0.87 (t,  $J$  = 6.7 Hz, 6H).

$^{13}\text{C}$  NMR (151 MHz,  $\text{CDCl}_3$ ):  $\delta$  (ppm) = 163.63 (s), 163.54 (s), 160.98 (s), 145.26 (s), 144.37 (s), 141.34 (s), 138.13 (s), 137.23 (s), 133.56 (s), 132.87 (s), 132.81 (s), 132.63 (s), 130.41 (s), 128.99 (s), 128.10 (s), 127.82 (s), 127.70 (s), 127.28 (s), 126.43 (s), 126.39 (s), 119.10 (s), 117.78 (s), 113.25 (s), 111.08 (s), 107.64 (s), 101.41 (s), 68.28 (s), 31.91 (s), 29.39 (s), 29.32 (s), 29.11 (s), 26.06 (s), 22.77 (s), 14.22 (s).

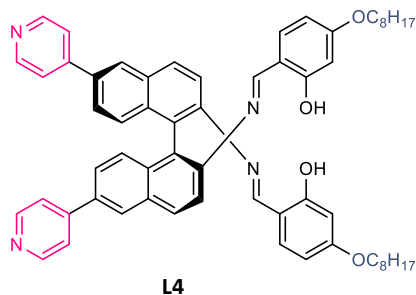
IR:  $\nu$  ( $\text{cm}^{-1}$ ) = 3034, 2923, 2852, 2225, 1604, 1559, 1509, 1490, 1468, 1391, 1339, 1288, 1247, 1190, 1135, 1114, 1020, 1003, 978, 934, 891, 814, 721, 689, 635, 561, 533, 465, 427.

MS (ESI-pos, 14200):  $m/z$  (%) = 1103.5471 (100,  $[\text{M}+\text{H}]^+$ ,  $[\text{C}_{76}\text{H}_{70}\text{N}_4\text{O}_4+\text{H}]^+$ , calc.:  $m/z$  = 1103.5470).

HTP (5CB) =  $318 \mu\text{m}^{-1}$ .

#### 6.3.6.4 L4

Described experiment: ms-312, repeated: ms-301, ms-302, ms-310



To a suspension of **44** (50.2 mg, 0.11 mmol) in DCM (2 mL) a solution of 4-alkoxysalicylaldehyde (85.6 mg, 0.34 mmol) in ethanol (3 mL) was added and the reaction mixture refluxed for 4 h. The mixture was cooled to room temperature and the solvent removed under reduced pressure. The residue was subsequently dissolved in a few

drops of DCM and methanol (1 – 2 mL) was added to form a bright yellow dispersion. The solution was sonicated to form a brown oily residue on the bottom of the flask. The methanolic solution was separated and the residue washed twice with methanol (0.2 mL). The steps were repeated until all aldehyde residues were removed. To increase the yield, all methanolic solutions were combined, the solvent removed, and the purification steps repeated to yield pure **L4** as bright yellow solid (41.7 mg, 0.05 mmol, 40%).

$^1\text{H}$  NMR (400 MHz,  $\text{CDCl}_3$ ):  $\delta$  (ppm) = 12.59 (s, 2H), 8.68 (dd,  $J$  = 4.5, 1.4 Hz, 4H), 8.60 (s, 2H), 8.25 (d,  $J$  = 1.5 Hz, 2H), 8.19 (d,  $J$  = 8.9 Hz, 2H), 7.71 (d,  $J$  = 8.9 Hz, 2H), 7.60 (dd,  $J$  = 4.7, 1.4 Hz, 4H), 7.55 (dd,  $J$  = 8.8, 1.8 Hz, 2H), 7.35 (d,  $J$  = 8.8 Hz, 2H), 7.10 (d,  $J$  = 8.7 Hz, 2H), 6.34 (dd,  $J$  = 8.6, 2.3 Hz, 2H), 6.19 (d,  $J$  = 2.3 Hz, 2H), 3.85 (t,  $J$  = 6.6 Hz, 4H), 1.75 – 1.65 (m, 4H), 1.31 (d,  $J$  = 42.6 Hz, 20H), 0.87 (t,  $J$  = 6.8 Hz, 6H).

$^{13}\text{C}$  NMR (101 MHz,  $\text{CDCl}_3$ ):  $\delta$  (ppm) = 163.66 (s), 163.60 (s), 161.32 (s), 150.50 (s), 148.10 (s), 144.97 (s), 135.15 (s), 133.64 (s), 133.50 (s), 132.41 (s), 130.68 (s), 128.81 (s), 127.43 (s), 127.02 (s), 125.76 (s), 121.84 (s), 118.10 (s), 113.16 (s), 107.73 (s), 101.38 (s), 68.29 (s), 31.91 (s), 29.35 (d,  $J = 7.4$  Hz), 29.09 (s), 26.05 (s), 22.77 (s), 14.22 (s).

IR:  $\nu$  ( $\text{cm}^{-1}$ ) = 3025, 2921, 2852, 1603, 1585, 1558, 1509, 1492, 1465, 1439, 1411, 1385, 1339, 1287, 1247, 1188, 1170, 1133, 1113, 1069, 1019, 989, 936, 893, 833, 811, 777, 725, 702, 687, 646, 626, 602, 571, 527, 464, 427.

MS (ESI-pos, 14008):  $m/z$  (%) = 452.2463 (100,  $[\text{M}+2\text{H}]^{2+}$ ,  $[\text{C}_{60}\text{H}_{62}\text{N}_4\text{O}_4+2\text{H}]^{2+}$ , calc.:  $m/z = 452.2458$ ).

HTP (5CB) =  $85 \mu\text{m}^{-1}$ .

### 6.3.7 Synthesis of BINIM Copper Complexes L1Cu – L4Cu

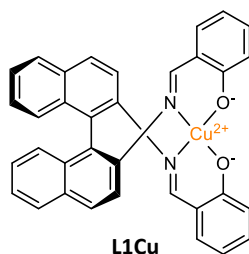
Copper complexes **L1Cu** – **L4Cu** were synthesized according to a modified literature known procedure.<sup>[212]</sup>

#### General Procedure for the Synthesis of Copper-(II) Complexes Using Copper Acetate

Ligand **L1** – **L4** (1 eq) was dispersed in ethanol and dissolved by addition of DCM. To this mixture a solution of copper acetate monohydrate (1 eq) in absolute ethanol was added and the mixture refluxed until full conversion (Cy:EA [4:1]). Subsequently, the solvent was removed, the obtained residue dissolved in a few drops of DCM and precipitated using methanol. The precipitate was filtered off, washed with methanol to remove remaining acetic acid, and dried under vacuum.

#### 6.3.7.1 L1Cu

Described experiment: ms-293



**L1** (20.3 mg,  $41.72 \mu\text{mol}$ ) yielded the desired product **L1Cu** (20.4 mg,  $36.81 \mu\text{mol}$ , 88%).

Analytical Data was in accordance with the literature.<sup>[200]</sup>

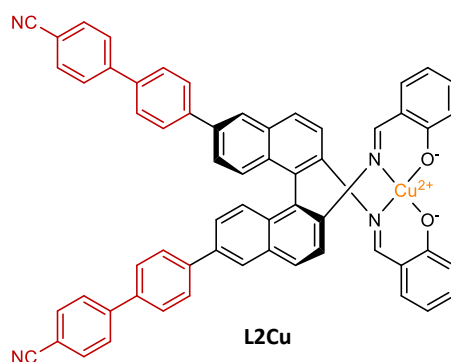
IR:  $\nu$  ( $\text{cm}^{-1}$ ) = 3421, 3052, 3016, 2914, 2821, 1604, 1587, 1530, 1461, 1441, 1383, 1351, 1312, 1253, 1205, 1184, 1148, 1128, 1072, 1028, 983, 954, 914, 865, 834, 809, 750, 687, 636, 597, 566, 524, 506, 485, 456, 420.

MS (ESI-pos, 13812):  $m/z$  (%) = 554.1051 (100,  $[\text{M}+\text{H}]^+$ ,  $\text{C}_{34}\text{H}_{22}\text{CuN}_2\text{O}_2+\text{H}^+$ , calc.:  $m/z$  = 554.1050).

HTP (5CB) =  $32 \mu\text{m}^{-1}$ .

### 6.3.7.2 L2Cu

Described experiment: ms-303, repeated: ms-295



**L2** (10.96 mg,  $12.91 \mu\text{mol}$ ) yielded the desired product **L2Cu** (8.6 mg,  $9.49 \mu\text{mol}$ , 73%).

IR:  $\nu$  ( $\text{cm}^{-1}$ ) = 3441, 3032, 2920, 2853, 2224, 1586, 1524, 1493, 1439, 1383, 1324, 1185, 1145, 978, 948, 891, 811, 754, 692, 645, 598, 553, 534, 505, 462.

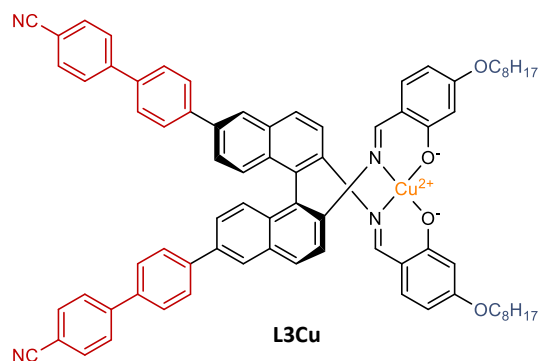
MS (ESI-pos, 13830):  $m/z$  (%) = 908.2206 (100,  $[\text{M}+\text{H}]^+$ ,  $[\text{C}_{60}\text{H}_{36}\text{CuN}_4\text{O}_2+\text{H}]^+$ , calc.:  $m/z$  = 908.2207).

CHN: calc. (%)  $\text{C}_{60}\text{H}_{36}\text{CuN}_4\text{O}_2 \times 3.2 \text{H}_2\text{O}$ : C 74.6, H 4.42, N 5.80; found (%): C 74.8, H 4.56, N 5.00.

HTP (5CB) =  $230 \mu\text{m}^{-1}$ .

### 6.3.7.3 L3Cu

Described experiment: ms-300, repeated: ms-296



**L3** (14.44 mg,  $12.87 \mu\text{mol}$ ) yielded the desired product **L3Cu** (8.6 mg,  $9.5 \mu\text{mol}$ , 73%).

IR:  $\nu$  ( $\text{cm}^{-1}$ ) = 3323, 2920, 2851, 2225, 1606, 1581, 1516, 1488, 1464, 1426, 1370, 1310, 1239, 1199, 1147, 1121, 1081, 998, 974, 952, 891, 835, 815, 790, 721, 692, 660, 618, 593, 559, 534, 471.

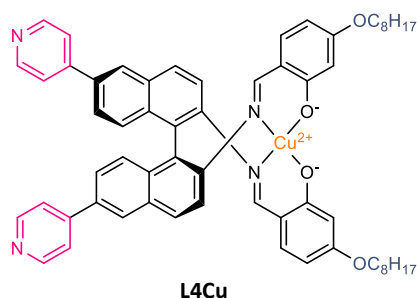
MS (ESI-pos, 13831):  $m/z$  (%) = 1164.4589 (100,  $[\text{M}+\text{H}]^+$ ,  $[\text{C}_{76}\text{H}_{68}\text{CuN}_4\text{O}_4+\text{H}]^+$ , calc.:  $m/z$  = 1164.4609).

CHN: calc. (%)  $\text{C}_{76}\text{H}_{68}\text{CuN}_4\text{O}_4 \times \text{H}_2\text{O}$ : C 77.17, H 5.96, N 4.74; found (%): C 77.60, H 5.90, N 4.47.

HTP (5CB) =  $375 \mu\text{m}^{-1}$ .

### 6.3.7.4 L4Cu

Described experiment: ms-309, repeated: ms-304



**L4** (8.14 mg, 9.01  $\mu\text{mol}$ ) yielded the desired product **L4Cu** (5.45 mg, 5.6  $\mu\text{mol}$ , 62%).

IR:  $\nu$  ( $\text{cm}^{-1}$ ) = 3066, 3027, 2923, 2852, 1609, 1580, 1514, 1485, 1466, 1430, 1370, 1337, 1313, 1242, 1196, 1146, 1120, 1082, 1018, 994, 973, 952, 894, 835, 813, 787, 729, 707, 687, 661, 612, 566, 526, 465.

MS (ESI-pos, 14278):  $m/z$  (%) = 482.7028 (100,  $[\text{M}+\text{H}]^{2+}$ ,  $[\text{C}_{60}\text{H}_{60}\text{CuN}_4\text{O}_4+2\text{H}]^{2+}$ , calc.:  $m/z$  = 482.7028).

CHN: calc. (%)  $\text{C}_{60}\text{H}_{60}\text{CuN}_4\text{O}_4 \times 1.5 \text{H}_2\text{O}$ : C 72.8, H 6.61, N 5.57; found (%): C 72.8, H 6.48, N 5.05

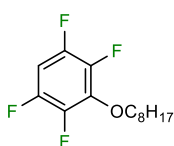
HTP (5CB) =  $254 \mu\text{m}^{-1}$ .

### 6.3.8 Synthesis of 4-Octyloxy-2,3,5,6-tetrafluoriodophenol (IC8)

4-Octyloxy-2,3,5,6-tetrafluoriodophenol (**IC8**) was synthesized according to a procedure reported in the literature.<sup>[29]</sup>

#### 6.3.8.1 4-Octyloxy-2,3,5,6-tetrafluorophenol

Described experiment: ms-313



2,3,5,6-tetrafluorophenol (586 mg, 3.53 mmol) gave 4-octyloxy-2,3,5,6-tetrafluorophenol (820 mg, 2.94 mmol, 83%).

Analytical data was in accordance with the literature.<sup>[29]</sup>

$^1\text{H}$  NMR (400 MHz,  $\text{CDCl}_3$ ):  $\delta$  (ppm) = 6.75 (tt,  $J$  = 10.0, 7.0 Hz, 1H), 4.21 (t,  $J$  = 6.6 Hz, 2H), 1.82 – 1.71 (m, 2H), 1.50 – 1.41 (m, 2H), 1.37 – 1.24 (m, 8H), 0.89 (t,  $J$  = 6.9 Hz, 3H).

$^{19}\text{F}$  NMR (376 MHz,  $\text{CDCl}_3$ ):  $\delta$  (ppm) = -140.14 – -140.37 (m, 2F), -157.02 – -157.20 (m, 2F).

### 6.3.8.2 4-Octyloxy-2,3,5,6-tetrafluoriodophenol (IC8)

Described experiment: ms-314



4-octyloxy-2,3,5,6-tetrafluorophenol (572 mg, 2.06 mmol) gave 4-octyloxy-2,3,5,6-tetrafluorophenol (**IC8**) (719 mg, 1.78 mmol, 86%) as colorless oil using cyclohexane for column chromatographic purification.

Analytical data was in accordance with the literature.<sup>[29]</sup>

$^1\text{H}$  NMR (400 MHz,  $\text{CDCl}_3$ ):  $\delta$  (ppm) = 4.23 (t,  $J$  = 6.6 Hz, 2H), 1.83 – 1.69 (m, 2H), 1.49 – 1.39 (m, 2H), 1.38 – 1.20 (m, 8H), 0.89 (t,  $J$  = 6.9 Hz, 3H).

$^{19}\text{F}$  NMR (376 MHz,  $\text{CDCl}_3$ ):  $\delta$  (ppm) = -121.52 – -121.68 (m, 2F), -154.32 – -154.47 (m, 2F).

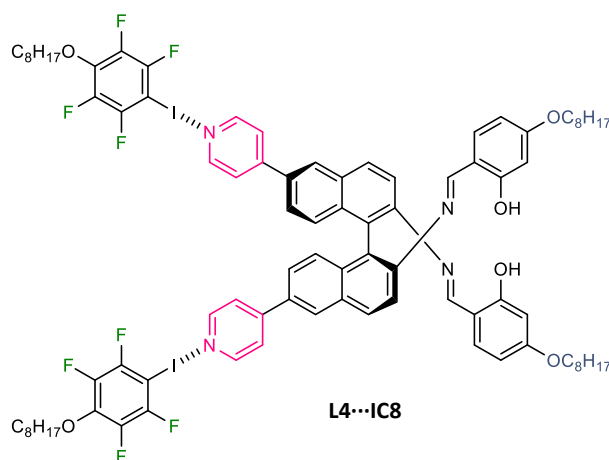
IR:  $\nu$  ( $\text{cm}^{-1}$ ) = 2955, 2926, 2856, 1631, 1480, 1385, 1274, 1098, 974, 941, 883, 801, 723.

## 6.3.9 Formation of XB-bonded BINIM complexes

For the formation of XB-bonded BINIM complexes **L4**⋯**IC8** and **L4Cu**⋯**IC8** the respective halogen bond acceptor and **47** were weighed separately, dissolved in DCM and the solutions combined. Upon solvent removal and drying under vacuum, the halogen-bonded complexes were obtained.

### 6.3.9.1 L4⋯IC8

Described experiment: msLC-331



$^1\text{H}$  NMR (400 MHz,  $\text{CDCl}_3$ ):  $\delta$  (ppm) = 12.59 (s, 2H), 8.68 (dd,  $J$  = 4.6, 1.6 Hz, 4H), 8.60 (s, 2H), 8.25 (d,  $J$  = 1.8 Hz, 2H), 8.19 (d,  $J$  = 8.7 Hz, 2H), 7.71 (d,  $J$  = 8.9 Hz, 2H), 7.61 (dd,  $J$  = 4.6, 1.6 Hz,

4H), 7.55 (dd,  $J = 8.8, 1.9$  Hz, 2H), 7.35 (d,  $J = 8.8$  Hz, 2H), 7.10 (d,  $J = 8.7$  Hz, 2H), 6.34 (dd,  $J = 8.6, 2.4$  Hz, 2H), 6.19 (d,  $J = 2.4$  Hz, 2H), 4.23 (t,  $J = 6.6$  Hz, 4H), 3.85 (t,  $J = 6.6$  Hz, 4H), 1.82 – 1.64 (m, 8H), 1.47 – 1.23 (m, 40H), 0.91 – 0.84 (m,  $J = 6.8$  Hz, 12H).

$^{19}\text{F}$  NMR (376 MHz,  $\text{CDCl}_3$ ):  $\delta$  (ppm) = -121.47 – -121.75 (m, 2F), -154.32 – -154.49 (m, 2F).

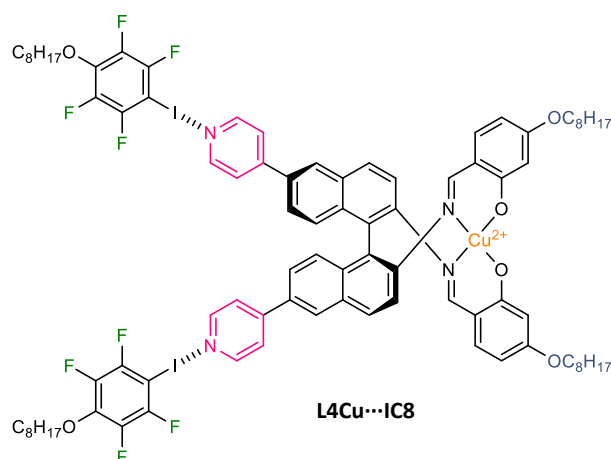
$^{13}\text{C}$  NMR (101 MHz,  $\text{CDCl}_3$ ):  $\delta$  (ppm) = 163.66 (s), 163.60 (s), 161.32 (s), 150.49 (s), 148.10 (s), 144.97 (s), 135.15 (s), 133.64 (s), 133.50 (s), 132.41 (s), 130.68 (s), 128.81 (s), 127.43 (s), 127.02 (s), 125.76 (s), 121.84 (s), 118.09 (s), 113.16 (s), 107.73 (s), 101.38 (s), 75.60 (t,  $J = 3.4$  Hz), 68.29 (s), 31.90 (s), 31.89 (s), 29.99 (s), 29.39 (s), 29.31 (s), 29.09 (s), 26.05 (s), 25.63 (s), 22.77 (s), 14.22 (s).

IR:  $\nu$  ( $\text{cm}^{-1}$ ) = 3069, 3033, 2951, 2924, 2854, 2725, 1623, 1604, 1587, 1560, 1511, 1479, 1383, 1340, 1290, 1248, 1191, 1172, 1135, 1098, 1020, 973, 938, 894, 834, 812, 779, 723, 703, 687, 647, 628, 603, 572, 528, 465, 427.

HTP (5CB) = 115  $\mu\text{m}^{-1}$ .

### 6.3.9.2 L4Cu $\cdots$ IC8

Described experiment: mslC-321



IR:  $\nu$  ( $\text{cm}^{-1}$ ) = 3657, 2978, 2968, 2958, 2925, 2854, 1609, 1580, 1515, 1481, 1468, 1429, 1375, 1337, 1312, 1241, 1195, 1146, 1121, 1097, 1017, 994, 971, 954, 894, 836, 814, 797, 724, 708, 687, 661, 628, 612, 592, 565, 524, 465, 421.

HTP (5CB) = 254  $\mu\text{m}^{-1}$ .



## 7. Appendix

### 7.1 Supplementary Information to Chapter 3.1.2

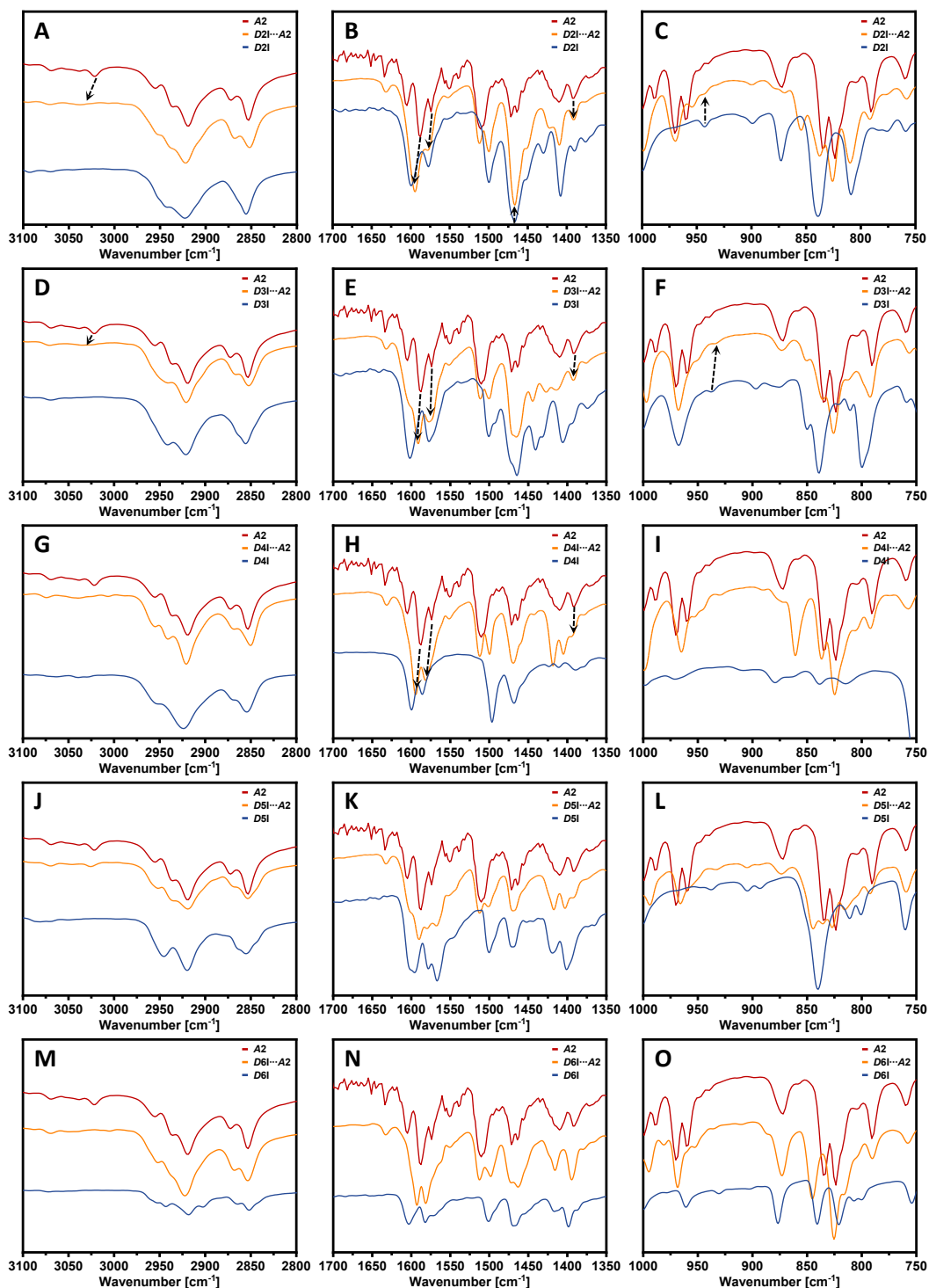


Figure 7.1: IR spectra overlay of supramolecular complexes of *A2* with *D2I* (A – C), *D3I* (D – F), *D4I* (G – I), *D5I* (J – L), and *D6I* (M – O) in the regions 3100 – 2800  $\text{cm}^{-1}$  (left column), 1700 – 1350  $\text{cm}^{-1}$  (middle column), and 1000 – 750  $\text{cm}^{-1}$  (right column).

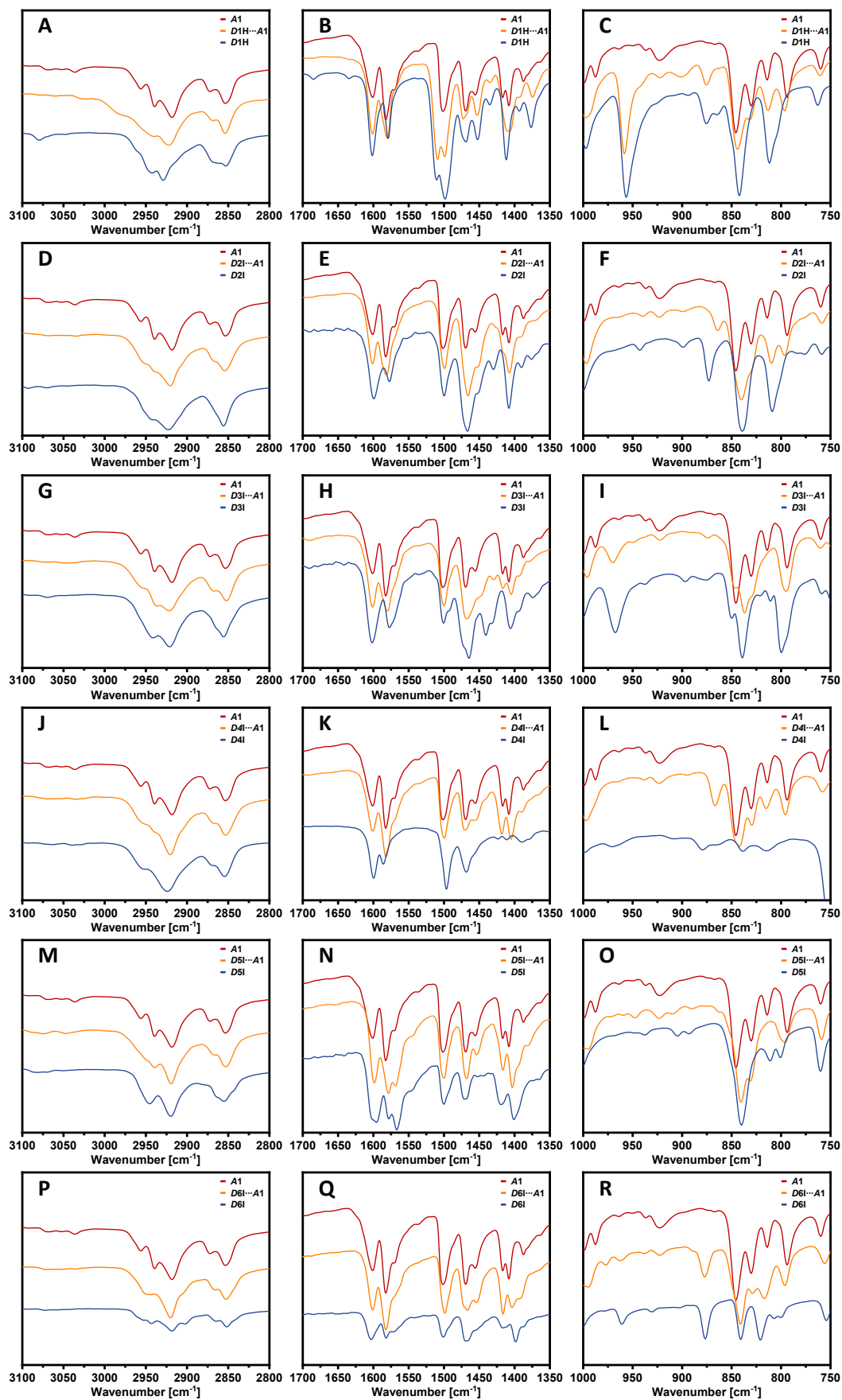


Figure 7.2: IR spectra overlay of supramolecular complexes of **A1** with **D1H** (A – C), **D2I** (D – F), **D3I** (G – I), **D4I** (J – L), **D5I** (M – O), and **D6I** (P – R).

Table 7.1: DFT-D computed (B97+D3/def2-TZVP) interaction energies in kJ/mol of the supramolecular halogen-bonded complexes of XB-donors **D1I** – **D6I** with XB-acceptors **A1** and **A2**.

	<b>A1</b>	<b>A2</b>
<b>D1I</b>	-30.15	-31.65
<b>D2I</b>	-27.52	-28.84
<b>D3I</b>	-26.17	-27.45
<b>D4I</b>	-25.31	-26.49
<b>D5I</b>	-22.56	-23.61
<b>D6I</b>	-21.78	-22.76

Crystal structure data of compound **D1I**···**A2**, CCDC-1866420

[C<sub>29</sub>H<sub>24</sub>F<sub>4</sub>IN<sub>3</sub>O<sub>2</sub>], M [g/mol] = 649.41, orange crystal, (0.080 × 0.048 × 0.022 mm); triclinic, space group *PI*; *a* = 6.1954(2) Å, *b* = 19.6656(7) Å, *c* = 22.1676(8) Å;  $\alpha$  = 99.849(2)°,  $\beta$  = 93.8885(19)°,  $\gamma$  = 91.8717(19)°, *V* = 2652.20(16) Å<sup>3</sup>; *Z* = 4;  $\mu$  = 10.021 mm<sup>-1</sup>;  $\rho_{\text{calc}}$  = 1.626 g·cm<sup>-3</sup>; 17283 reflections ( $\theta_{\text{max}}$  = 79.199°), 9947 unique (*R*<sub>int</sub> = 0.0890); 716 parameters; largest max./min in the final difference Fourier synthesis 1.619 e·Å<sup>-3</sup>/ -1.136 e·Å<sup>-3</sup>; max./min. transmission 0.75/0.55; *R*<sub>1</sub> = 0.0891 (*I* > 2σ(*I*)), *wR*<sub>2</sub> = 0.1912 (all data).

Crystal structure data of compound **D2I**···**A2**, CCDC-1866422

[C<sub>29</sub>H<sub>25</sub>F<sub>3</sub>IN<sub>3</sub>O<sub>2</sub>], M [g/mol] = 631.42, orange crystal, (0.269 × 0.155 × 0.068 mm); monoclinic, space group *P2<sub>1</sub>*; *a* = 6.5527(4) Å, *b* = 8.3651(5) Å, *c* = 24.1757(16) Å;  $\alpha$  = 90°,  $\beta$  = 97.7796(17)°,  $\gamma$  = 90°, *V* = 1312.97(14) Å<sup>3</sup>; *Z* = 2;  $\mu$  = 10.045 mm<sup>-1</sup>;  $\rho_{\text{calc}}$  = 1.597 g·cm<sup>-3</sup>; 24321 reflections ( $\theta_{\text{max}}$  = 79.011°), 5261 unique (*R*<sub>int</sub> = 0.0453); 365 parameters; Flack-Parameter *x* = 0.062(7); largest max./min in the final difference Fourier synthesis 0.516 e·Å<sup>-3</sup>/ -0.413 e·Å<sup>-3</sup>; max./min. transmission 0.75/0.35; *R*<sub>1</sub> = 0.0263 (*I* > 2σ(*I*)), *wR*<sub>2</sub> = 0.0628 (all data).

Crystal structure data of compound **D3I**···**A2**, CCDC-1866421

[C<sub>29</sub>H<sub>25</sub>F<sub>3</sub>IN<sub>3</sub>O<sub>2</sub>], M [g/mol] = 631.42, pale orange crystal, (0.162 × 0.084 × 0.072 mm); monoclinic, space group *P2<sub>1</sub>*; *a* = 10.8609(5) Å, *b* = 7.1392(3) Å, *c* = 33.7700(14) Å;  $\alpha$  = 90°,  $\beta$  = 92.586(2)°,  $\gamma$  = 90°, *V* = 2615.8(2) Å<sup>3</sup>; *Z* = 4;  $\mu$  = 10.084 mm<sup>-1</sup>;  $\rho_{\text{calc}}$  = 1.603 g·cm<sup>-3</sup>; 57527 reflections ( $\theta_{\text{max}}$  = 79.652°), 10889 unique (*R*<sub>int</sub> = 0.0910); 699 parameters; Flack-Parameter *x* = 0.443(8); largest max./min in the final difference Fourier synthesis 0.666 e·Å<sup>-3</sup>/ -0.715 e·Å<sup>-3</sup>; max./min. transmission 0.75/0.50; *R*<sub>1</sub> = 0.0381 (*I* > 2σ(*I*)), *wR*<sub>2</sub> = 0.0899 (all data).

## 7.2 Supplementary Information to Chapter 3.1.3

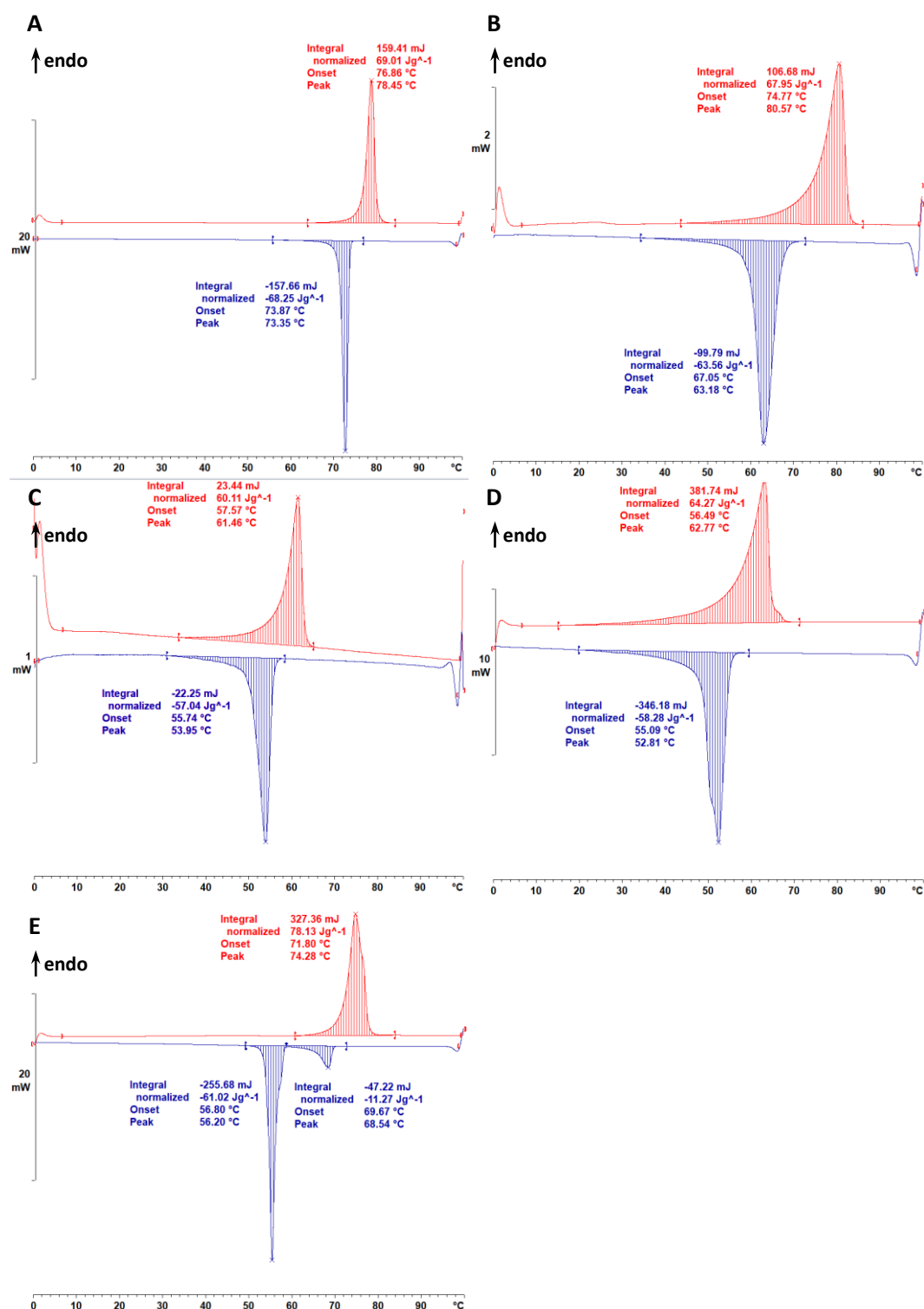


Figure 7.3: DSC traces of *D11* (A), *D21* (B), *D31* (C), *D51* (D), *D61* (E) upon heating (red) and cooling (blue). DSC traces of *D61* reveal the formation of a monotropic liquid crystalline phase upon cooling from the isotropic melt. *D41* is liquid at room temperature and was therefore not measured.

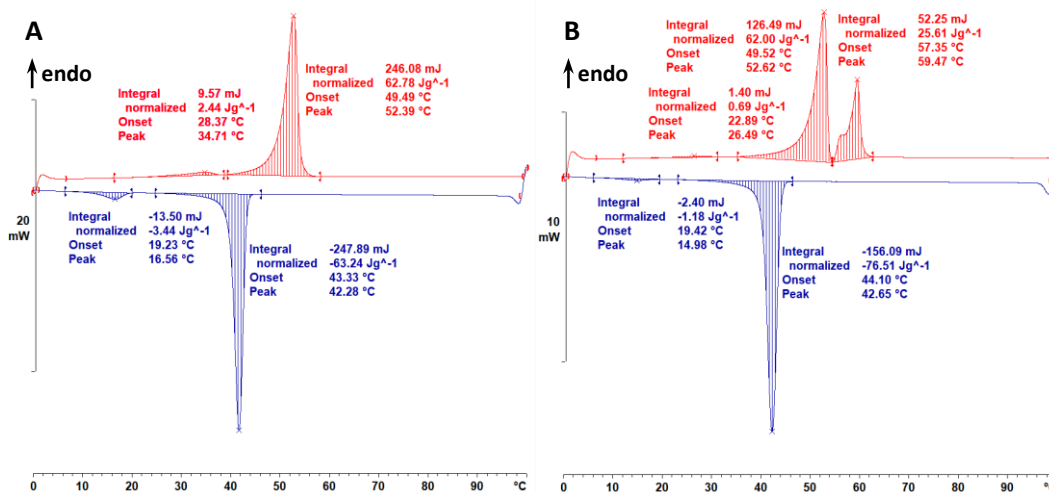


Figure 7.4: DSC traces of *D1H*...*A1* (A) and *D1H*...*A2* (B) upon heating (red) and cooling (blue).

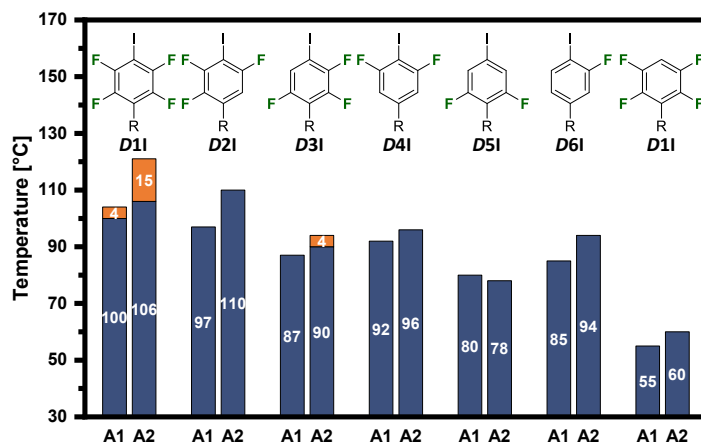


Figure 7.5: Mesophase diagram of all halogen-bonded assemblies revealing the thermal behavior upon cooling as observed under POM.

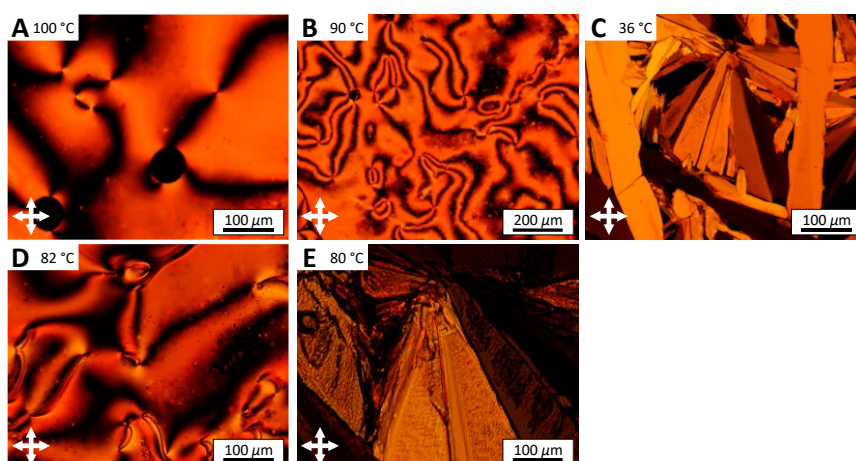


Figure 7.6: POM images of the LC assemblies *D11*...*A1* upon heating (A) and cooling (B, C), and *D21*...*A1* upon cooling (D, E).

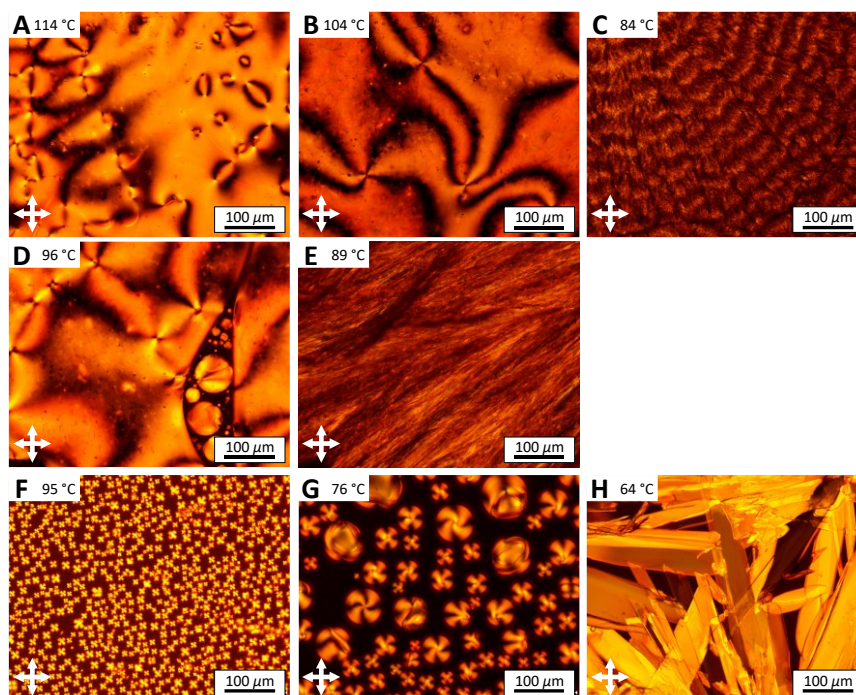


Figure 7.7: POM images of the LC assemblies  $D11 \cdots A2$  upon heating (A) and cooling (B, C),  $D21 \cdots A2$  upon cooling (D, E), and  $D31 \cdots A2$  upon heating (F) and cooling (G, H).

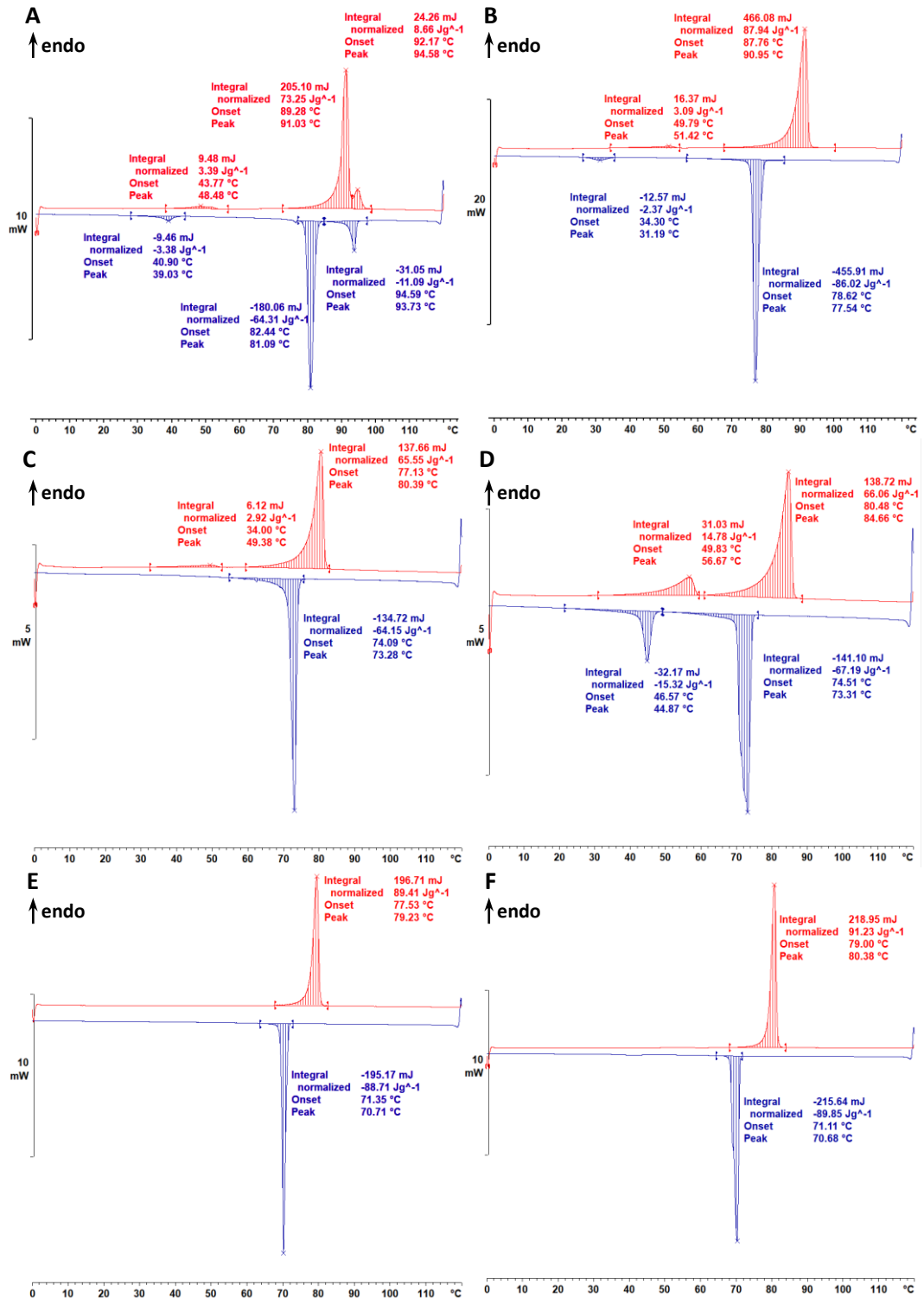


Figure 7.8: DSC traces of *D1I...A1* (A), *D2I...A1* (B), *D3I...A1* (C), *D4I...A1* (D), *D5I...A1* (E), *D6I...A1* (F) upon heating (red) and cooling (blue).

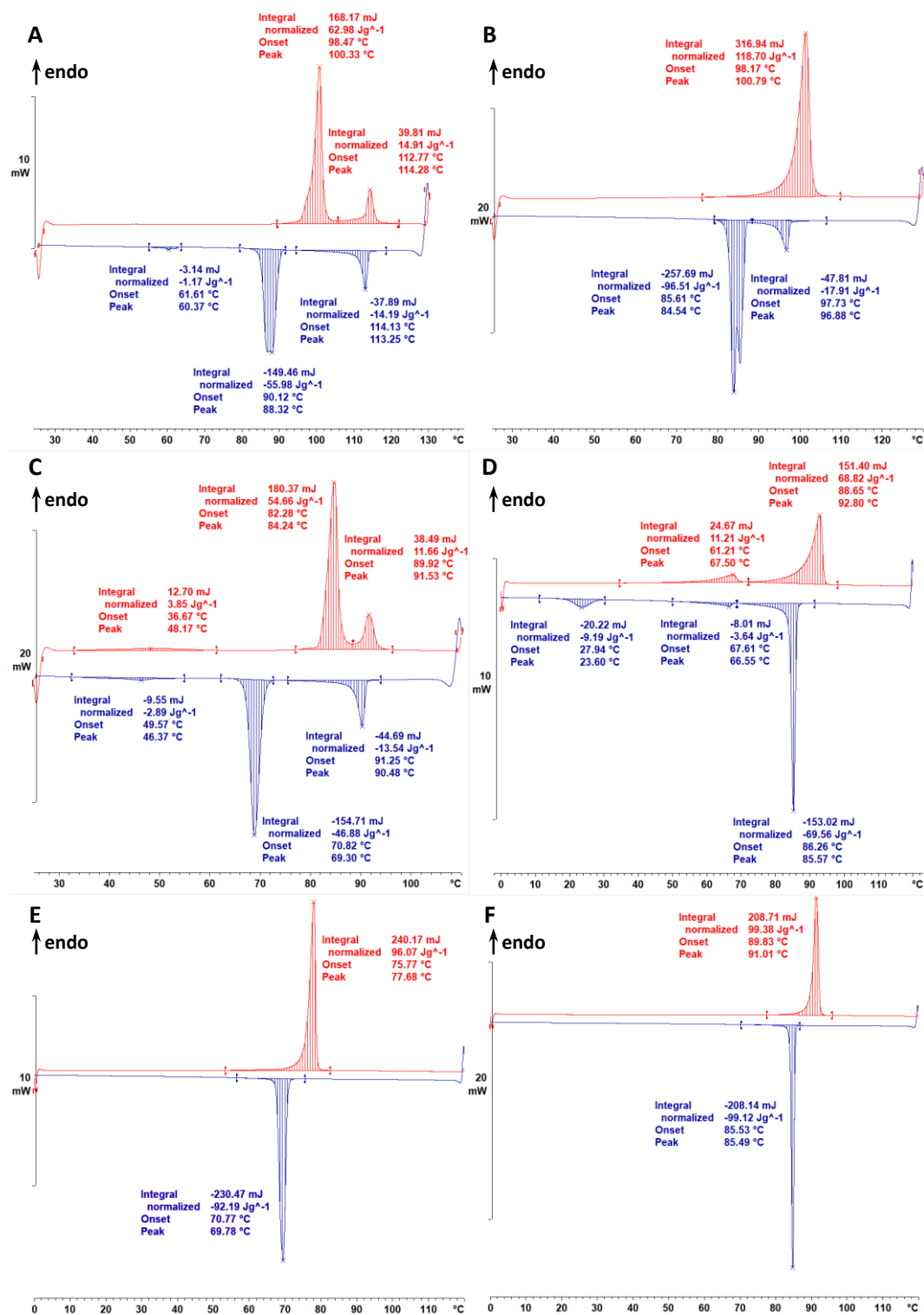


Figure 7.9: DSC traces of **D11...A2** (A), **D21...A2** (B), **D31...A2** (C), **D41...A2** (D), **D51...A2** (E), **D61...A2** (F) upon heating (red) and cooling (blue).

## 7.3 Supplementary Information to Chapter 3.1.4

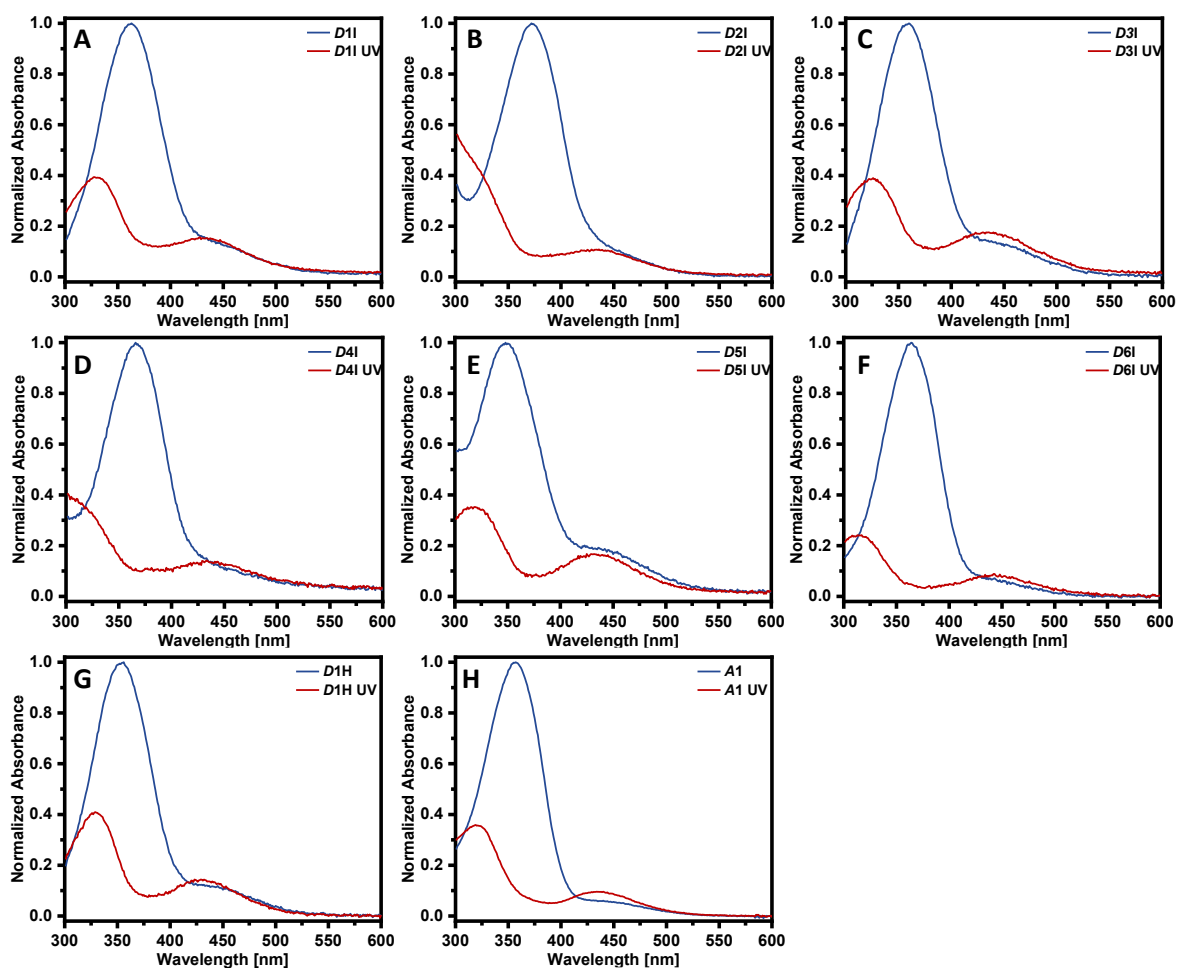


Figure 7.10: Normalized absorption spectra of compounds *D1I* – *D1H* (A – G) and *A1* (H) before (blue) and after irradiation (red) with 365 nm UV light.

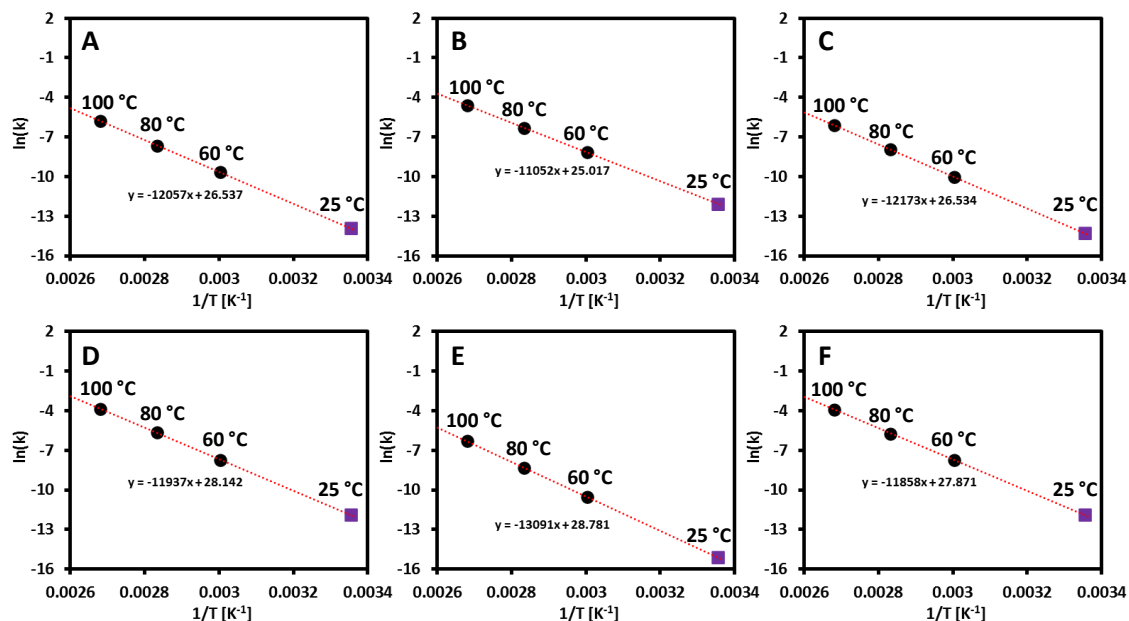


Figure 7.11: Arrhenius plots of **D1I – D6I** (A – F) with  $\ln(k)$  values at 100, 80, and 60 °C. Values at 25 °C (purple square) were extrapolated using the linear fit (red dotted line).

Table 7.2: Lifetime constants of **D1I – D1H** as obtained at 100, 80, and 60 °C, respectively, using the linear plot at a selected wavelength of 380 nm. Values at 25 °C are extrapolated values using the Arrhenius plot.

	$k_{100}$ [s <sup>-1</sup> ]	$k_{80}$ [s <sup>-1</sup> ]	$k_{60}$ [s <sup>-1</sup> ]	$k_{25}$ [s <sup>-1</sup> ]
<b>D1I</b>	$3.16 \cdot 10^{-3}$	$4.66 \cdot 10^{-4}$	$6.48 \cdot 10^{-5}$	$9.18 \cdot 10^{-7}$
<b>D2I</b>	$1.01 \cdot 10^{-2}$	$1.80 \cdot 10^{-3}$	$2.87 \cdot 10^{-4}$	$5.85 \cdot 10^{-6}$
<b>D3I</b>	$2.21 \cdot 10^{-3}$	$3.61 \cdot 10^{-4}$	$4.40 \cdot 10^{-5}$	$6.19 \cdot 10^{-7}$
<b>D4I</b>	$2.08 \cdot 10^{-2}$	$3.52 \cdot 10^{-3}$	$4.46 \cdot 10^{-4}$	$6.83 \cdot 10^{-6}$
<b>D5I</b>	$1.82 \cdot 10^{-3}$	$2.44 \cdot 10^{-4}$	$2.68 \cdot 10^{-5}$	$2.70 \cdot 10^{-7}$
<b>D6I</b>	$2.00 \cdot 10^{-2}$	$3.25 \cdot 10^{-3}$	$4.38 \cdot 10^{-4}$	$6.78 \cdot 10^{-6}$
<b>D1H</b>	$2.01 \cdot 10^{-3}$	$2.71 \cdot 10^{-4}$	$2.92 \cdot 10^{-5}$	$2.89 \cdot 10^{-7}$

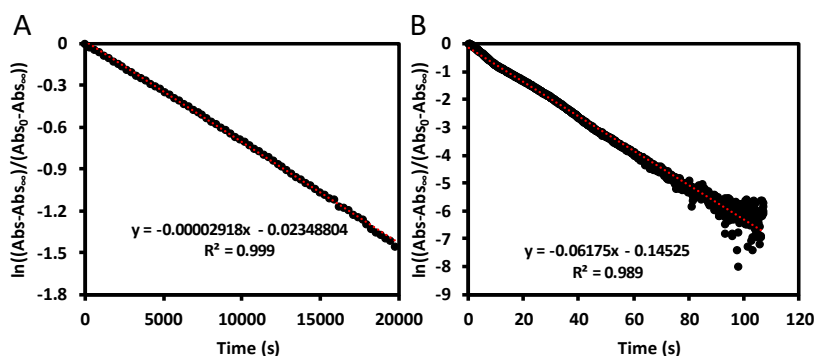


Figure 7.12: Linear plots of the *cis* lifetime measurements of **A1** at 25 °C (A) and 94 °C (B) giving *cis* lifetimes of 3.8 h and 16.2 s, respectively.

## 7.4 Supplementary Information to Chapter 3.2.2

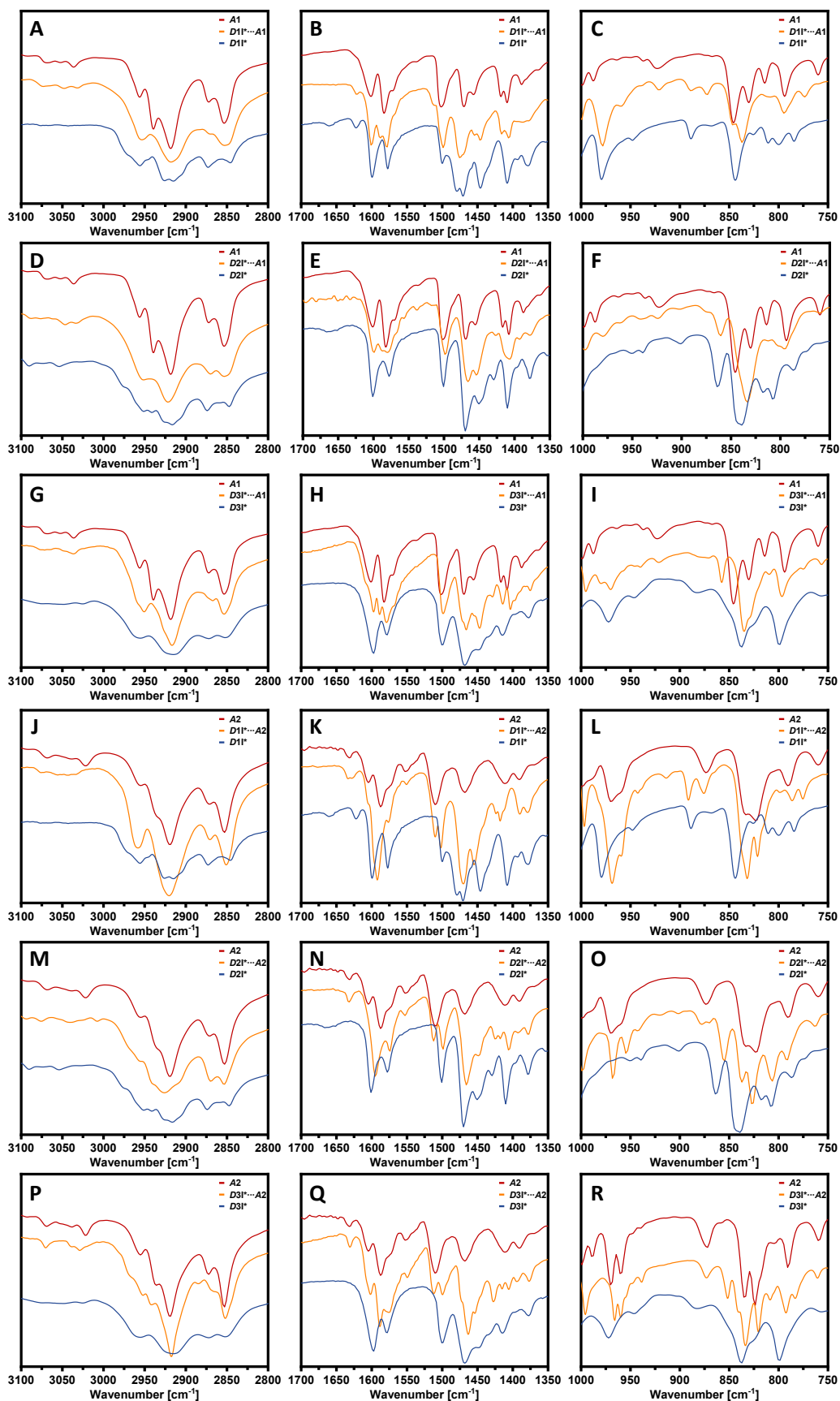


Figure 7.13: IR spectra overlay of supramolecular chiral Assemblies of  $D11^*$ ,  $D21^*$ , and  $D31^*$  using acceptors  $A1$  (A – I) and  $A2$  (J – R).

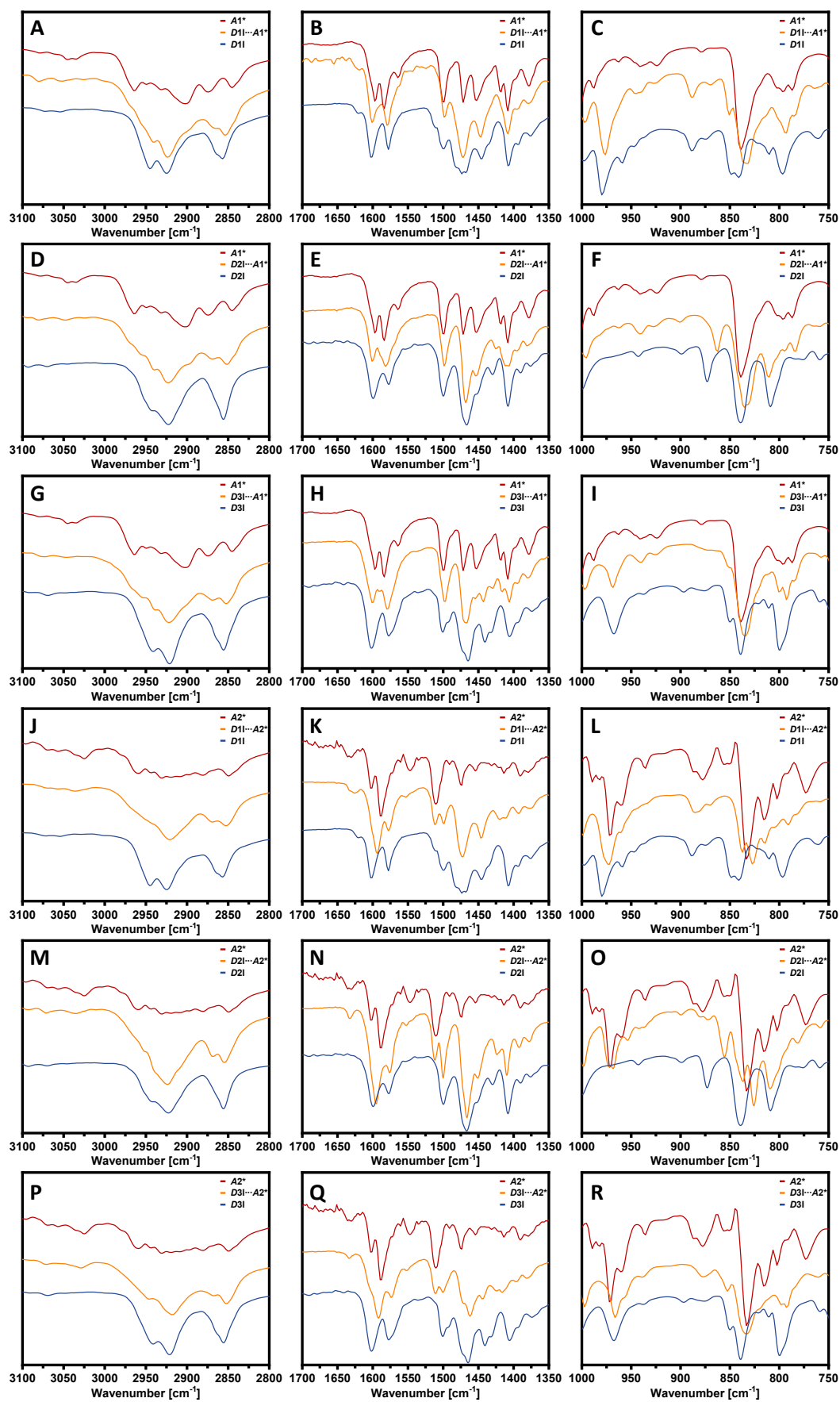


Figure 7.14: IR spectra overlay of supramolecular chiral Assemblies of *D11*, *D21*, and *D31* using acceptors *A1\** (A – I) and *A2\** (J – R).

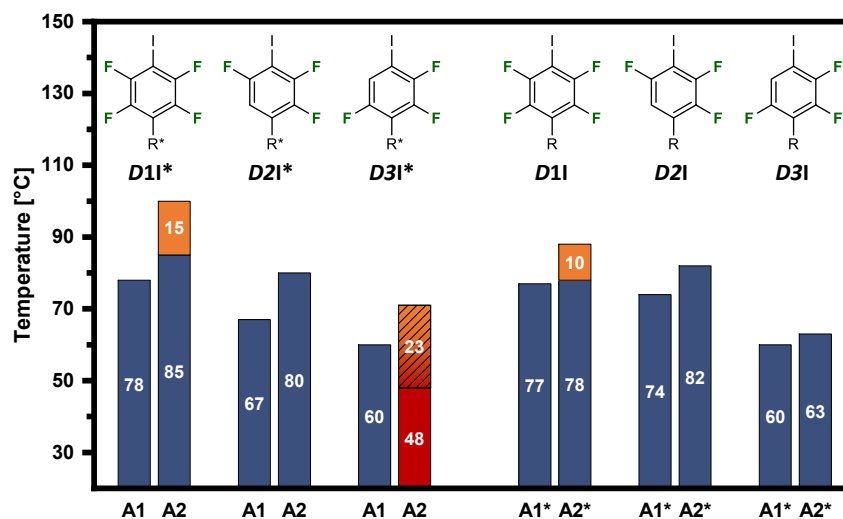


Figure 7.15: Temperature ranges of all chiral halogen-bonded assemblies upon heating as observed using POM.

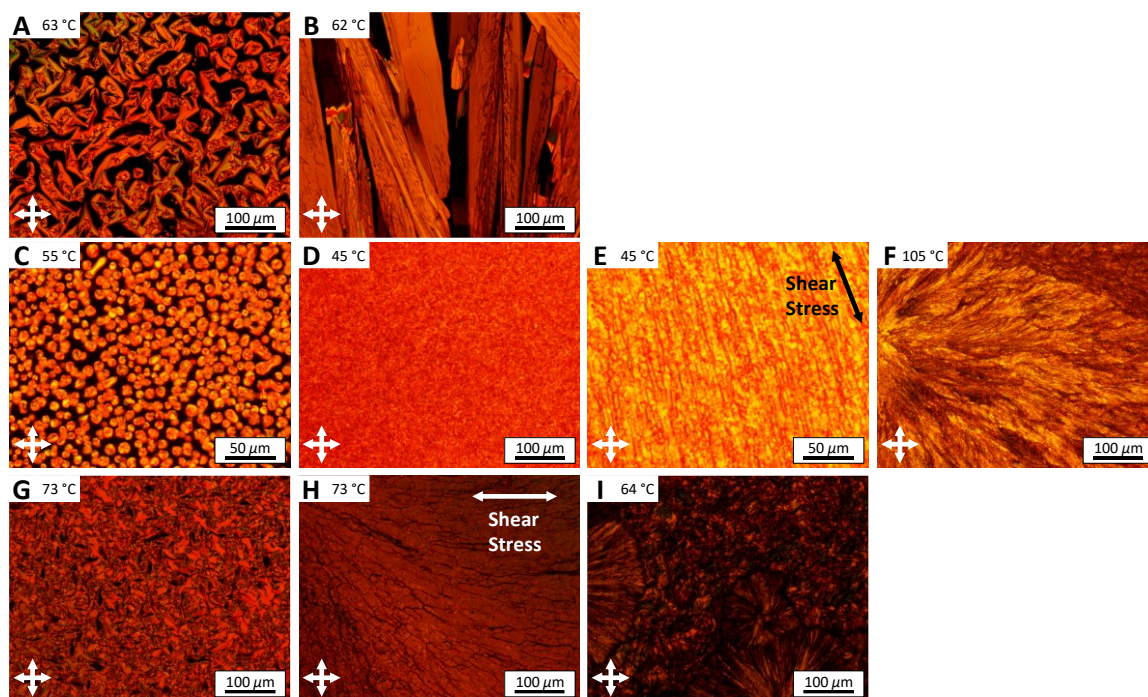


Figure 7.16: POM images of assemblies *D11\*...A1* (A, B), *D21\*...A1* (C – F), and *D21\*...A2* (G – I) upon cooling from the LC state to the crystalline state (B, F, I).

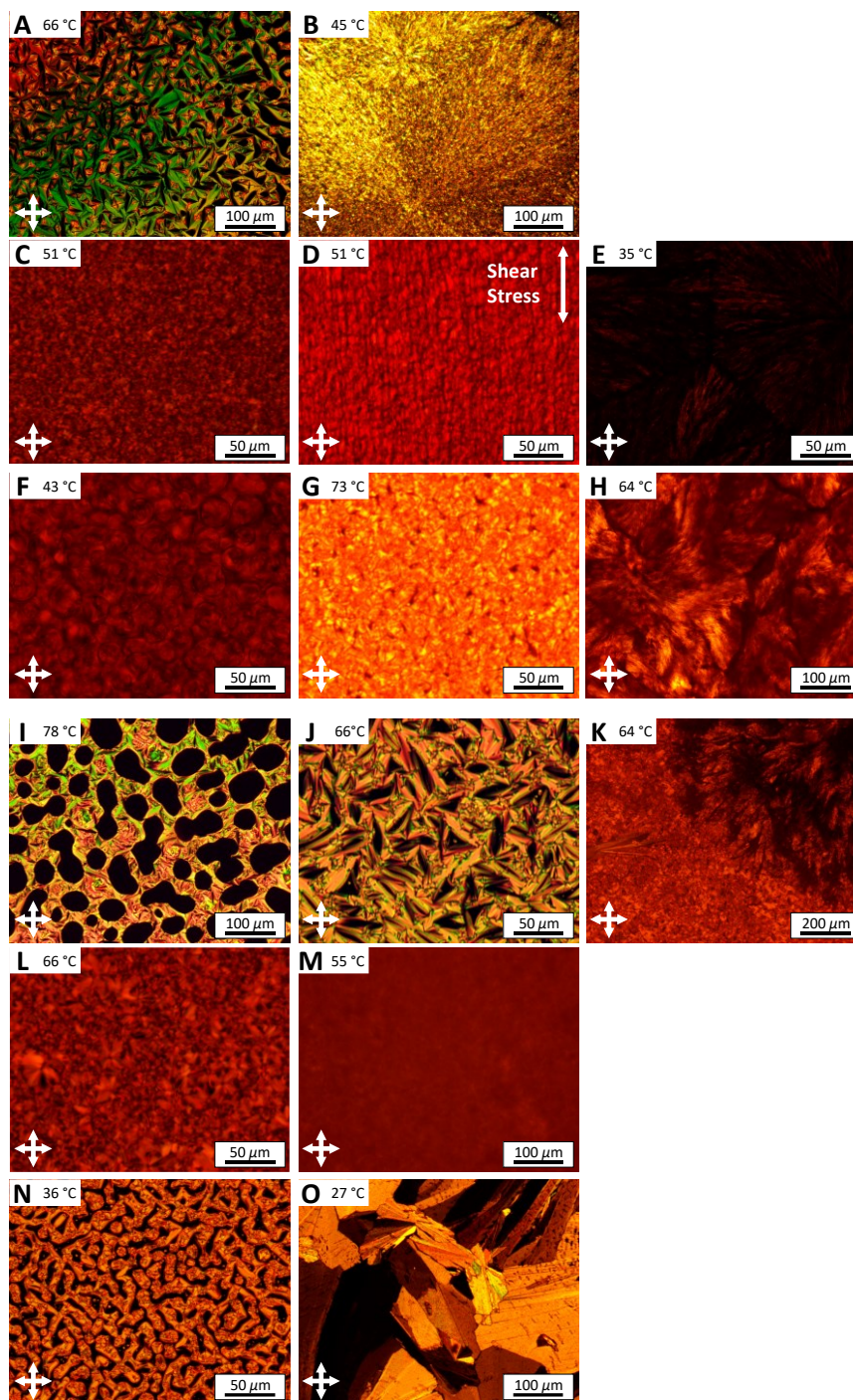


Figure 7.17: POM images of assemblies  $D1I \cdots A1^*$  (A, B),  $D2I \cdots A1^*$  (C – E),  $D3I \cdots A1^*$  (F – H),  $D1I \cdots A2^*$  (I – K),  $D2I \cdots A2^*$  (L, M),  $D3I \cdots A2^*$  (N, O) upon cooling from LC state to the crystalline phase. I) Image was taken upon heating to the isotropic melt.

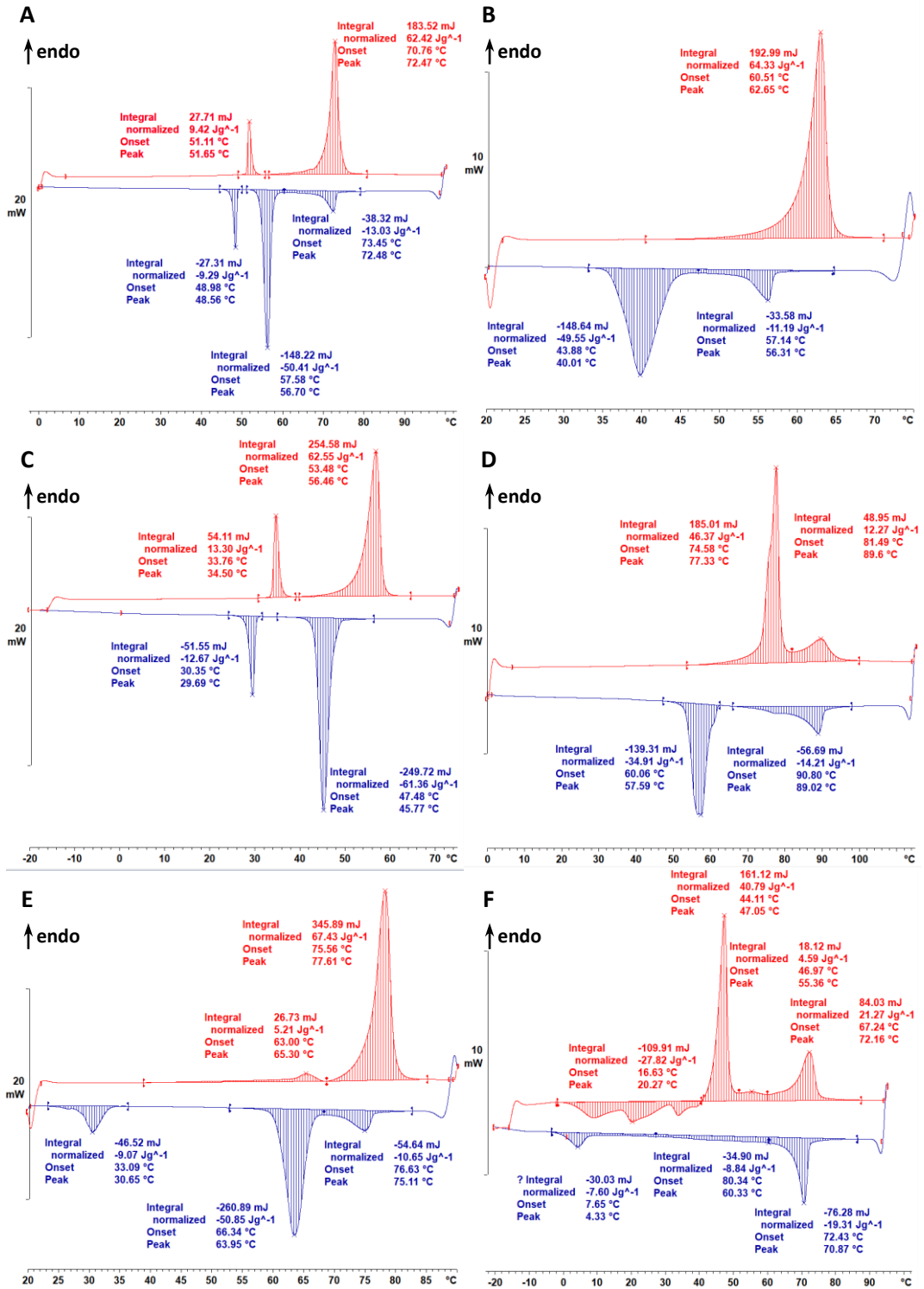


Figure 7.18: DSC traces of  $D11^* \cdots A1$  (A),  $D21^* \cdots A1$  (B),  $D31^* \cdots A1$  (C),  $D11^* \cdots A2$  (D),  $D21^* \cdots A2$  (E),  $D31^* \cdots A2$  (F) upon heating (red) and cooling (blue). DSC traces of  $D31^* \cdots A2$  show the slow  $sCr \rightarrow Cr$  transition upon reheating of the sample.

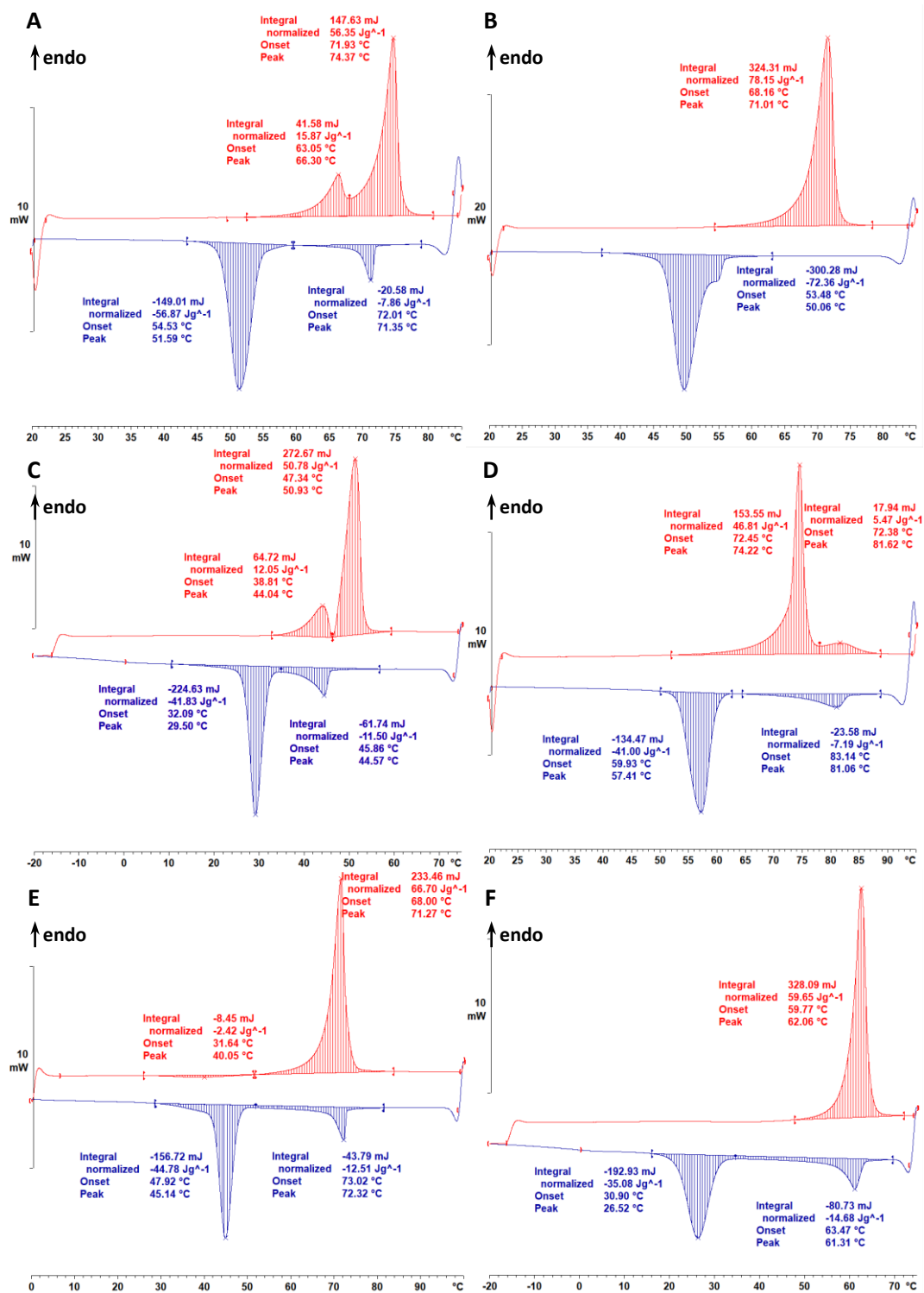


Figure 7.19: DSC traces of  $D1I \cdots A1^*$  (A),  $D2I \cdots A1^*$  (B),  $D3I \cdots A1^*$  (C),  $D1I \cdots A2^*$  (D),  $D2I \cdots A2^*$  (E),  $D3I \cdots A2^*$  (F) upon heating (red) and cooling (blue).

## 7.5 Supplementary Information to Chapter 3.2.3

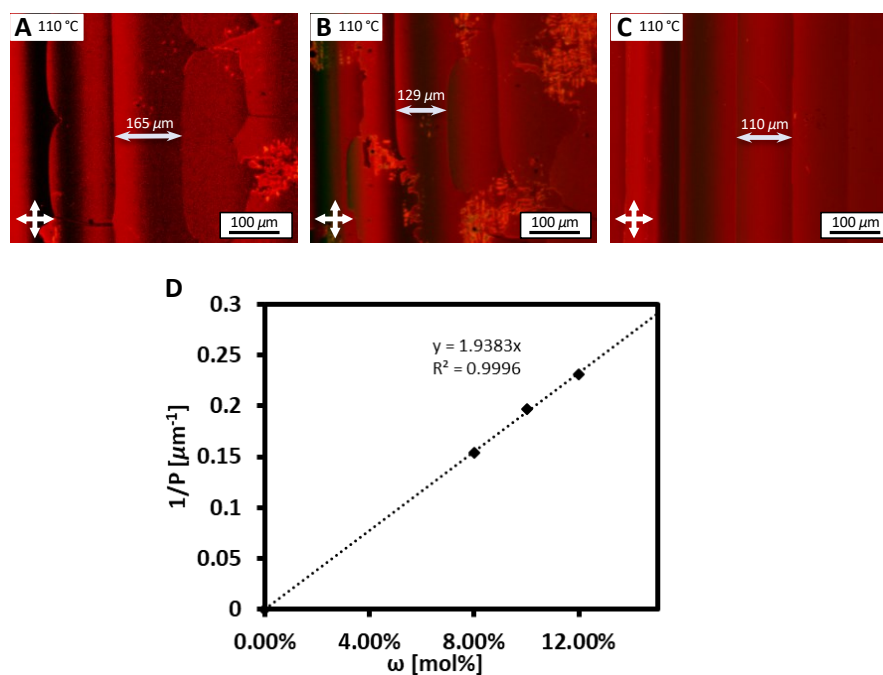


Figure 7.20: POM images of the wedge cell experiments of  $D11^* \cdots A2 @ D11 \cdots A2$  with increasing concentration of 8 mol% (A), 10 mol% (B) and 12 mol% (C) and the resulting linear plot.

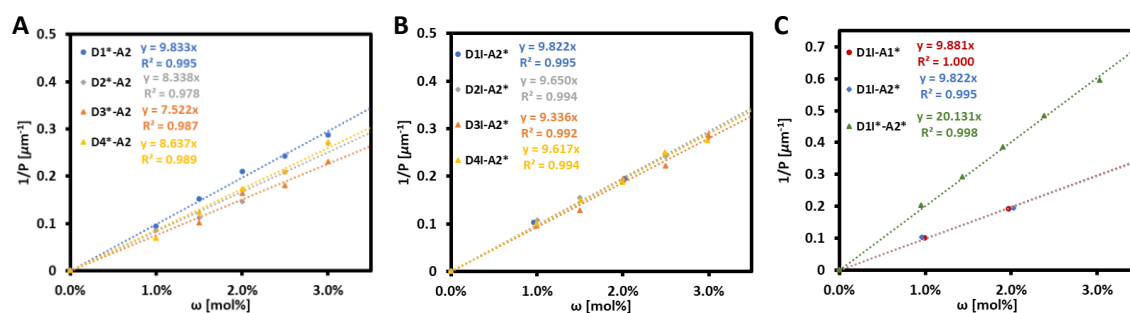


Figure 7.21: Linear plots of the HTP value measurements of the XB-complexes using either chiral donors (A), or acceptors (B), or both a chiral donor and a chiral acceptor (C) in 5CB at 20 °C.

## 7.6 Supplementary Information to Chapter 3.3

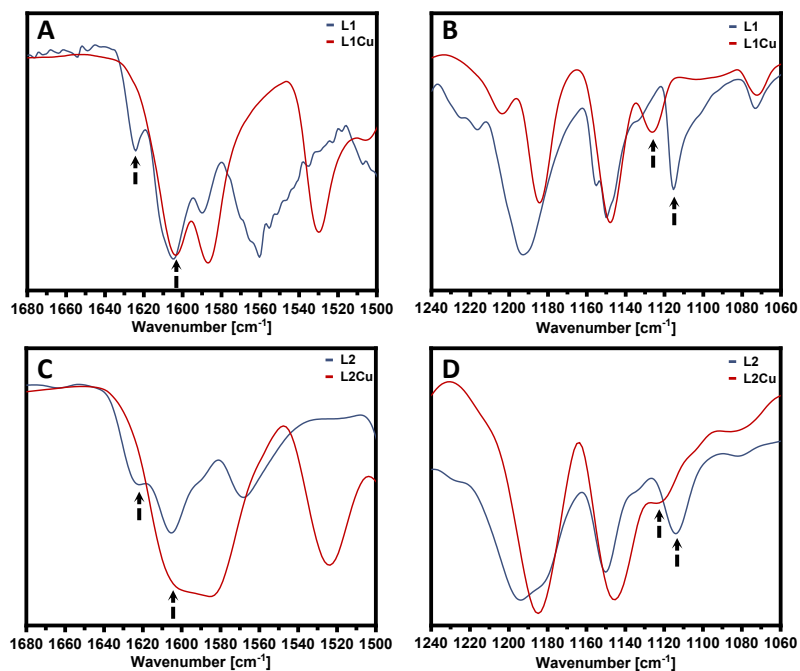


Figure 7.22: IR spectra of L1 and L1Cu (A/B) and L2 and L2Cu (C/D).

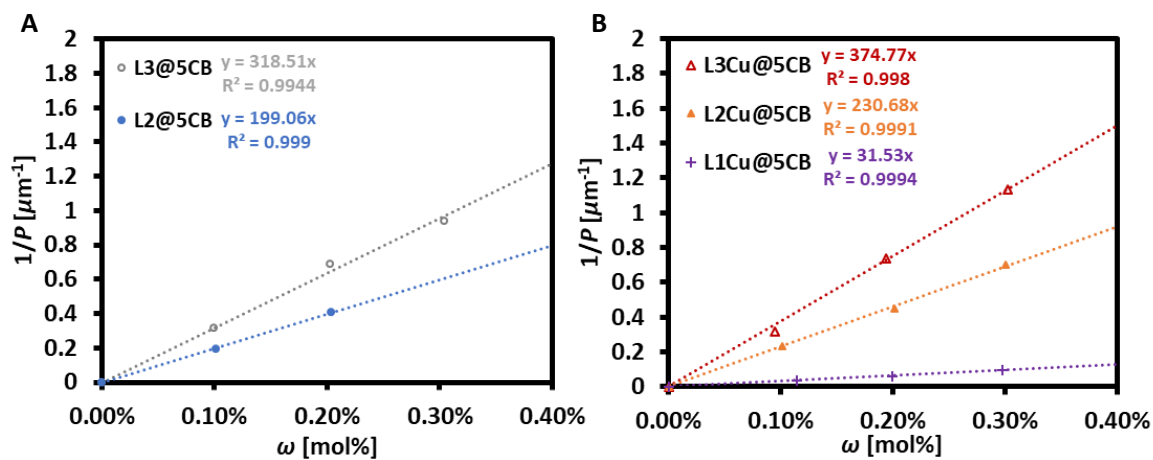


Figure 7.23: Linear plots of the inverse of the helical pitch as a function of the dopant concentration of Ligands L2 and L3 (A) and copper complexes L1Cu, L2Cu, and L3Cu (B).

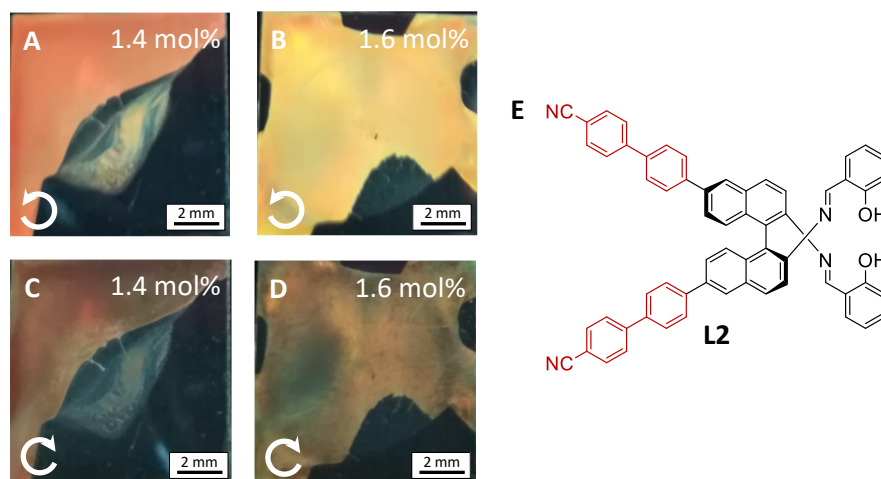


Figure 7.24: Photographs of the structural color of thin LC films of E7 doped with L2 under circularly polarizing filters for L-CPL (A/B) and R-CPL (C/D) and molecular structure of dopant L2 (D).

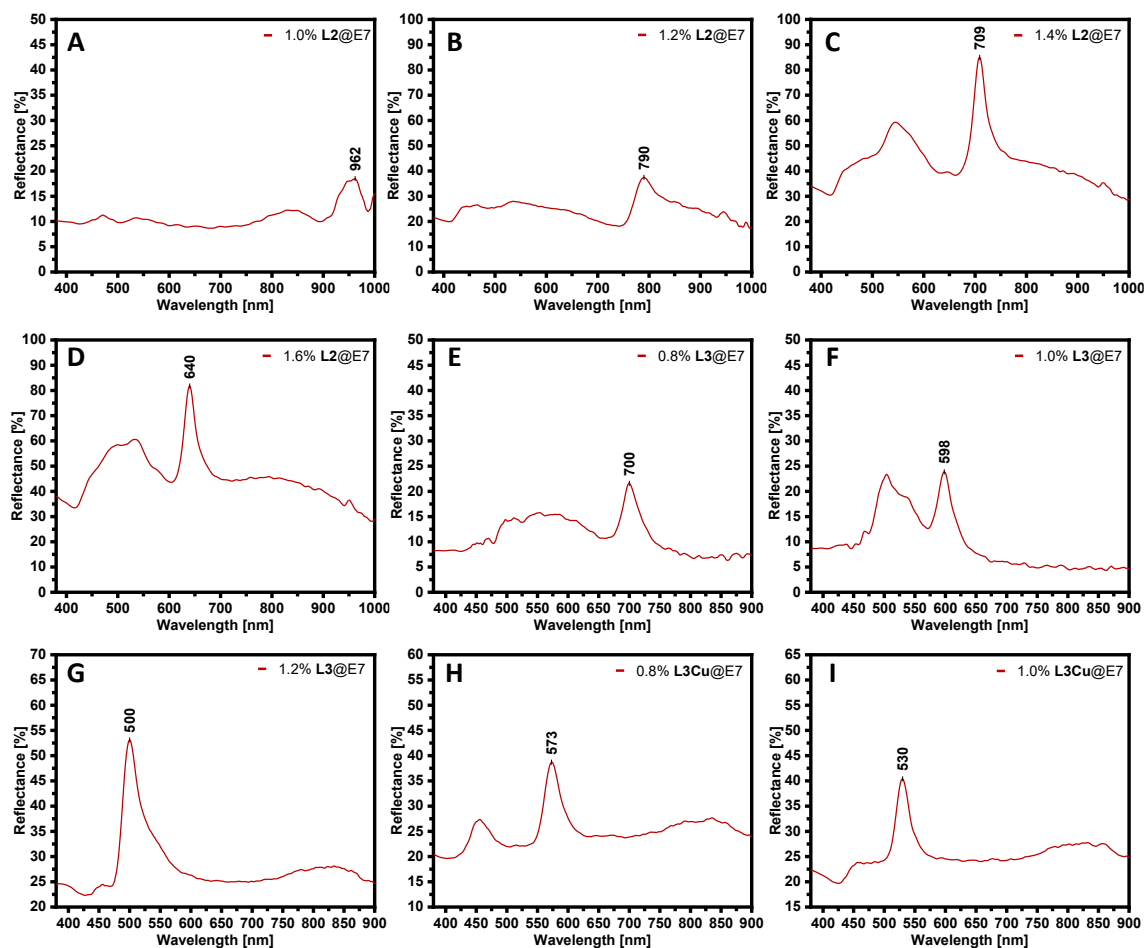


Figure 7.25: Reflectance spectra of E7 doped with different concentrations of L2 (A–D), L3 (E–G), and L3Cu (H–I).

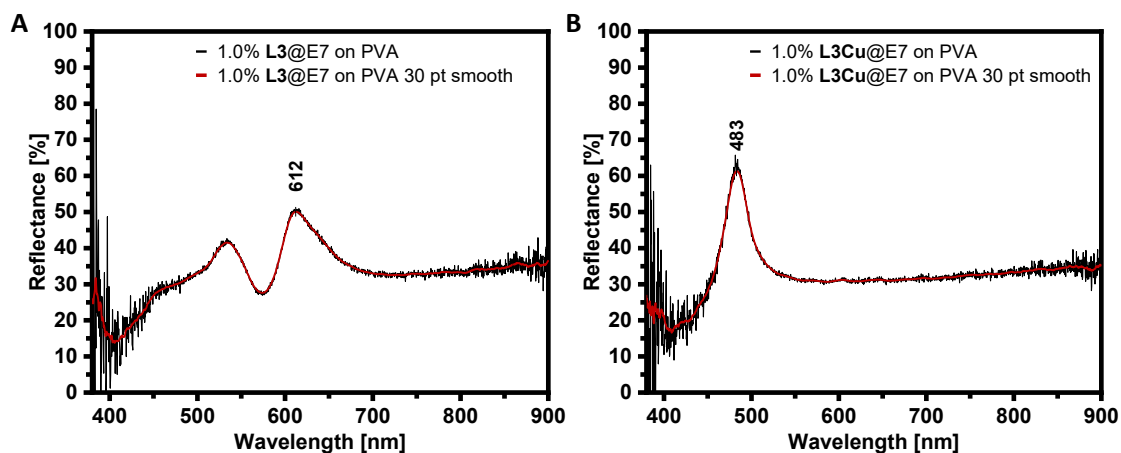


Figure 7.26: Reflectance spectra of E7 doped with 1.0 mol% L3 (A) and L3Cu (B) on PVA.

### 7.1 Supplementary Information to Chapter 3.4

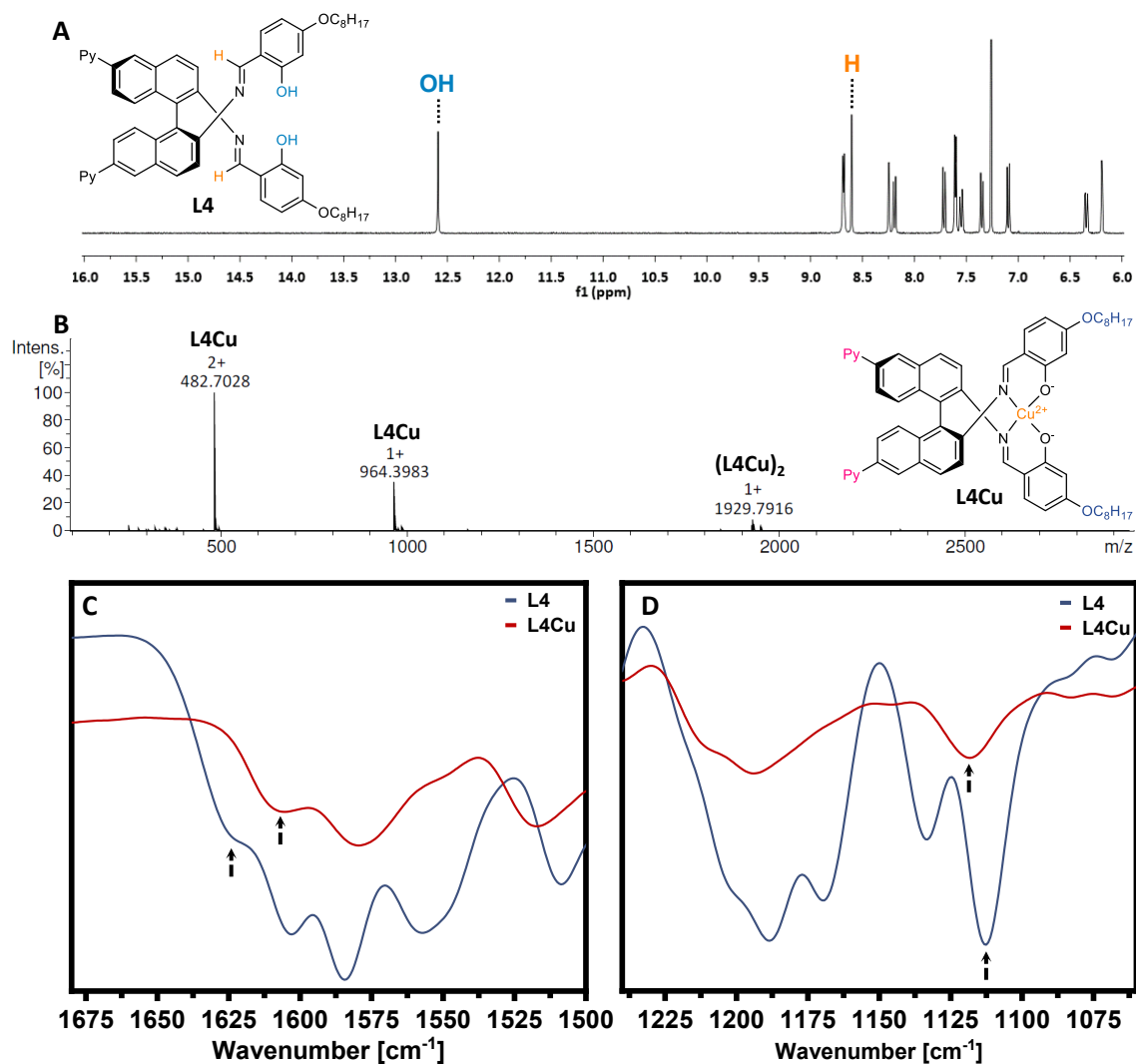


Figure 7.27: NMR spectrum of L4 (A), mass spectrum of L4Cu (B) and relevant sections of the IR spectra of L4 (blue) and L4Cu (red) reconfirm the formation of ligand and complex.

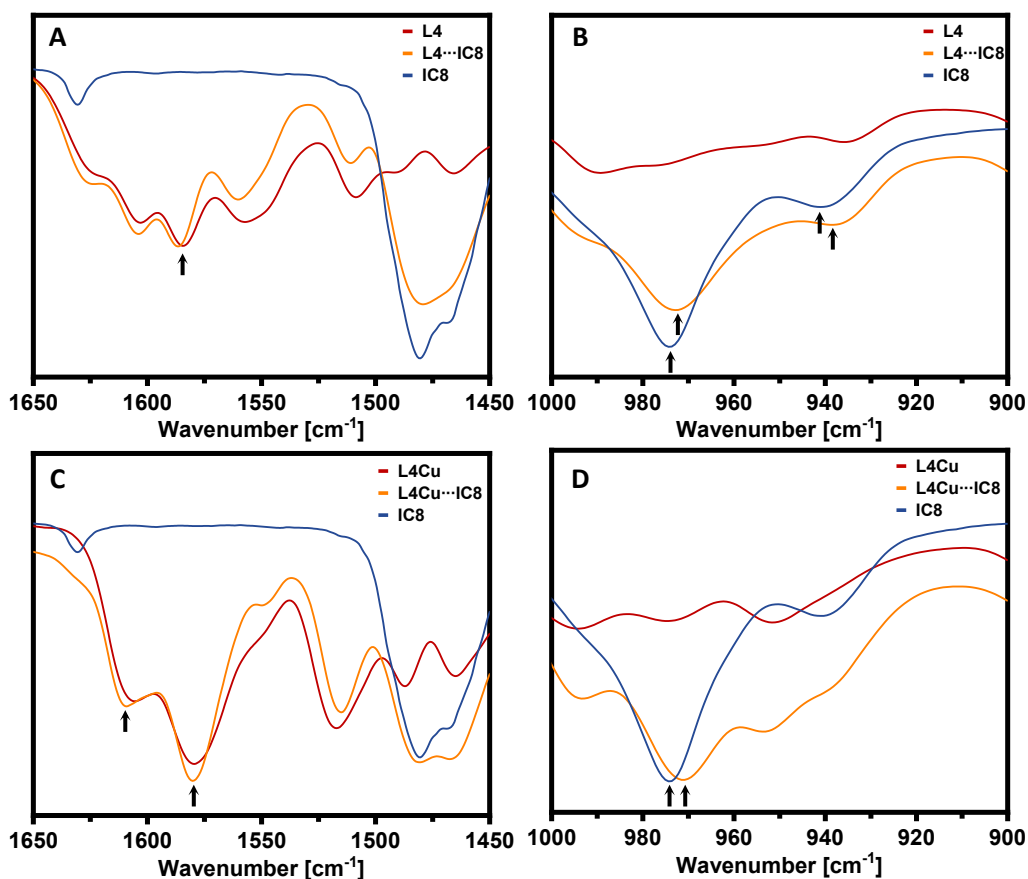


Figure 7.28: Overlay of sections of the IR spectra of L4-IC8 (A/B) and L4Cu-IC8 (C/D) and their individual building blocks.

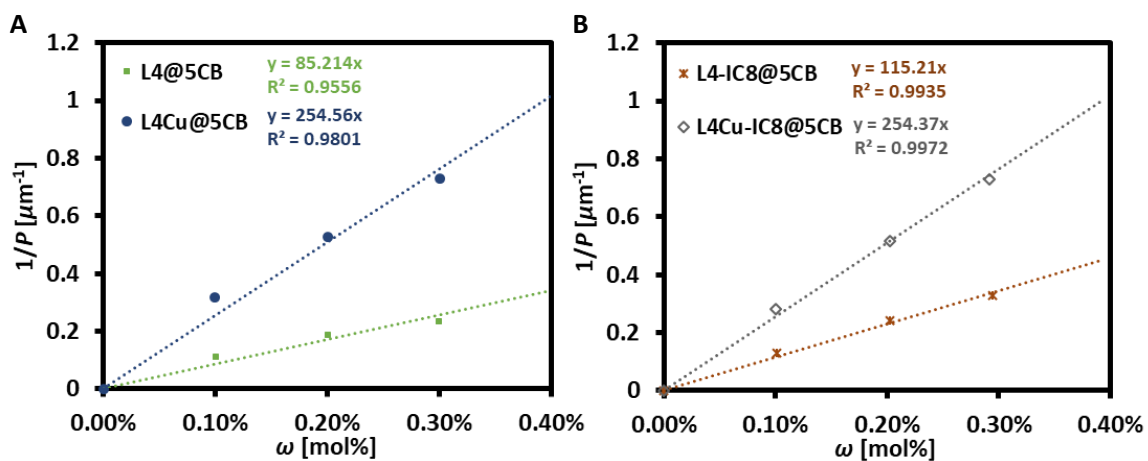


Figure 7.29: Linear plots of the inverse of the helical pitch as a function of the dopant concentration of dopants L4 and L4Cu (A) and XB-dopants L4-IC8 and L4Cu (B) in 5CB.

Table 7.3: Summary of the HTP values of L4 and L4Cu and their XB assemblies with IC8 in 5CB.

Dopant	HTP ( $\beta_M$ ) [ $\mu\text{m}^{-1}$ ]
L4	$85 \pm 6$
L4Cu	$254 \pm 12$
L4-IC8	$115 \pm 3$
L4Cu-IC8	$254 \pm 5$

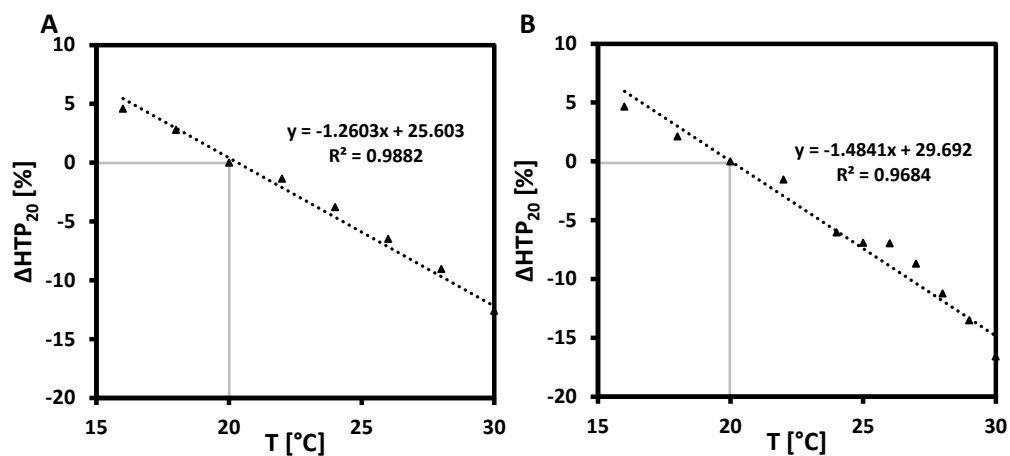


Figure 7.30: Linear plots of the relative HTP changes as a function of the temperature of L2 (A) and L4 (B).

Table 7.4: HTP Values and Temperature dependence of chiral BINIM dopants.

Dopant	HTP ( $\beta_M$ ) [ $\mu\text{m}^{-1}$ ]	$\Delta\text{HTP}_{\text{t.d.}}$ [%·°C <sup>-1</sup> ]
L2	$199 \pm 3$	$-1.26 \pm 0.05$
L3	$318 \pm 8$	N/D
L4	$85 \pm 6$	$-1.42 \pm 0.08$
L4Cu···IC8	$115 \pm 3$	$-1.72 \pm 0.04$

---

## 8. Literature

---

- [1] J. Lehn, *Science* **1993**, 260, 1762.
- [2] H. J. Schneider, A. K. Yatsimirsky, *Chem. Soc. Rev.* **2008**, 37, 263.
- [3] N. Basilio, U. Pischel, *Chem. Eur. J.* **2016**, 22, 15208.
- [4] S. Valimaki, N. K. Beyeh, V. Linko, R. H. A. Ras, M. A. Kostiainen, *Nanoscale* **2018**, 10, 14022.
- [5] R. Dong, Y. Zhou, X. Huang, X. Zhu, Y. Lu, J. Shen, *Adv. Mater.* **2015**, 27, 498.
- [6] P. Besenius, G. Portale, P. H. Bomans, H. M. Janssen, A. R. Palmans, E. W. Meijer, *PNAS* **2010**, 107, 17888.
- [7] M. Suárez, J.-M. Lehn, S. C. Zimmerman, A. Skoulios, B. Heinrich, *J. Am. Chem. Soc.* **1998**, 120, 9526.
- [8] J. Xu, X. Liu, J. K.-P. Ng, T. Lin, C. He, *J. Mater. Chem.* **2006**, 16, 3540.
- [9] M. Pfletscher, C. Wolper, J. S. Gutmann, M. Mezger, M. Giese, *Chem. Commun.* **2016**, 52, 8549.
- [10] J. M. T. Thompson, P. A. Gale, *Phil. Trans. R. Soc. Lond. A* **2000**, 358, 431.
- [11] S. Sivakova, S. J. Rowan, *Chem. Soc. Rev.* **2005**, 34, 9.
- [12] Y. Hisamatsu, S. Banerjee, M. B. Avinash, T. Govindaraju, C. Schmuck, *Angew. Chem. Int. Ed.* **2013**, 52, 12550.
- [13] M. Li, M. Radic Stojkovic, M. Ehlers, E. Zellermann, I. Piantanida, C. Schmuck, *Angew. Chem. Int. Ed.* **2016**, 55, 13015.
- [14] E. Moulin, L. Faour, C. C. Carmona-Vargas, N. Giuseppone, *Adv. Mater.* **2019**, 32, 1906036.
- [15] K. Liu, Y. Kang, Z. Wang, X. Zhang, *Adv. Mater.* **2013**, 25, 5530.
- [16] Y. Yang, X. Ding, M. W. Urban, *Prog. Polym. Sci.* **2015**, 49-50, 34.
- [17] Y. Yang, M. W. Urban, *Chem. Soc. Rev.* **2013**, 42, 7446.
- [18] X. Yan, F. Wang, B. Zheng, F. Huang, *Chem. Soc. Rev.* **2012**, 41, 6042.
- [19] J. W. Steed, J. L. Atwood, *Supramolecular Chemistry*, John Wiley & Sons, Ltd, Chichester, UK **2009**.
- [20] G. W. Gokel, J. L. Atwood, Eds., in *Comprehensive Supramolecular Chemistry II: General Principles of Supramolecular Chemistry and Molecular Recognition*, Vol. 1, Elsevier, Oxford **2017**.
- [21] K. Rissanen, *CrystEngComm* **2008**, 10, 1107.
- [22] G. R. Desiraju, P. S. Ho, L. Kloo, A. C. Legon, R. Marquardt, P. Metrangolo, P. Politzer, G. Resnati, K. Rissanen, *Pure Appl. Chem.* **2013**, 85, 1711.
- [23] T. Caronna, R. Liantonio, T. A. Logothetis, P. Metrangolo, T. Pilati, G. Resnati, *J. Am. Chem. Soc.* **2004**, 126, 4500.
- [24] R. Puttreddy, O. Jurcek, S. Bhowmik, T. Makela, K. Rissanen, *Chem. Commun.* **2016**, 52, 2338.
- [25] R. B. Walsh, C. W. Padgett, P. Metrangolo, G. Resnati, T. W. Hanks, W. T. Pennington, *Cryst. Growth Des.* **2001**, 1, 165.
- [26] G. Berger, J. Soubhye, F. Meyer, *Polym. Chem.* **2015**, 6, 3559.
- [27] A. Priimagi, G. Cavallo, A. Forni, M. Gorynsztejn-Leben, M. Kaivola, P. Metrangolo, R. Milani, A. Shishido, T. Pilati, G. Resnati, G. Terraneo, *Adv. Funct. Mater.* **2012**, 22, 2572.
- [28] J. E. Stumpel, M. Saccone, V. Dichiarante, O. Lehtonen, M. Virkki, P. Metrangolo, A. Priimagi, *Molecules* **2017**, 22, 1844.
- [29] D. W. Bruce, P. Metrangolo, F. Meyer, T. Pilati, C. Prasang, G. Resnati, G. Terraneo, S. G. Wainwright, A. C. Whitwood, *Chem. Eur. J.* **2010**, 16, 9511.
- [30] Y. Chen, H. Yu, L. Zhang, H. Yang, Y. Lu, *Chem. Commun.* **2014**, 50, 9647.
- [31] F. Fernandez-Palacio, M. Poutanen, M. Saccone, A. Siiskonen, G. Terraneo, G. Resnati, O. Ikkala, P. Metrangolo, A. Priimagi, *Chem. Mater.* **2016**, 28, 8314.
- [32] L. González, N. Gimeno, R. M. Tejedor, V. Polo, M. B. Ros, S. Uriel, J. L. Serrano, *Chem. Mater.* **2013**, 25, 4503.
- [33] P. Metrangolo, C. Prasang, G. Resnati, R. Liantonio, A. C. Whitwood, D. W. Bruce, *Chem. Commun.* **2006**, 3290.
-

- [34] H. L. Nguyen, P. N. Horton, M. B. Hursthouse, A. C. Legon, D. W. Bruce, *J. Am. Chem. Soc.* **2004**, 126, 16.
- [35] P. Metrangolo, G. Resnati, Eds., in *Halogen Bonding II: Impact on Materials Chemistry and Life Sciences*, Springer-Verlag, Berlin, Heidelberg, New York **2015**.
- [36] P. Politzer, J. S. Murray, *Theor. Chem. Acc.* **2002**, 108, 134.
- [37] P. Politzer, D. G. Truhlar, *Chemical Applications of Atomic and Molecular Electrostatic Potentials: Reactivity, Structure, Scattering, and Energetics of Organic, Inorganic, and Biological Systems*, Springer US, **1981**.
- [38] J. S. Murray, P. Lane, P. Politzer, *J. Mol. Model* **2009**, 15, 723.
- [39] P. Politzer, J. S. Murray, T. Clark, *Phys. Chem. Chem. Phys.* **2013**, 15, 11178.
- [40] T. Clark, M. Hennemann, J. S. Murray, P. Politzer, *J. Mol. Model* **2007**, 13, 291.
- [41] P. Politzer, J. S. Murray, P. Lane, *Int. Journal Quantum Chem.* **2007**, 107, 3046.
- [42] S. C. Nyburg, C. H. Faerman, *Acta Cryst.* **1985**, B41, 274.
- [43] P. Scilabra, G. Terraneo, G. Resnati, *J. Fluor. Chem.* **2017**, 203, 62.
- [44] J. Fanfrlik, W. Zierkiewicz, P. Svec, Z. Ruzickova, J. Rezac, M. Michalczyk, A. Ruzicka, D. Michalska, P. Hobza, *J. Mol. Model* **2017**, 23, 328.
- [45] W. Wang, B. Ji, Y. Zhang, *J. Phys. Chem. A* **2009**, 113, 8132.
- [46] C. B. Aakeroy, D. L. Bryce, G. R. Desiraju, A. Frontera, A. C. Legon, F. Nicotra, K. Rissanen, S. Scheiner, G. Terraneo, P. Metrangolo, G. Resnati, *Pure Appl. Chem.* **2019**, 91, 1889.
- [47] G. R. Desiraju, R. Parthasarathy, *J. Am. Chem. Soc.* **1989**, 111, 8725.
- [48] P. Metrangolo, G. Resnati, *IUCrJ* **2014**, 1, 5.
- [49] A. Forni, P. Metrangolo, T. Pilati, G. Resnati, *Cryst. Growth Des.* **2004**, 4, 291.
- [50] S. H. Jungbauer, S. M. Walter, S. Schindler, L. Rout, F. Kniep, S. M. Huber, *Chem. Commun.* **2014**, 50, 6281.
- [51] F. C. Pigge, V. R. Vangala, D. C. Swenson, *Chem. Commun.* **2006**, 2123.
- [52] V. Dichiarante, T. Kaiho, P. Metrangolo, T. Pilati, G. Resnati, G. Terraneo, M. Ursini, *Chem. Commun.* **2019**, 55, 4234.
- [53] T. A. Schaub, R. Sure, F. Hampel, S. Grimme, M. Kivala, *Chem. Eur. J.* **2017**, 23, 5687.
- [54] J. W. Zou, Y. J. Jiang, M. Guo, G. X. Hu, B. Zhang, H. C. Liu, Q. S. Yu, *Chem. Eur. J.* **2005**, 11, 740.
- [55] C. Präsang, A. C. Whitwood, D. W. Bruce, *Cryst. Growth Des.* **2009**, 9, 5319.
- [56] K. E. Riley, J. S. Murray, J. Fanfrlik, J. Rezac, R. J. Sola, M. C. Concha, F. M. Ramos, P. Politzer, *J. Mol. Model* **2011**, 17, 3309.
- [57] F. Topic, K. Rissanen, *J. Am. Chem. Soc.* **2016**, 138, 6610.
- [58] A. Jamadar, A. Das, *Polym. Chem.* **2020**, 11, 385.
- [59] A. Vargas Jentsch, S. Matile, *J. Am. Chem. Soc.* **2013**, 135, 5302.
- [60] V. Govindaraj, H. Ungati, S. R. Jakka, S. Bose, G. Muges, *Chem. Eur. J.* **2019**, 25, 11180.
- [61] A. Jamadar, C. K. Karan, L. Roy, A. Das, *Langmuir* **2020**.
- [62] A. Huang, L. Zhou, D. Zhang, J. Yao, Y. Zhang, *J. Mol. Graph. Model.* **2016**, 70, 40.
- [63] C. Tschierske, Ed. in *Liquid Crystals: Materials Design and Self-assembly*, Springer Berlin, Berlin **2014**.
- [64] T. Kato, Ed. in *Liquid Crystalline Functional Assemblies and Their Supramolecular Structures*, Vol. 128, Springer Berlin Heidelberg, Berlin, Heidelberg **2008**.
- [65] C. Tschierske, *Annu. Rep. Prog. Chem. C* **2001**, 97, 191.
- [66] A. Ramamoorthy, *Thermotropic Liquid Crystals: Recent Advances*, Springer, Dordrecht **2007**.
- [67] V. M. Balasubramaniam, S. K. Sastry, *J. Food Eng.* **1995**, 26, 219.
- [68] J. F. Algorri, V. Urruchi, N. Bennis, J. M. Sánchez-Pena, *IEEE Electron Device Lett.* **2014**, 35, 666.
- [69] C. R. Smith, D. R. Sabatino, T. J. Praisner, *Exp. Fluids* **2001**, 30, 190±201.
- [70] J. Pan, S. Liu, Y. Yang, J. Lu, *Nanomaterials* **2018**, 8, 413.
- [71] A. G. P. Kottapalli, M. Asadnia, J. M. Miao, G. Barbastathis, M. S. Triantafyllou, *Smart Mater. Struct.* **2012**, 21, 115030.

- [72] P. Kirsch, M. Bremer, *Angew. Chem. Int. Ed.* **2000**, 39, 4216.
- [73] P. Kirsch, *J. Fluor. Chem.* **2015**, 177, 29.
- [74] A. J. Seed, M. E. Walsh, J. W. Doane, A. Khan, *Mol. Cryst. Liq. Cryst.* **2010**, 410, 201.
- [75] K. K. Chaudhary, P. Kannoja, N. Mishra, in *Novel Approaches for Drug Delivery* **2017**, Ch. 9, 217.
- [76] C. Guo, J. Wang, F. Cao, R. J. Lee, G. Zhai, *Drug Discov. Today* **2010**, 15, 1032.
- [77] J. Mo, G. Milleret, M. Nagaraj, *Liq. Cryst. Rev.* **2017**, 5, 69.
- [78] C. R. Safinya, K. K. Ewert, C. Leal, *Liq. Cryst.* **2011**, 38, 1715.
- [79] A. Pardakhty, E. Moazeni, *Nanomed. J.* **2013**, 1, 1.
- [80] R. J. Mandle, J. W. Goodby, in *Handbook of Liquid Crystals*, Wiley-VCH **2014**, Ch. 6, 1.
- [81] H. Stegemeyer, Ed. in *Lyotrope Flüssigkristalle: Grundlagen, Entwicklung, Anwendung*, Steinkopff, Darmstadt **1999**.
- [82] C. Tschierske, *Angew. Chem. Int. Ed.* **2013**, 52, 8828.
- [83] S. Kumar, *Liquid Crystals: Experimental Study of Physical Properties and Phase Transitions*, Cambridge University Press, Cambridge **2001**.
- [84] S. J. Cowling, in *Handbook of Liquid Crystals* **2014**, 1.
- [85] H. T. Srinivasa, *Mol. Cryst. Liq. Cryst.* **2019**, 680, 10.
- [86] H.-S. Kitzerow, C. Bahr, Eds., in *Chirality in Liquid Crystals*, Springer, **2001**.
- [87] C. Tschierske, *Liq. Cryst.* **2018**, 45, 2221.
- [88] J. W. Goodby, *Current Opinion in Colloid & Interface Science* **2002**, 7, 326.
- [89] L. Rao, Z. Ge, S.-T. Wu, S. H. Lee, *Applied Physics Letters* **2009**, 95, 231101.
- [90] Z. Ge, L. Rao, S. Gauza, S.-T. Wu, *J. Disp. Technol.* **2009**, 5, 250.
- [91] P. J. Jessy, V. Bambole, R. R. Deshmukh, N. Patel, *J. Mol. Liq.* **2019**, 281, 480.
- [92] L.-L. Tian, F. Chu, H. Dou, L. Li, Q.-H. Wang, *Liquid Crystals* **2019**, 46, 1353.
- [93] M. Saccone, M. Pfletscher, E. Dautzenberg, R. Y. Dong, C. A. Michal, M. Giese, *J. Mater. Chem. C* **2019**, 7, 3150.
- [94] N. Okada, D. Zhu, D. Cai, J. B. Cole, M. Kambe, S. Kinoshita, *J. Opt.* **2012**, 42, 25.
- [95] R. O. Prum, R. L. Morrison, G. R. Ten Eyck, *J. Morphol.* **1994**, 222, 61.
- [96] S. Vignolini, P. J. Rudall, A. V. Rowland, A. Reed, E. Moyroud, R. B. Faden, J. J. Baumberg, B. J. Glover, U. Steiner, *PNAS* **2012**, 109, 15712.
- [97] R. Eelkema, B. L. Feringa, *Org. Biomol. Chem.* **2006**, 4, 3729.
- [98] M. Mathews, N. Tamaoki, *J. Am. Chem. Soc.* **2008**, 130, 11409.
- [99] L. Shang, W. Zhang, K. Xu, Y. Zhao, *Mater. Horiz.* **2019**, 6, 945.
- [100] G. Chilaya, *Revue Phys. Appl.* **1981**, 16, 193.
- [101] M. R. Wilson, D. J. Earl, *J. Mater. Chem.* **2001**, 11, 2672.
- [102] Ł. Duda, M. Czajkowski, B. Potaniec, P. Vaňkátová, *Liq. Cryst.* **2019**, 46, 1769.
- [103] H. J. Deußen, P. V. Shibaev, R. Vinokur, T. Bjørnholm, K. Schaumburg, K. Bechgaard, V. P. Shibaev, *Liq. Cryst.* **1996**, 21, 327.
- [104] H. Finkelmann, H. Stegemeyer, *Ber. Bunsenges. Phys. Chem.* **1978**, 82, 1302.
- [105] M. Saito, H. Sato, Y. Mori, Y. Fukuda, *Bull. Chem. Soc. Jpn.* **2009**, 82, 1266.
- [106] G. Gottarelli, G. P. Spada, *J. Org. Chem.* **1986**, 51, 589.
- [107] G. Quintieri, M. Saccone, M. Spengler, M. Giese, A. H. Gröschel, *Nanomaterials* **2018**, 8, 1029.
- [108] C. Fouquey, J. M. Lehn, A. M. Levelut, *Adv. Mater.* **1990**, 2, 254.
- [109] T. Kato, J. M. J. Frechet, *Macromolecules* **1989**, 22, 3818.
- [110] T. Kato, J. Uchida, T. Ichikawa, B. Soberats, *Polym. J.* **2018**, 50, 149.
- [111] M. Suárez, J.-M. Lehn, S. C. Zimmerman, A. Skoulios, B. Heinrich, *Journal of the American Chemical Society* **1998**, 120, 9526.
- [112] K.-M. Lee, Y.-T. Lee, I. J. B. Lin, *J. Mater. Chem.* **2003**, 13, 1079.
- [113] J.-F. Xiong, S.-H. Luo, J.-P. Huo, J.-Y. Liu, S.-X. Chen, Z.-Y. Wang, *J. Org. Chem.* **2014**, 79, 8366.
- [114] B. Feringán, P. Romero, J. L. Serrano, R. Giménez, T. Sierra, *Chem. Eur. J.* **2015**, 21, 8859.
- [115] M. Chawla, R. Kumar, P. F. Siril, *J. Mol. Catal. A: Chem.* **2016**, 423, 126.

- 
- [116] N. Herzer, H. Guneysu, D. J. Davies, D. Yildirim, A. R. Vaccaro, D. J. Broer, C. W. Bastiaansen, A. P. Schenning, *J. Am. Chem. Soc.* **2012**, 134, 7608.
- [117] Y. Ni, X. Li, J. Hu, S. Huang, H. Yu, *Chem. Mater.* **2019**, 31, 3388.
- [118] Y. Huang, D. Wang, L. Xu, Y. Cong, J. Li, L. Li, *Eur. Polym. J.* **2013**, 49, 1682.
- [119] T. Kato, J. M. J. Frechet, *Macromol. Symp.* **1995**, 98, 311.
- [120] T. Kato, N. Mizoshita, K. Kanie, *Macromol. Rapid Commun.* **2001**, 22, 797.
- [121] C. M. Paleos, D. Tsiourvas, *Liq. Cryst.* **2001**, 28, 1127.
- [122] M. Saccone, M. Pfletscher, S. Kather, C. Wölper, C. Daniliuc, M. Mezger, M. Giese, *J. Mater. Chem. C* **2019**, 7, 8643.
- [123] M. Pfletscher, M. Mezger, M. Giese, *Soft. Matter.* **2018**, 14, 6214.
- [124] M. Spengler, R. Y. Dong, C. A. Michal, M. Pfletscher, M. Giese, *J. Mater. Chem. C* **2017**, 5, 2235.
- [125] R. Bertani, P. Metrangolo, A. Moiana, E. Perez, T. Pilati, G. Resnati, I. Rico-Lattes, A. Sassi, *Adv. Mater.* **2002**, 14, 1197.
- [126] D. W. Bruce, P. Metrangolo, F. Meyer, C. Präsang, G. Resnati, G. Terraneo, A. C. Whitwood, *New J. Chem.* **2008**, 32, 477.
- [127] D. Bleger, J. Schwarz, A. M. Brouwer, S. Hecht, *J. Am. Chem. Soc.* **2012**, 134, 20597.
- [128] C. Knie, M. Utecht, F. Zhao, H. Kulla, S. Kovalenko, A. M. Brouwer, P. Saalfrank, S. Hecht, D. Bléger, *Chem. Eur. J.* **2014**, 20, 16492.
- [129] J. Moreno, M. Gerecke, L. Grubert, S. A. Kovalenko, S. Hecht, *Angew. Chem. Int. Ed.* **2016**, 55, 1544.
- [130] S. Castellanos, A. Goulet-Hanssens, F. Zhao, A. Dikhtiarenko, A. Pustovarenko, S. Hecht, J. Gascon, F. Kapteijn, D. Bléger, *Chem. Eur. J.* **2016**, 22, 746.
- [131] R. Saha, G. Babakhanova, Z. Parsouzi, M. Rajabi, P. Gyawali, C. Welch, G. H. Mehl, J. Gleeson, O. D. Lavrentovich, S. Sprunt, A. Jáklí, *Mater. Horiz.* **2019**, 6, 1905.
- [132] Y. Mizumura, D. Högberg, K. Arai, J. Sakuda, B. Soberats, M. Yoshio, T. Kato, *Bull. Chem. Soc. Jpn.* **2019**, 92, 1226.
- [133] A. Kumar, A. K. Srivastava, S. N. Tiwari, N. Misra, D. Sharma, *Mol. Cryst. Liq. Cryst.* **2019**, 681, 23.
- [134] R. Chang, F. B. Jones, J. J. Ratto, *Mol. Cryst. Liq. Cryst.* **2007**, 33, 13.
- [135] A. T. M. Marcelis, A. Koudijs, E. J. R. Sudhölter, *Liq. Cryst.* **2006**, 18, 843.
- [136] L. V. Politanskaya, I. P. Chuikov, E. A. Kolodina, M. S. Shvartsberg, V. D. Shteingarts, *J. Fluor. Chem.* **2012**, 135, 97.
- [137] R. Weiss, F. G. Pühlhofer, *J. Am. Chem. Soc.* **2007**, 129, 547.
- [138] G. Cavallo, P. Metrangolo, R. Milani, T. Pilati, A. Priimagi, G. Resnati, G. Terraneo, *Chem. Rev.* **2016**, 116, 2478.
- [139] A. Priimagi, M. Saccone, G. Cavallo, A. Shishido, T. Pilati, P. Metrangolo, G. Resnati, *Adv. Mater.* **2012**, 24, OP345.
- [140] H. Wang, H. K. Bisoyi, L. Wang, A. M. Urbas, T. J. Bunning, Q. Li, *Angew. Chem. Int. Ed.* **2018**, 57, 1627.
- [141] S. Grimme, *J. Comput. Chem.* **2006**, 27, 1787.
- [142] K. Eichkorn, F. Weigend, O. Treutler, R. Ahlrichs, *Theor. Chem. Acc.* **1997**, 97, 119.
- [143] S. Grimme, J. Antony, S. Ehrlich, H. Krieg, *J. Chem. Phys.* **2010**, 132, 154104.
- [144] F. Weigend, M. Häser, H. Patzelt, R. Ahlrichs, *Chem. Phys. Lett.* **1998**, 294, 143.
- [145] C. B. Aakeroy, M. Baldrighi, J. Desper, P. Metrangolo, G. Resnati, *Chem. Eur. J.* **2013**, 19, 16240.
- [146] S. V. Rosokha, M. K. Vinakos, *Cryst. Growth Des.* **2012**, 12, 4149.
- [147] J. S. Murray, P. Politzer, *Croat. Chem. Acta* **2009**, 1, 267.
- [148] E. D'Oria, J. J. Novoa, *CrystEngComm* **2004**, 6, 367.
- [149] A. Gavezzotti, in *Advanced X-Ray Crystallography* (Ed: K. Rissanen), Springer Berlin Heidelberg, Berlin, Heidelberg **2012**, 1.
- [150] J. Dunitz, *IUCrJ* **2015**, 2, 157.
- [151] S. Alvarez, *Dalton Trans.* **2013**, 42, 8617.
- [152] J. P. M. Lommerse, A. J. Stone, R. Taylor, F. H. Allen, *J. Am. Chem. Soc.* **1996**, 118, 3108.
-

- [153] M. Saccone, G. Terraneo, T. Pilati, G. Cavallo, A. Priimagi, P. Metrangolo, G. Resnati, *Acta Cryst.* **2014**, 70, 149.
- [154] M. Saccone, M. Spengler, M. Pfletscher, K. Kuntze, M. Virkki, C. Wölper, R. Gehrke, G. Jansen, P. Metrangolo, A. Priimagi, M. Giese, *Chem. Mater.* **2019**, 31, 462.
- [155] J. Kim, H. Yoshida, H. Moritake, M. Ozaki, *Ferroelectrics* **2012**, 431, 74.
- [156] P. J. Collings, J. W. Goodby, *Introduction to Liquid Crystals: Chemistry and Physics, Second Edition*, CRC Press, **2019**.
- [157] M. Hird, *Chem. Soc. Rev.* **2007**, 36, 2070.
- [158] J. W. Goodby, I. M. Saez, S. J. Cowling, J. S. Gasowska, R. A. MacDonald, S. Sia, P. Watson, K. J. Toyne, M. Hird, R. A. Lewis, S.-E. Lee, V. Vaschenko, *Liq. Cryst.* **2009**, 36, 567.
- [159] M. Syz, H. Zollinger, *Fasciculus 2* **1965**, 48, 383.
- [160] N. Houbenov, R. Milani, M. Poutanen, J. Haataja, V. Dichiarante, J. Sainio, J. Ruokolainen, G. Resnati, P. Metrangolo, O. Ikkala, *Nat. Commun.* **2014**, 5, 4043.
- [161] M. Pfletscher, S. Hölscher, C. Wölper, M. Mezger, M. Giese, *Chem. Mater.* **2017**, 29, 8462.
- [162] O. S. Bushuyev, T. Friščić, C. J. Barrett, *CrystEngComm* **2016**, 18, 7204.
- [163] Z. Ahmed, A. Siiskonen, M. Virkki, A. Priimagi, *Chem. Commun.* **2017**, 53, 12520.
- [164] X. Tong, G. Wang, Y. Zhao, *J. Am. Chem. Soc.* **2006**, 128, 8746.
- [165] X. Tong, Y. Zhao, *Chem. Mater.* **2009**, 21, 4047.
- [166] R. Y. Dong, C. A. Michal, M. Saccone, M. Spengler, C. Wölper, M. Giese, *Chem. Phys. Lett.* **2018**, 710, 39.
- [167] I. Dierking, *Textures of Liquid Crystals*, WILEY-VCH, **2003**.
- [168] F. Malotke, M. Saccone, C. Wölper, R. Y. Dong, C. A. Michal, M. Giese, *Mol. Syst. Des. Eng.* **2020**, 5, 1299.
- [169] D. F. Ester, V. E. Williams, *Liq. Cryst.* **2018**, 46, 76.
- [170] F. Grandjean, R. Cano, *Acad. Sci.* **1921**, 172.
- [171] R. Cano, *Bull. Soc. Franc. Mineral. Crist.* **1967**, 90.
- [172] G. Heppke, F. Oestreicher, *Z. Naturforsch.* **1977**, 32, 899.
- [173] Y. Li, M. Wang, A. Urbas, Q. Li, *J. Mater. Chem. C* **2013**, 1.
- [174] R. D. Kamien, in *Soft Matter Self-Assembly*, Vol. 193 (Eds: C. N. Likos, F. Sciortino, P. Zihlerl, E. Zaccarelli), IOS Press, Amsterdam **2016**, 417.
- [175] P. Im, Y. J. Choi, W. J. Yoon, D. G. Kang, M. Park, D. Y. Kim, C. R. Lee, S. Yang, J. H. Lee, K. U. Jeong, *Sci. Rep.* **2016**, 6, 36472.
- [176] H.-G. Kuball, B. Weiß, A. K. Beck, D. Seebach, *Helv. Chim. Acta* **1997**, 80, 2507.
- [177] K. Kishikawa, Y. Furukawa, T. Watanabe, M. Kohri, T. Taniguchi, S. Kohmoto, *Liq. Cryst.* **2016**, 44, 956.
- [178] M. Z. Alam, T. Yoshioka, T. Ogata, T. Nonaka, S. Kurihara, *Chem. Eur. J.* **2007**, 13, 2641.
- [179] R. Kaushik, A. Ghosh, D. Amilan Jose, *Coord. Chem. Rev.* **2017**, 347, 141.
- [180] S. S. Shendage, V. L. Patil, S. A. Vanalakar, S. P. Patil, N. S. Harale, J. L. Bhosale, J. H. Kim, P. S. Patil, *Sens. Actuators B Chem.* **2017**, 240, 426.
- [181] Y. Zhou, G. Liu, X. Zhu, Y. Guo, *Sens. Actuators B Chem.* **2017**, 251, 280.
- [182] D. L. Kamble, N. S. Harale, V. L. Patil, P. S. Patil, L. D. Kadam, *J. Anal. Appl. Pyrolysis* **2017**, 127, 38.
- [183] S. Liu, Z. Wanga, Y. Zhanga, C. Zhanga, T. Zhang, *Sens. Actuators B Chem.* **2015**, 211, 318.
- [184] Y. Xia, J. Wang, J. L. Xu, X. Li, D. Xie, L. Xiang, S. Komarneni, *ACS Appl. Mater. Interfaces* **2016**, 8, 35454.
- [185] S. T. Shishiyanu, T. S. Shishiyanu, O. I. Lupan, *Sens. Actuators B Chem.* **2005**, 107, 379.
- [186] K. K. Sadasivuni, D. Ponnamma, H.-U. Ko, H. C. Kim, L. Zhai, J. Kim, *Sens. Actuators B Chem.* **2016**, 233, 633.
- [187] H. Ma, L. Yu, X. Yuan, Y. Li, C. Li, M. Yin, X. Fan, *J. Alloys Compd.* **2019**, 782, 1121.
- [188] J. D. Wright, P. Roisin, G. P. Rigby, R. J. M. Nolte, M. J. Cook, S. C. Thorpe, *Sens. Actuators B Chem.* **1993**, 13-14, 276.
- [189] N. Kılınc, S. Öztürk, D. Atilla, A. G. Gürek, V. Ahsen, Z. Z. Öztürk, *Sens. Actuators B Chem.* **2012**, 173, 203.
- [190] J. Shi, L. Luan, W. Fang, T. Zhao, W. Liu, D. Cui, *Sens. Actuators B Chem.* **2014**, 204, 218.

- 
- [191] D. M. Krichevsky, A. V. Zasedatelev, A. Y. Tolbin, S. Y. Luchkin, A. B. Karpo, V. I. Krasovskii, L. G. Tomilova, *Thin Solid Films* **2017**, 642, 295.
- [192] A. D. Gülmez, M. S. Polyakov, V. V. Volchek, S. T. Kostakoğlu, A. A. Esenpinar, T. V. Basova, M. Durmuş, A. G. Gürek, V. Ahsen, H. A. Banimuslem, A. K. Hassan, *Sens. Actuators B Chem.* **2017**, 241, 364.
- [193] A. Sen, K. A. Kupcho, B. A. Grinwald, H. J. Vantreeck, B. R. Acharya, *Sens. Actuators B Chem.* **2013**, 178, 222.
- [194] Y. Han, K. Pacheco, C. W. M. Bastiaansen, D. J. Broer, R. P. Sijbesma, *J. Am. Chem. Soc.* **2010**, 132, 2961.
- [195] L. Pschyklenk, T. Wagner, A. Lorenz, P. Kaul, *ACS Appl. Polym. Mater.* **2020**, 2, 1925.
- [196] L. Leoni, R. Puttreddy, O. Jurcek, A. Mele, I. Giannicchi, F. Y. Mihan, K. Rissanen, A. Dalla Cort, *Chem. Eur. J.* **2016**, 22, 18714.
- [197] L. Leoni, A. Dalla Cort, *Inorganics* **2018**, 6.
- [198] M. Cametti, M. Nissinen, A. Dalla Cort, L. Mandolini, K. Rissanen, *J. Am. Chem. Soc.* **2005**, 127, 3831.
- [199] F. F. van de Watering, M. Lutz, W. I. Dzik, B. de Bruin, J. N. Reek, *ChemCatChem* **2016**, 8, 2752.
- [200] Y.-M. Shen, W.-L. Duan, M. Shi, *J. Org. Chem.* **2003**, 68, 1559.
- [201] M. Benjamin, D. Manoj, K. Thenmozhi, P. R. Bhagat, D. Saravanakumar, S. Senthilkumar, *Biosens. Bioelectron.* **2017**, 91, 380.
- [202] C. Che, *Coord. Chem. Rev.* **2003**, 242, 97.
- [203] T. Katsuki, *Chem. Soc. Rev.* **2004**, 33, 437.
- [204] A. Sakakura, K. Suzuki, K. Ishihara, *Adv. Synth. Catal.* **2006**, 348, 2457.
- [205] M. Yoshimura, T. Muraoka, H. Nakatsuka, H. Huang, M. Kitamura, *J. Org. Chem.* **2010**, 75, 4315.
- [206] S. Ahn, S. Yamakawa, K. Akagi, *J. Mater. Chem. C* **2015**, 3, 3960.
- [207] M. Yoshimura, T. Muraoka, H. Nakatsuka, H. Huang, M. Kitamura, *J. Org. Chem.* **2010**, 75, 4315.
- [208] M. Blanke, M. Giese, *unpublished results* **2020**.
- [209] L. Meca, D. Řeha, Z. Havlas, *J. Org. Chem.* **2003**, 68, 5677.
- [210] D. C. Patel, R. M. Woods, Z. S. Breitbach, A. Berthod, D. W. Armstrong, *Tetrahedron: Asymmetry* **2017**, 28, 1557.
- [211] C. R. Bhattacharjee, C. Datta, G. Das, P. Mondal, *Phase Transit.* **2012**, 85, 956.
- [212] M. Ferguson, N. Giri, X. Huang, D. Apperley, S. L. James, *Green Chem.* **2014**, 16, 1374.
- [213] G. Gottarelli, M. Hibert, B. Samori, G. Solladie, G. P. Spada, R. Zimmermann, *J. Am. Chem. Soc.* **1983**, 105, 7318.
- [214] Y. Narazaki, H. Nishikawa, H. Higuchi, Y. Okumura, H. Kikuchi, *RSC Adv.* **2018**, 8, 971.
- [215] G. Gottarelli, G. Proni, G. P. Spada, *J. Org. Chem.* **1996**, 61, 2013.
- [216] C. Kühn, M. Bremer, P. R. Schreiner, *Liq. Cryst.* **2019**, 1.
- [217] A. Ferrarini, G. J. Moro, P. L. Nordio, *Phys. Rev. E* **1996**, 53, 681.
- [218] J. Yoshida, H. Sato, A. Yamagishi, N. Hoshino, *J. Am. Chem. Soc.* **2005**, 127, 8453.
- [219] N. Hoshino, Y. Matsuoka, K. Okamoto, A. Yamagishi, *J. Am. Chem. Soc.* **2003**, 125, 1718.
- [220] H. Sato, A. Yamagishi, J. Yoshida, H. Nakano, N. Hoshino, *Jpn. J. Appl. Phys.* **2005**, 44, 4067.
- [221] J. Yoshida, K. Kuwahara, S. Tamura, H. Yuge, G. Watanabe, *Mol. Cryst. Liq. Cryst.* **2017**, 647, 179.
- [222] G. Watanabe, J. Yoshida, *J. Phys. Chem. B* **2016**, 120, 6858.
- [223] A. Mouquinho, M. Saavedra, A. Maiou, K. Petrova, M. T. Barros, J. L. Figueirinhas, J. Sotomayor, *Mol. Cryst. Liq. Cryst.* **2011**, 542, 132.
- [224] Y.-L. Lee, C.-Y. Sheu, R.-H. Hsiao, *Sens. Actuators B Chem.* **2004**, 99, 281.
- [225] Y.-L. Lee, C.-Y. Hsiao, C.-H. Chang, Y.-M. Yang, *Sens. Actuators B Chem.* **2003**, 94, 169.
- [226] L. Lozzi, S. Picozzi, S. Santucci, C. Cantalini, B. Delley, *J. Electron Spectrosc. Relat. Phenom.* **2004**, 137-140, 101.
- [227] G. W. Gray, D. G. McDonnell, *Mol. Cryst. Liq. Cryst.* **1976**, 37, 189.
-

- 
- [228] H. K. Koduru, Y. G. Marinov, G. B. Hadjichristov, A. G. Petrov, N. Godbert, N. Scaramuzza, *J. Non Cryst. Solids* **2018**, 499, 107.
- [229] P. Crutzen, *Ann. Rev. Earth Planet. Sci.* **1979**, 7, 443.
- [230] L. Li, Z. Duan, H. Li, C. Zhu, G. Henkelman, J. S. Francisco, X. C. Zeng, *PNAS* **2018**, 115, 7236.
- [231] A. Hosseinian, Z. Asadi, L. Edjlali, A. Bekhradnia, E. Vessally, *Computational and Theoretical Chemistry* **2017**, 1106, 36.
- [232] R. Tongpool, S. Yoriya, *Thin Solid Films* **2005**, 477, 148.
- [233] B. Bialek, *Opt. Appl.* **2005**, 35, 323.
- [234] Z. Dong, X. Kong, Y. Wu, J. Zhang, Y. Chen, *Inorg. Chem. Commun.* **2017**, 77, 18.
- [235] K. J. Wallace, S. R. Cordero, C. P. Tan, V. M. Lynch, E. V. Anslyn, *Sens. Actuators B Chem.* **2007**, 120, 362.
- [236] M. Sun, H. Yu, H. Li, H. Xu, D. Huang, S. Wang, *Inorg. Chem.* **2015**, 54, 3766.
- [237] A. Mirzaei, S. S. Kim, H. W. Kim, *J. Hazard. Mater.* **2018**, 357, 314.
- [238] F. I. M. Ali, F. Awwad, Y. E. Greish, S. T. Mahmoud, *IEEE Sens. J.* **2019**, 19, 2394.
- [239] A. Sen, J. Albarella, J. Carey, P. Kim, W. McNamaraiii, *Sens. Actuators B Chem.* **2008**, 134, 234.
- [240] F. Malotke, M. Giese, *unpublished results* **2020**.
- [241] K. Kakisaka, H. Higuchi, Y. Okumura, H. Kikuchi, *Chem. Lett.* **2014**, 43, 624.
- [242] G. Proni, G. P. Spada, P. Lustenberger, R. Welti, F. Diederich, *J. Org. Chem.* **2000**, 65, 5522.
- [243] L. V. Politanskaya, V. D. Shteingarts, E. V. Tretyakov, *J. Fluor. Chem.* **2016**, 188, 85.
- [244] M. Giese, T. Krappitz, R. Y. Dong, C. A. Michal, W. Y. Hamad, B. O. Patrick, M. J. MacLachlan, *J. Mater. Chem. C* **2015**, 3, 1537.
- [245] S. Brasselet, F. Cherioux, P. Audebert, J. Zyss, *Chem. Mater.* **1999**, 11, 1915.
- [246] S. Yamakawa, K. Wada, M. Hidaka, T. Hanasaki, K. Akagi, *Adv. Funct. Mater.* **2019**, 29, 1806592.
- [247] Q. W. Zhang, D. Li, X. Li, P. B. White, J. Mecinovic, X. Ma, H. Agren, R. J. M. Nolte, H. Tian, *J. Am. Chem. Soc.* **2016**, 138, 13541.
-



---

## 9. Acknowledgements

---

Ganz besonders möchte ich mich bei *Jun. Prof. Dr. Michael Giese* für die Möglichkeit bedanken, die du mir gegeben hast, meine Promotion unter deiner Leitung anzufertigen und dafür, dass du mir dabei in den letzten 4 Jahren die Freiheiten gelassen hast, meine Ideen zu verfolgen und mir bei Problemen stets mit deinem Rat zur Seite gestanden hast.

Herr *Prof. Dr. Haberhauer*, Ihnen danke ich allem voran für die Übernahme der Zweitbegutachtung dieser Arbeit und für die wissenschaftlichen Ratschläge, die mir eine große Hilfe waren. Darüber hinaus bedanke ich mich bei Ihnen für die Nutzung Ihres CD-Spektrometers und bei *Petra Schneider* für deine Hilfe und die vielen unterhaltsamen Stunden während der Messungen.

*Prof. Dr. Peter Kaul* und *Lukas Pschyklenk* von der Fachhochschule Bonn-Rhein-Sieg gilt ein ganz besonders Dank. Ohne euer Equipment und vor allem deine fachliche Expertise, Lukas, wären die Gassensingexperimente und somit ein großer Teil dieser Arbeit in diesem Umfang niemals möglich gewesen.

I would also like to thank *Prof. Arri Priimägi*, *Kim Kuntze*, *Matti Virkki*, and all other cooperation partners from the Tampere University of Technology, Finland, for the execution and evaluation of the photo-switching experiments.

*Dr. Christoph Wölper* danke ich für die zahlreichen spontanen Gespräche und die viele Zeit, die du in die Lösung der Kristallstrukturen investiert hast.

Bei *Dr. Felix Niemeyer* und *Dr. Thorsten Schaller* möchte ich mich für euren Einsatz bedanken, immer die bestmöglichen NMR Spektren zur Verfügung zu stellen und für die zahlreichen NMR Messungen und Hilfestellungen bei der Auswertung auch noch so komplizierter Spektren.

Mein Dank geht ebenfalls an *Jun. Prof. Dr. Markus Mezger* vom Max-Planck-Institut für Polymerforschung in Mainz für die Zurverfügungstellung der Unterkunft, Räumlichkeiten und Messinstrumente für die SAXS und WAXS Messungen.

Bedanken möchte ich mich auch bei der Professor-Werdelmann Stiftung und dem Kuratorium für die finanzielle Unterstützung während der Zeit meiner Promotion.

---

Ein Großer Dank geht auch an die Mitarbeiter der Arbeitskreise Schmuck, Voskuhl, Niemeyer und Giese für eure Hilfe und Unterstützung und das gemeinsame Beisammensein während der vergangenen Jahre. Allen voran *Meik Blanke* und *Alexander Kappelt* danke ich für die vielen fachlichen und nicht-fachlichen Gespräche, die gemeinsame Zeit im Labor und die feierabendlichen Munchkin-Sessions als angenehme Abwechslung zum Laboralltag. Außerdem bedanken möchte ich mich bei *Kevin Rudolph*, *Simon Thölke*, *Angus Hawkey*, *Christopher Walters* und *Sascha Ernst*, sowie den Auszubildenden *Leonard Kaufmann*, *Christian Müller*, *Tobias Grünenbaum*, *Sarah Arnts*, *Sebastian Gehrke* und *Lina Lantermann* für eure Hilfsbereitschaft und Unterstützung bei der Synthese und wissenschaftlichen Arbeit.

*Fescilia Octa-Smolin*, *Meik Blanke*, und *Michael Pfletscher*, vielen Dank dafür, dass ihr euch der Korrektur meiner Arbeit angenommen habt und für die vielen und nützlichen Kommentare, Tipps und Hilfestellungen. Michael, dir danke ich dabei ganz besonders für deine Zeit und unsere ausgiebigen Gespräche.

Zu guter Letzt möchte ich mich bei meiner Familie bedanken, vor allem meiner Mutter *Karin* und meinem Vater *Reinhold*, dafür, dass Ihr mich die ganzen 28 Jahre begleitet habt, mir geholfen habt, wo immer ihr konntet, mich unterstützt habt, wie immer es euch möglich war und immer für mich da wart, wenn ich euch gebraucht habe.

*Danke! Thank you!*

---

---

## **10. Curriculum Vitae**

---

Der Lebenslauf ist in der Online-Version aus Gründen des Datenschutzes nicht enthalten.

---